UNIVERSITY OF SOUTHAMPTON

FACULTY OF ENGINEERING AND PHYSICAL SCIENCES

Optolelectronics Research Centre

The fabrication and characterization of infra-red optical fibre, ultra-thin fibre and large diameter chalcogenide glass

Bruno Jean Moog

A thesis submitted for the degree of Doctor of Philosophy

April 2021

UNIVERSITY OF SOUTHAMPTON

ABSTRACT

FACULTY OF ENGINEERING AND PHYSICAL SCIENCES
Optoelectronics Research Centre
Thesis for the degree of Doctor of Philosophy
Bruno Jean Moog

The development of speciality infra-red glasses has produced a number of alternative compositions which have become well established for many applications, both for industrial use and academic research. Among them, gallium lanthanum sulphide glass (GLS) is a particularly suitable competitor. This glass possesses a tunable and uniquely located transmission window among chalcogenides, ranging from 500 nm to 15 μm in bulk glass. In addition to its mechanical strength and high transition temperatures, the combination of visible and infra-red transmission makes this glass an exceptional candidate for a variety of applications, such as thermal imaging and chemical sensing. The thermal properties of GLS make shaping it to conform to a particular application delicate and challenging work. In particular, its crystallization temperature lies near its softening temperature, making any process involving softened or molten glass highly time constrained. In this work, previously established techniques have been revisited and improved upon, and a set of novel methods have been developed and employed, in order to enable gallium lanthanum sulphide to fulfil new applications. In particular, oxygen-free GLS fibre has been fabricated, significantly increasing the breadth of its transmission window in fibre form. Optimization through design of experiments (DOE) has allowed to fabricate crucible-drawn GLS fibre for the first time. Further refinements of GLS processing developed herein include the fabrication of ultra-thin fibre (less than 10 μm in diameter), casting and cutting into fibre drawing preforms and the fabrication of large diameter (>90mm) windows. Its glass formation range has also been expanded by increasing the quenching rate, new characterization methods have been implemented, and in-house polishing techniques for cylindrical sections of glass have been developed. Overall, this work has advanced the use of chalcogenides based on GLS for a number of applications which include infra-red optical fibre fabrication, multi-spectral windows, chemical sensing and imaging fibre bundles.

Contents

List of Figures

List of Tables

Academic Thesis: Declaration of Authorship

I, Bruno J. Moog declare that this thesis and the work presented in it are my own and has been generated by me as the result of my own original research.

The fabrication and characterization of infra-red optical fibre, ultra-thin fibre and large diameter chalcogenide glass.

I confirm that:

1. This work was done wholly or mainly while in candidature for a research degree at this University;
2. Where any part of this thesis has previously been submitted for a degree or any other qualification at this University or any other institution, this has been clearly stated;
3. Where I have consulted the published work of others, this is always clearly attributed;
4. Where I have quoted from the work of others, the source is always given. With the exception of such quotations, this thesis is entirely my own work;
5. I have acknowledged all main sources of help;
6. Where the thesis is based on work done by myself jointly with others, I have made clear exactly what was done by others and what I have contributed myself;
7. Part of this work has been published as:

- Morgan, K. Zeimpeikis, I., Huang, CC., Feng, Z. Craig, C., Weatherby, E., Aspiotis, N., Alzaidy, G.A., Ravagli, A., **Moog, B.J.**, Guzman Cruz, F.A.,Lewis, A., Delaney, M. and Hewak, D. (2019) *"Chaclogenide materials and applications: from bulk to 2D (Invited Talk)"*. Electronic Materials and Applications 2019 (EMA 2019), Orlando, United States. 23-25 Jan 2019. 1pp.
- Guzman Cruz, F.A., Ravagli, A., Craig, C., **Moog, B.J.** and Hewak, D. (2019) *"Fabrication of structured GLS-Se glass preforms by extrusion for fibre drawing"*. OSA Fron- tiers in Optics Laser Science APS/DLS, Washington, United States. 15-19 Sep 2019. 2pp. (doi.org/10.1364/fio.2019.jw4a.11).

- Ravagli, A., **Moog, B.J.**, Guzman Cruz, F.A., Craig, C., Kar, A., Mackenzie, M., Morris, J. and Hewak, D. (2018) *"Chalcogenide materials: Novel compositions and new applications"*. Advanced Architectures in Photonics 2018, Cambridge, United Kingdom. 02-05 Sep 2018.
- Guzman Cruz, F.A., Ravagli, A., Craig, C., **Moog, B.J.** and Hewak, D. (2018) *"Chalcogenide optical fibres based on gallium lanthanum sulphide-Se for passive and active applications"*. São Paulo School of Advanced Science on Frontiers in Lasers and their Applications, São Paulo, Brazil. 16-27 Jul 2018.
- Guzman Cruz, F.A., Craig, C., **Moog, B.J.**, Ravagli, A. and Hewak, D. (2020) *"GLS-Se optical fibre from extruded glass structured preforms and rods for the IR region"* Optical Materials Express 11(1):157-170 (doi.org/10.1364/OME.411571)
- **Moog, B.J.**, Craig, C., Guzman Cruz, F.A. and Hewak, D. (2021) *"Processing of Infrared Chalcogenide Glass Fabrication of Infrared Fibre, Ultra-thin Fibre, Multi-Spectral Windows, and extending the composition range of Gallium Lanthanum Sulphide (GLS)"* Royce Student Summit 2021 (Poster). 2-3 Mar 2021.
- **Moog, B.J.**, Craig, C., Guzman Cruz, F.A. and Hewak, D. (2021) *"The fabrication of infrared chalcogenide glass fibre, ultra-thin fibre and large diameter gallium lanthanum sulfide windows."* Royce Student Summit 2021. 2-3 Mar 2021 (Presentation).
- Guzman Cruz, F.A., Craig, C., **Moog, B.J.**, Ravagli, A., Morgan, K. and Hewak, D. (20201) *"Manufacturing of GLS-Se glass rods and structured preforms by extrusion for optical fiber drawing for the IR region"* Optical Engineering 60(4): 045101 (doi.org/10.1117/1.OE.60.4.045101)

Signed: ....
Date: ....

Acknowledgements

I would like to thank our group technician Chris Craig and our facilities manager Ed Weatherby, for their outstanding efforts and impeccable work ethics. None of this work could have been possible without either of them.

I would like to thank my supervisor Dan Hewak, for his insightful advice and tenacious support. His expertise has been invaluable in guiding my efforts.

I would like to thank my colleagues of the novel glass group. In particular, Fernando Guzman, Ellis Archer, Katrina Morgan, Ioannis Zeimpekis, Kevin Huang, Nikos Aspiotis and Andrea Ravagli. They have been most generous, both in terms of help and advice in order to achieve the highest scientific standard.

I would like to thank the support staff of the Optoelectronics Reseach Centre and Electronics and Computer Science workshop. In particular Glenn Topley, Steve Helm, Mike Bartlett, Jon Kerly, Denny Jack, Mike Perry, Mark Lessey, Niel Fagan and Mark Long. The vital maintenance and support they provide are the cornerstone of the ORC.

I would like to thank the technical staff from other research groups Nick White, Rob Standish, Niel Sessions, Austin Taranta, Monika Glanc-Gostkiewicz. I have been able to rely on their unique skills and expertise more times than I can count.

Finally, special thanks to Paul Frampton and Lee Mulholland of the Caplin glass blowing workshop. Their rare skillset acquired from constantly meeting arduous requests from too imaginative researchers of various fields is the often undervalued gem of the University of Southampton.

To my family and friends for their support.

"Labor improbus omnia vincit[1]*"*

Ambroise Paré, surgeon of kings, king of surgeons.

---

[1] Un travail acharné vient à bout de tout/Hard work conquers all.

Abbreviations

cP: Centipoise
CVD: Chemical Vapour Deposition
DOE: Design of Experiments
DTA: Differential Thermal Analyser
EDX: Energy-dispersive X-ray spectroscopy
FTIR: Fourier Transform Infra-Red (Spectrometer)
GLS: Gallium Lanthanum Sulphide
GLSO: Gallium Lanthanum Oxysulphide
GLSSe: Gallium Lanthanum Sulphide Selenide
GLSSe20%: Gallium Lanthanum Sulphide Selenide (45%Ga_2S_3, 20%Ga_2Se_3, 35%La_2S_3)
OSA: Optical Spectrum Analyser
ppm: Parts per million
PSI: Pounds per square inch
PTFE: Polytetrafluoroethylene
rpm: Revolutions per minute
SCCM: Standard cubic centimetres per minute
TMA: Thermo-Mechanical Analyser
TG-DTA: Thermo-Gravimetric Differential Thermal Analyser
T_g: Glass transition temperature
T_x: Crystallization temperature
T_m: Solidus temperature
T_l: Liquidus temperature
T_f: Fictious temperature

1 Introduction

Research into the manufacturing of specialty infra-red glasses has produced a number of compositions which have become well established for many applications, both for industrial use and academic research. Together, these glass compositions cover the full infra-red range and well suited niches have been found for each of them. Among the applications, however, fibre optics remains one placed under particularly high demand. Indeed, the exceptional quality of optical fibre made to address other wavelength ranges has set a precedent for the quality expected of infra-red fibre, with particular incentive being placed on thermal stability, mechanical strength as well as good optical properties. Gallium lanthanum sulphide glass (GLS) and its derivatives, with their high melting temperature and unique optical transmission window, is one of the most well established competitors capable of meeting that demand. It has previously been made into optical fibre on several occasions, although composition changes were required so that it can be draw into fibre more readily, specifically with the addition of at least a few percentage points of lanthanum oxide to form gallium lanthanum oxysulphide (GLSO) [9, 10]. This composition change however limits the transmission range of the fibre produced. The work described here justifies a composition change and attempts to establish a suitable experimental process that would enable to produce oxygen-free core-clad GLS and gallium lanthanum sulfur selenide (GLSSe) fibre, with an uncompromised transmission window. Pure GLS or GLSSe fibre produced is compared to commercially available infra-red fibre as well as GLSO in both transmission range, overall loss, and physical strength. From this core motivation several novel techniques to shape and adapt gallium lanthanum sulphide glasses to meet industrial requirements have been developed and documented. In particular, lathe turning, cylindrical polishing, ultra-thin fibre, glass casting and large diameter window fabrication have been investigated. In addition, two approaches to fibre drawing are investigated: rod/preform drawing and crucible drawing, with particular focus placed on the necessary adaptations undertaken so as to achieve successful crystal-free GLS fibre production.

2 Background

2.1 The history of glass

Glass is a material that derives its inherent value from its uncommon properties that liken it to natural gems. Its transparency, hue, polishable surface, the ease with which it can be moulded and shaped, and the low cost of the materials needed to fabricate it all contribute to making glass an attractive option for decorative objects, both for artistic and architectural pursuits [11]. It is a remarkably ancient material, demonstrating its consistent fabrication and usage in many archaeological artefacts dating back all the way to 3500 BC. There are many candidates as to where its fabrication may have first been implemented, such as Mesopotamia and Egypt [12]. The fabrication of glass and the development of glass technology often took advantage of the advances of other manufacturing processes, such as metallurgy and chemistry, in particular as it relates to the availability of high temperature furnaces and chemical purification techniques. It however exclusively benefited from the invention of the glass blowing pipe in Syria, 2000 years ago. This simple piece of technology greatly facilitated the production of glass vessels and thin layers of glass. Because of the latter, transparency became an increasingly desirable property. In particular, glass pane windows became available in 11^th century Germany, where the glass blowing of cylinders that could be cut open and flattened while still hot was developed by glass blowing artisans [13]. Glass windows were also popularized in 14th century France in the form of the bull's eye pane, which are made using a simpler spinning method, but present an eponymous defect in the form of a thicker bulb of glass in the centre of the pane [14, 15].

In the meantime, considerable efforts were placed on achieving transparency and elegant colors by improving the selection process of raw materials. This resulted in more chemically stable, mechanically resilient, and optically attractive glass, which in turn facilitated the development of its branching applications. In L'Arte Vetraria, initially published in 1612, Antonio Neri was already placing a considerable amount of importance on the selection, purification and filtering of raw materials to ensure the highest clarity of the final product [16]. His work is one of the earliest comprehensive handbooks on the art of glass fabrication and glass blowing, and contributed to the spread of Venetian glass blowing techniques to all of Europe [13].

Throughout the medieval period, most glass, however, was soda-lime. Its core components are SiO_2, Na_2O and CaO [17]. Soda-lime is still the most commonly used type of glass today, as the materials used to make it are abundant and its manufacturing process is simple. It was originally made using beach sand, combined with a natural source of alkali. The source of alkali was either natron that could be harvested from dry lake beds in Egypt, or if that resource was too difficult to access due to geographic location and trade difficulties, plant ash (referred to as potash) [18]. Pure silica (SiO_2) glass is considerably more difficult to manufacture, as it requires to be melted above 2000 °C, and could only be obtained in the natural form of fulgurite until 1934, when James Hyde Franklin established a vitrification process taking place below the extremely high melting point of silica [19, 20].

In 1676, George Ravenscroft in England produced the first lead glass as an alternative to soda lime glass that did not require the importation of potash. Starting in the 17th century, the chemical durability of soda-lime glass was gradually improved due to the spreading realization that the originally accidental lime content from the sand (which originated from seashell fragments) used in the fabrication process was an essential component of soda-lime glass, as it considerably improved its chemical durability, in particular regarding its resistance to moisture [21]. Stirring techniques during melting were introduced quite late, in the early 19th century by Pierre Louis Guinand, and are yet another element that heavily contributed to the improvement of the optical quality of glass. From 1879 to 1886, a collaborative effort between glass maker Otto Schott, and optical scientists Ernst Abbe and Carl Zeiss produced and characterized the first borosilicate glasses. They also pioneered a more systematic approach in tailoring glass properties to a desired application, and to that end, introduced the first composition-property models [17].

This slow and laborious improvement of glass technology spanning several millennia, often based on trial and error and accidental discoveries underlies the nature of glass as a unique phenomenon in material sciences. In combination with its elegant properties, it has made glass and its scientific study a subject of fascination for a considerable number of scholars, and it is still the seemingly irreplaceable cornerstone of modern optics to this day.

> “Glass [...] is much more gentile, graceful, and noble than any Metal [...] it is more delightful, polite, and sightly than any other material at this day known to the world” [16] Antonio Neri, 1612

2.2 The glass state

From a chemical standpoint, glass is a rather complex phenomenon that isn't based on any particular composition, but rather reflects a unique state of matter. This is adequately addressed by P. W. Anderson of Princeton University in 1995:

> "The deepest and most interesting unsolved problem in solid state theory is probably the theory of the nature of glass and the glass transition. This could be the next breakthrough in the coming decade. The solution of the problem of spin glass in the late 1970s had broad implications in unexpected fields like neural networks, computer algorithms, evolution, and computational complexity. The solution of the more important and puzzling glass problem may also have a substantial intellectual spin-off. Whether it will help make better glass is questionable. [22]"

Glass is commonly described as an amorphous (non-crystalline) solid: a solid that presents the disorder expected of a liquid. This property is responsible for the common myth according to which glass is a liquid, and that it flows under the effects of gravity, albeit very slowly. This legend is illustrated by medieval stained glass panes that allegedly have, after centuries of being held upright, become thicker at the bottom and thinner at the top. This attractive misconception is however not supported by any historical or scientific evidence and it was disproved by tests performed on 20 million years old pieces of amber demonstrating that glass does not flow [23, 24]. However, the similarities with liquids are still striking enough for glass to be often compared to a liquid, in spite of the flaws in the analogy [25]. Indeed, the crystal state is an ordered, and thus a lower energy, more stable state than a disorderly glass state. The higher-energy glass state is achieved by cooling down the material too fast for the restructuring of the atomic distribution into an ordered lattice to occur (crystallization). The system is instead maintained at a temperature sufficiently low for its viscosity to be too high for the molecular structure to be able to spontaneously rearrange itself into a low-energy crystalline lattice [26]. Glass is therefore a unique, metastable state of matter. This glass formation process is illustrated in Figure 1.

The glassy state presents attractive optical and mechanical properties, as a crystalline structure scatters light and is typically more brittle than a disorderly glass structure due to its higher density and reduced plastic flow [27]. However, glass is still quite brittle due to its propensity for crack propagation, in addition to its flexibility usually only becoming

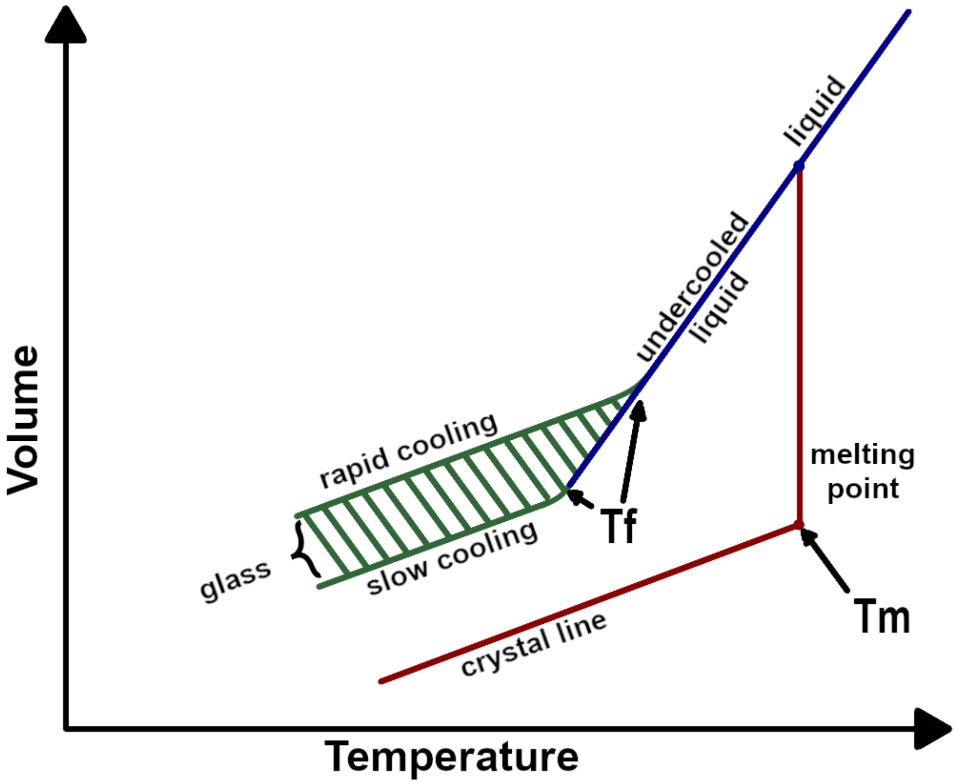

Figure 1: The glass formation process, as illustrated by the variations in volume of the system as a function of temperature. A successful melt-quench procedure starts from the right side of the liquid (blue) curve, beyond the melting point, and follows a downwards trend into the glass forming region.

significant on the microscopic scale. And yet even in the form of glass fibres a few hundreds of microns thick, its brittleness is self-evident from the common use of polymer coatings to prevent scratches that would otherwise considerably weaken the fibre.

2.3 Optical fibre

Using a stream of water to transport sunlight was famously used by Jean-Daniel Colladon in 1841 to better demonstrate fluid flow. As it turns out, this beautiful optical experiment also demonstrates one of the founding principle of optical fibre: total internal reflection. This phenomenon was popularized by the 1889 Universal Exposition held in Paris, where it was used to demonstrate the power of electric lights in a spectacular fashion, by illuminating the water jets of the fountains of the exposition from within. Nearly simultaneously to Colladon, in 1840, French physicist Jacques Babinet was performing a similar demonstration, this time the focus being the optical phenomenon of total internal reflection itself. He went so far as to mention similar light guiding properties in bent glass rods, in spite of the very limited glass purity available at the time [12]. Later, this phenomenon was greatly popularized by John Tyndall in his lectures at the Royal Institution of London, starting in 1854 [28].

The endoscopic applications of light pipes both for the delivery of light as well as imaging first appear in 1888 with Austrian doctors Roth and Reuss, and 1930 with Heinrich Lamm respectively [29, 30]. As for the modern rise in popularity of optical fibres, it is primarily linked to its use in communications [31]. Their becoming a competitive medium for communication was initially theorized in 1966 by Charles K. Kao and George Hockham in their paper 'Dielectric Fibre Surface Waveguides for Optical Frequencies', in which they made this prediction assuming a minimum 10-fold reduction of the loss [32]. They estimate the relative contributions of dielectric, bending and radiation losses, and suggest that the relatively high best loss of 200 dB/km recorded at a wavelength of 1 μm is mostly caused by the presence of impurities in the form of ferrous ions (Fe^{2+}) in the glass. Therefore, improved purification techniques would be the principal enhancement required to reduce loss down to below 20 dB/km, and thus produce optical fibres suitable for communication.

In 1970, Kapron *et al.* published an article titled 'Radiation Losses in Glass Optical Waveguides' in which they demonstrate optical fibre they developed for Corning Glass Works with a loss of 7±2 dB/km, vindicating Kao *et al.*'s prediction [33]. Since then, subsequent improvements have taken silica to a minimum loss of 4 dB/km, and then even further by exploiting the wavelength-dependent nature of optical loss. Today it is usually around 0.2dB/km. As the technique has advanced, the production cost of silica fibre has also fallen significantly [34].

Auxiliary components, such as light sources associated with optical fibres, in particular laser diodes have also undergone tremendous improvements in terms of power and durability, and have contributed to the telecommunication revolution starting in the 1980s. Building on the subsequent popularity it gained in telecommunications, the field of fibre optics has developed to tackle an increasingly wide and complex array of applications. These applications are under a constant demand for increased quality of optical fibre. In that regard, fused silica has been distinguished as the example to follow, with its exceptional physical strength and chemical stability. Its transmission range is however limited, with absorption in the infra-red rising exponentially past its 1.5 μm transmission optimum, enabling several alternative glass compositions to compete over the optical window starting at around 2μm [4].

One of the most significant milestones in the development of optical fibres was the production of core-clad fibres, also known as step-index fibres. Their structure is shown in Figure 2. These fibres are structured, having one layer of material deposited on the outside of a concentric fibre, the cladding and the core, respectively. This structure enables to avoid the significant losses that take place when the surface of the fibre is in contact with materials that are either absorbent to the light it carries or have a higher refractive index than the fibre, which would result in the light escaping the fibre rather than undergo total internal reflection at the interface. This structure also protects the core against scratches,

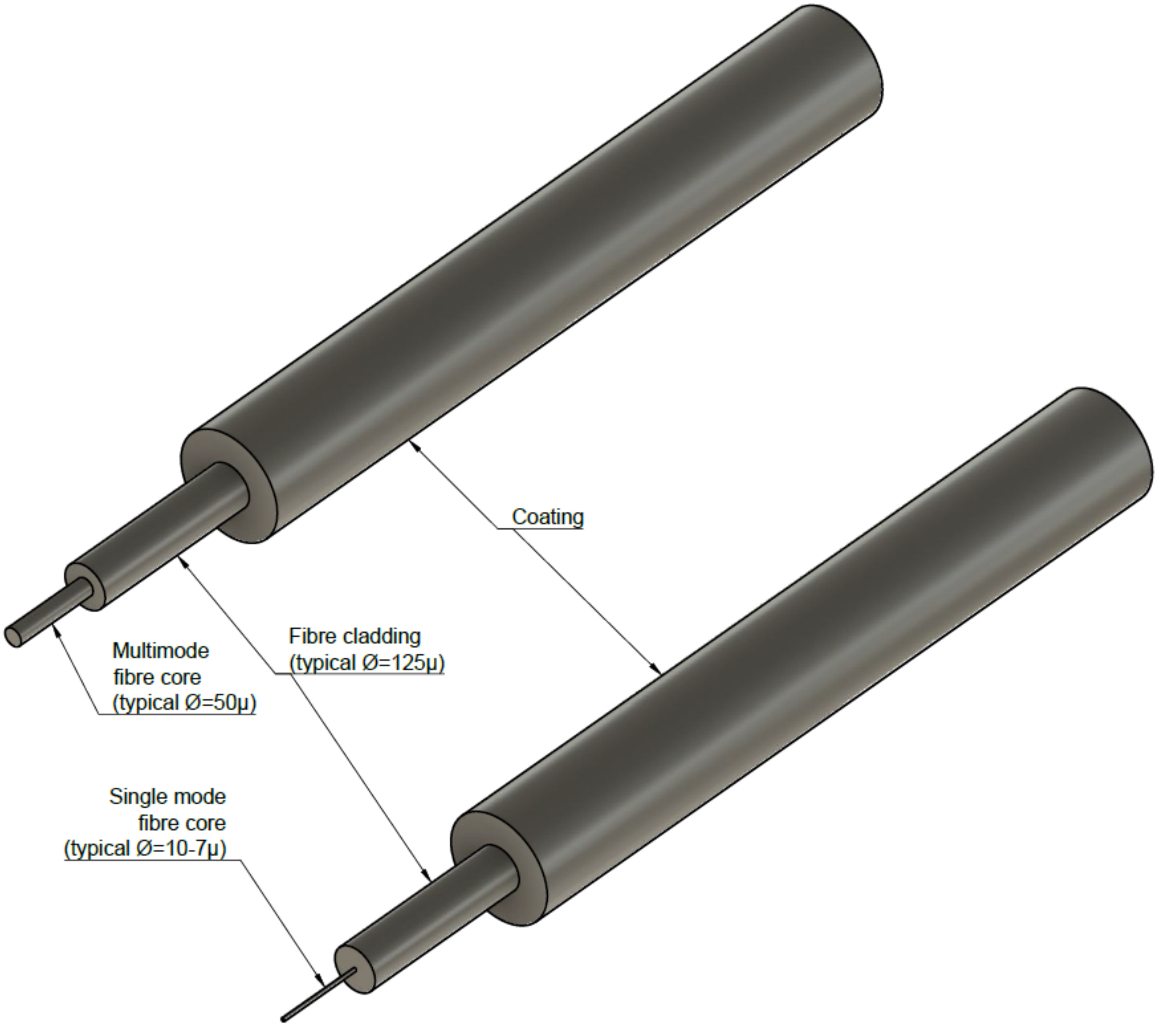

Figure 2: Schematic comparison of the structural difference between multimode and single mode fibres.

which not only reduce transmission by introducing additional sources of scattering, but also mechanically weakens the fibre. In such a step index fibre, one can calculate the numerical aperture, which is the sine of the maximum angle of incident light the fibre can guide. This maximum corresponds to the angle of the ray that, after being successfully introduced in the core of the fibre gets reflected at the core-clad boundary at the largest possible angle that allows for total internal reflection. The formula used to calculate it is as follows:

$$\sin\theta_{\mathrm{max}} = \frac{\mathrm{NA}}{\mathrm{n}} = \frac{\sqrt{\mathrm{n}_{\mathrm{core}}^2 - \mathrm{n}_{\mathrm{clad}}^2}}{\mathrm{n}} \tag{1}$$

Among step-index fibres can be further distinguished multimode and single-mode fibres. The key difference between them is the size of the core and its implications regarding the light-guiding properties than ensue. Multimode fibres have a core of around 50 μm, which is considerably larger than the wavelength of the light it guides, while single core fibres usually have a core of less than 10 μm. As their name indicates, multimode fibres can guide several modes of light as opposed to single-mode fibre. In mathematical terms, this translates to there being several solutions to the wave equation for light propagation in multimode fibres, but only one for light propagation in single-mode fibres. The V-number is commonly used in step-index fibres in order to distinguish single-mode fibres from multimode fibres, as well as to estimate the number of modes in the latter. It is calculated as per the equation:

$$\mathrm{V} = \frac{2\pi}{\lambda} \cdot \mathrm{a} \cdot \mathrm{NA} \tag{2}$$

where λ is the wavelength used in m, a is the radius of the core in m, and NA is the numerical aperture of the fibre defined in Equation 1. If V is below the 2.405 cut-off, the fibre is single mode. For high V, the number of modes M$\approx 4 \cdot V^2/\pi^2$ [4]. Multimode fibres are easier to couple into for purely mechanical reasons, as their core is considerably larger. However, multimode fibres present the issue of modal dispersion. As the entrance angle for each mode is different, the path length through the fibre for each mode is different as well, resulting in a spread of the arrival times for modes sent down the fibre simultaneously. That issue can be partially addressed by using graded index fibres, the principle of which is shown in Figure 3 [35].

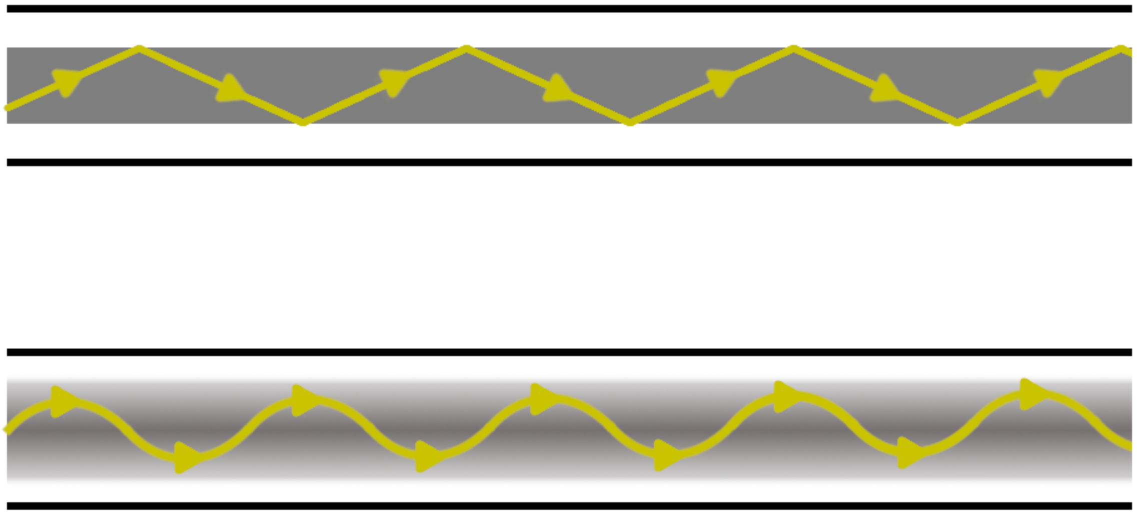

Figure 3: Schematic representation of the path followed by guided light within a step index fibre (top) compared to a graded index fibre (bottom).

As can be observed in Figure 3 in a step index fibre the refractive index is constant for light guided in the core no matter the mode. However, in a graded index fibre while the path length is still different for each mode, the higher the amplitude of the oscillations, the lower the average refractive index felt by the ray of light, resulting in a faster travelling speed that partially compensates for the longer distance the mode travels as per the equation: v=c/n, where v is the speed of light in the material, c is the speed of light in a vacuum, and n is the refractive index of the material. This also means that the profile of a graded index fibre can be optimized to minimize modal dispersion around a specific wavelength. In contrast, single mode fibres do not suffer from modal dispersion, but they still are subject to chromatic dispersion. Chromatic dispersion is caused by the dependency of propagation speed on refractive index. It takes three sub-forms. Material dispersion, where the spectral width of a pulse combined with the wavelength-dependant refractive index of the core results in dispersion. Waveguide dispersion, where the cladding overlap that occurs from treating guided light as a wave results in dispersion because the lower speed of light in the cladding. And finally profile dispersion, the smallest component of chromatic dispersion, caused by the refractive index as a function of wavelength curves not having the same slopes for the core and cladding, producing an additional source of wavelength-dependent dispersion. Besides chromatic dispersion and modal dispersion, polarization mode dispersion should also be briefly mentioned. In real fibres, there is always a small amount of birefringence: refractive index is polarization dependent. As such, the propagation speed will vary depending on polarization as well [4, 3].

2.4 Chalcogenides

Chalcogenide compounds produce glasses with the properties required to seize the opportunity made available by the limitations of fused silica in the infra-red. This is caused by their low phonon energy, allowing them to transmit above 2 μm [36]. These glasses are composed primarily of elements from the 16^{th} column of the periodic table known as chalcogens. This column contains the natural elements oxygen, sulphur, selenium, tellurium, and polonium. As oxygen provides glasses with significantly distinct properties than the other chalcogens, oxide glasses are typically treated separately to chalcogenide glasses, even though oxygen belongs to the chalcogen group [9]. The potential of various chalcogenide glass compositions in terms of infra-red transmission is show in Figure 4 compared to silica and fluoride glasses.

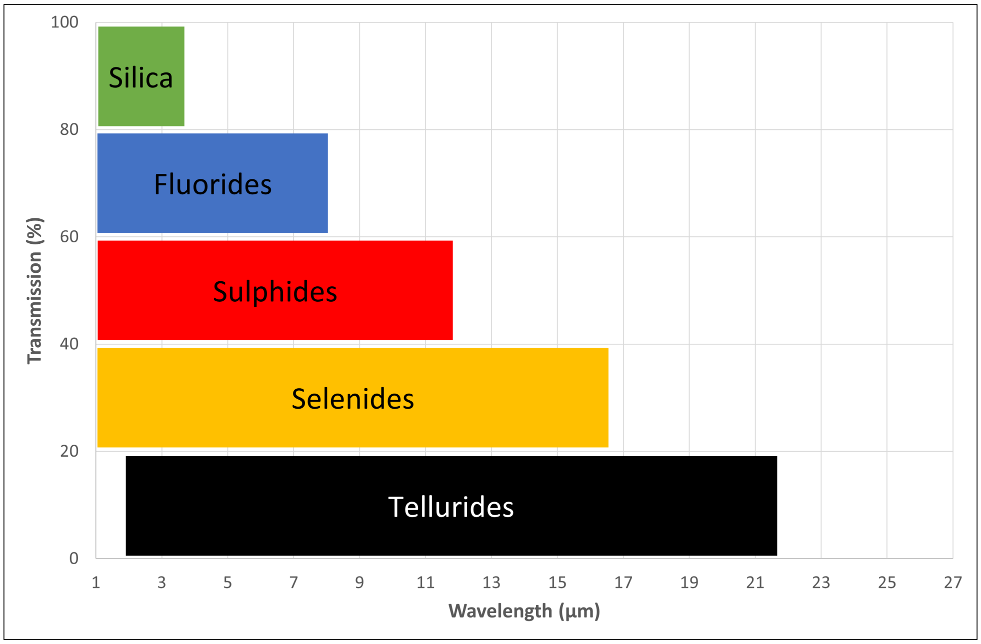

Figure 4: Transmission range for different glass families in the infra-red [1, 2].

As for silica, there has been a strong incentive placed on the improvement of the purity of chalcogenide materials to enhance transmission. In the case of chalcogenides, however, purification is particularly important due to ubiquitous contaminants. This is illustrated by the absorption bands of OH at 2.9 μm and H_2O at 5.5 μm, which lie in the transmission range of all of the chalcogenide glasses shown in Figure 4. Therefore, a strong incentive is placed on eliminating all traces of moisture in the fabrication process, no matter how minute.

The first examples of infra-red fibres were produced in 1965, by Kapany *et al.*, and were made from the chalcogenide glass arsenic trisulphide (As_2S_3) with a very high recorded loss of 10 dB/m from 2 to 8 μm, effectively preventing their use for the wide majority of optical applications [37]. There have been various types of infra-red fibres developed following this first attempt, such as fluoride and chalcogenide glass solid-core fibre, sapphire and halide crystalline solid-core fibres, as well as hollow-core fibres. Infra-red-transmitting optical fibre is of particular interest for many applications such as laser-power delivery, chemical sensors in the fingerprint region of the infra-red spectrum (6 to 20 μm), black-body radiation-based temperature sensors, or thermal imaging. However, due to the optical, chemical and physical variability of these different fibre types, their ability to compete may be restricted to particularly well suited applications. For example, hollow-core fibres have an extremely high damage threshold, which gives them a strong competitive edge against most of their alternatives for laser power delivery. Similarly, chalcogenide solid core fibres are ideally suited for sensing applications in the fingerprint region (above 6.6 μm) due to their high refractive index and ideally located transmission window [4]. The relation between the transmission window of optical fibre materials and key applications is shown in Figure 5.

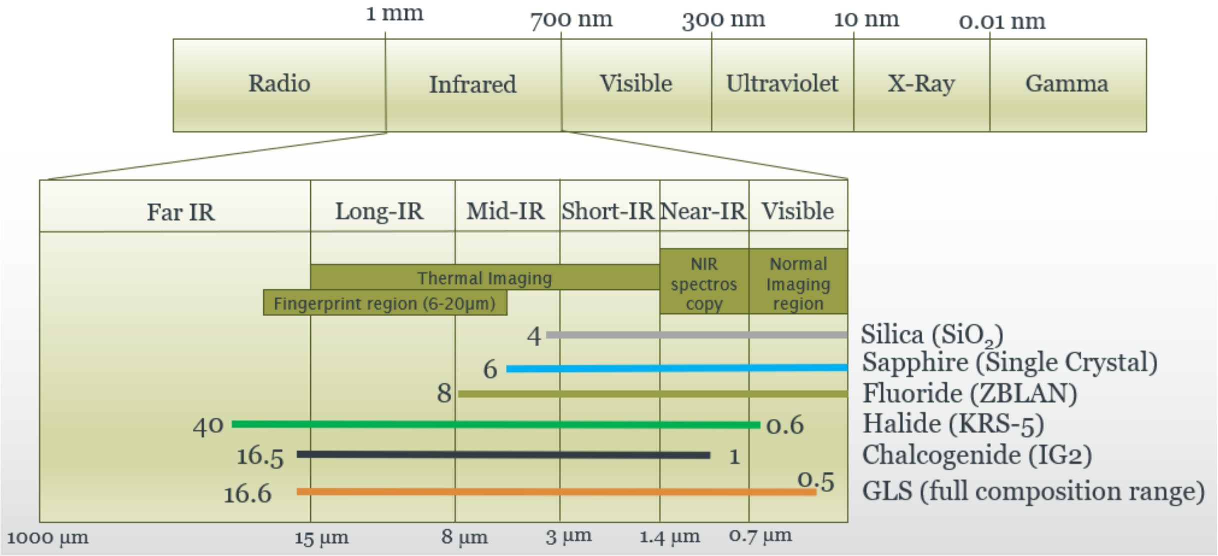

Figure 5: Location of the infra-red electromagnetic spectrum, its breakdown into spectral regions of interest, their key applications, and the transmission range of the glass families used to address them [3, 4, 5, 6].

Most of the materials used to fulfil the demand for infra-red fibre are, however, far more fragile and chemically sensitive than fused silica. Their drawing into optical fibre from bulk glass may often be more challenging and require more complex methods in order to successfully transform them into fibre while retaining their optical and mechanical properties.

2.5 Gallium lanthanum sulphide (GLS)

Among chalcogenide glasses is GLS, first introduced by Loireau-Lozac'h *et al.* in 1976 [38], who pointed out the composition variability of the glass phase for lanthanum based glasses, as well as their excellent transmission range from the visible up to 7 μm. This flexibility in composition enables to adapt GLS to a wide array of practical applications such as macroscopic infra-red optics, thin films, micro-spheres, waveguides and optical fibres [9]. For GLS, an addition of oxygen in the form of lanthanum oxide is often used to hinder the formation of crystals within the glass, at the cost of a shifted multi-phonon absorption edge towards shorter wavelengths caused by the presence of La_2O_3 [39]. Chalcogenide glasses in general and some variations of GLS in particular have been successfully drawn into infra-red optical fibre on many occasions [40, 41].

Pure Ga_2S_3 forms a crystalline lattice, in which gallium atoms bond covalently to two sulphur atoms and dativly to one [42]. When La_2S_3 is introduced, the increased amount of sulphur anions S^{2-} produces GaS_4 tetrahedrals network formers, while the La^{3+} cations act as network modifiers. The La bonds ionically to a negatively charged cavity formed by 8 sulphur atoms [43]. Once the original long-range crystalline order of Ga_2S_3 is suficiently disrupted, it allows for the formation of glass via suitably fast quenching [44, 45, 43]. The chemical structure of this glass network and its interaction with the network modifier La^{3+} is shown in Figure 6.

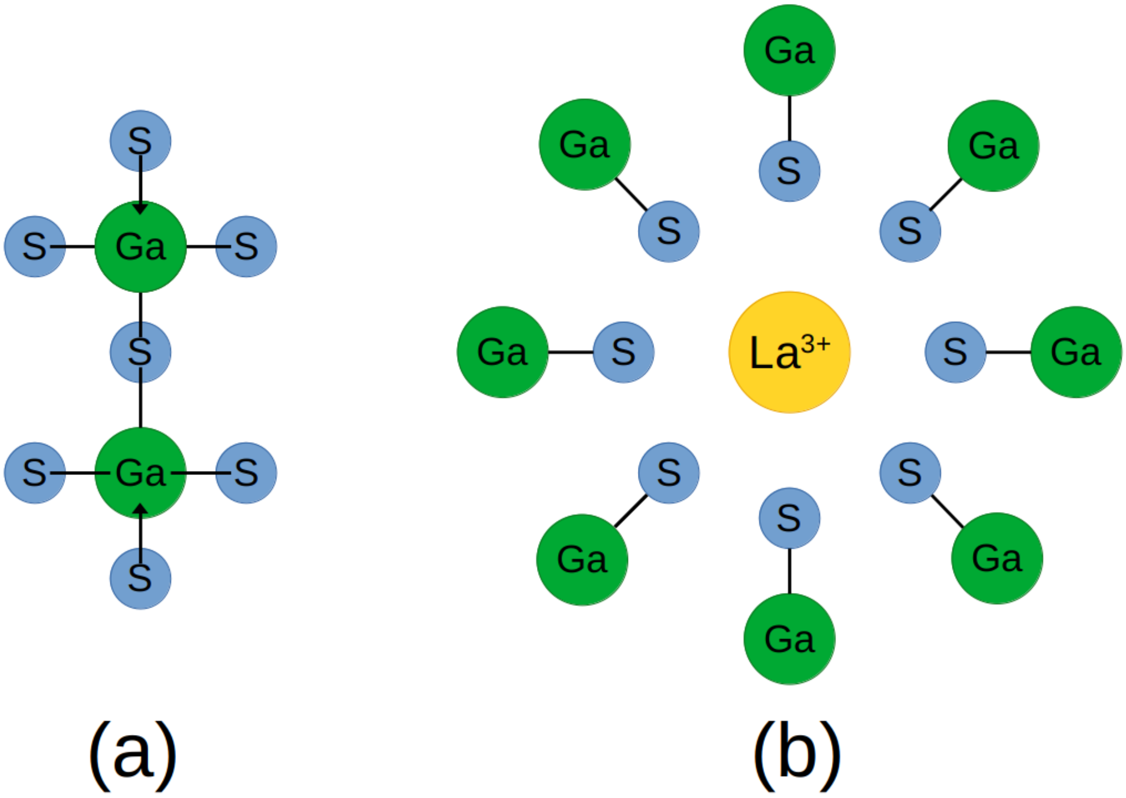

Figure 6: Structure of GLS glass. (a) Glass network of Ga_2S_4 tetrahedra, (b) Environment of network modifier La^{3+} ions compensating for charge.

The transmission range of modern GLS glasses is quite variable due to the flexibility of its composition. It finds its practical limits in the visible at around 500nm, due to electronic absorption, and goes up to 15μm in the infra-red due to the multi-phonon edge [46]. In addition, its high transition temperature, non-toxicity and chemical resistance make it an attractive candidate for chemical sensing and harsh environments [9, 47].

2.6 Fibre fabrication methods

In most cases, fibre is drawn from a cylindrical preform. A preform is a macroscopic version of the desired fibre reflecting its structure in proportion. It typically is less than 1 m long and a few centimetres in diameter. This preform is suspended in a vertical furnace, in which it gets heated to the point where it starts to soften, neck and stretch. Its falling end is then attached to a rotating drum to produce fibre while its upper end is slowly fed into the furnace [48]. This process is illustrated in Figure 7. Conservation of volume allows to calculate the fibre diameter from the preform feeding speed, the drum speed and the preform diameter according to the following equation:

$$\mathrm{d_{fibre}} = 10^3 \cdot \mathrm{D_{preform}} \sqrt{\frac{\mathrm{S_{feed}}}{\mathrm{S_{drum}}}} \tag{3}$$

where $\mathrm{d_{fibre}}$ is the diamete of the fibre in μm, $\mathrm{D_{preform}}$ is the diameter of the preform in mm, $\mathrm{S_{feed}}$ is the speed of the preform feed in mm/min, and $\mathrm{S_{drum}}$ is the speed of the drum in m/s.

The preform may be fabricated using chemical vapour deposition (CVD), inserting or casting a rod of glass in a hollow glass tube of another composition [49] , or by using extrusion, the latter being able to produce long preforms with potentially complex structures with relative ease [50, 51, 52, 53] . The vast array of techniques available enable to address the thermal and mechanical properties of each glass composition. CVD has been attempted for chalcogenide deposition, but it is not as suitable for chalcogenides as the other preform fabrication methods due to the the propensity of this glass family for oxidation and hydrolysis, as well as the slow deposition of their components [54, 55, 56].

Fibre may also be drawn using double crucible drawing [57, 58], which enables to reduce the amount of imperfections in the fibre, namely the formation of bubbles and cracks between the core and cladding glasses [40]. This improved quality comes at the cost of an increased complexity of the system. This complexity stems from the introduction of a wider range of controls, such as the application of a different temperature and/or pressure to the core and cladding glasses, which are not applicable to rod/preform drawing [59, 60].

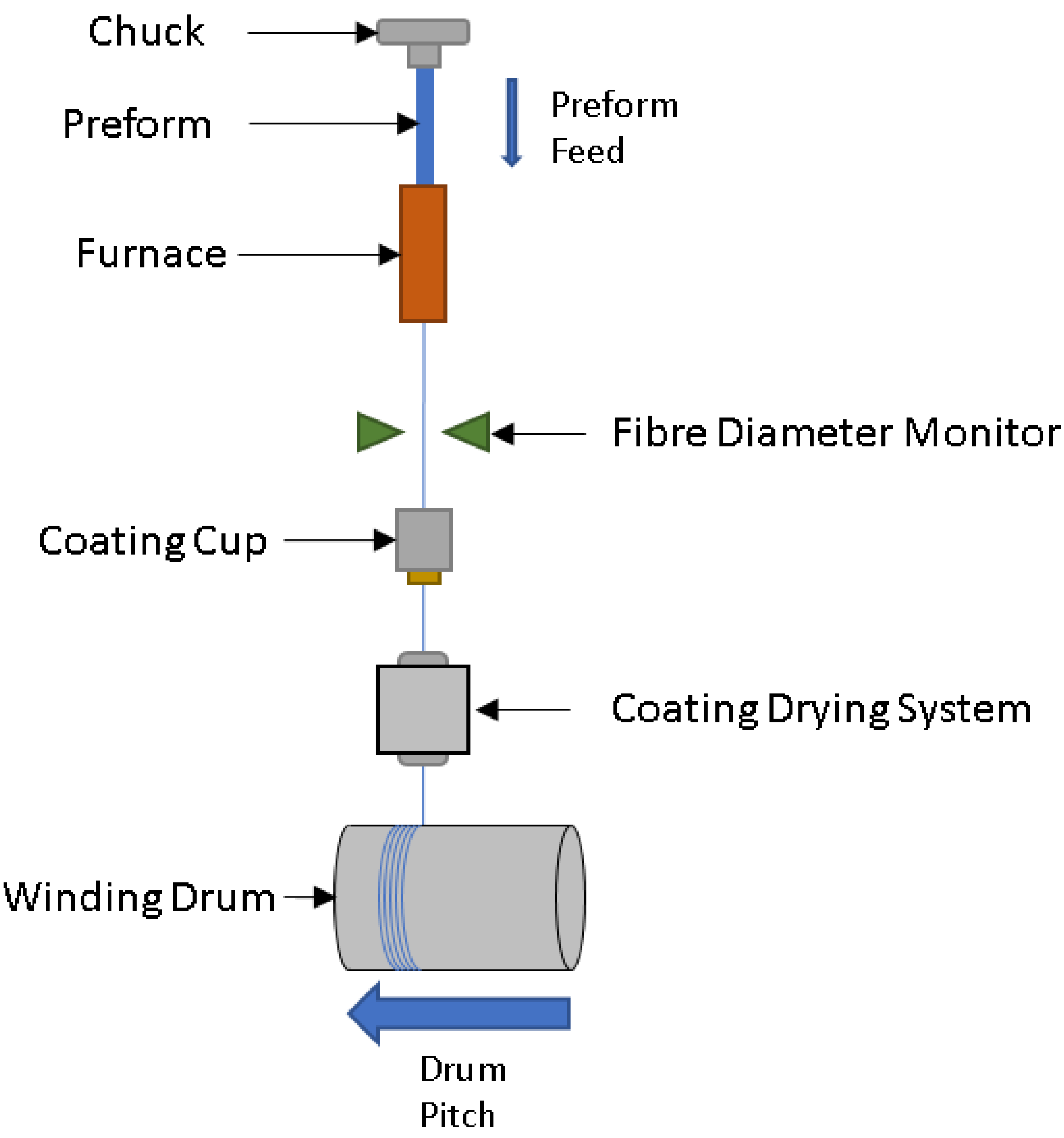

Figure 7: Schematic of the standard rod/preform fibre drawing procedure, represented at the stage where the fibre has been attached to the drum and optical fibre is being continuously drawn.

3 Glass fabrication

3.1 State of the art fabrication method

GLS is fabricated in a high-temperature furnace under argon purge, using the melt-quench technique, from a combination of high purity Ga_2S_3 (99.999% purity) and La_2S_3 (99.9% purity) powders from Great Western Inorganics and Lorad Chemical Corporation respectively [61, 62]. The powder containers are placed in a constantly Nitrogen-purged glovebox, with moisture level <1 parts per million (ppm), before being mixed. Each component is poured into a polytetrafluoroethylene (PTFE) container using disposable gloves and spatulas, to avoid cross-contamination, and is weighed using scales with 0.01 g precision. The container is sealed within the glovebox, and then placed on a rolling mixer to homogenise the sample for at least 1 hour. It is then opened inside the glovebox, and its contents are manually poured into vitreous carbon crucibles [63]. The maximum mass of a GLS sample fabricated this way is around 320 g. Additional components may be added depending of the desired composition, be it in the form of powder, pellets, or even high-purity wire for metals such as silver or copper. The crucibles must be made out of graphite or vitreous carbon, due to the reactivity of La_2S_3 with silica [64], and the fact commonly used platinum, boron nitride and alumina crucibles react with or dissolve in molten GLS due to the high reactivity of sulphur [46, 42]. The loaded crucibles are then inserted in a horizontal melting furnace, installed around an argon-purged silica tube directly connected to the glovebox. The mix is baked at 350 °C for 24 hours to ensure that any hydroxide, as well as SeO_2 and SO_2 impurities that may remain within the mix are removed due to their lower sublimation point in combination with the flowing gas purge [65, 46, 56].

The mixture is then melted at 1150 °C for 24 hours, to homogenize the glass. Its viscosity at this temperature is low enough (approximately 1 poise) to produce visually homogenous glass without the need for mechanical mixing [10]. At the end of the melting phase, the furnace is slid aside so that the melt cools down faster than the critical cooling rate and forms a glass, rather than having the time to arrange itself into a lower energy, higher density and opaque crystalline lattice [17]. This process is referred to as quenching. When the temperature becomes low enough so that the viscosity exceeds 10^{12} Pa.s, known as T_g, the glass transition temperature, the glass is meta stable and does not undergo further atomic rearranging, remaining in its amorphous phase indefinitely. The critical cooling rate can be estimated [66] and matched. However, as the temperature of the glass during melting is remarkably high (1150 °C), the quenching rate when the furnace is flushed aside and the argon gas flow is set to 500 standard cubic centimetres per minute (SCCM) is sufficient to form a glass for all the established GLS compositions [6].

The current glass fabrication method advantageously replaced the previously employed method for the manufacturing of GLS, which is the sealed ampoule method, still applied for the manufacturing of other chalcogenide glasses. The ampoules were made of silica, and had to either be carbon coated, or for a crucible to be inserted inside them to contain the molten glass and prevent contamination from silica. Because the melting occurred in a sealed environment, any pre-existing source of contamination, be it from the ampoule, the crucible or the raw materials would affect the quality of the glass, as no fining steps could be implemented. Also, this method presented significant risks due to the pressure build up that would occur within the sealed ampoule. The sealed ampoules were placed on a rocking furnace to homogenize the glass. This particular feature was also removed with no significant impact to glass quality, due to the low viscosity of the melt (around 0.1 Pa.s) allowing the glass to mix on its own via the natural diffusion and convection of its components alone [9, 40, 10].

3.2 The glass forming region

The core components of GLS, gallium sulphide (Ga_2S_3) and lanthanum sulphide (La_2S_3) are varied in their proportion to produce glassy compositions approximately ranging from 50% gallium sulphide-50% lanthanum sulphide to 75% gallium sulphide-25% lanthanum sulphide.

The composition ratio of pure GLS samples is typically noted in the form XX:YY, where XX is the molar percentage of Ga_2S_3 and YY is that of La_2S_3. This composition variability affects the physical and chemical properties of the glass [46]. The exact size of the glass forming region depends on the purity of the composition: the purer the components, the narrower it becomes, centring around the most stable composition 65% Ga_2S_3 and 35% La_2S_3 (GLS 65:35). This illustrates the fact gallium network is tetrahedral while lanthanum forms 8 fold co-ordination, both with sulphur. This in turn explains a close to 2:1 ratio for the most stable composition. This range is visually illustrated in Figure 8. Ceramized compositions can be seen forming the boundaries on either end of the range.

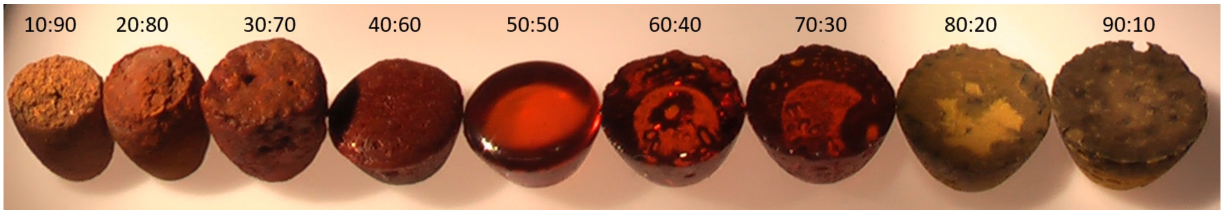

Figure 8: Pure GLS samples of varying proportions of Ga_2S_3 to that of La_2S_3, visually demonstrating the glass-forming region (glass samples courtesy of Christopher Craig).

The composition of the glass may be altered further, by adding oxygen, selenium, tellurium, indium or caesium [46]. In particular, the addition of oxygen, in the form of lanthanum oxide (La_2O_3) or selenium, in the form of gallium selenide (Ga_2Se_3) enables to shift the transmission window towards the visible and the infra-red respectively [10, 46]. In this work, gallium lanthanum oxysulphide (GLSO) has been used to refer to a routinely fabricated composition of 70% Ga_2S_3 and 30% La_2O_3.

3.3 Interface bubbles

Bubbles can always be seen in the unpolished glass samples (60:40 and 70:30 in Figure 8). These bubbles form at all interfaces between the glass and the vitreous carbon walls of the crucible. This phenomenon is responsible for an amount of unavoidable waste proportional to the extent of the interface, as the parts of the glass affected by these bubbles need to be cut off or polished out before the glass can be used. Such polishing produces the result seen in the 50:50 sample of Figure 8, that is: defect-free glass, but significantly smaller sample. Although vitreous carbon has a significantly lower porosity than non-vitreous carbon [67], there is a non-negligible amount of gas trapped within any surface that may be released when heating occurs. At the high temperature at which the glass is produced, such a process could easily explain the formation of bubbles at the glass-crucible interface. The Clausius–Clapeyron relation shows that vapour pressure increases with temperature as well [68, 69]. This could mean bubbles form in the melt at the highest temperatures and do not have time to dissolve in the glass or be reabsorbed by the walls of the crucible during quenching. Gas trapped in the bulk of the glass instead becomes aggregated at the imperfections of the crucible inner surface, thus forming bubbles. Other possible explanations for these bubbles are gas being trapped in the glass as the powder melts, either stemming from the small gaps between the grains of powder, or incorporated into the melt by the convection of molten glass from the surface of the sample that is exposed to flowing argon.

These bubbles made the fabrication of GLS rods more difficult, as it required cutting and polishing of cylindrical sections in-house, a process that had yet to be implemented. Several variations of the fabrication process have been tried to avoid or minimize these bubbles, such as vibrating the samples as they melt, stirring and altering the quenching process, without significantly impacting the size or number of bubbles. A few remelts were also performed in silica test tubes with a thin carbon layer deposited on the inside. The coating was produced by flowing acetone inside the tube, and immediately exposing the outside of the tube to the flame of a glass blowing torch, heating it rapidly to temperatures above 1200 °C. This process burned the acetone inside the test tube, depositing a semi-rigid layer of carbon on the surface. Unfortunately, this method was too fickle to implement on any other silica surface than the inside of short and narrow pieces of tubing, as the layers would become uneven and break off into flakes when attempts were made to apply this technique to larger surfaces. The remelts performed inside the successfully carbon coated test tubes produced the same surface bubbles as observed during a standard melting procedure. The carbon coating occasionally had imperfections, and in these spots the glass formed no bubbles. Instead, GLS would bind to silica in these exposed sections and shatter during quenching, as illustrated in Figure 9. This demonstrates that the formation of bubbles is inherent to the use of graphite or vitreous carbon crucibles. Unfortunately, any attempt at using other materials has proven unsuccessful so far, as molten GLS will dissolve, become contaminated with or bond with any other material it is in contact with, including platinum, silica and alumina [46]. These attempts confirm that the use of carbon crucibles (and as a consequence the presence of surface bubbles) is, as far as we have been able to test, an unavoidable artefact of GLS fabrication via the melt-quench technique.

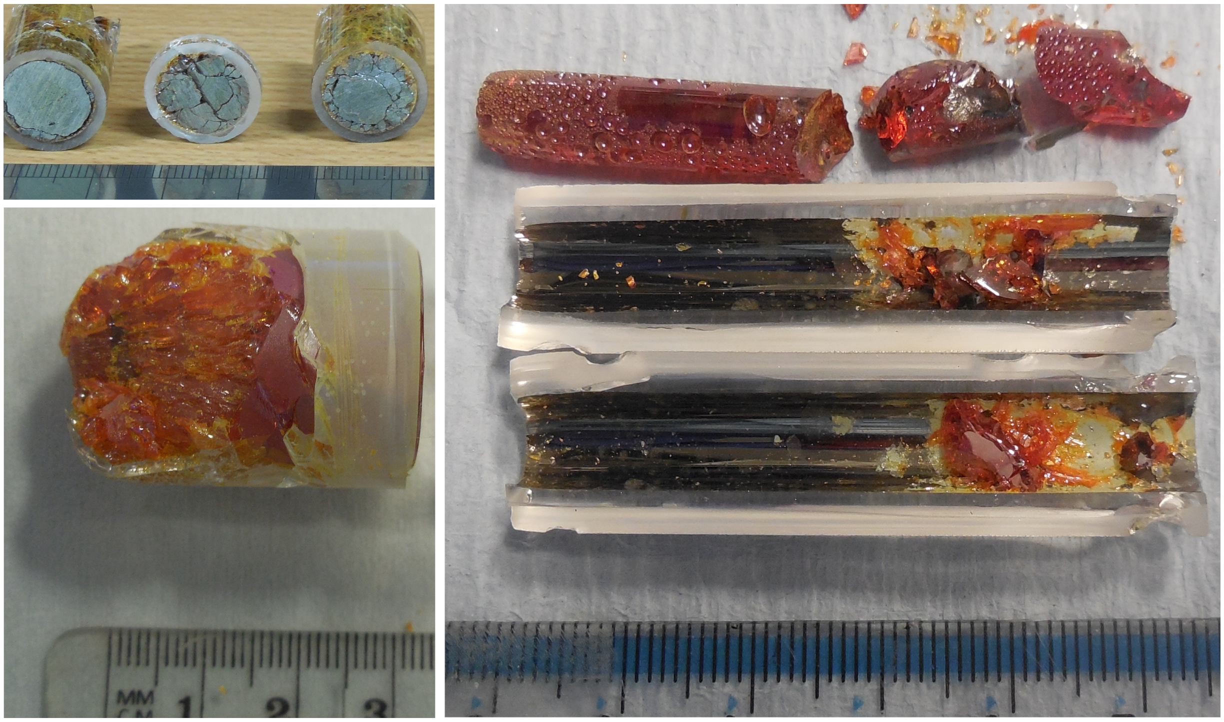

Figure 9: On the left, results of remelting GLS in silica tubes of varying diameter. The blue-gray hue of the glass shown in the top left picture is caused by the glass being cut with a diamond-bladed saw, giving it a rough surface. As can be observed, GLS bonds to the silica and shatters upon quenching. This makes the glass irrecoverable in one piece, and also destroys the silica crucible. On the right, result of a GLS remelt in a carbon-coated silica tube. Bubbles are visible on the section that had a continuous carbon layer, whereas in the uncoated middle section, the GLS stuck and shattered as expected.

3.4 Annealing

Once the glass is formed and cooled down to room temperature, it is removed from the crucibles and heated up again to 490 °C for 24 hours. This process is called annealing. Taking them out of the crucibles is most often necessary, because although it is expected that annealing reduces the volume of glass [17], the thermal expansion of the glass before reaching the annealing temperature often results in it cracking or shattering the crucible and glass sample in the process. This thermal treatment enables the glass to release as much of the internal stress resulting from its rapid quenching as possible. The outcome is glass ingots that are much more resistant and can withstand further processing with reduced risks of shattering. This increase in physical resilience is the result of the structural relaxation of the glass network [70]. The temperature of 490 °C is selected as it has been empirically demonstrated to be low enough to avoid crystallization, even for prolonged exposure. This temperature is below the T_g of most GLS compositions [6], yet it still allows for the desired relaxation due to the relative weakness of the chemical bonds of GLS, as it is above its strain point temperature T_s [26].

3.5 Polishing

After being cut down to the desired size using a water-cooled circular saw combined with diamond-coated saw blades, the samples are polished on a Logitech Lapper PM5 combined with a PP6 sample holder [71, 72]. The sample holder is held faced down on a lapping plate on which an ethane-diol/ alumina powder mix is dripped at a constant rate. Ethane-diol solutions are preferred to water-based solutions to avoid chemical reactions with sulphides. The sample is usually polished in several steps, using finer and finer alumina powder grit, ranging from 10 to 0.7 μm until it achieves the desired optical finish. Thin samples are more challenging to polish in this manner, as they have a tendency to shatter due to excessive pressure. However, samples of 1 mm thickness are routinely polished using this technique. For samples that are to be optically characterized, they must be polished on both faces, and the polishing is carried out until the sample thickness is as close as possible to the desired target, which is typically a round number of millimetres.

4 Glass characterization

4.1 Infra-red transmission

The transmission range of GLS glass is determined by a combination of factors. There is a band gap between electronic transitions towards short wavelengths and multi-phonon excitations towards longer wavelengths. The location of the electronic transitions is derived from the molecular bonds formed within the glass. The more ionic bonding facilitates transmission to shorter wavelengths before the onset of electronic absorption [73]. The transmission range of GLS compositions is thus limited in the visible to around 500 nm, which is considerably further towards the visible than other chalcogenide glasses. This electronic absorption edge is attributed to the presence of the ionic compound La_2S_3 [38]. On the other end of the transmission window are phonon excitations, referring to molecular vibrations of the atoms within the glass network. The heavier the atoms and the weaker their bonds, the longer the wavelength at which multi-phonon absorption take place to render the glass opaque, marking the end of the transmission range [74, 75]. For GLS based glasses, the band gap ends in the infra-red at around 12 μm to 15 μm due to this multi-phonon absorption.

The practical limitations on the quality of transmission in GLS glasses arise from short-range composition inhomogeneities, chemical defects, striations and small scattering centres such as crystals or graphite particles from the melting crucibles. These imperfections result in Rayleigh scattering [46, 76]. Equally problematic is the presence of chemical impurities within the glass. The wavelength of the absorptions caused by commonly encountered impurities in GLS are listed in Table 1.

Impurity	Wavelength
OH	2.7-3.12 μm [77]
SH	4.00 μm [78]
SeH/SeH_2	7.8 μm, 4.57 μm/4.61 μm, 4.15 μm [78]
SO	8.7 μm [79]
SeO_2/GeO_2/As_4O_6	7.96 μm [65]/7.81 μm/7.91 μm
SeO	10.67 μm/11.06 μm [80]
(GaO)OH	10.59/9.83 μm [81]
LaO	21.64 μm [82]
CS_2	6.68/4.65 μm [83]
CSe_2	7.8 μm [83]

Table 1: Commonly encountered impurities in GLS glasses and the wavelengths at which they form absorption bands in the infra-red.

Because of these impurities, it is common practise to perform transmission measurements from 1.5 μm to 25 μm on polished GLS. These transmission measurements are made in the infra-red using a Varian 670 Fourier transform infra-red spectrometer (FTIR). A flat sample of GLS polished on both sides is inserted in a sample holder fitted with rubber gaskets, to avoid damaging the sample surface. This holder is then inserted in the nitrogen purged chamber, where it intersects the beam path at a normal angle and enables to produce an absorption spectrum from which the empty sample holder background is subtracted.

In these measurements, the absorbance α (cm^{-1}) is automatically calculated by the software following Equation 6:

$$\alpha(\mathrm{cm}^{-1}) = -\frac{\ln(\frac{\mathrm{I}}{\mathrm{I}_0})}{\mathrm{d}} \tag{4}$$

where I is the detector response with the sample intersecting the beam path, I_0 is the detector response with the empty sample holder and d is the sample thickness in cm.

This measurement is averaged to reduce any noise and ensure its reliability. Several examples are shown in Figure 10. The absorbance is normalized to the sample thickness, but this normalization doesn't take into account the Fresnel reflections from the polished sample surfaces, which are experimentally estimated to roughly correspond to a 28 to 30% loss of overall transmission. These reflections estimates are consistent with the theoretical calculations from the refractive index of the sample, using the Fresnel equations for normal incidence:

$$R = \left| \frac{n_1 - n_2}{n_1 + n_2} \right|^2 \tag{5}$$

where n_1 and n_2 are the refractive indices of the incident and transmitted media respectively.

Consequently, all of the samples have a highly overestimated absorbance that negatively correlates with their thickness. Since the absorption of the glass in the infra-red is very low, the variation in surface quality is significant enough to prevent subtracting these reflections, as it may occasionally result in a negative calculated absorbance. As such, these measurements prove useful to rapidly assess the presence of absorption peaks but cannot be used to accurately ascertain the quality of a sample in terms of minimum loss.

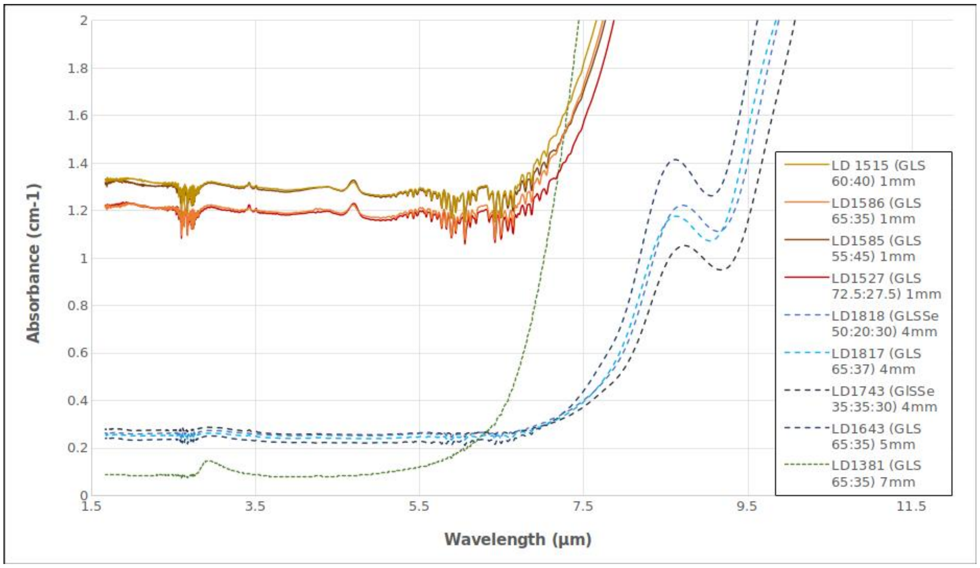

Figure 10: Single FTIR transmission measurements demonstrating the spurious difference in measured absorption between samples of varying thickness.

The most reliable way to address the effect of reflections is to perform a thick/thin measurement, where the background is measured using a thinner sample of the same batch, polished in the same conditions, to ensure identical surface quality and absorption. The normalization is then performed using the thickness difference between the two samples. The absorbance calculated then becomes:

$$\alpha(\mathrm{cm}^{-1}) = -\frac{\ln(\frac{I_T}{I_t})}{d_T - d_t} \tag{6}$$

where I_T and I_t are the detector response for the thick and thin sample respectively, and d_T and d_t are the corresponding sample thickness in cm. Such a measurement is shown in Figure 11. It can be observed that the actual absorbance of the sample is practically naught from 2 to 6 μm, whereas the single measurement shows an overestimated absorbance of 0.75 cm^{-1} over the same range. For the single measurement, the presence of atmospheric moisture in the chamber produces noise at 2.5-2.8 μm and from 5.5 to 7 μm. A double peak at 4.2-4.3 μm can also be seen, which is characteristic of the presence of CO_2 in the chamber. Using a stopwatch to purge the chamber for the same amount of time during the background and the measurement helps keep these artefacts to a minimum, but as timing can never be perfect, they are never fully eliminated. Past 7.5μ, the multi-phonon edge is responsible for the steady increase in absorbance that marks the end of the optical transmission window [10].

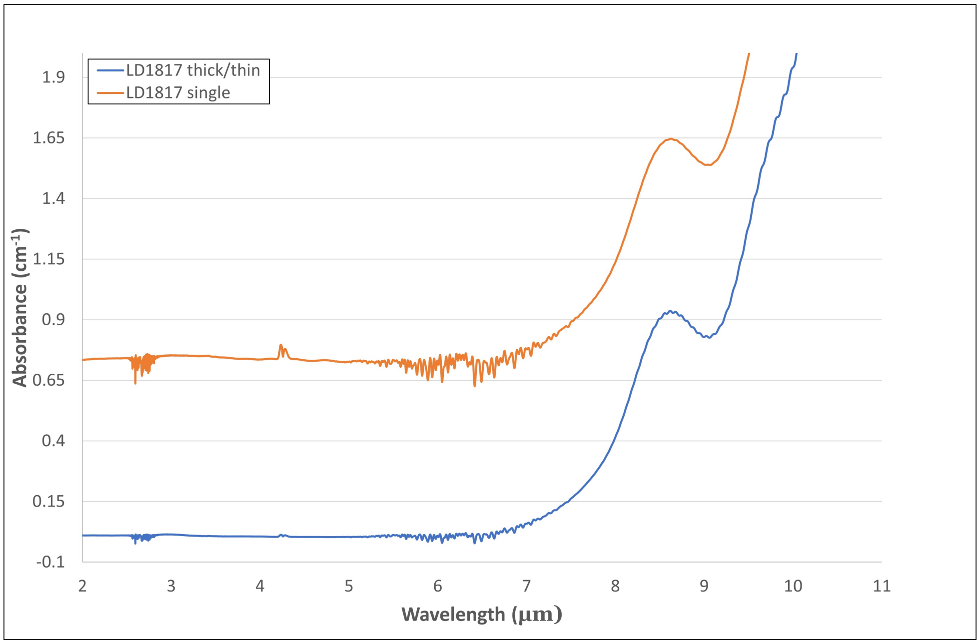

Figure 11: FTIR measurement made using the thick-thin method compared to a single transmission measurement made using the same glass sample (LD1817).

In Figure 12 can be seen the effect of remelting a sample of GLS in silica. As this is not a thick/thin measurement, the overall absorption level is dependent on the sample thickness. Also, the remelted GLS sample showed striations, which could be attributed to the short remelting time of only 2 minutes, which did not allow the sample to thoroughly homogenize. More importantly, the presence of absorption peaks reveals contamination at both 2.9 and 5.5 μm, corresponding to OH and H_2O respectively as per Table 1. Such contamination may be addressed by either coating the inside of the crucible with a layer of carbon or using hydroxyl-free silica to manufacture them. Finding ways to address this contamination is particularly relevant to crucible drawing, as the crucibles used were eventually made of silica, prioritizing their ease of manufacture and versatility in spite of the source of contamination to optimize other crucible drawing parameters. Any such source of contamination that affects the glass used in fibre drawing must eventually be minimized, as they are magnified in several metres of fibre when compared to a sample only a few mm thick.

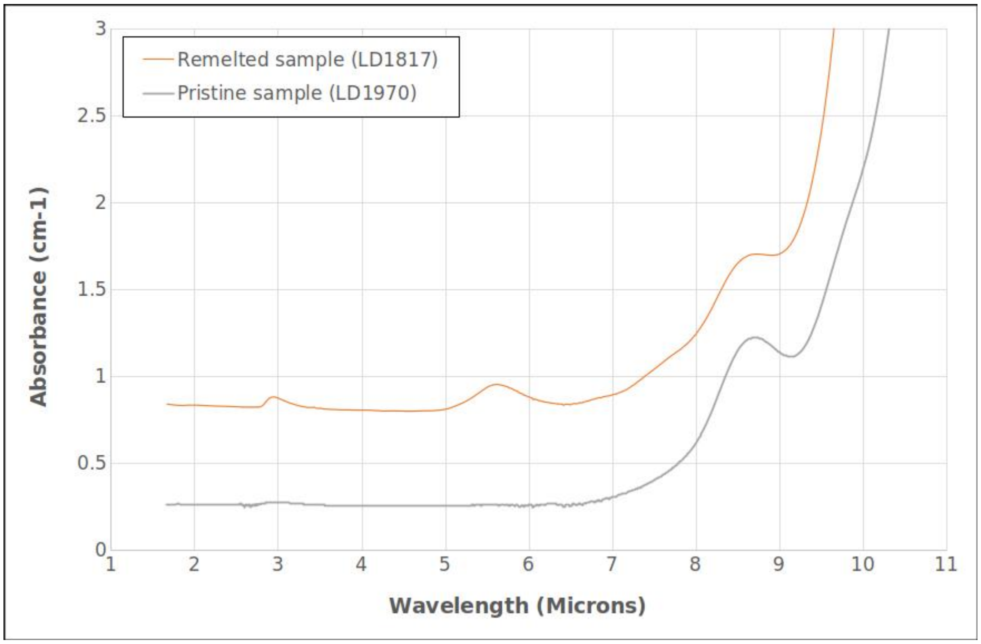

Figure 12: FTIR transmission measurement demonstrating the effect of remelting GLS 65:35 in silica on its infra-red transmission, enabling to identify contamination from impurities leached from the silica crucible.

In Figure 13 can be seen a thick/thin measurement performed on cured Desolite^{TM} [84], which is the material used to coat fibre as soon as it is formed. This material has a large amount of OH absorption at 3-3.5 μm and a transmission cut-off at 5.5 μm. This is expected to significantly affect the transmission of unstructured fibres, as the light propagating through the glass will interact with this coating.

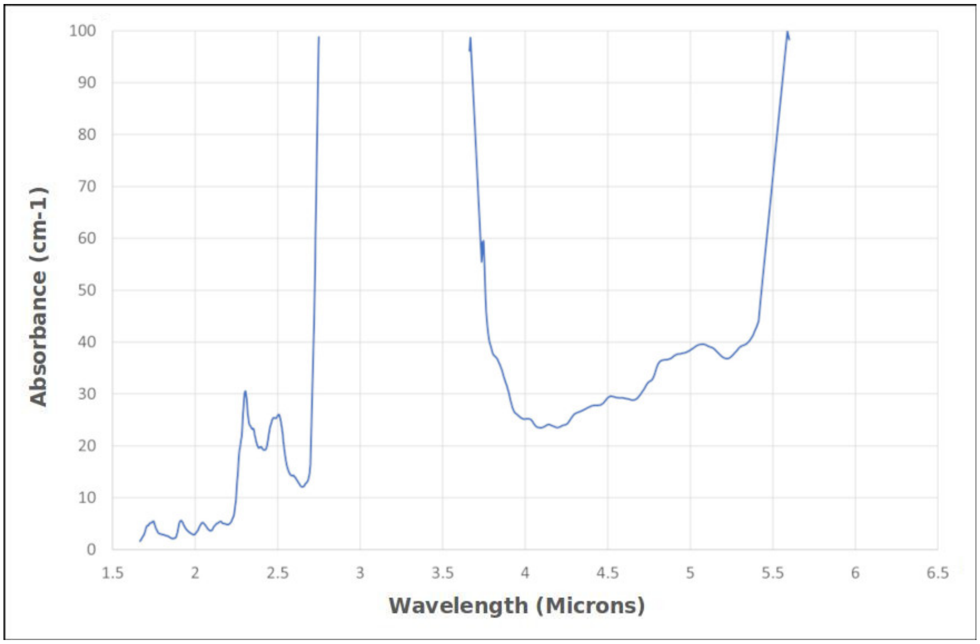

Figure 13: Thick-thin FTIR transmission measurement performed on cured Desolite$^{\text{TM}}$ samples to assess the effect of Desolite$^{\text{TM}}$ coating on unstructured fibre.

4.2 Ellipsometry

Ellipsometry is a method commonly used to measure the refractive index, the absorption and/or thickness of solids. It is particularly attractive for thin films characterization, as it is non-invasive and highly surface sensitive. In order to calculate the refractive index of a flat reflective sample, the ellipsometer measures the horizontal to vertical polarization ratio of the light reflected onto it, and fits to it an adequate model [85]. For a single interface of isotropic homogeneous media, the following equations are used:

$$\rho = \frac{\mathrm{r_p}}{\mathrm{r_s}} = \tan(\psi)\mathrm{e}^{\mathrm{i}\Delta} \tag{7}$$

$$\mathrm{r_p} = \frac{\tilde{\mathrm{n}}_2 \cos\phi_\mathrm{i} - \tilde{\mathrm{n}}_1 \cos\phi_\mathrm{t}}{\tilde{\mathrm{n}}_2 \cos\phi_\mathrm{i} + \tilde{\mathrm{n}}_1 \cos\phi_\mathrm{t}} \tag{8}$$

$$\mathrm{r_s} = \frac{\tilde{\mathrm{n}}_1 \cos\phi_\mathrm{i} - \tilde{\mathrm{n}}_2 \cos\phi_\mathrm{t}}{\tilde{\mathrm{n}}_1 \cos\phi_\mathrm{i} + \tilde{\mathrm{n}}_2 \cos\phi_\mathrm{t}} \tag{9}$$

where ρ is the ratio of the horizontal to vertical polarization (r_p and r_s respectively), ψ and Δ are the polarization transformation coefficients, $\tilde{n}_1$ and $\tilde{n}_2$ are the complex refractive indices of the incident and refractive media respectively, and ϕ_1 and ϕ_2 are their corresponding angles of incidence and refraction. These equations can be combined with Snell's law ($\tilde{\mathrm{n}}_1 \sin\phi_\mathrm{i} = \tilde{\mathrm{n}}_2 \sin\phi_\mathrm{t}$) in order to extract the complex refractive index of the medium of interest ($\tilde{n}_2$). For real samples, the models applied are sufficiently complex to take into account sample defects, surface roughness and back reflections of a transparent sample polished on both sides [86].

Ellipsometry measurements were taken on such two-side polished 1 mm thick samples using a a rotating compensator ellipsometer Woollam M-2000 [87], and they were fitted using the CompleteEASE^{TM} software [88], using a B-Spline model for glass substrate with surface roughness, taking into account both surface polishing defects and the presence of backside reflections. An ellipsometry measurement performed on GLS is shown in Figure 14. This measurement may be fitted using the Sellmeier equation:

$$\mathrm{n}^2(\lambda) = 1 + \sum_{\mathrm{i}}^{\infty} \frac{\mathrm{B_i}\lambda^2}{\lambda^2 - \mathrm{C_i}} \tag{10}$$

where n is the refractive index, λ is the wavelength, B$_i$ and C$_i$ are fitting parameters [89]. This equation is often simplified for glasses to only include the first 3 terms of the mathematical series [90]. As can be observed in Figure 14, repeated measurements with a set of 1 mm thick GLS 65:35 appear to be consistent with one another, and the attempts at manually removing back reflections by either coating the bottom surface or de-polishing it proved to be unnecessary to achieve a good fit. However, it was observed that some samples show striations due to uneven mixing during their fabrication. Unfortunately, these imperfections can only be observed after samples have been cut and polished. They produce distortions of the transmitted light due to their anisotropy, and as a consequence, they have an inconsistent refractive index [91].

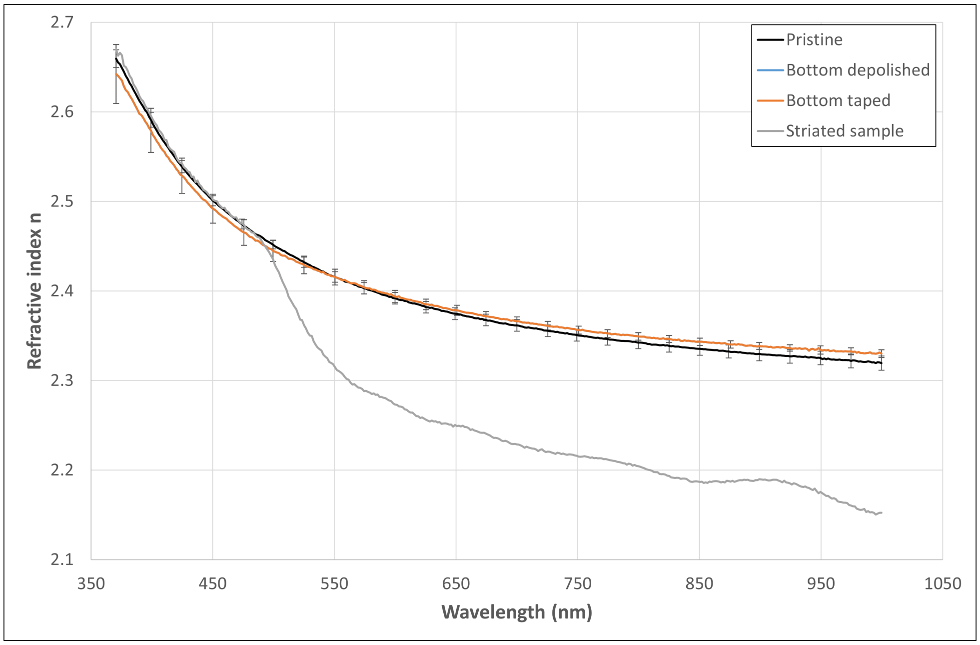

Figure 14: Ellipsometry measurement comparing the refractive index of flat 1 mm GLS samples to assess the effect of de-polishing the bottom surface or coating it with carbon. Refractive index measurement on a heavily striated sample is also shown for comparison.

4.3 Plasma ashing

As the glass is made by using the melt-quench technique in either graphite or vitreous carbon crucibles, the surface of the glass is often contaminated with carbon. During the cutting and polishing of the glass, the carbon deposits are removed, but it wastes expensive material, reduces the maximum achievable sample thickness, and the additional amount of processing required to remove these particles increases the risk of damaging the glass. So as to avoid these issues and minimize the amount of material lost to and the length

Sample Number	Plasma Ashing Treatment
LD1999(1)	10min O_2
LD1999(2)	10min SF_6
LD1999(3)	10min SF_6 and O_2
LD1999(4)	10min $O_2 \rightarrow$ 10min SF_6

Table 2: Plasma ashing array of treatments of each polished 1mm GLS sample.

of the polishing step, samples were placed in a K1050X Plasma Asher [92] and treated using either SF_6 or O_2, in an attempt to remove some of the surface carbon deposits. The amount of power used was 80 W at 6×10^{-1} mbar of gas pressure. The results of initial tests are shown in Figure 15. It appears that, contrary to SF_6, O_2 plasma ashing rapidly removes carbon deposits.

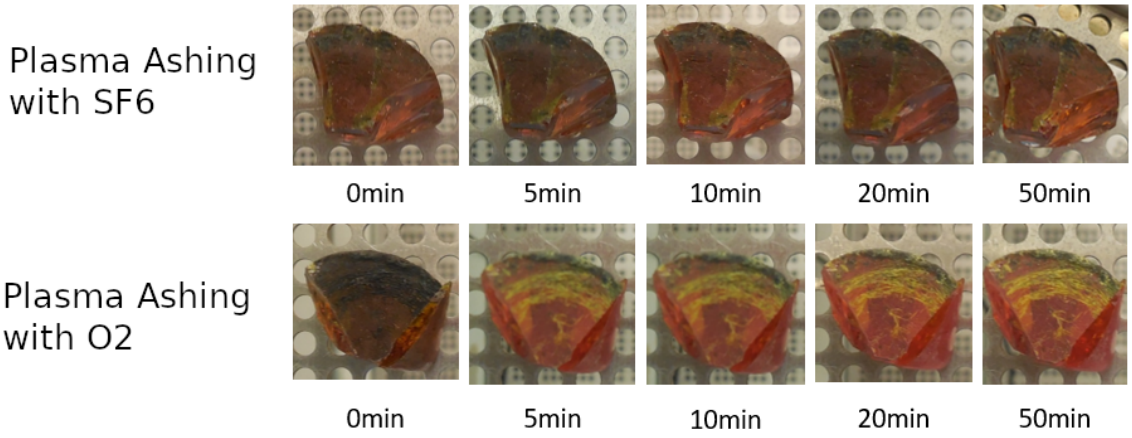

Figure 15: Comparative effect of increasing the exposure time to plasma ashing on carbon contaminated GLS samples using either SF_6 or O_2.

Following this observation, 1 mm polished flat samples of GLS 65:35 were plasma ashed using the protocols detailed in Table 2 in order to assess whether plasma ashing contaminates the samples to any significant degree. The samples were then taken out of the chamber and had their infra-red transmission spectrum measured, as shown in Figures 16 and 17.

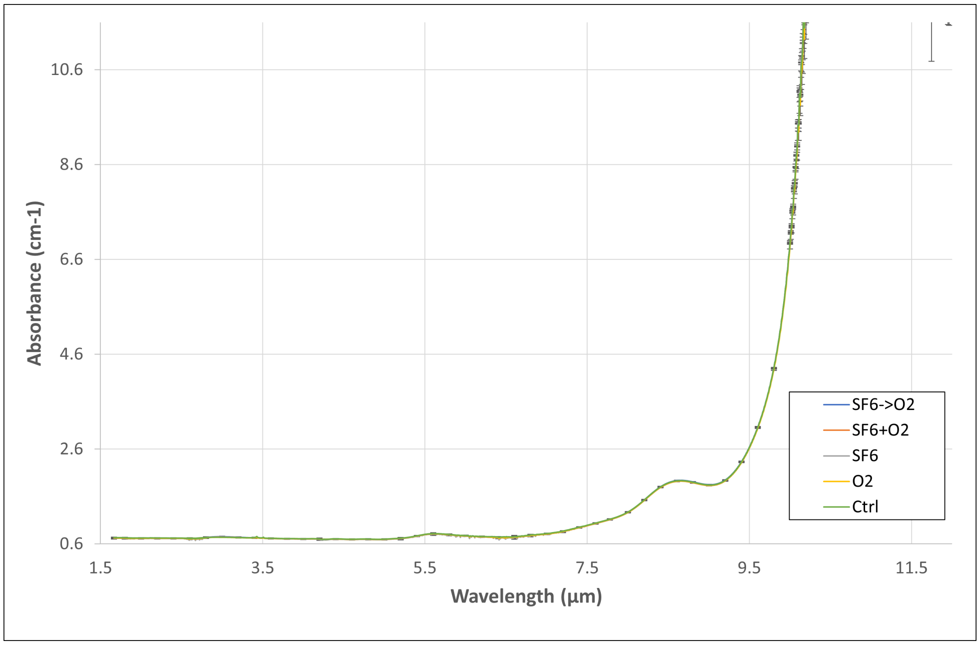

Figure 16: Single FTIR transmission measurement of 1 mm thick plasma ashed GLS samples (LD1999).

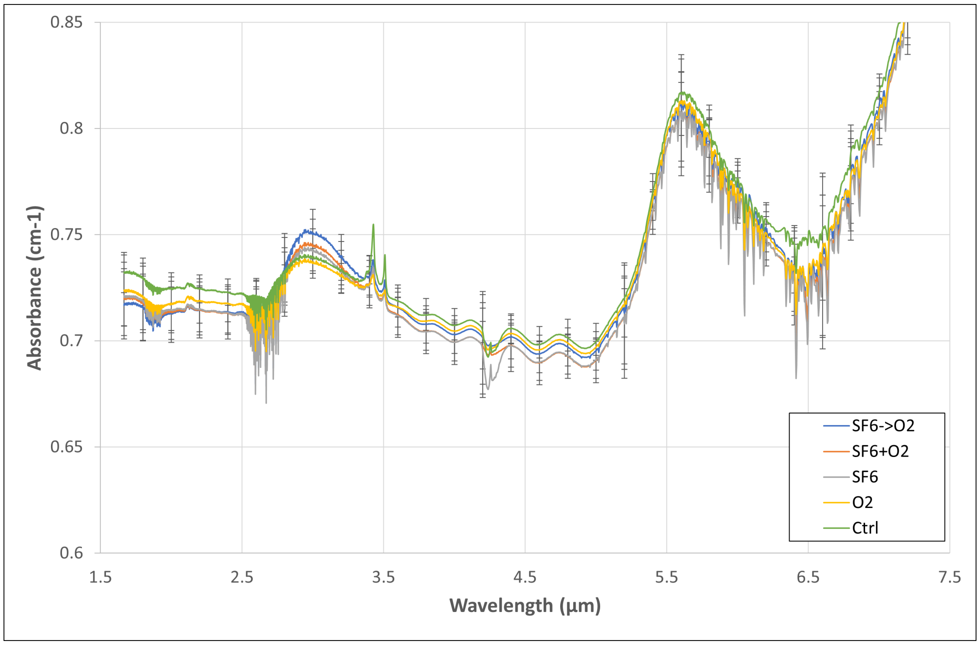

Figure 17: Single FTIR transmission measurements of plasma ashed GLS samples zoomed in on the 1.5 to 7.5 μm region, where the key absorption peaks for relevant contamination is expected.

As can be observed in Figure 16 and 17, there is no visible contamination introduced in the infra-red from either O_2 or SF_6 plasma ashing. The focused view shown in Figure 17 demonstrates that each curve lies well within the experimental margin of error of one another, no matter the gas used during the ashing process. This is a positive sign for the use of plasma ashing as a cleaning step for GLS intended for fibre drawing experiments, as it appears oxygen plasma does not contaminate the glass. To complement this information, an ellipsometry measurement was made from 370 to 1000 nm to determine whether the surface had its refractive index changed during the plasma ashing process. The results are shown in Figure 18. It appears that the refractive index, and thus the chemical make-up of the surface has indeed been altered by plasma ashing. The apparent contradiction between the outcomes of infra-red transmission and ellipsometry measurements can be explained by the plasma reacting exclusively with the surface, producing an ultra-thin layer of a different composition to that of bulk glass, and it may be the case that this layer is too thin to be picked up by infra-red transmission measurements. For the sample that was plasma ashed using SF_6 and O_2 in succession, it appears that the refractive index no longer follows the trend expected from a Cauchy or Sellmeier equation and becomes anomalous, increasing with wavelength rather than decreasing [93]. This observation was verified by making ellipsometry measurements on the same samples before and after plasma ashing and obtaining identical trends.

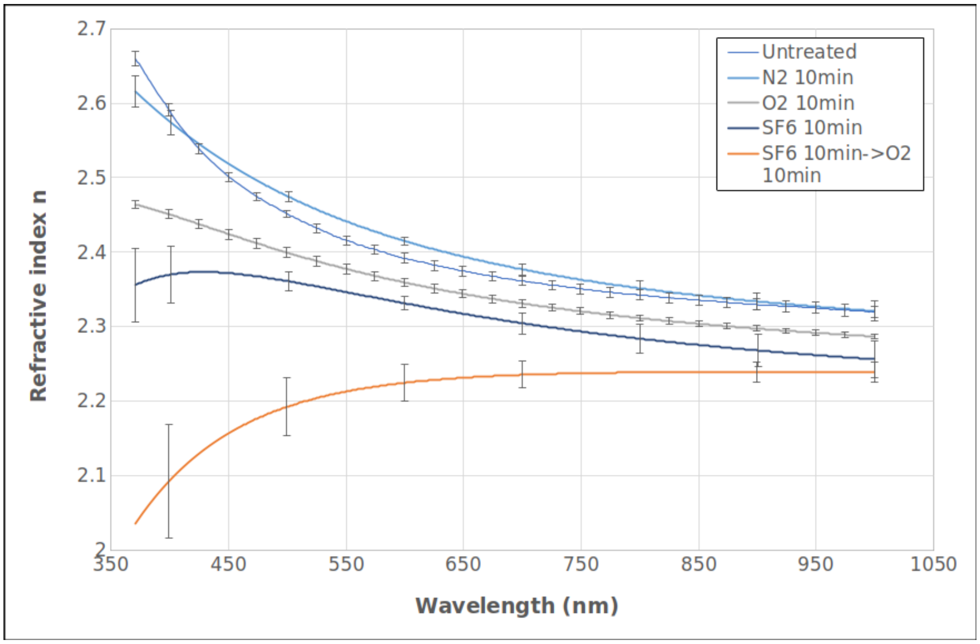

Figure 18: Array of ellipsometry measurements of the refractive index of 1mm thick GLS samples plasma ashed with varying gas combinations.

In Figure 19, it is also demonstrated that the effect of plasma ashing on the refractive index of the surface greatly depends on the time of exposure to plasma. A large variety of gases may be used in conjunction with the K1050X Plasma Asher [92], and the observations detailed here are enough to motivate a thorough investigation of the modification of the surface composition of GLS glasses using plasma ashing and its effects.

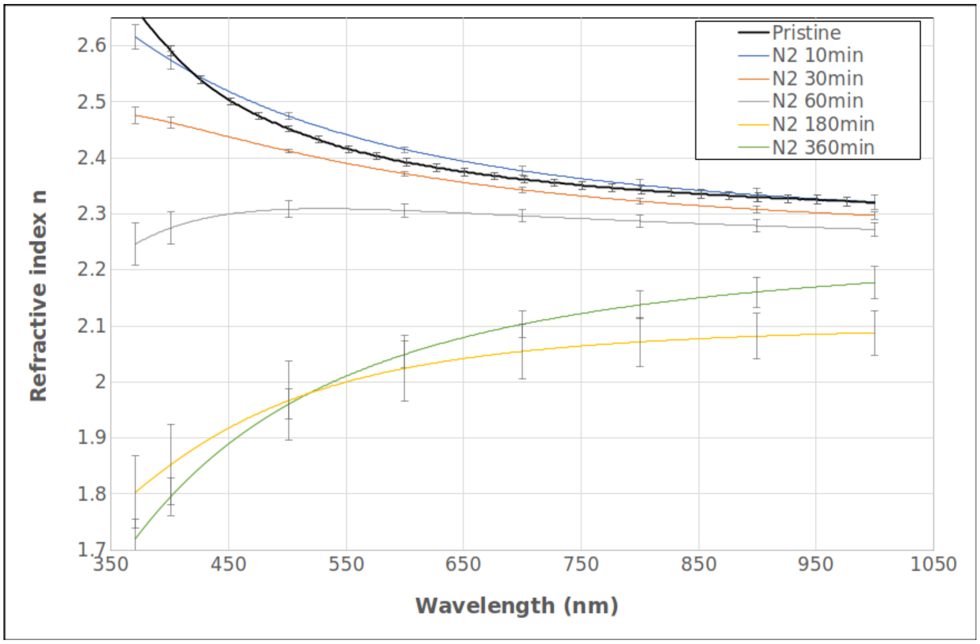

Figure 19: Ellipsometry measurement of the refractive index of 1 mm thick GLS samples plasma ashed with nitrogen for an increasing amount of time, demonstrating the gradual change of the chemistry of the surface.

4.4 Thermal conductivity

Thermal properties are a particularly relevant aspect of infra-red glasses. Indeed, being used in the field implies exposure to harsh environmental conditions, including extreme temperatures. It follows that thermal insulation is a key parameter to consider when designing durable field equipment. Although the phase transition temperatures and thermo-mechanical properties are well documented for GLS composition variants [10], its thermal conductivity has yet to become a standard measurement despite its practical relevance. In addition, thermal conductivity is also essential to fibre drawing, as it is a key parameter in determining the time required for temperature to stabilize within the glass as well as the final temperature gradient between the surface and the core of the preforms [94].

In order to measure thermal conductivity, several methods are available. One of the most commonly used for thermally insulating materials such as glass is Lee's disk method [95]. It requires relatively large (50 to 100 mm in diameter), disk shaped samples. Producing such large samples would be impractical for the sake of a single thermal conductivity measurement. Also, the wide majority of samples of GLS from previous melts are much smaller (typically 30 mm in diameter maximum). There exists another, more suitable method available for such samples. Known as the divided-bar method, this technique was primarily developed for applications in geology, and is able to provide reliable estimates of thermal conductivity for relatively insulating materials [96]. As such, it seems ideal to measure the thermal conductivity of a glass. The experimental setup constructed to employ this method for thermal conductivity measurements in glass is schematically illustrated in Figure 20.

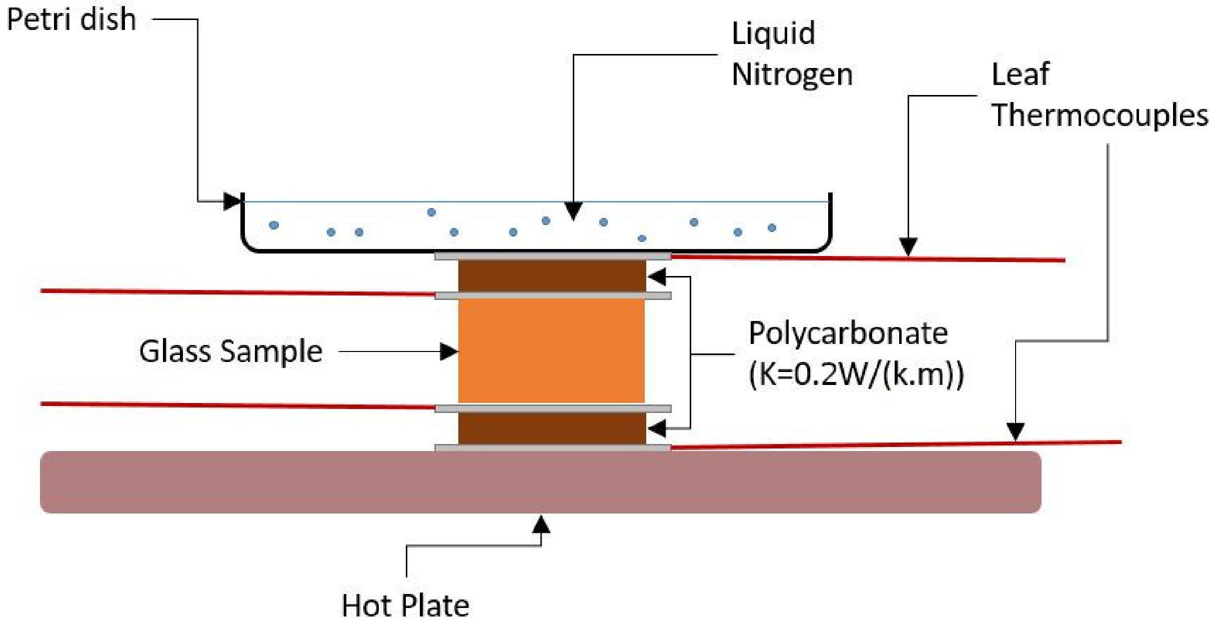

Figure 20: Schematic representation of the divided bar setup used to measure thermal conductivity, where a thermal gradient is established using liquid nitrogen combined with a hot plate. Leaf thermocouples are used to monitor the temperature across samples of interest.

It was implemented using a hot plate set to a fixed temperature at the bottom, and a petri dish filled with boiling liquid nitrogen at the top to ensure a constant heat flow across the stack once the temperature equilibrium is reached. Several samples of known thermal conductivity (from highly insulating polycarbonate: 0.20 W/(m.K) to highly conductive brass alloys: 123 W/(m.K)) [97] were used to determine the amount of heat flowing through the divided bar for a given sample cross-section and temperature setting. Once heat flow has been calculated for a given sample size, thermal conductivity for an unknown sample of the same dimensions can be determined by simply substituting it to the reference sample and measuring the change to the temperature gradient across it. Two polycarbonate samples of known thermal conductivity are kept in the stack at all time, one before and one after the sample of interest, to ensure that the stack is sufficiently clamped. If it isn't, their measured thermal conductivity is underestimated due to the presence of air gaps within the stack. Eliminating these air gaps requires delicate adjustments to the clamping of the stack, due to the brittleness of the glass samples measured. Indeed, excessive pressure combined with thermal expansion damaged samples on several occasions.

The equation used to extract the heat flow and the thermal conductivity is as follows:

$$\mathrm{K} = \frac{\mathrm{Q/A}}{\Delta\mathrm{T/L}} \tag{11}$$

where K is the thermal conductivity in W/K.m, Q is the heat flow in W, A is the cross-section area in m^2, L is the thickness of the sample in m and ΔT is the temperature difference between either of its sides in °C. The results obtained using this setup and equation are shown in Figure 21. It can be observed that the average thermal conductivity obtained is 0.87± 0.04 W/(K.m). This is not in agreement with the information available online, which shows a value closer to 0.5 W/(K.m) [98]. However, it appears that this piece of information is sourced to a 2003 publication aiming to determine the primary mechanism of light attenuation in GLS at 1.55μm using laser calorimetry, and it doesn't appear at

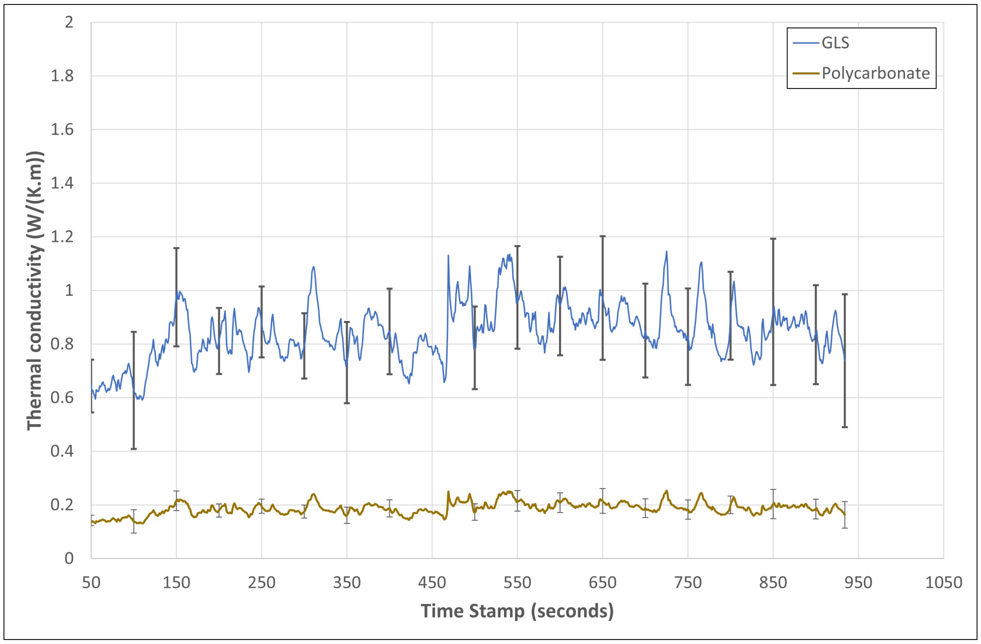

Figure 21: Evolution of the thermal conductivity calculated based on Formula 11 as a function of time for a 5 mm thick GLS65:35 sample. A measurement made on a 1mm polycarbonate sample is given as a reference.

any point to measure or calculate the thermal conductivity of GLS [99]. In addition, a verification performed using the same setup on a 1 mm piece of polycarbonate yields a thermal conductivity of 0.17±0.02 W/(K.m), which is close to its thermal conductivity as specified by the manufacturer of 0.2 W/(K.m) [97]. For comparison, arsenic selenide and germanium arsenic selenide glasses of the IG glass family show a thermal conductivity close to 0.2 W/(K.m)[5, 100].

4.5 Corrosion study

With similar motivations as for thermal conductivity, the resistance of GLS to exposure to chemically harsh environments is also a relevant characteristic to monitor. It has been stated in previous work that corrosive substances may be used for chemical etching and polishing of glass preforms and fibres [47, 101, 102]. The primary mechanism for the corrosion of glasses is leaching, which is a process by which ions are removed from the glass structure and incorporated into the solvent in contact with it in a chemically uneven process. It only becomes visible once the surface of the glass has been altered to the point where it starts to dull, which occurs once around 100 μm of the surface has been damaged [17]. Many different methods have been implemented to assess the extent and chemical process of corrosion. For example, Adam and Evans crushed borate glass into powder of a pre-defined grit to maximize the area of contact and exposed the powder to deionized water for 24 hours. They then measured the amount of sodium and boron in the water via flame spectroscopy [103]. Alternatively, a number of advanced techniques, namely elastic recoil detection analysis, Rutherford backscattering, sodium diffusion measurements, and nuclear magnetic resonance (NMR) were used by Bunker *et. al.* in 1986 to study leaching in borosilicate glasses [104]. In the context of the search for in-house rapid measurements for contamination-sensitive chalcogenides, a method for the measurement of corrosion resistance of industrial glasses was implemented based on an International Organization for Standardization (ISO) standard instead [105]. This method was chosen as it is suitable for both strong acids and strong bases. The experimental setup used for exposing sample to corrosive solutions is illustrated in Figure 22. Samples of known weight and dimensions are suspended in a highly acidic or basic stirred solution using Tungsten wire for extensive periods of time (up to thousands of hours). The key difference with the standard is the use of Tungsten wire and Pyrex glass, rather than stainless steel, as iron ions produce a strong (above 1 dB.m^{-1}.ppm^{-1}) and very broad (from 1 to past 5 μm) absorption peak in contaminated GLS, and should be avoided wherever possible [10]. After corrosion has visibly started, the samples are taken out of the solution, cleaned, and weighed to determine the amount of time required to etch 0.1 μm of the sample surface for a given corrosive substance. This value, combined with an assessment of visible surface changes illustrated in tables 3 and 4 was used to compare glasses across composition and sample sizes.

Acid resistance class	pH	Time in hours needed to etch a depth of 0.1 μm
1	0.3	>100
2	0.3	10-100
3	0.3	1-10
4	0.3	0.1-1
5	0.3	<0.1

Table 3: Acid corrosion resistance scale (ISO 8424) based on the amount of material lost.

Acid resistance class first decimal	Optical variation
.0	no visible changes
.1	clear, but irregular surface
.2	staining and/or interference colours
.3	tenacious thin whitish layer
.4	loosely adhering thick layer, such as insoluble friable surface deposit

Table 4: Classification of acid resistance according to the visible surface changes (given as a decimal figure) from ISO 8424.

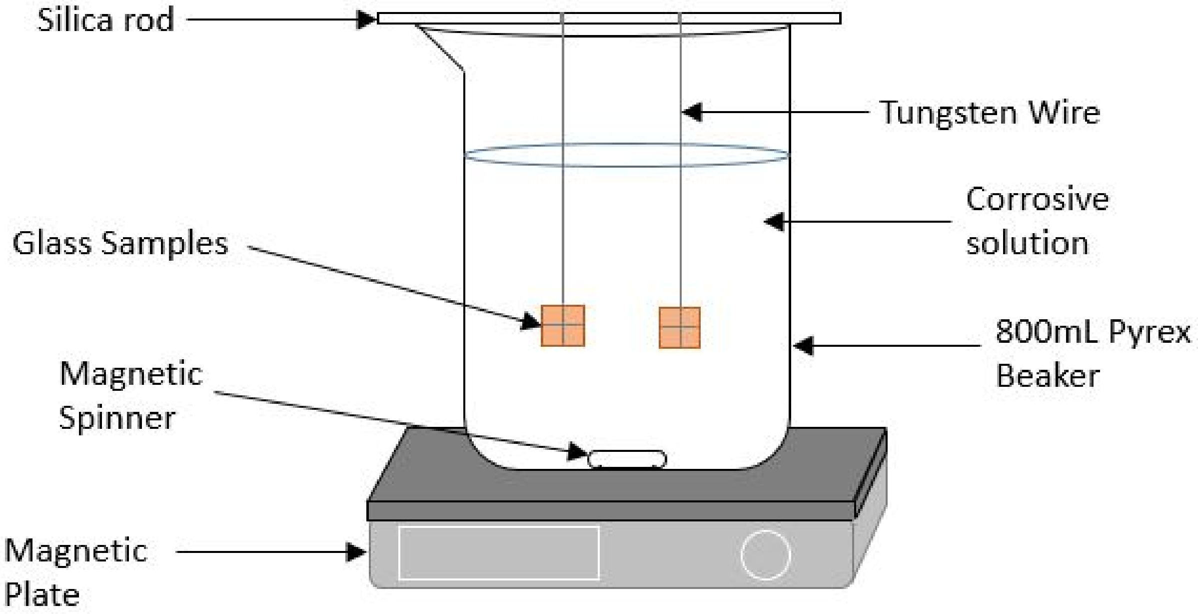

Figure 22: Schematic representation of the corrosion measurement setup used, based on a custom variation of ISO 9241-210.

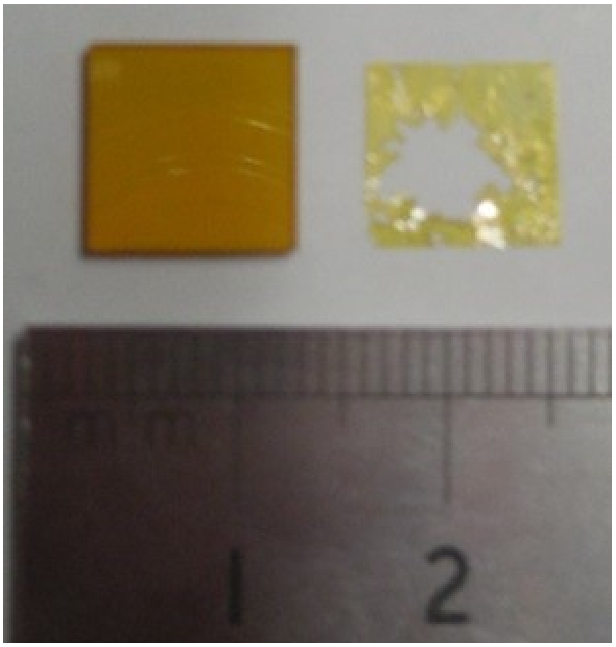

Figure 23: GLS 65:35 sample before and after submersion in pH 0.3 nitric acid for 337 hours.

Using this method, the resistance of 65:35 GLS to 0.5 mol.L^{-1} pH 0.3 nitric acid was classified as 5.1, the lowest, according to the ISO standard. The sample used in this test is almost completely dissolved, as shown in Figure 23. The resistance of an IG4 ($Ge_{10}As_{40}Se_{50}$) window was found to be 1.0, after it had been submerged in a solution of nitric acid at the same concentration and pH. The sample was not coated, as verified by cleaving the sample in half and re-suspending it in the solution with its pristine face exposed. It was also compared to a fresh IG4 sample in a transmission measurement using the FTIR, to verify if the submersion in such a strongly acidic solution had produced measurable leaching. As shown in Figure 24, no significant difference in terms of chemical contamination was observed between the two samples. However, there appears to be a significant difference in transmission, as an approximately 6 to 7% reduction below 16 μm. So, in spite of its unaltered aspect, the IG4 sample reacted with nitric acid. This brings into question the assessment method used in the ISO standard, as they do not take into account such an essential effect of corrosion. However, considering the stark contrast between the GLS sample and the IG4 sample, it can only be concluded that, compared to GLS, IG4 has an exceptional resistance to corrosion from nitric acid. The experiment was repeated using a molar ($1mol.L^{-1}$) solution of sodium hydroxide (NaOH), and it was found after 1450 hours of immersion of both GLS and IG4, that the resistance of both samples to NaOH was 1.0, with no significant changes in transmission. It was also observed that, for such a long time of exposure, evaporation became an issue, as it causes the concentration of OH to increase with time and requires weekly replacement of the test solution.

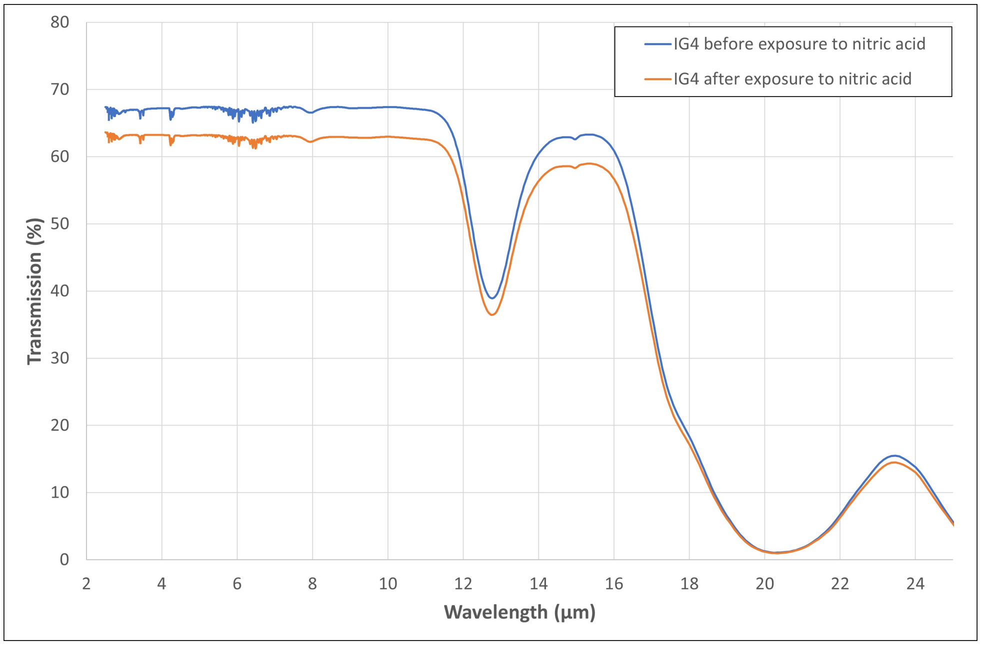

Figure 24: FTIR transmission measurement of a 2mm thick IG4 window before and after prolonged (950hours) immersion in nitric acid.

Overall, the conclusion of these tests is that the assessment criteria of corrosion needs to be improved upon and varied, for although mass loss and visual appearance are key observations, they do not take into account subtler chemical changes that effect the properties of the glass. Also, for lengthy exposure of highly resistant materials, using a closed vessel would ensure a higher degree of reliability, as the concentration of the corrosive solution would be more stable, since it would not suffer from evaporation. Thorough testing of the effects of corrosion on a variety of glasses, using a wide range of chemicals (including solvents) at higher temperatures to increase the reaction speed, combined with more detailed assessment methods is envisioned, but goes beyond the scope of these tests.

4.6 Differential thermal analysis (DTA)

In the study of various GLS compositions, the thermogravimetric differential thermal analyser (TG-DTA) plays an essential role, as it provides an understanding of the thermal properties of glass in order to identify the compositions most suitable for different fibre drawing methods. It is composed of a small furnace in which two crucible-carrying thermocouples are inserted, as shown in Figure 25.

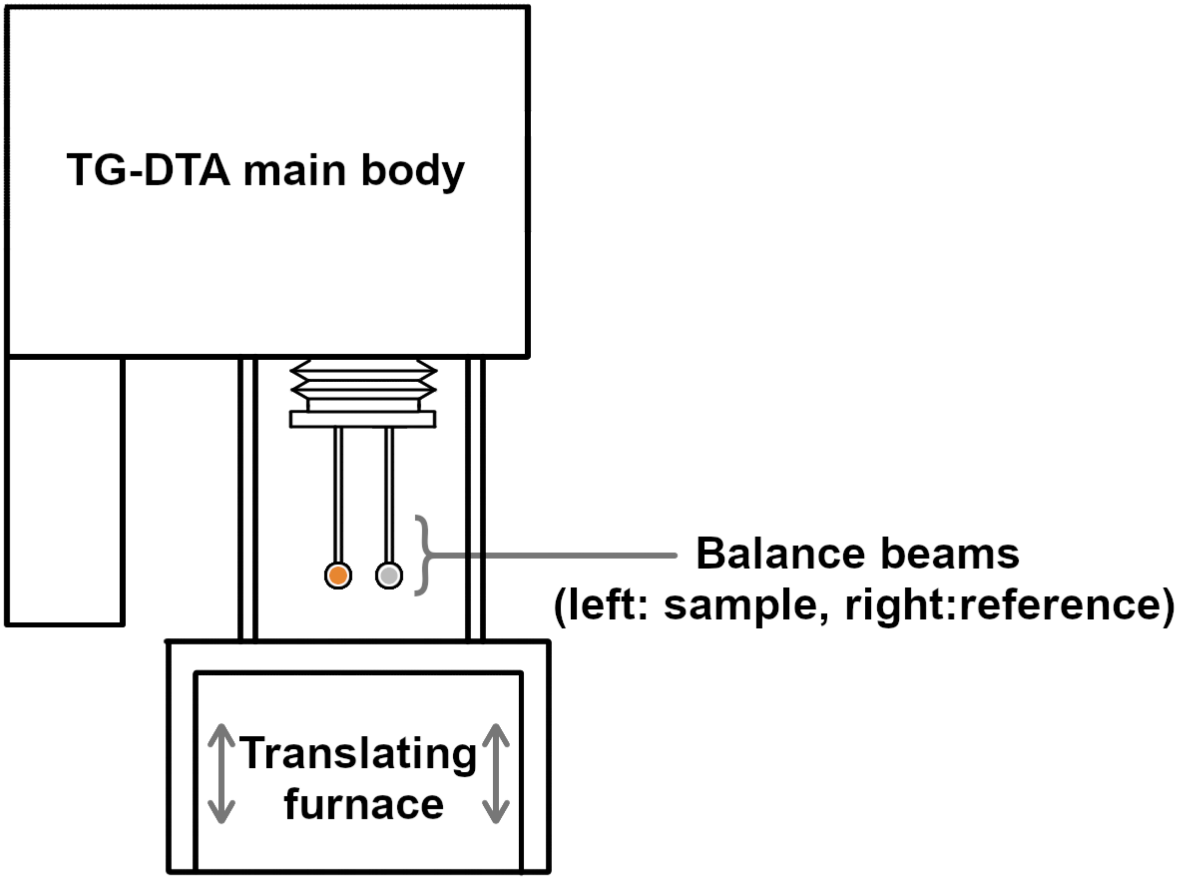

Figure 25: Schematic representation of the TG-DTA loaded with a GLS sample before the translating furnace is closed.

The TG-DTA monitors heat flow, weight, and temperature for each individual arm in the furnace as it performs a temperature scan. From the collected data, the phase transition temperatures of the chemicals loaded in the crucibles can be obtained. This enables to make an informed decision regarding the quenching parameters required for glass melting as well as predict the temperature range that may be utilized in the fibre drawing process. In the standard method used here, one of the crucibles is loaded with a 10 mg sample of interest and the other is loaded with 10 mg of alumina powder, to act as a thermal inertia reference. The crucibles used are also made of alumina. The furnace is closed, the weight carried by each thermocouple arm is zeroed, the nitrogen purge is activated at 20 mL/min, and temperature is ramped up from 25 °C to 1150 °C at 10 °C/min. A small amount of alumina power may be added underneath the crucibles so as to facilitate heat transfer to the crucible and ensuring it doesn't stick to the thermocouple arm. However, placing some alumina powder inside the sample crucible to achieve the same goal is strongly advised against in the literature, as it is claimed that it may lead to unwanted chemical reactions and introduce new nucleation sites [106]. The ramping rate must be sufficiently low for the phase change temperatures to be determined with precision, and yet be sufficiently rapid for these phase changes to appear as discrete peaks and dips. It must also be the same across all the samples under test, to enable reliable comparisons to be made across different experimental runs. The typical standard used in these experiments is 10 °C/min. An example of the recorded heat flow through the chamber is illustrated in Figure 26, where several endothermic and exothermic phase transitions take place within the samples. The compositions of GLS tested in Figure 26 were each varying from one another in the proportion of gallium sulphide (Ga_2S_3) to that of lanthanum sulphide (La_2S_3). Their individual compositions are listed in Table 5.

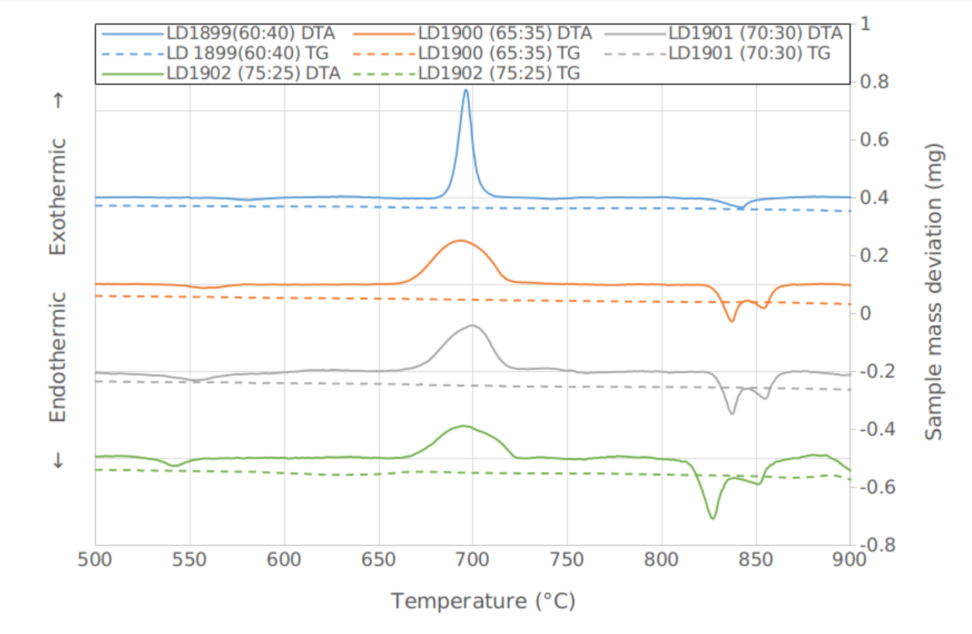

Figure 26: TG-DTA measurement for various GLS compositions. The variations in sample mass can be estimated using the scale on the right (each sample weighed 10±1 g), and the heat flow is recorded on the left scale in arbitrary units.

It is best practise to use sealed crucibles to perform a DTA on volatile compounds, such as chalcogenides. However, this precaution is unnecessary for most gallium lanthanum sulphide glass compositions. This is due to their low volatility even at high temperatures. Indeed the measured mass loss only exceeds 1% past 1020 °C for all compositions tested. At this point, all the phase transitions have already taken place, and the sample is fully

Name	Ga2S3	La2S3
LD1899	60%	40%
LD1900	65%	35%
LD1901	70%	30%
LD1902	75%	25%

Table 5: Composition variation in the GLS samples used for DTA and TMA in Figure 26 and 31.

molten. Even at the end of the TG-DTA run at 1150 °C, the total mass loss is only 3 to 5%. In Figure 26, several phase transitions can be observed, starting with the faint endothermic glass transition (Tg), located between 520 °C and 570 °C for all samples. This endothermic event is most visible on the LD1902 curve but is nonetheless apparent for all samples under test. The onset of T_g is estimated by extrapolating the baseline and the steepest part of the glass transition dip. The T_g measured will depend on the thermal history of the glass, in particular, properly annealed samples will have a lower T_g, as annealing enabled it to reach lower energy and higher density while still maintaining a vitreous state. In order to accurately compare samples of different compositions, it is therefore necessary to ensure that all of them have been thoroughly annealed. For GLS, all samples are annealed for 24 hours at 490 °C, as described in Section 3.4.

Next is the exothermic crystallization event, located between 660 °C and 690 °C (T_x). It is the most prominent variation in the heat flow for all samples. Unlike the T_g, it shouldn't be estimated by extrapolating the steepest slope of the peak, but rather, by visually assessing the temperature at which the heat flow departs from the baseline. The motivation for this difference in the standard used to determine the phase transition temperature is the irreversible and self-encouraging nature of crystallization. Indeed, if the temperature ramp-up were halted as soon as the heat flow departs from the baseline, the sample would still continue developing crystals until it became entirely devitrifed, and the heat flow would evolve accordingly. As such, an extrapolated onset is not as meaningful to determine the crystallization temperature T_x than it is for the glass transition T_g. This crystallization event is noticeably more discrete and sharp in the case of LD1899 than the others. This could be a sign that the 60:40 composition has pre-existing nucleation. This nucleation should result in a shift of the crystallization peak towards lower temperatures [107]. However, that doesn't seem to be the case. On the contrary, the T_x for LD1899 is higher than for the other samples. The crystallization temperature T_x is particularly important for fibre drawing. Indeed, fibre drawing is assumed to be possible at an ideal temperature where viscosity is both sufficiently low for the glass to stretch under the action of gravity and/or the pull of the drum to which it is attached, yet sufficiently high for the glass to fall in a slow and controllable fashion. This ideal temperature, however, may be too close to the crystallization peak, which would at best require fibre drawing to be performed very quickly, and at worst prevent any crystal-free fibre from being drawn, if the glass starts to crystallize before it even softens. From the experience gathered in previous work, this seems to be a recurring issue for GLS [10, 108].

Finally, between 810 °C and 830 °C, the solidus, which is the point where the glass starts to melt and liquidus, where the glass is fully molten (T_s and T_l respectively) are visible for most samples except for the 60:40 composition again, which only shows a single melting event. It could however be the case that the two peaks are too close to be distinguished from one another. Because of the anomalous behaviour depicted in TG-DTA measurements, GLS 60:40 composition is of particular interest for fibre drawing. It may be noted that both T_g and T_s increase with the proportion of La_2S_3 to that of Ga_2S_3. This may seem counter-intuitive, as the increased amount of network modifier should result in a lower overall bond strength, as the proportion of ionic bonds to that of covalent bonds increases. However, the introduction of larger amounts of lanthanum also comes with an increased amount of sulphur. And as described in Figure 6, this in turn increases the proportion of gallium atoms that are in a fully co-ordinated glassy tetrahedral network configuration, which does more than offset for the increased amount of lanthanum in the glass.

Two fibre drawing approaches have been explored in this work, which are complimentary depending on which side of the crystallization peak the ideal drawing temperature is located. If the fibre drawing temperature is lower than the crystallization temperature T_x, the glass can be heated directly in solid form until it becomes soft enough to be drawn. This approach is suitable for rod-preform drawing from solid glass. If this ideal temperature is higher than the onset of crystallization T_x, the glass can be heated past the crystallization event and above its melting point, thereby removing all crystals that may have formed within the glass. It may then be brought down from this high temperature, progressively increasing viscosity to the point where it can be drawn into fibre. This approach is suitable for crucible drawing, as long as the crucible used is fitted with a tight plug. Consequently, the fibre drawing parameters of interest extracted from DTA measurements will vary depending on the method used to draw fibre. For rod and preform drawing, the ideal situation is brought about by compositions for which T_x-T_g

is the largest, providing a wide stable temperature range in the search for an optimum below the crystallization temperature. This value is known as the Hruby parameter [109]. According to this criterion, the best composition is 75:25 (LD1902). In reverse for crucible drawing, the equivalent of the Hruby parameter is T_m-T_x. It must be maximized to provide the widest workable range above the crystallization temperature. The best composition based on this criterion is 65:35 (LD1900). For both approaches, however, it also seems the 60:40 (LD1899) composition is an attractive candidate, due to its noticeably sharp crystallization peak, which could avoid the early onset of crystallization when approaching in temperature from either side.

The operation of the DTA was modified to obtain additional thermal information believed to be particularly relevant for crucible drawing. After ramping the temperature from 25 °C to 1150 °C at 10 °C/min to obtain the phase transition temperatures in a standard ramp up process, two following steps were added. First, temperature was maintained at 1150 °C for 10 minutes so as to ensure the sample is homogeneously melted. This may not be necessary for the small amount of glass used in the TG-DTA (around 20 mg), but it is performed during crucible drawing experiments. Therefore, in an attempt to imitate the experimental process of crucible drawing as closely as possible, it was also added to TG-DTA measurements. Then, temperature was ramped down from 1150 °C to 25 °C. This also mimics the experimental process developed for crucible drawing, which is twofold, with a melting step at 1150 °C followed by a ramp down to the drawing temperature before finally unplugging the crucible. This DTA measurement enables to determine the temperature for the onset of crystallization during a ramp down, which is a key issue for crucible drawing attempts from a melt. The result of this experiment is shown in Figure 27.

In this figure, the baseline was not subtracted and only the raw data is shown, to prevent the ramp up and down from overlapping with one another. During the newly implemented ramp down, a singular exothermic event can be observed. By comparing the TG-DTA data with initial crucible drawing experiments of varying temperature, it is believed that this peak corresponds to the temperature at which the glass crystallizes on a ramp down. Hence crucible drawing has to be performed above this temperature, or at the very least, maintain this temperature for the shortest possible amount of time.

Due to the time constraints applied to the crucible drawing process by crystallization, the DTA was also used to determine the critical cooling rate. As the DTA is calibrated for a 10 °C/min ramping rate, the actual temperature of the glass is expected to lag behind the

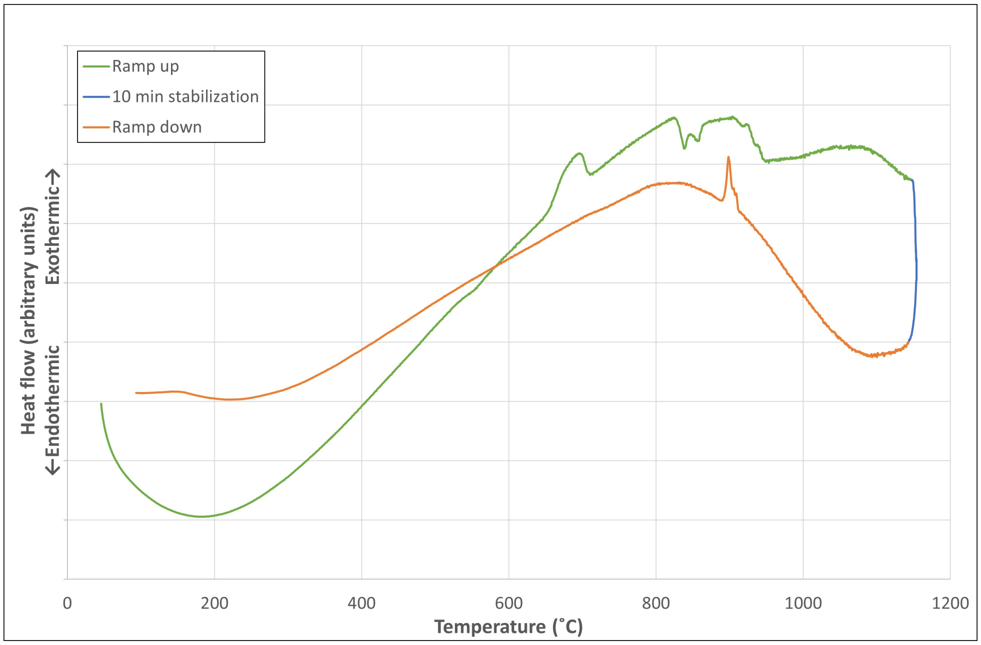

Figure 27: DTA measurement for LD1900 GLS 65:35 ramp up and ramp down test designed to emulate crucible drawing.

thermocouple reading. As a consequence, such an experiment cannot be used to determine the temperatures of phase changes, but it can still be used to monitor the presence of the crystallization peak for a given ramp-down speed. The temperature region where crystallization peaks are located is shown in Figure 28. The height of the crystallization peak is inversely correlated with the ramping rate, to the point where it is no longer visible at 100 °C/min. The significance of its absence was confirmed by the corresponding sample still being glassy after taking it out of the TG-DTA. For additional confirmation, an experiment was performed in the fibre drawing tower where a small amount of GLS (20 g) was melted in a silica crucible at 1150 °C for 5 minutes and temperature was then ramped down to 200 °C at 100 °C/min. The resulting sample is shown in Figure 29. The observation that it is crystal-free demonstrates that the DTA can indeed be used in this way to predict a cooling rate high enough to prevent crystallization in a crucible drawing experiment from a melt.

The TG-DTA however does not provide information regarding the softening point nor the evolution of viscosity as a function of temperature. As previously stated, if the drawing temperature lies too close to the crystallization peak for a given GLS composition, any attempt at approaching will only result in the glass crystallizing and therefore failing to be drawn into fibre. In order to complement the information provided by the DTA, the viscosity of these compositions must be obtained as a function of temperature. This measurement can be made using a thermo-mechanical analyzer (TMA) and the technique of three-point bending, commonly used to determine the flexural properties of various plastics, rubbers and composite materials [110].

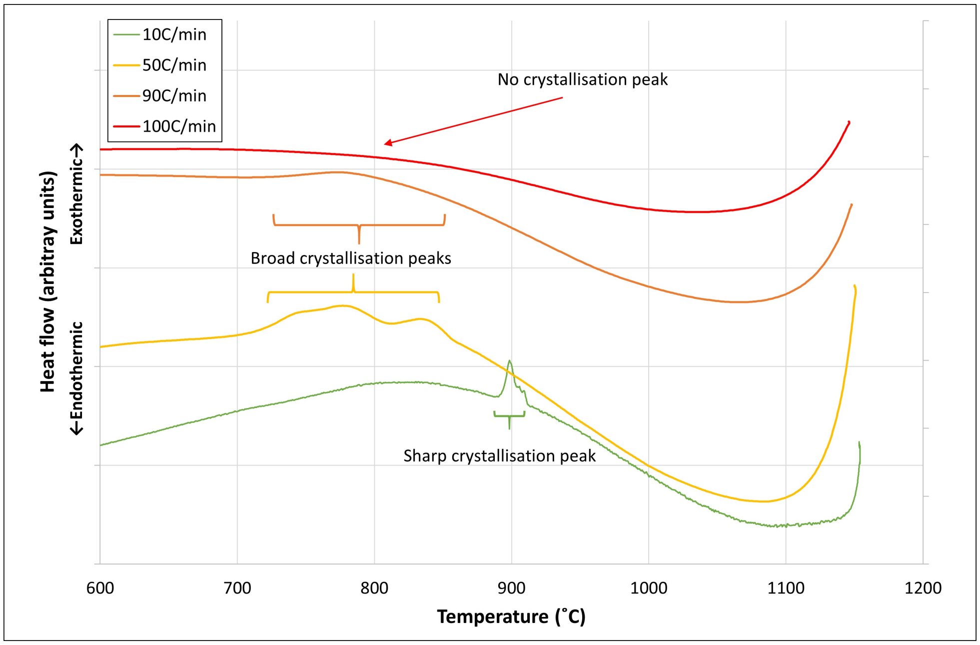

Figure 28: Using the TG-DTA in a ramp down from 1150 °C to estimate the critical cooling rate of GLSSe20%.

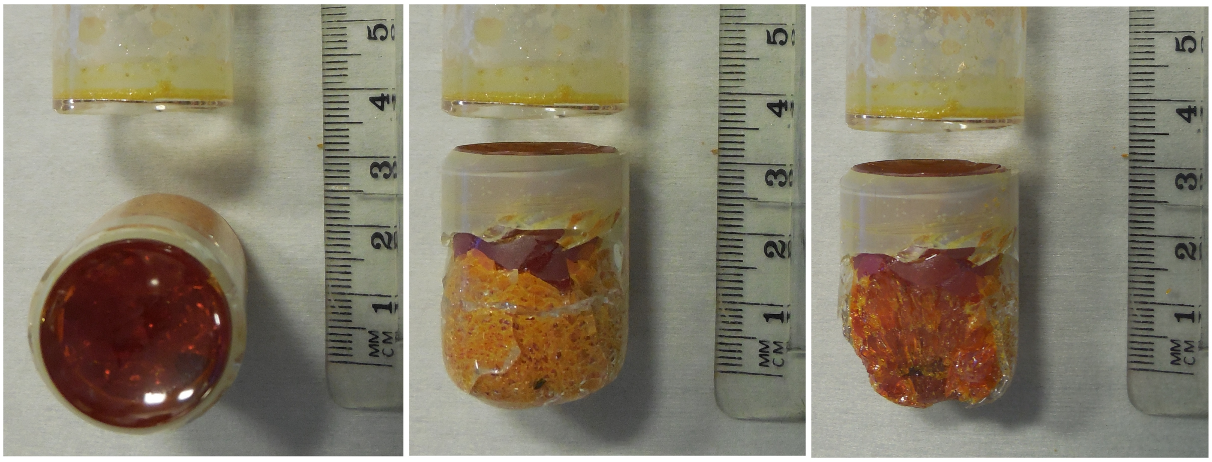

Figure 29: Shattered GLS sample melted in glass and quenched at 100 °C/min.

4.7 Thermo-mechanical analyzer (TMA), 3-point bending

Three-point bending is a method used to assess the elastic properties of a material, usually determining its flexural modulus [110]. For this work, the glass samples assessed were cut into 5 mm x 5 mm x 1 mm slabs, balanced onto a 5 mm x 5 mm parallel bar support as illustrated in Figure 30. They were then placed at the bottom of the silica tube in which the TMA probe is inserted. The TMA knife edge probe was used to exert a constant force on the sample, while the furnace performed a temperature scan. All samples were heated from room temperature to 650 °C following the same procedure.

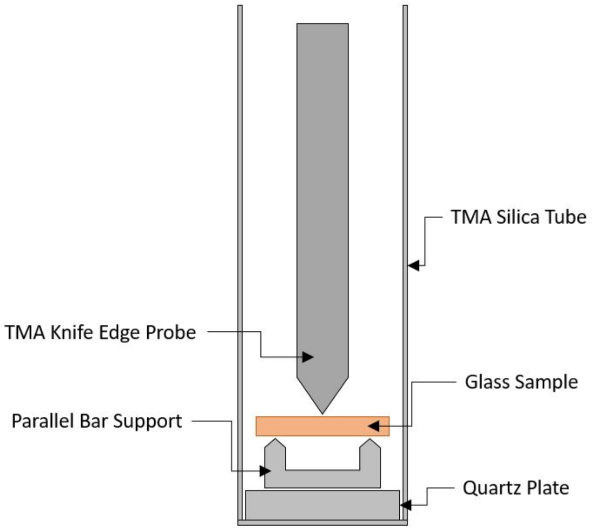

Figure 30: Schematic representation of three-point bending measurement performed using the TMA.

The samples are heated to 500 °C at a rate of 20 °C/min, and then from 500 °C to 650 °C at a rate of 5 °C/min. This change in the rate of the temperature scan was motivated by initial measurements demonstrating that these samples start to bend under a force of 500 mN only after reaching at least 500 °C, with 520 °C being the lowest value recorded for any sample to start bending. This rate was used to enable faster measurements as well as to increase the number of data points in the relevant temperature region where the samples start to bow, as opposed to the standard procedure wherein the sample is heated from 25 °C to 650 °C at 10 °C/min. The probe used is a knife 5 mm long edge probe applying force in the middle of the sample. The vertical motion of the probe and the force applied to the sample are monitored as a function of temperature in order to calculate the flexural properties of the material under test.

$$\mathrm{E_a} = \frac{\mathrm{PL}^2}{4\mathrm{bD}^3\Delta_\mathrm{f}}(1 + 2.9(\frac{\mathrm{t}}{\mathrm{L}})^2) \tag{12}$$

Using Equation 12, where P is the force applied to the sample in Newtons, L x b x D are the sample dimensions in metres (support span L x sample length b x thickness D) and Δ_f is the probe displacement from its initial resting position in metres, one can calculate the flexural modulus $\mathrm{E_a}$ in Pascals as a function of temperature [110], as illustrated in Figure 31. Each GLS composition was tested for 3 different amounts of force exerted by the probe: 500 mN, 300 mN and 100 mN. Occasional repeats were taken for imperfectly shaped samples.

$$\eta = 10^{-3}.\frac{\mathrm{gL}^3}{2.4\mathrm{I_C V}}(\mathrm{M} + \frac{\mathrm{AL}\rho}{1.6}) \tag{13}$$

A second relation, Equation 13, where g is the gravity of Earth in $\mathrm{m.s}^{-2}$, L is the support span in metres, $\mathrm{I_C}$ is the cross-sectional moment of inertia for a rectangular cross-section in m^4, V is the rate of deflection in $\mathrm{m.min}^{-1}$, M is the mass of the applied load in g, A is the cross-section of the sample under test in m^{-2} and ρ is the density of the sample in $\mathrm{g.m}^{-3}$, can be used to alternatively obtain the viscosity of the sample η in poise (or dP.s) as a function of temperature [111], as illustrated in Figure 32. The data displayed is cut-off when the temperature is too high, to remove the spurious data collected when the sample has been completely bent and is pressed against the bottom of the parallel bar support. As expected, the two formula used yield the same overall trend. There is however relatively low precision from one repeat measurement to the next of the same composition at the start of the experiment, where viscosity is the highest. This low precision is explained by the corresponding data being acquired when the vertical movement of the TMA probe is practically zero, which in turn maximizes the impact of any source of error. The uncertainty is sufficiently high for the values of flexural modulus to start nearing one another even across different compositions, as shown in both Figure 31 and 32. This observation demonstrates the importance of taking repeat measurements when estimating the flexural modulus/viscosity of each composition using the TMA. Some sources of error were identified, such as variations in sample dimensions, the bending stage not being permanently fixed in place but simply resting at the bottom of the wider tube, and the occasional probe misalignment, images of which are shown in Figure 33. It can nevertheless be determined that for all of the temperature range tested, the higher the proportion of lanthanum sulphide $\mathrm{La_2S_3}$, the higher the viscosity of the composition.

From these results, LD1902 (75:25) seems to be the best composition for rod drawing. Since it softens first near 530 °C, its ideal drawing temperature is expected to be the lowest of them all. In reverse, LD1899 (60:40) seems to be the best composition for crucible drawing, since it softens only past 555 °C, after all other compositions, followed by LD1900 (65:35) at 600 °C. This should help ensure glass viscosity remains as high as possible at the drawing temperature, improving control over the falling fibre drawn from a crucible. This information complements the one obtained from DTA and points to the same compositions being best suited for either fibre fabrication method.

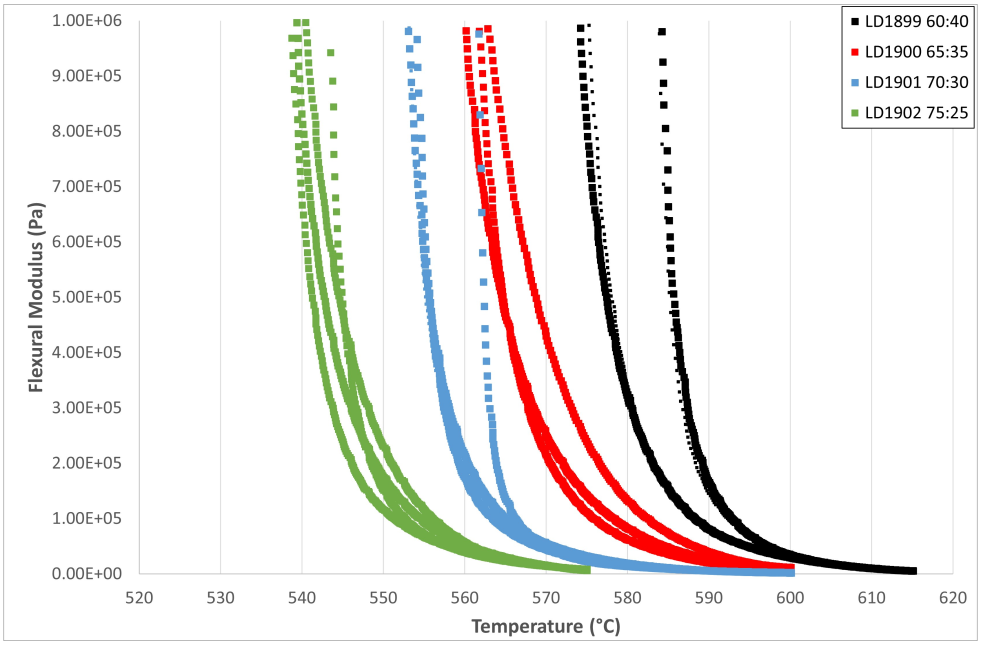

Figure 31: Flexural modulus measured as a function of temperature using TMA three-point bending for a range of compositions of pure GLS.

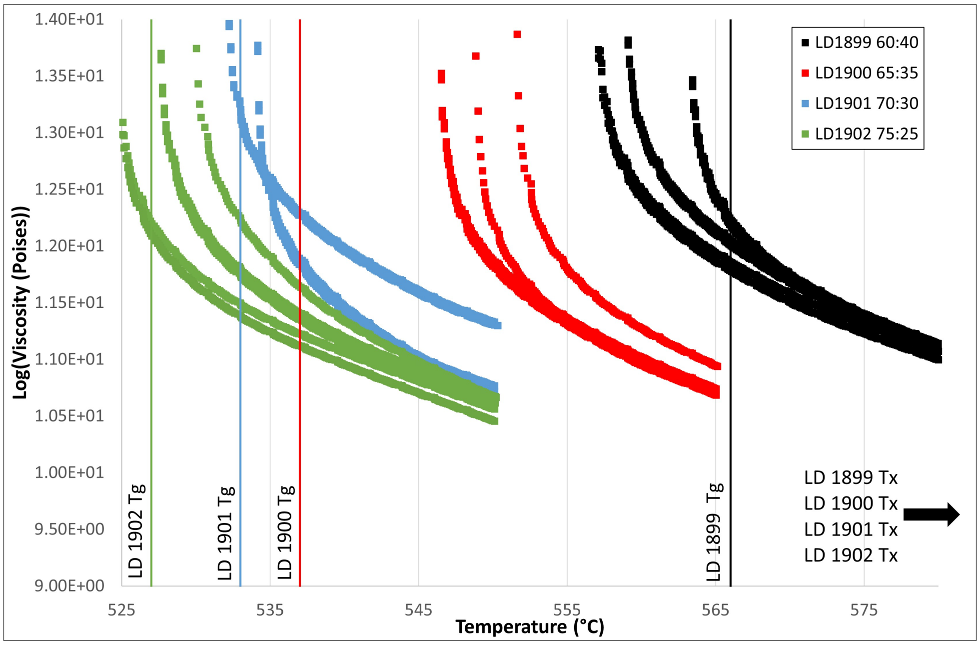

Figure 32: Viscosity measured as a function of temperature using TMA three-point bending for a range of compositions of pure GLS.

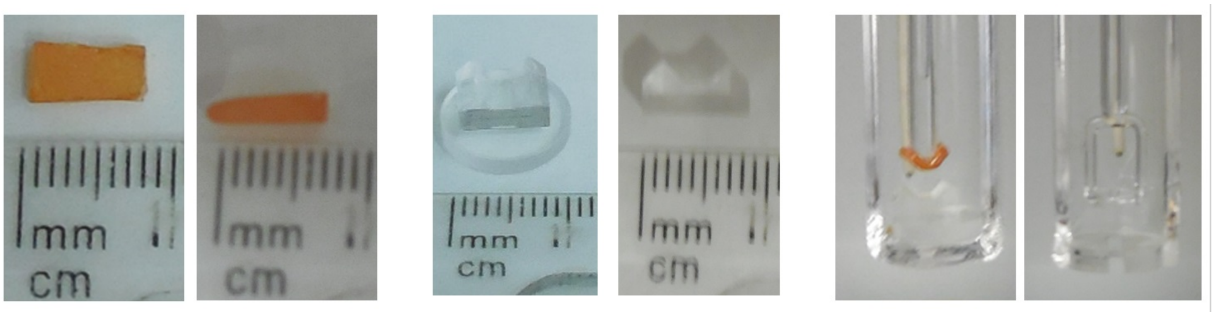

Figure 33: Identified sources of error for TMA three-point bending measurements, from left to right: sample dimensions, free bending stage, and probe alignment.

It was noted when taking the bent samples out of the TMA that all of them were fully crystallized, with the exception of LD1899 (60:40), as can be observed in Figure 34. This observation was made even though all samples were heated to the same temperature, 650 °C at the same ramping rate and for the same amount of time. This observation can be linked to and confirms the peculiar crystallization event of LD1899, as seen in Figure 26. This unique behaviour makes the 60:40 GLS composition a particularly attractive candidate for fibre drawing, as its propensity for crystallization seems to be the lowest of them all.

Figure 34: Sample remains of TMA three-point bending: crystallized (LD1900) on the left, non-crystallized (LD1899) on the right.

4.8 Gallium lanthanum sulphide selenide (GLSSe)

The addition of selenium in the glass is known for increasing the transmission window in the infra-red as shown in Figure 35. The selenium is added in the form of Ga_2Se_3. In this work, the proportion of Ga_2Se3 is denoted GLSSeX%, where X corresponds to the molar percentage of Ga_2Se_3 that is introduced in replacement of Ga_2S_3 in GLS65:35. For example, GLSSe20% refers to 45% Ga_2S_3, 20% Ga_2Se_3 and 35% La_2S_3. The higher the proportion of selenium, the further the transmission window is shifted towards the infra-red. However, the addition of selenium reduces the viscosity of the glass at any given temperature, as shown in Figure 36). This can be explained by the lower bond strength between gallium and selenium to that of gallium and sulphur [46].

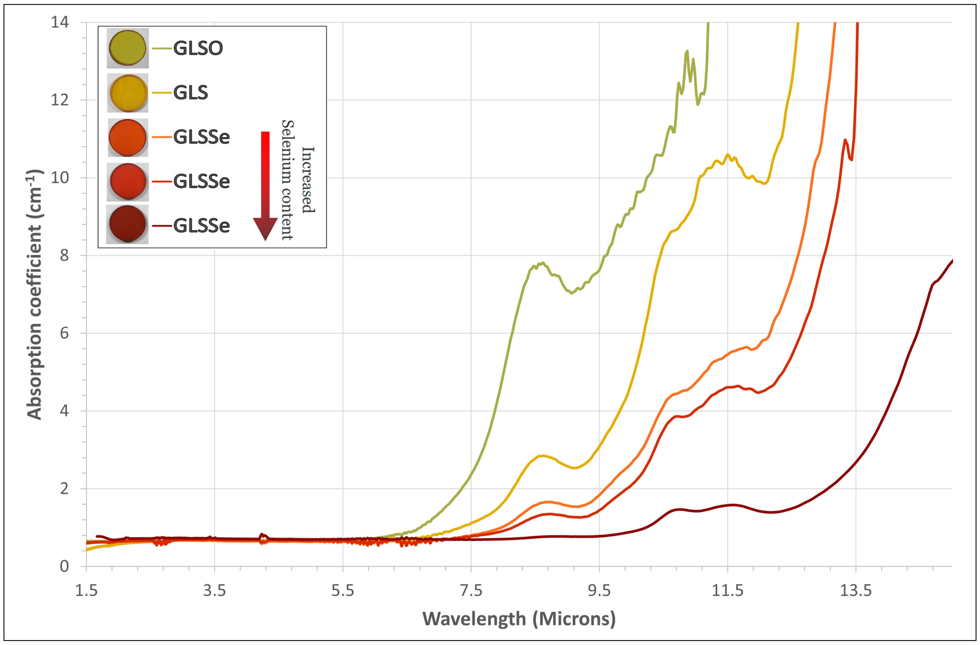

Figure 35: Transmission cutoff of **GLSO** (20$\mathbf{Ga_2O_3}$/ 50Ga_2S_3/ 30La_2O_3), pure **GLS** (LD1503: 70Ga_2S_3/ 30La_2S_3), **GLSSe20%** (LD1818: 50Ga_2S_3/ 20$\mathbf{Ga_2Se_3}$/ 30La_2S_3), **GLSSe35%** (LD 1819: 35Ga_2S_3/ 35$\mathbf{Ga_2Se_3}$/ 30La_2S_3) and **GLSSe60%** (LD1752: 10Ga_2S_3/ 60$\mathbf{Ga_2Se_3}$/ 30La_2S_3) in the Infra-red pushed towards longer wavelengths by removing oxygen and adding selenium into the glass (data for GLSSe 60% courtesy of Andrea Ravagli).

While this lower viscosity is advantageous for rod drawing, it is a hindrance for crucible drawing. Indeed, for rod drawing, the ideal scenario to avoid crystallization is the neck to form at the lowest temperature possible. On the contrary, for crucible drawing from a melt, the ideal scenario occurs when the glass becomes sufficiently viscous to be drawn yet temperature is still as high as possible. Furthermore, regarding crystallization, the addition of selenium shifts the crystallization event towards higher temperatures during a heat-up of the glass and towards lower temperatures during a cool-down of the glass. Overall, the addition of selenium is entirely beneficial for rod drawing, however it yields mixed results for crucible drawing, as delayed crystallization may compensate for the lower viscosity of the glass by enabling to draw fibre at lower temperatures.

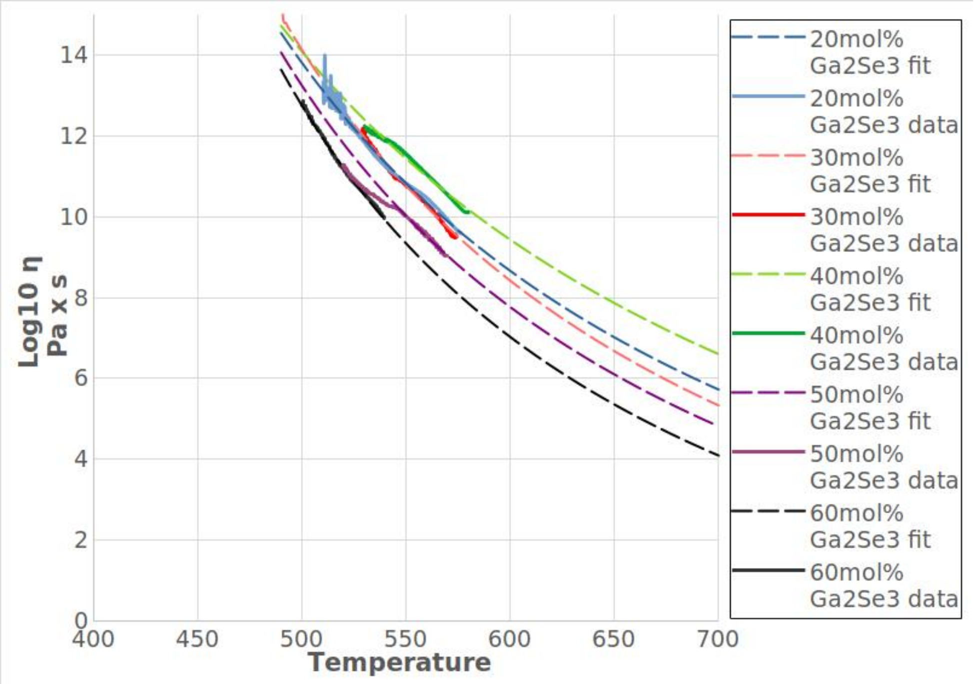

Figure 36: GLSSe viscosity comparison as a function of selenium content (data and plot courtesy of Andrea Ravagli). Fits are produced using the Vogel–Fulcher–Tammann equation ($\log_{10}\nu = k + \frac{a}{T-b}$) , where η is the viscosity, T the temperature in °C, k, a and b are fitting constants [7].

5 Fibre characterization and processing

5.1 Loss measurements

The most essential feature of passive optical fibre is the attenuation of light as it travels through it. To measure the power from a light source before and after going through a piece of fibre, however, yields imprecise results, as such a measurement does not take into account the effect of coupling in and out of a fibre, where a significant amount of variability occurs, both from the quality of the fibre input face, and the mode mismatch between the input and the guided modes. When fabricating optical fibre on a regular basis, it isn't cost-efficient to have them professionally polished and terminated so as to perform routine loss measurements. As such, optical fibre is left non-connectorized, and must be cleaved manually. The process involves stripping the fibre end of its coating using acetone, which softens Desolite^{TM} after a few minutes, allowing it to be pried off mechanically. Then, a small scratch perpendicular to the fibre axis is made using a ceramic cleaver. Finally, the fibre is bent so that the crack propagates, producing a normal face with a smooth finish. This technique is based on the same principle as snap cutting pieces of macroscopic glass. However, it is much more delicate due to the considerably smaller scale at which it takes place. An effective scratch is always deeper than what is strictly necessary, and the smooth end produced when snap-cutting the fibre this way will never be perfectly flat or normal to the axis of the fibre. In addition to these flaws, coupling loss is still expected from the light source not being fully translated into guiding modes. Some of it will propagate in the cladding and be scattered away, and some of it will be reflected back, via seemingly unavoidable Fresnel losses. These reflection losses are all the more prevalent in the case of high refractive index chalcogenides. For these reasons, the typical method used to measure fibre loss is a cutback loss measurement [112], where the light source is coupled into a long piece of fibre, and the other end of the fibre is coupled into a suitable detector for the wavelength of the source. Both ends of the fibre are aligned to maximize the measured power output. After alignment, the input side is to remain undisturbed for all subsequent measurements. A length of the fibre is then cut off from the output end using a ceramic cleaver. The new end is then recoupled to the detector and is carefully re-adjusted to maximize the power output on that end only. The length of the cut piece is measured, and the power increase is recorded. Thus, the loss is calculated as a function of fibre length according to Equation 14, where R_1 and R_2 are the detector responses before and after the cutback respectively, and l is the length of fibre removed.

$$\mathrm{Loss(dB.m^{-1})} = \frac{10 * \log\frac{\mathrm{R_1}}{\mathrm{R_2}}}{\mathrm{l}} \tag{14}$$

In order to account for the aforementioned fibre cleaving imperfections several small (2 to 5 mm) cleaves are made to obtain an average value before and after a longer section of the fibre is cut. The length of each of these small cleaves is recorded and taken into account for the calculation performed using Equation 14. This enables to produce a more reliable loss measurement featuring an estimate for experimental error without having to waste excessive amounts of fibre. Two main setups are available to perform continuous loss measurements in the infra-red. The FTIR adapter illustrated in Figure 37 which can be rapidly deployed to assess the quality of the optical fibre manufactured from 1.5 μm to 25 μm, and a custom setup illustrated in Figure 38, which requires more effort to deploy due to the use of nitrogen-cooled detectors and manual alignment, but benefits from detectors with higher sensitivity, from 2.5 to 5.5 μm. This setup may also be used with visible light from 0.4 to 2 μm, by swapping the light source and the detector used. These two alternatives are supplemented by the use of an optical spectrum analyser (OSA, 0.6 to 1.7 μm) for fast loss measurements in the visible, and point-sources such as an erbium laser source (1.535 μm) and a selection of pigtailed laser diodes (at 639.4 nm, 1.3126 μm, and 1.6245 μm), to accurately splice together and verify the accuracy of loss measurements obtained using these different setups. A combined loss measurement from the OSA, the FTIR Fibermate^{TM} adapter, the nitrogen-cooled detector setup and the erbium laser source is shown in Figure 39. It demonstrates that the loss measurements performed using this variety of systems, light sources and detectors can indeed be crossed-referenced with one another to produce a reliable estimate of loss across all available wavelength ranges.

A particular source of concern for the FTIR Fibermate^{TM} 2 is the lack of fine-tuning screws for alignment of the bare fibre adapters. A test was performed to assess the reliability of the alignment provided by the simple plug-in/plug-out system it features. In Figure 40 is shown a loss measurement averaged over 10 small cleaves compared to a loss measurement of the same fibre averaged over 10 plug-in/plug-out of the bare fibre adapter with no cleaves performed. It appears that the experimental error is of the same magnitude in either case, which demonstrates that the error introduced by the small cleaves is negligible compared to the error introduced by taking the bare fibre adapter in and out, as the magnitude of the experimental error is nearly identical in both cases.

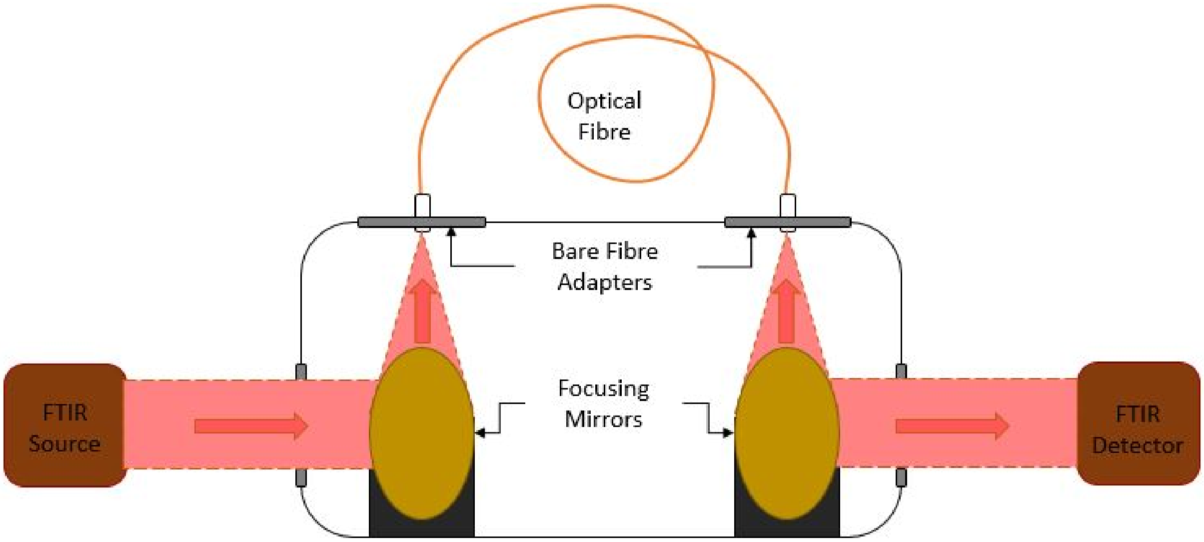

Figure 37: Operating principle of the FTIR Fibermate^{TM} adapter [8].

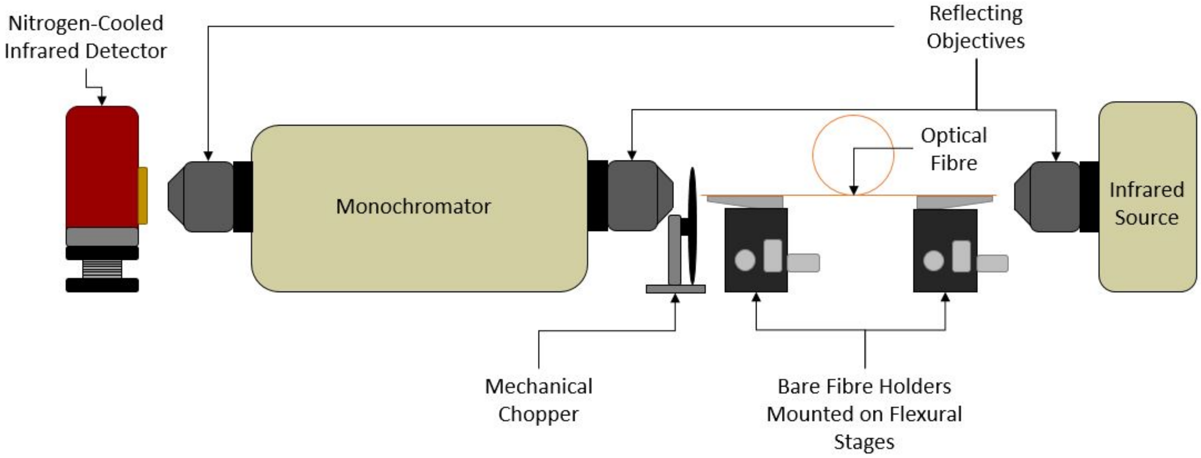

Figure 38: Custom fibre loss measurement setup in the infra-red using a monochromator combined with liquid nitrogen-cooled infra-red detectors.

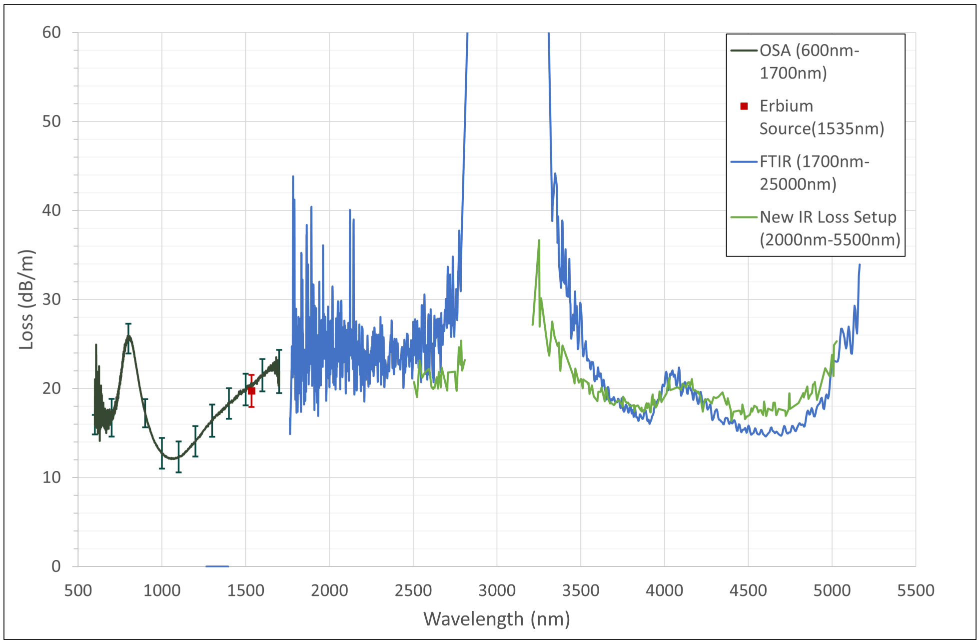

Figure 39: Combined loss measurements using the erbium point source, the OSA, the FTIR bare fibre adapter and the nitrogen-cooled detector setups.

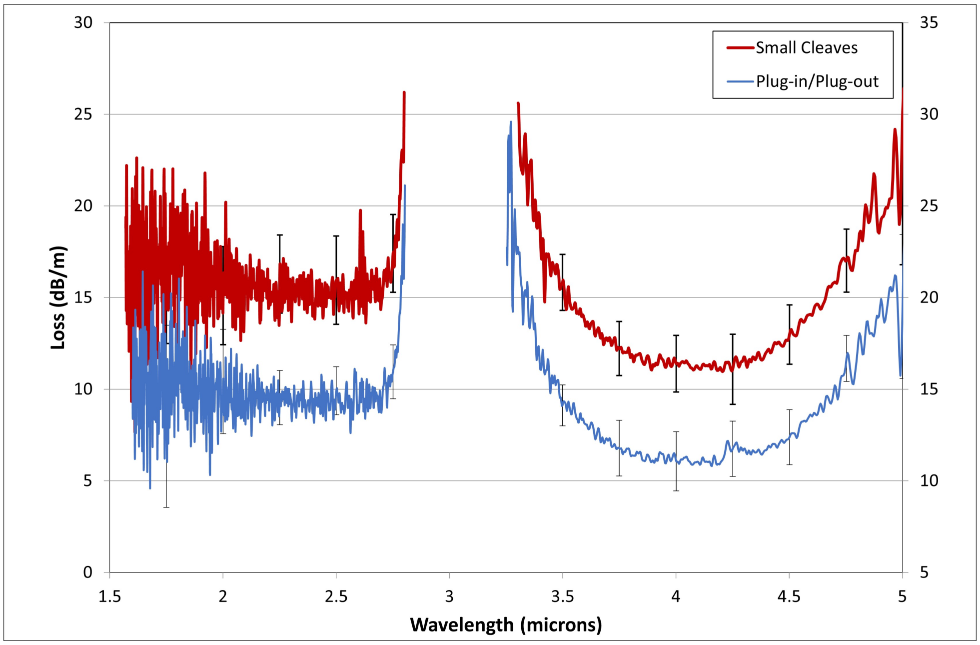

Figure 40: Compared effect of 1 mm cleaves to plug-out/plug-in of the bare fibre adapter on the experimental error of the loss measurement of LF273. The scale of the "small cleaves" (red) curve is on the left, and the "plug-in/plug-out" (blue) curve is on the right. They are represented on separate offset axes to enable clear comparison.

5.2 Bending resistance tests

The mechanical resilience of passive chalcogenide fibres is their second most crucial characteristic, as they are considerably more fragile than silica [113]. The manipulation of a wide variety of optical fibre in the course of this work has motivated the construction of a suitable experimental station to assess and compare the resistance of fabricated fibres to bending. Equation 15 was obtained from Fluoride Glass Optical Fibres [3], and an experimental setup was constructed to use it in bending tests is shown in Figure 41.

$$\sigma = 1.198\mathrm{E}\frac{2\mathrm{r}}{\mathrm{D}-\mathrm{d}} \tag{15}$$

In equation 15, the fracture stress is σ, E is Young's Modulus of the glass (59GPa) [75] r is the radius of the fibre, D is the distance between the two plates, and d is the diameter of the fibre. r and D must be measured in the same units.

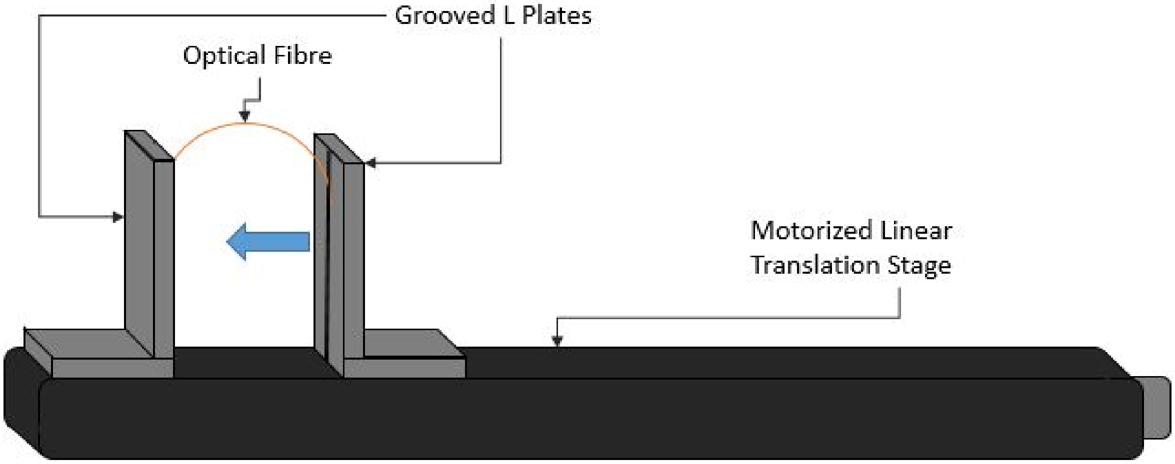

Figure 41: Parallel plate setup constructed to assess fibre resistance to bending.

In all of the experiments, the parallel plates were brought together at 1mm/s. After a number of measurements on small lengths of fibre are made (typically around 10 to 20 measurements performed on 10 cm long pieces), the outcome is recorded to produce a Weibull distribution where F is the failure percentage, and ensure that the failure rate of the fibre is statistically consistent. This consistency is apparent through the linearity of the distribution [114]. An example of a successful statistical test is shown in Figure 42.

The outcome of a number of such tests performed on Vitron IG fibres and GLS based fibres is shown in Table 6. From the data shown in Table 6, it appears that GLS fibre

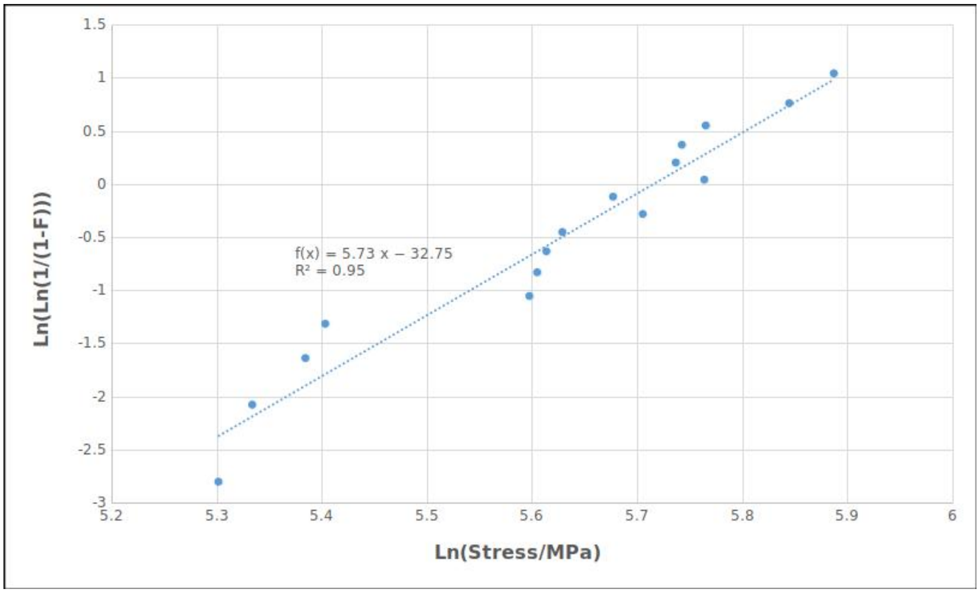

Figure 42: Failure rate/fracture stress Weibull distribution for a sample of unstructured and uncoated IG2 ($Ge_{33}As_{12}Se_{55}$) fibre. The linearity of the distribution demonstrates the statistical reliability of the test.

is more resistant to bending than IG fibre, whether they are coated in Desolite^{TM} or not. The presence of coating is expected to make these measurements more consistent across the board, as coating is primarily meant to prevent scratches that would otherwise significantly weaken fibre. When comparing the performance of GLS to other published data for other chalcogenide fiber tested using the same method such as $Ge_{15}As_{25}Se_{40}Te_{20}$ (50% failure strain at 180.67MPa), it appears that GLS is capable of withstanding higher strain (50% failure strain for both uncoated and coated GLSO is above 340 MPa, as shown in Table 6) [115].

Name	Coated	50% Failure Stress (MPa)
IG2	Yes	117
IG2	No	102
IG5	Yes	75.8
IG5	No	88.1
GLS57 (GLSO)	No	343
LF158 (GLSO)	Yes	373

Table 6: 50% failure stress measured across a selection of chalcogenide fibres.

6 Preform fabrication

So as to fabricate glass rods suitable for fibre drawing tests, past common practise was to send an annealed GLS ingot to a hired industrial collaborator for processing. Previously, Crystran Ltd was called upon to cut these ingots into rectangular sections, roll them into rods and finally polish them down to 0.7μm grit using silicon carbide polishing compound [108]. However, to reduce cost, delays and unknown sources of contamination, in-house alternatives have been explored, in the form of rod turning, preform casting and hand polishing of cylindrical cross-section GLS glasses.

6.1 Rod turning

A thick glass ingot can be turned into a rod by first using a water-cooled grinding saw to cut a GLS ingot lengthwise. A 30 ° support plate was 3D-printed for the water-cooled saw to cut a 60 ° equilateral triangle section from a flat ingot. Then this section had each of its points truncated, to produce a rod with a hexagonal cross section, as shown in Figure 43. Then, this rod was turned into a cylinder on a lathe using a diamond blade. The hexagonal shape was chosen, as it enables to use a 3 jaw self-centring chuck with each of its jaws perpendicularly pressed against a flat surface, as shown in Figure 44.

In addition to facilitating centring of the sample, a hexagonal cross section also reduces the magnitude of the torque-induced vibrations that occur when turning an equilateral or square cross-section of glass into a rod. Initial tests performed on such triangular rods produced strong vibrations that often ended up breaking the rod or unevenly chipping its surface during turning. In addition to pre-cutting the rod into a hexagonal shape, the subsequent turning process was carried out in small 20 mm steps so as to minimize chipping and breaks. The smallest diameter achieved using this method was 4mm for a length of 120 mm. This procedure demonstrates potential for rapid determination of fibre drawing parameters for novel compositions, especially if it is combined with the development of surface polishing techniques. An example of a preform turned and polished in-house using these methods is shown in Section 10.3.3, Figure 82, along with its corresponding fibre drum and loss measurement.

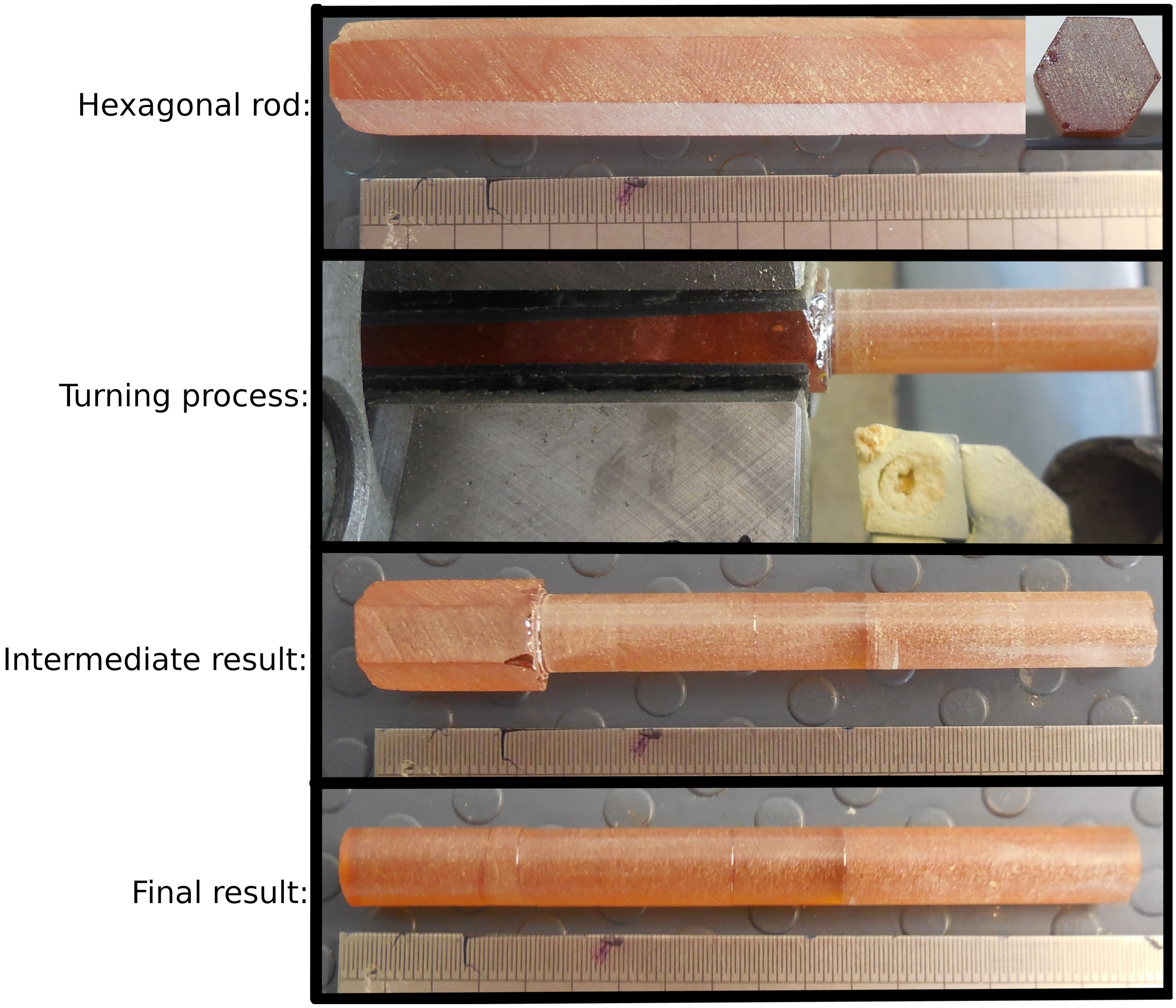

Figure 43: Successive stages of the GLS rod turning procedure developed using a lathe.

6.2 Rod casting

6.2.1 Unstructured rods

Rod casting experiments were carried out using a portable SNOL 3/1100 LHM01 furnace [116]. Around 40 g of glass shards were placed into a vitreous carbon crucible and heated up to 1100 °C for 10 minutes, to ensure the glass is fully molten and homogenized. Then, the vitreous carbon crucible was taken out of the furnace and its contents were carefully poured into a pre-heated graphite or bronze mould around 100 mm in length and 10 mm inner diameter. This receiving mould was wrapped with silica wool and held in a small tube furnace maintained at constant temperature. This mould would then immediately

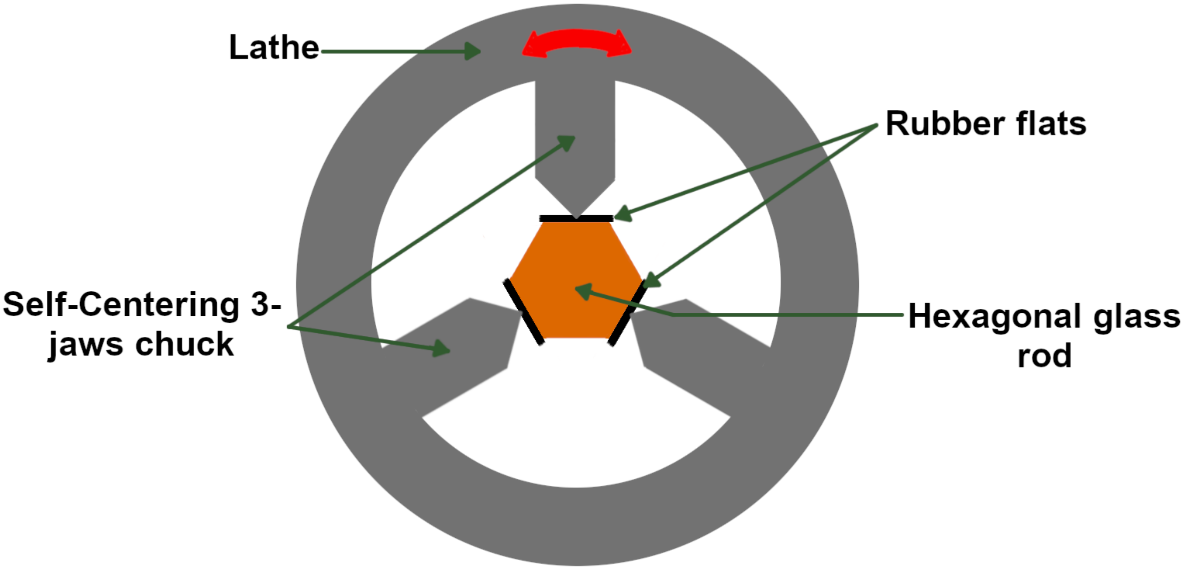

Figure 44: Schematic representation of a hexagonal section GLS rod held in a self-centring chuck for rod turning.

be quenched to prevent crystallization after being filled to the brim. The temperature of the receiving mould was varied in order to optimize the process, which is illustrated in Figure 45.

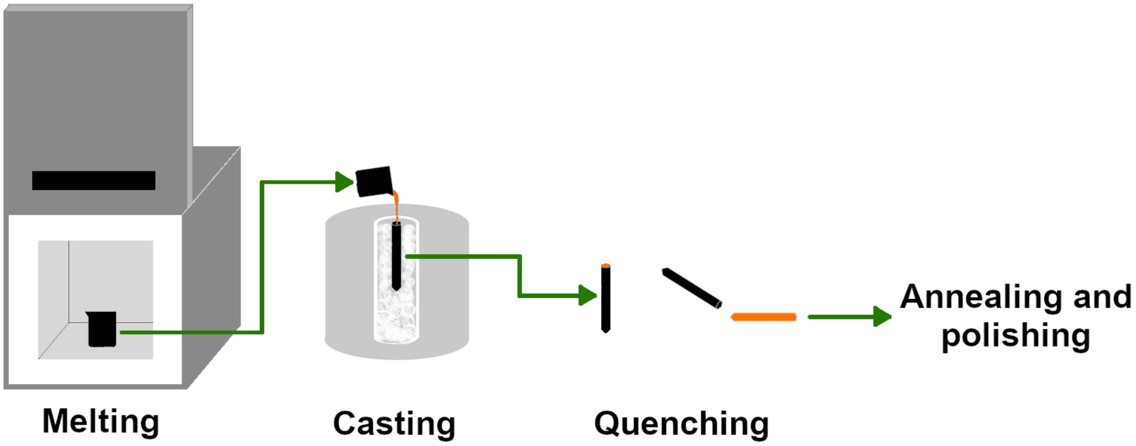

Figure 45: Typical casting procedure as it is carried out in a nitrogen-purged glovebox.

Due to the difficulty of removing GLS from such narrow and long moulds, the original use of single-piece moulds was abandoned. They were replaced with moulds designed to either be taken apart, or to enable the rod to be flushed out, as shown in Figure

46. The results of the first set of attempts carried out using these moulds are shown in Figure 47. As can be observed, these early casts have few bubbles on their surface if any. However, crystals and bubbles tend to form within the bulk of the glass, and the surface of the produced rods is occasionally imperfect. Avoiding the formation of crystals was understood to be a matter of selecting the correct mould temperature for the glass composition used. The bubbles could also be avoided by using a larger amount of glass

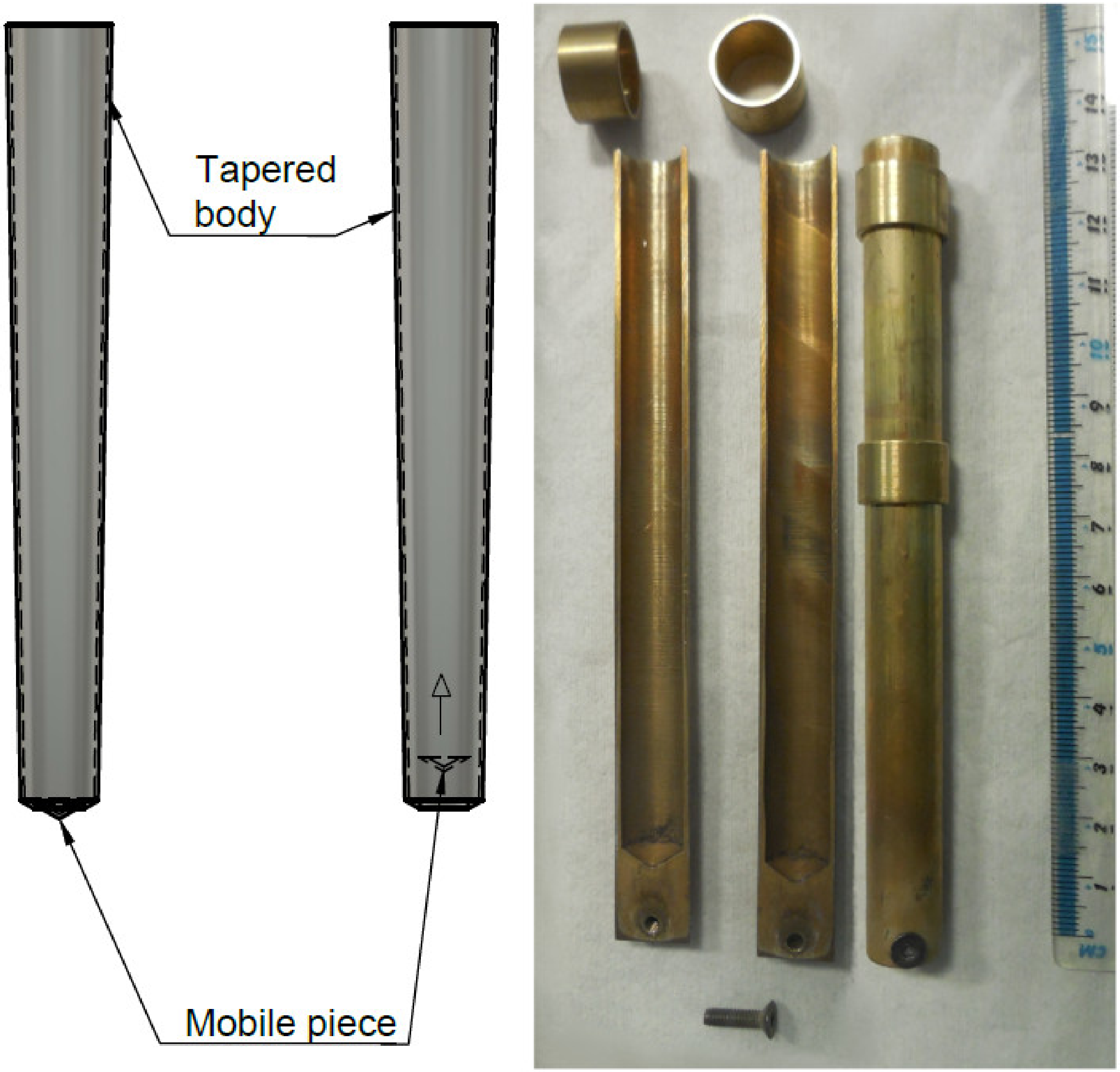

Figure 46: Moulds used for casting. On the left, 120 mm long tapered vitreous carbon crucible with its end cut off and placed inside, to enable flushing out of the rods. On the right, bronze mould machined to be taken apart lengthwise. A single screw closes its end, and a pair of tight bronze rings are inserted around its length to avoid warping.

than necessary. Indeed, since these pockets of gas form against the walls of the crucible during melting, they will only be transferred to the cast when the glass in contact against the walls is poured. If there is enough glass in the crucible to fill the mould while keeping the layer of glass coating the walls intact, the amount and size of bubbles transferred to the cast is minimized. In Figure 47, cast (a) was produced by casting GLSSe 20% in a 100 °C crucible, cast (b) in a 400 °C crucible, cast (c) in a 530 °C crucible and cast (d) in a 1000 °C crucible. This result demonstrates that the ideal mould temperature is above 530 °C to avoid both the wrinkled surface and the formation of crystals. Because of this, the subsequent casts were significantly smoother, crystal-free, crack-free and usually bubbles-free. They were used in attempts to produce fibre to demonstrate the viability of casting for preform fabrication and justify further testing. After two unsuccessful fibre drawing attempts due to inadequate experimental parameters that resulted in the formation of crystals (NT744 and NT745), several metres of crystal-free fibre were produced in NT746, where the preform neck was achieved sufficiently fast to prevent crystal formation in the fabricated fibre. Following this success, GLSO and pure GLS were also made into cast

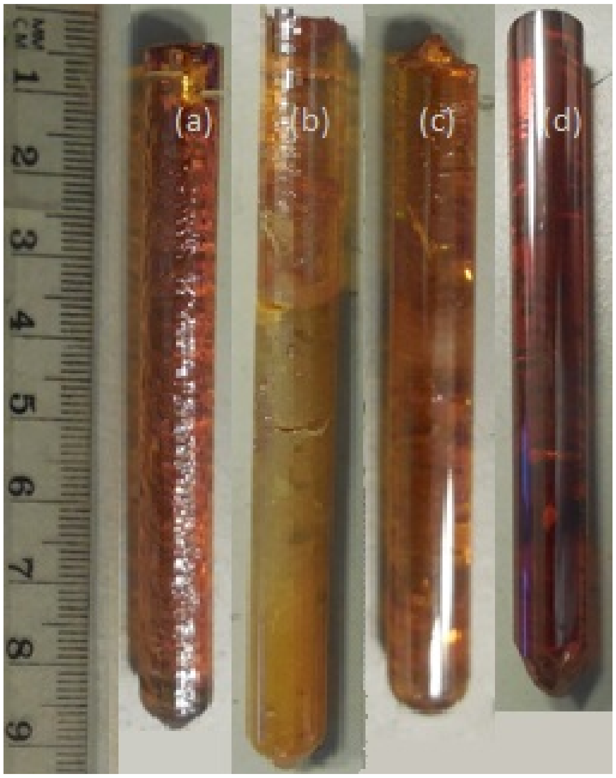

Figure 47: Array of casting experiments performed to determine the ideal receiving mould temperature. (a) 100 °C, (b) 400 °C, (c) 530 °C, and (d) 1000 °C.

rods, which were then polished and drawn into canes. Four unpolished cast rods made of GLSSe20% are shown in Figure 48.

Figure 48: GLSSe20% glass cast into 300 °C vitreous carbon moulds, fabricated to later be drawn into canes using the fibre drawing tower.

As stated, pre-heating the crucibles to increasingly higher temperatures was deemed necessary from observing the surface wrinkling apparent in Figure 48. This wrinkling was caused by the transferring of 1100 °C molten glass to an excessively low-temperature vessel, as the molten glass solidifies too fast to mould itself against the vitreous carbon surface perfectly, it produces this imperfect appearance. Any such surface imperfections formed during the casting process can be removed by using the polishing steps outlined in the dedicated section, however, this should be avoided or minimized to simplify the fabrication process. A temperature of 400 °C for the receiving mould resulted in the extensive crystallization seen in Figure 47 cast (b). This can be explained by the 1100 °C glass and the 400 °C mould temperature averaging out to a temperature close to the crystallization temperature of the GLS composition used, resulting in the glass being maintained near this crystallization temperature for significantly longer than it would have been if the glass had instead been cast in a hotter or colder mould. For temperatures higher than 530 °C, crystallization is successfully avoided and the surface imperfections are also prevented. The bronze mould is unsuitable for temperatures above 600 °C as it starts to warp and become unusable beyond this point. Such temperatures are however perfectly suitable for the vitreous carbon mould.

The next step carried out was to try produce a core-clad structure from casting. Two different approaches were experimented with. Either a material suitable to be a core was dipped into a solidifying cast, or molten glass was poured around the core material. All of the following trials were attempted by pouring molten GLSO into a vitreous carbon crucible with a mobile bottom piece.

6.2.2 Casting around metal

The first tests were inspired by the capability of molten GLS to dissolve metals they are in contact with for a sufficient amount of time [46]. Exposing a 0.5 mm thick copper mesh to molten GLSO for 10 minutes, for example, would result in the metal getting partially dissolved into the glass. Also, due to the large amounts of copper involved, the composition was shifted out of the glass forming region, forming a ceramic in the region immediately surrounding the mesh. This devitrification must be avoided by optimizing the amount of metal used.

For the purpose of casting, a thin metal wire was placed in a pre-heated vitreous carbon crucible and molten glass at 1100 °C was poured around it. In the ideal case scenario, the metal was expected to dissolve, and assuming the cooling rate is high enough, it would not have time to diffuse through the glass evenly, thus forming a radial compositional gradient, enabling to achieve proof of principle for graded index GLS preforms. The material chosen for the first test was a 0.5 mm thick copper wire as it seemed a good combination of rigidity and low cost compared to silver, gold or tin wire. In addition, it had previously been observed partially dissolving in GLSO. These first tests did not produce the expected result, as rather than becoming embedded in the glass, the copper wire would instead be pushed aside by the molten glass. It was also noted that the copper wire did not react or bond with the glass at all, and could be manually pried off without shattering the cast. The only suitable way to address this issue would be to attach the metal wire at both ends and keep it perfectly taught, to prevent it from being flushed aside. It would also be necessary to melt glass around it, as opposed to cast glass around, so as to ensure that the wire becomes dissolved, rather than the glass simply enveloping it. This process goes beyond the scope of casting and would require the fabrication of custom vitreous carbon moulds with attachments that could hold the metal wire in place at both ends while in the furnace at 1100 °C.

Following these attempts, glass canes were substituted to metal wire, as they are more rigid, and thus are less likely to be flushed to the side, in addition to not needing to dissolve in order to produce a suitable core-clad structure.

6.2.3 Casting around a glass cane

A variety of GLS, GLSO and GLSSe canes that had been manufactured during the course of previous fibre drawing experiments were put to use in these casting tests. The cane was initially held in place by resting it at the centre of the movable piece at the bottom, attaching and centring it in the vitreous carbon mould using a piece of nichrome wire at the top. These first attempts resulted in the movable piece being flushed to the side along with the cane. As molten glass could then easily fall through the bottom of the mould and damage the furnace, this approach had to be immediately improved upon for further experiments. The next attempts instead consisted of pouring a small amount of molten glass at the bottom of the empty vitreous carbon crucible, followed by dipping the glass cane in it, and finally pouring the remainder of the cladding glass around the now solidly held cane. Even though the glass cane was well-centered at the bottom of the cast following the first step, the cane would typically soften during the casting step and end up pushed to the side in the mid-section of the preform, as molten glass rapidly softened and pushed it aside. It was however observed that the cane did not shatter in spite of thermal shock, and was successfully embedded in the cladding glass near the top and bottom sections of the cast, as those were the points where it was held in place and not allowed to bend or be flushed aside.

6.2.4 Inserting glass canes

Pure GLSO glass canes were fabricated by using the in-house fabrication method for unstructured preforms. These preforms were drawn into 2 to 3 mm thick glass canes, and several casting experiments were performed with GLSSe20% cullet glass as the cladding material. This is purely a technology demonstrator based on the glasses available, as such a preform would make anti-guiding fibre. Attempts at inserting glass canes in a fresh GLSSe20% cast were met with mitigated success at first, as the cooling glass solidifies rapidly, resulting in many canes shattering, bending, or failing to be pushed through the cladding glass to any significant degree. Eventually, practise enabled to plunge the cane in the fresh cast more rapidly and the receiving mould was incrementally placed deeper into the tube furnace to ensure a more even temperature throughout. As a consequence, these cane insertion experiments were met with increasingly successful results. In addition, a steel guide was fabricated to help insert the canes as close as possible to the centre of the cast, as well as keep them as straight as possible while pushing them through. A selection of photos demonstrating the main outcomes of this process are shown in Figure 49.

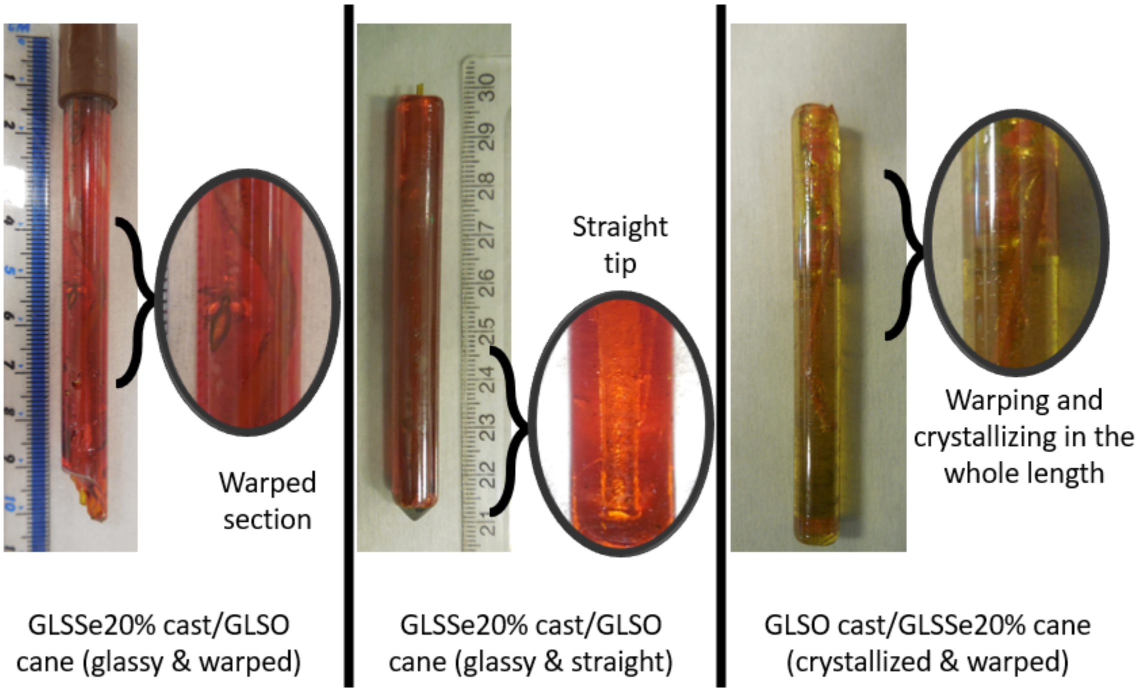

Figure 49: Examples of glass cane insertion in fresh glass casts, demonstrating commonly observed variations in the outcome.

To maximize surface quality, the temperature of the receiving vitreous carbon crucible was scanned once again for this set of experiments. This was deemed necessary, as the insertion of the cane increases pressure on the crucible walls, resulting in a tighter fit of the final cast. It was observed that temperatures below 400 °C result in a wrinkled surface, as previously determined. Even with the fast insertion speed acquired with practise, these temperatures still proved to be unreliable as to whether the cane could be inserted successfully. They may shatter, become stuck halfway or warp excessively. On the other end of the temperature range, it was observed that using temperatures above 650 °C for the receiving crucible would result in an excessively tight fit of the preform, which would often make removing it from the mould challenging, and typically resulted in the cast shattering and coming out in pieces, as shown in Figure 50.

The most reliable temperature enabling the best surface while still allowing easy removal of the cast from the mould was deemed to be around 600 °C for these cane insertion tests. After a number of cane insertion attempts were met with success, the tendency of these casts to shatter had to be addressed next. Indeed, it was observed that when the

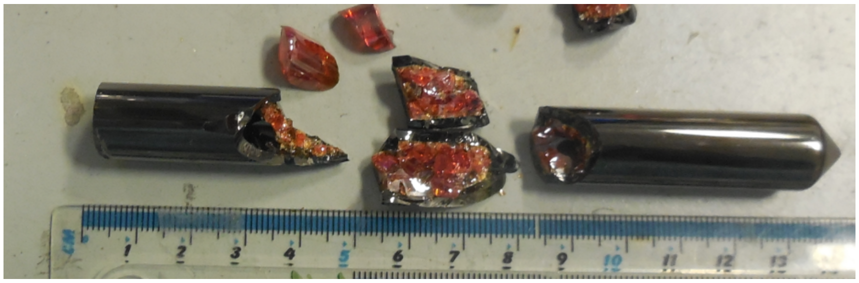

Figure 50: Result of casting molten GLSSe 20% into an excessively hot receiving mould (700 °C)

cane is excessively warped or close to the surface, cracks would form and propagate in the entirety of the cast, albeit the cast would usually remain in one piece. Even for casts in which the cane was perfectly aligned throughout the entirety of its length, a long crack would usually form and run along the full length of the preform. The presence of any cracks disqualifies these casts from being drawn into fibre, as the preform would simply fall apart rather than stretch when heated. In order to resolve this issue, the casts were annealed immediately after being made. The tube furnace in which the mould is preheated was ramped down to 490 °C as soon as the cane had been successfully inserted, and it was left to anneal overnight. As a consequence of this change, the cracks became increasingly uncommon, except for casts in which the cane was heavily bent and warped.

The first successful casts forming a core-clad were achieved using GLSSe 20% cladding and GLSO cores. Coupled white light into the core was shown to travel and exit the other end, demonstrating that the core was continuous and uncrystallized. This cast was successfully drawn into optical fibre shown in Section 10.3.4, Figure 84. After this success, the aim was shifted towards achieving the most desirable composition using these two glasses, which would be the reverse: a GLSSe 20% core in a GLSO cladding. Indeed, such a preform would simultaneously benefit from the increased transmission range of GLSSe in the infra-red, as well as from the increased thermal stability of GLSO. The higher refractive index of GLSSe would also enable the resulting fibre to guide light. Several experiments were made in order to produce such preforms, where GLSSe20% canes were fabricated using the fibre drawing tower and inserted in GLSO casts using the same experimental process. Unfortunately, the stronger propensity of GLSSe 20% for crystallization compared with GLSO resulted in the cane always becoming fully crystallized, with no light transmission allowed. Attempts were made to prevent crystallization by reducing both the crucible temperature and the annealing time. This resulted in a re-emergence of cracks, without solving the issue of crystallization, no matter the temperatures and timing used. It is likely that the fabrication of canes in the fibre drawing tower promoted nucleation which resulted in this seemingly unavoidable crystallization. Cutting and turning GLSSe20% canes using the lathe was attempted to produce canes with as little thermal history as possible, but the glass would shatter on the lathe once their diameter was reduced to less than 3 mm. As a consequence of this failure, an alternative was sought out so as to use casting techniques to produce hollow preforms. Such hollow preforms would provide a wider degree of flexibility, as they could easily be combined with the rod in tube technique to produce any core-clad composition.

6.2.5 Graphite casting experiments

In order to circumvent the issues caused by having to find a compromise around the thermal behaviour of two different glass compositions simultaneously, an initial experiment was carried out wherein a thick piece of graphite (4 mm in diameter) was inserted in a fresh GLSO cast. As graphite is a soft, inert material that can withstand much higher temperatures than GLS, it was believed to be possible to remove it after casting, by either pulling it out or drilling, and then plasma ashing the remains of graphite powder from the glass, as demonstrated in Section 4.3, to produce a hollow cast.

The graphite rod was turned on a lathe from a 5 mm thick square section down to a 4 mm cylindrical rod. It was then inserted in a fresh GLSO cast that had been poured in a 600 °C vitreous carbon mould. After annealing at 490 °C overnight and being left to naturally cool down to room temperature, the cast was removed from the crucible. The cast was crystal-free and appeared to be solidly stuck around the graphite rod. The cast showed no visible cracks and did not shatter. Attempts made to remove the rod by mechanically pulling it out failed. Attempts to plasma ash the carbon rod away in a similar fashion as carbon residue were not successful either, most likely due to the excessively large amount of graphite to be removed and the small size of its exposed surface area. After purchasing 2 mm thick graphite rods, the steel guide could be used to embed graphite in GLSO casts. As can be seen in Figure 51 cast G1 and G2, the resistance of the glass upon entry of the flexible graphite rods results in it bending even when using a steel guide.

Finally, the method of pouring cladding glass around was attempted again, taking advantage of the thermal resistance of the graphite rod, which was assumed would prevent it from being flushed to the side, unlike metal wire and glass canes. A 2 mm hole was drilled at the bottom of a new vitreous carbon crucible and the rod was inserted in it. Combined

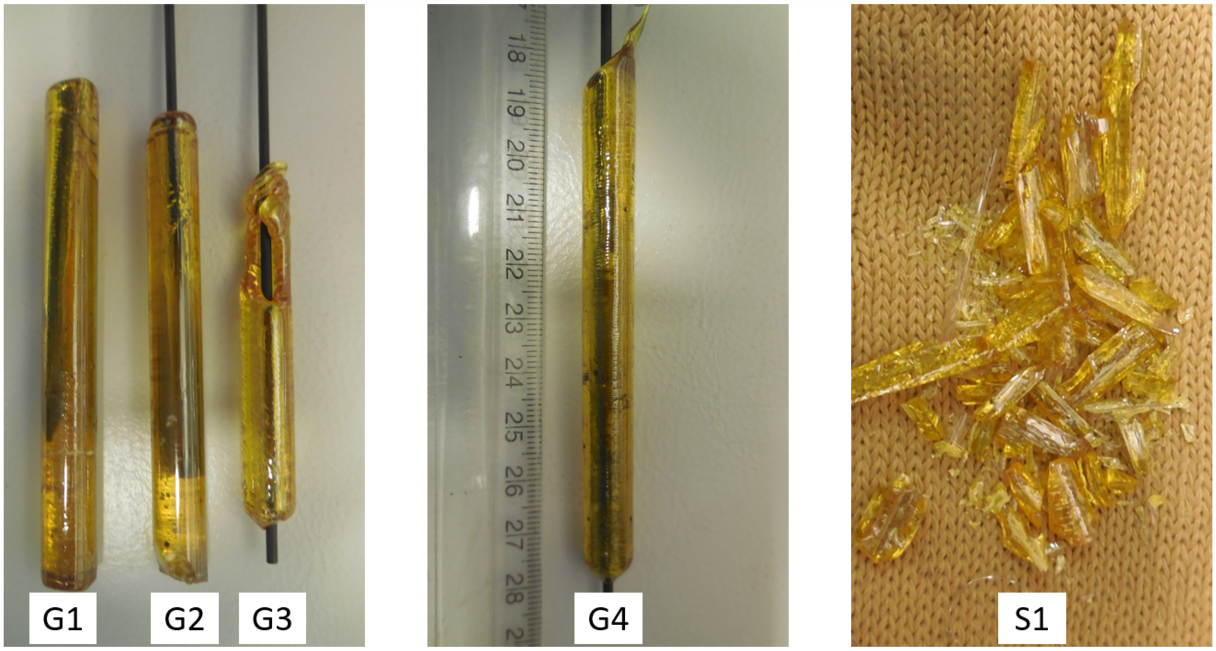

Figure 51: Attempts at making hollow-core preforms. From left to right: G1, first test with graphite. Established the viability of the process. G2, introduction of a steel visor for accurate insertion. G3, attempt at casting around the graphite rod rather than insert it in a cast. G4, repeat of G3 using the maximum amount of GLSO that would fit in the receiving mould. S1, attempt at casting around a hollow 2 mm silica cane with 100 nm walls.

with using nichrome wire at the top, this ensured the graphite rod couldn't move during casting. It could still be flushed out by exerting pressure on the protruding end of the graphite rod. The resulting preforms are shown in Figure 51 casts G3 and G4. Even after 48 hours of annealing and despite the consistency of their diameter, however, the graphite rods could not be removed by prying them out without shattering the glass. So they were ultimately cut off on both side and manually drilled out successfully, producing a hollow GLSO rod. The graphite being softer than GLS, it provided a self-guiding mechanism for the drill that enabled to exclusively remove graphite without damaging the glass.

This technique was then attempted with GLSSe20%. It was observed than in spite of annealing, the GLSSe20% rods would crack upon reaching room temperature, as shown in Figure 52.

Enhancing the annealing process by using a devoted annealing furnace with a more even temperature than the tube furnace would be the next logical step, along with a systematic array of tests to optimize the hollow preform fabrication process to prevent cracks for

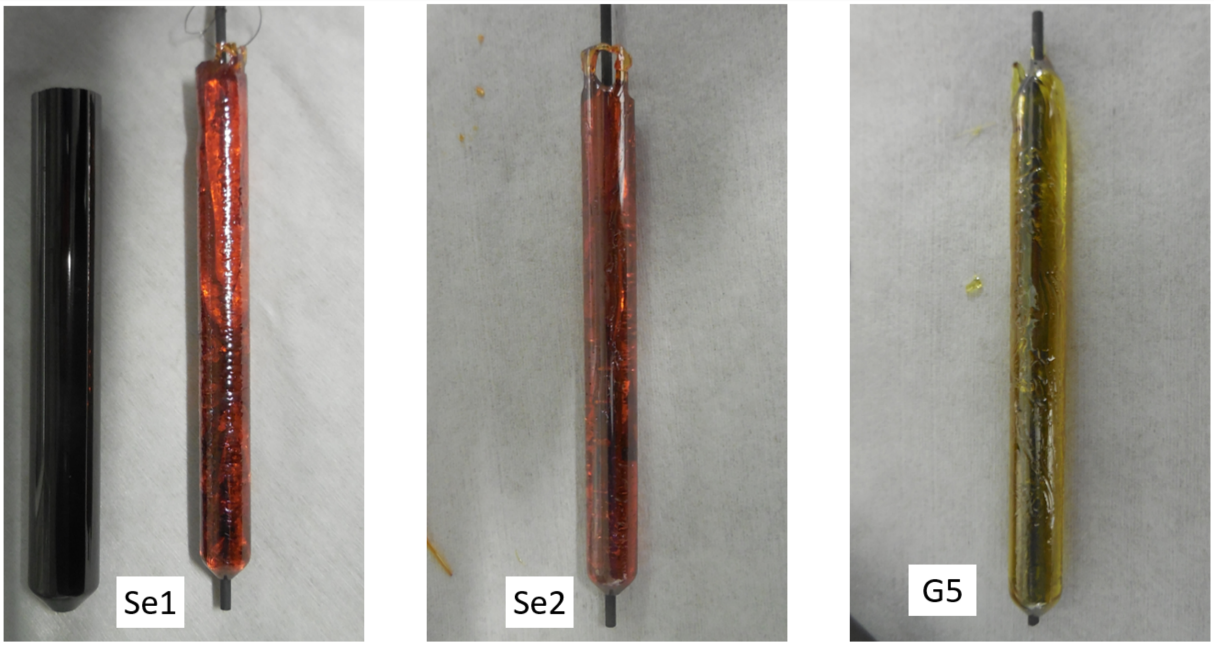

Figure 52: Embedding 2 mm graphite rods in GLSSe20% by casting around. Se1, first test with graphite, GLSSe20% cast in a 600 °C mould. Length-wise cracks are visible. Se2, repeat in a 650 °C mould. Appeared intact at the time, but spontaneously cracked after being taken out. G5, repeat of Se2 using GLSO instead, to ensure the reproducibility of the success achieved with GLSO. Cast remained intact indefinitely.

each composition. However, these sets of casting experiments still enabled to achieve the fabrication of suitable hollow-core GLSO preforms and demonstrates the feasibility of the method. Once drilled, cleaned and polished inside and out, the hollow GLSO preform was drawn into optical fibre, the results of which are shown in Section 10.3.4 Figure 85.

6.3 Cane drawing

In order to produce a core-clad structure from casting, the fabrication of canes from unstructured preforms was undertaken. The process is similar to that of fibre drawing from a solid rod, the key difference being that the necked preform is fed into the cane puller rather than the fibre collecting drum. It is then drawn at a much slower rate than for fibre drawing (measured in mm/min as opposed to m/min) to form a glass cane a few millimetres thick rather than spoolable fibre. Because a glass cane is thicker than a fibre, it can withstand higher tension. This results in the cane drawing process being usually performed at lower temperatures than fibre drawing, which greatly reduces the risks of crystallization. Due to the placement of the cane puller, uninterrupted canes of up to 2 m in length can be fabricated, although in practise the produced cane is cut off in pieces as it is drawn, the exact length depending on their intended use. Such uses can be the production of core-clad fibre, by being combined with either casting or extrusion using the rod in tube technique [117, 118]. Cane drawing is often used as a preliminary step for fibre drawing. It enables to approximate the fibre drawing temperature, and the material produced can be kept for later use. These canes are stored in silica tubes and sealed at both ends to maintain their quality in storage.

6.4 Rod polishing

To address the prevalence of the issue of surface crystallization during fibre drawing, particular focus was placed on enhancing the surface quality of all glass rods or preforms intended for fibre drawing experiments. Extruded rods show longitudinal scratches from the steel dye, turned rods have a rough, chipped finish, and cast rods occasionally have small imperfections due to the rapid cooling of the glass not always allowing for the perfect moulding of the rod. Examples of such defects are shown in Figure 53.

Attempts were made to flame polish GLS preforms without success, as thermal shock would instantly shatter the preform upon rapid heating. An in-house, room temperature polishing method was implemented using a small portable lathe and a set of varying grit polishing paper, shown in Figure 54. One end of the rod was wrapped in electric tape and held in a self-centring chuck, while the other had a small cone-shape indentation drilled in its center for the lathe tailstock to hold it in place. Pieces of polishing paper were cut, wrapped around the preform and manually translated along the length of the rod while it was spinning at 350 revolutions per minute (rpm). The grit of the lapping sheets used was slowly reduced from 30 μm to 0.02 μm. Using alumina or diamond based polishing paper made no noticeable difference to the quality of the polishing achieved, or the speed at which it was attained. The gradual improvement of surface quality achieved by polishing glass rods in this manner is shown in Figure 55.

The meticulous observation of the surface using an optical microscope is necessary in between each of the polishing steps, to ensure the surface has been evenly polished in the entirety of its length. Otherwise, the surface will develop pits, as shown in the left-hand side of Figure 56. These polishing defects were observed by P. Bastock [108] in diamond polished preforms made by external contractors, and identified in his thesis as carbon

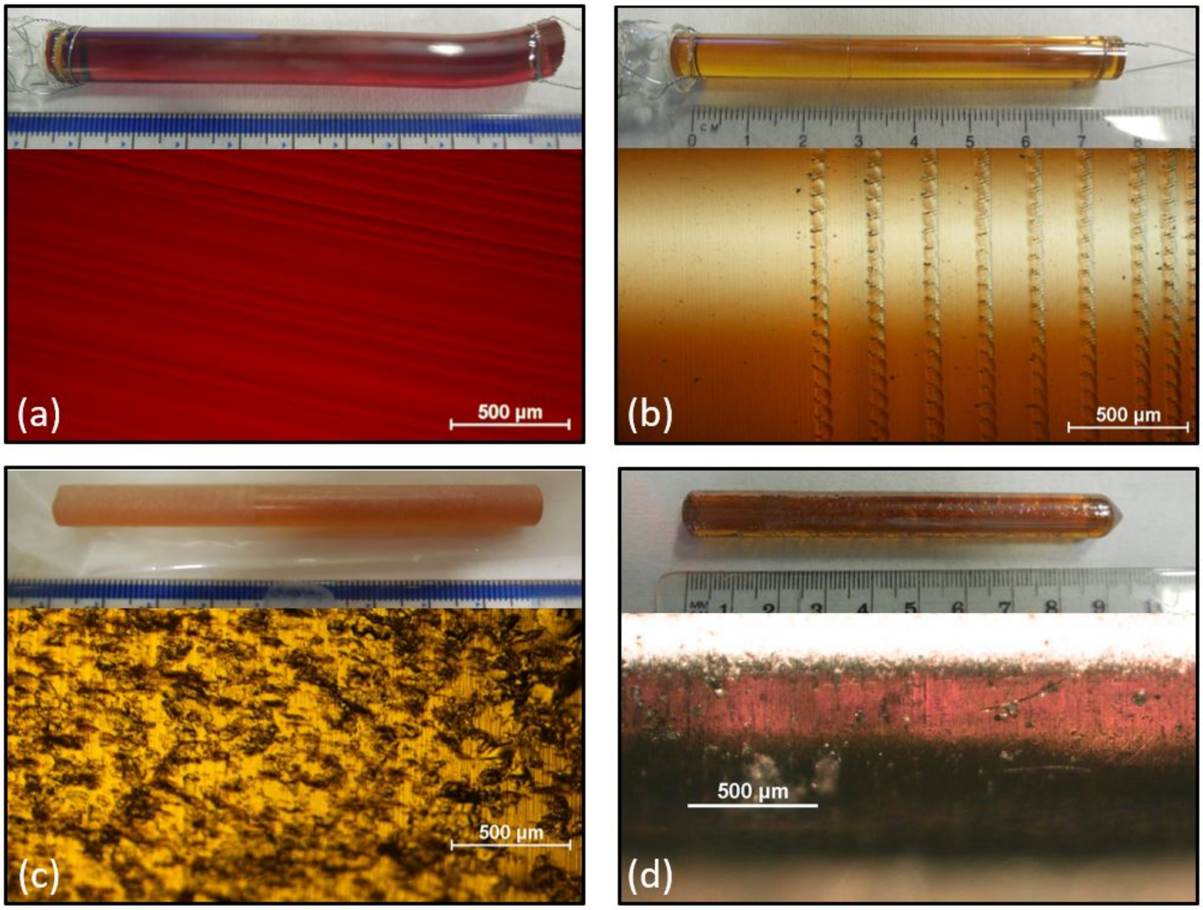

Figure 53: Surface imperfections motivating the development of in-house polishing techniques. (a) Extruded rod (extruded rod courtesy of Fernando Guzman), (b) Diamond turned rod, (c) Lathe turned rod, (d) Cast rod.

particles. However, the experience gathered in this work shows that these defects instead correspond to pitting left in the rod by switching to a lower grit too early. These holes then get filled by polishing residue, made up of a mixture of ground glass and carbon, which appears as carbon particles when performing energy-dispersive X-ray spectroscopy (EDX). This is the reason why these defects are exclusively visible on the surface of the rod rather than throughout the bulk of the glass, and why they cannot be removed via cleaning. They gradually disappear, however, when polishing is undertaken more thoroughly.

The most common issue that can occur during polishing aside from pitting caused by switching to the next polishing step too early is re-scratching of the surface, an example of which can be seen in the left of Figure 56. This issue tends to happen when the polishing paper is changed for a lower grit, and the preform/rod hasn't been cleaned thoroughly.

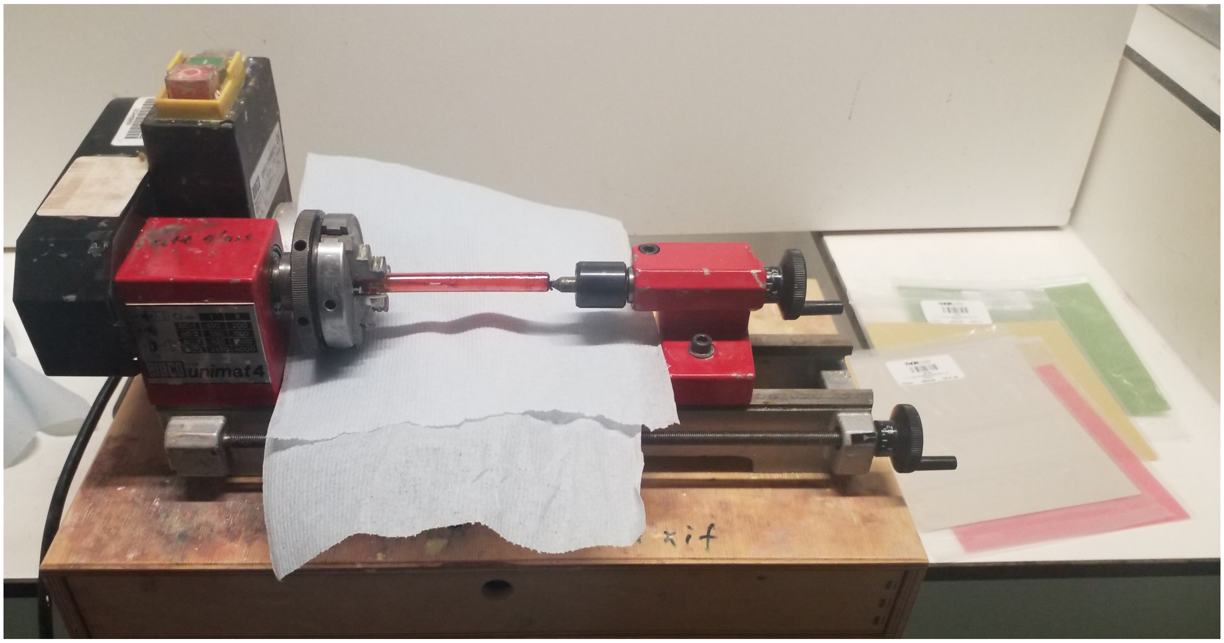

Figure 54: Small lathe used for hand polishing set up for polishing a GLSSe20% cast, Thorlabs lapping sheets on the right-hand side.

Then, some abrasive particles from the previous polishing step may get caught between the lower grit polishing paper and the glass, producing deep scratches on the surface of the rod and requiring to redo the previous polishing step until the scratches are removed. In order to avoid these time-consuming incidents, thorough cleaning of the rod is necessary between each step. This cleaning was performed using an ultrasonic bath, in which the rod inserted in a sealed vial filled with ethane-diol was placed. The ethane-diol was changed 2 to 3 times so as to ensure that all of the abrasive polishing particles are removed, as any would suffice to damage the surface and force to go back to the previous polishing step. In spite of the degree of care necessary, an optical finish on par with the one demonstrated in the bottom right panel of Figure 55 could be achieved in a single day, once enough experience had been acquired. Examples of polished rods of various lengths, diameters and composition are shown in Figure 57.

For the hollow GLSO casts around a graphite rod and successfully drilled through, an additional method had to be developed to remove the carbon residue as well as polish the inside of these rods. Plasma ashing didn't appear to have a significant impact on the amount of carbon deposited inside the preforms, even when they were exposed to it for several hours. Attempts were made to use coiled polishing paper wrapped around

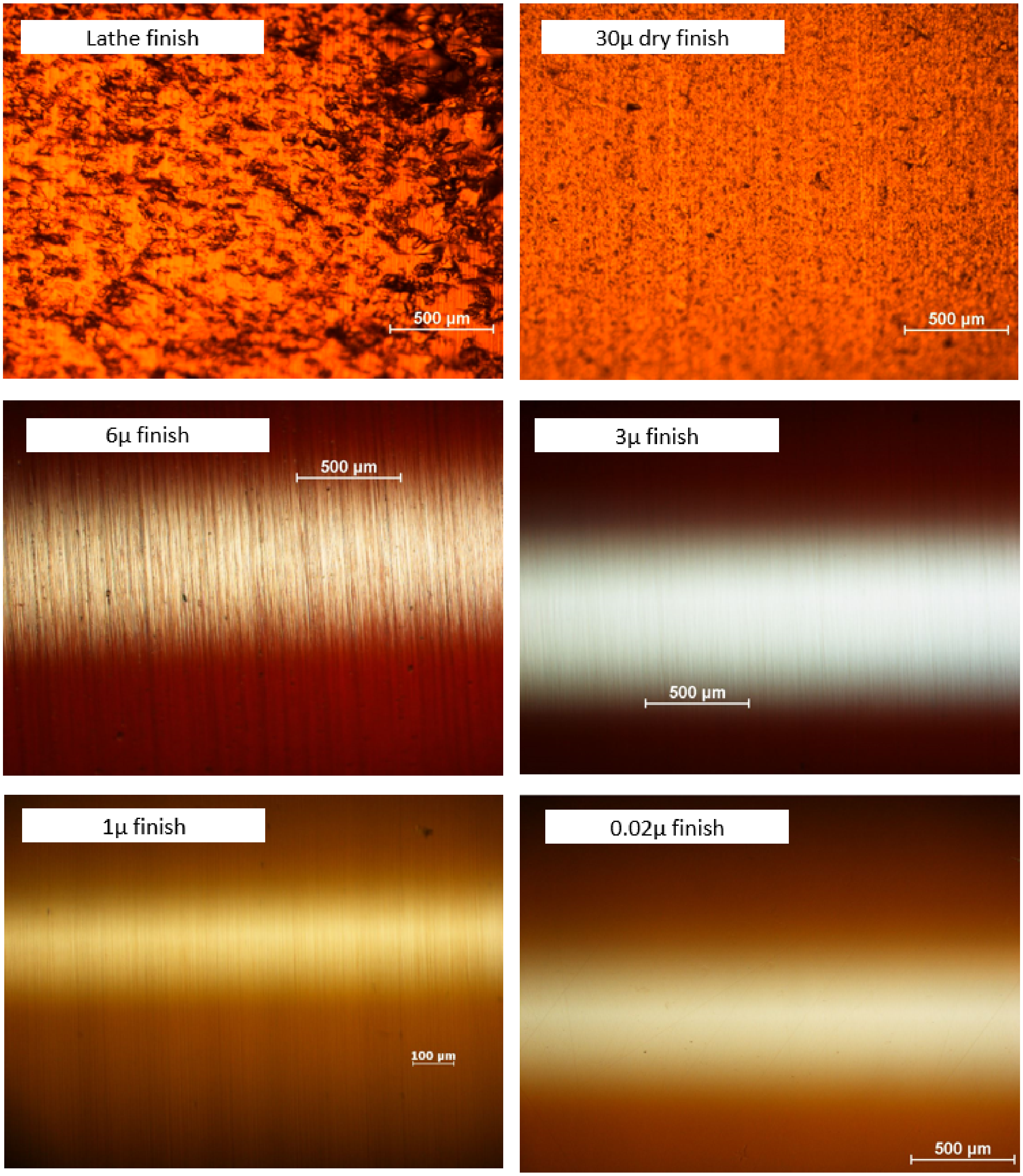

Figure 55: Gradual improvements of the surface quality of a GLS rod from being turned on a lathe to the final optical finish that can be achieved using the in-house polishing method.

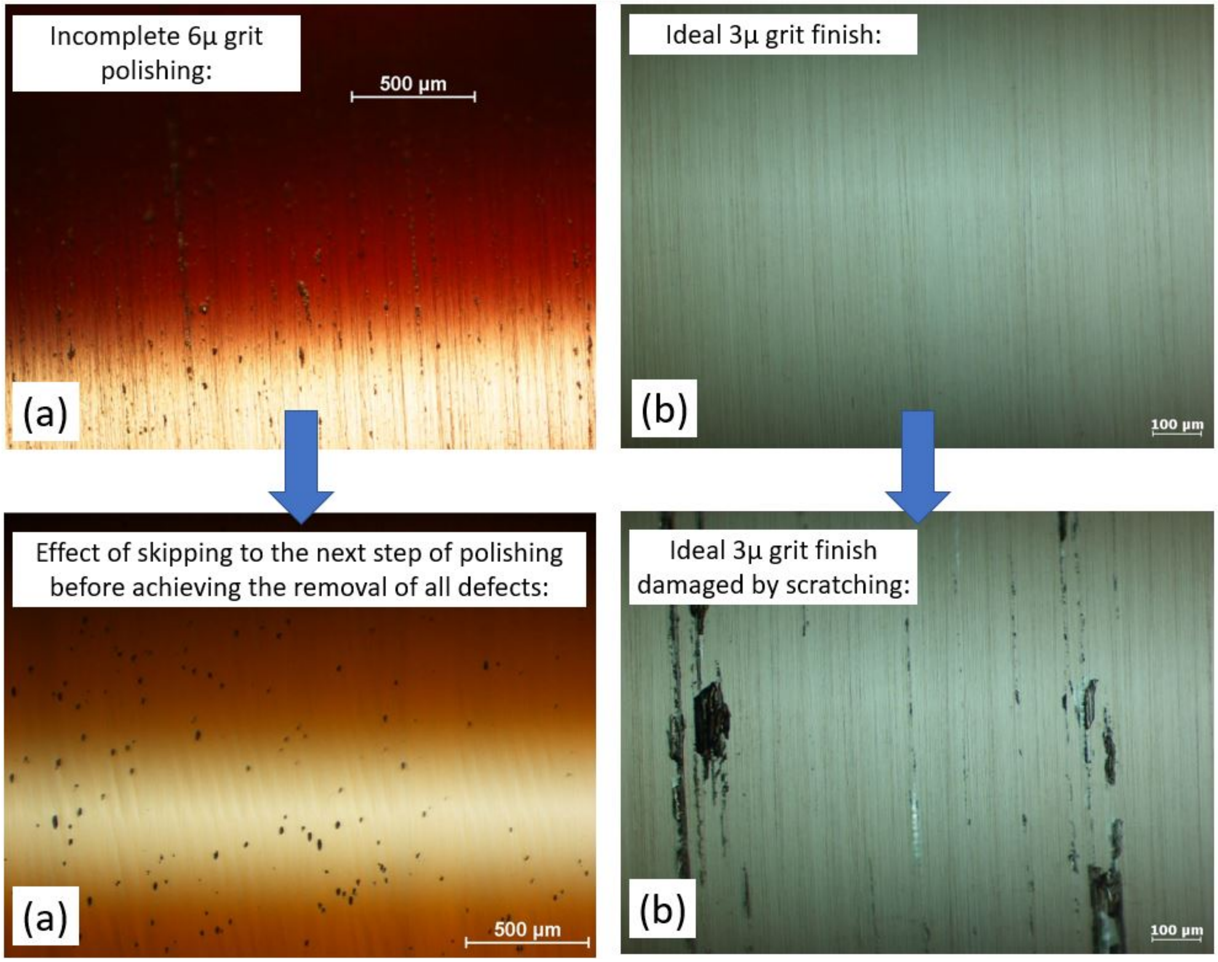

Figure 56: Common challenges of cylindrical rod polishing. (a), effect of skipping to the next polishing step too early. (b), effect of cross-contamination from abrasive particles used in an earlier (coarser) polishing step.

nichrome wire to both remove the carbon deposits and polish the inside, but to no avail. A pair of disposable plastic syringes were loaded with abrasive diamond polishing compound paste (grit 1 μm) mixed with a small amount of ethane-diol. The syringes were attached on both ends of the hollow GLSO preform using PVC tubing and tightened using nichrome wire. The paste could then be flowed from one syringe to the other, passing through the core, and hopefully polishing the inside. This attempt is shown in Figure 58.

Even after several hours of this paste manually flowed through the hollow preform, however, the optical quality did not seem to improve, and neither was the graphite residue removed. As a last resort, the pressure applied to the system was increased to the maximum it could be without the PVC tubing slipping off, making no noticeable improvement.

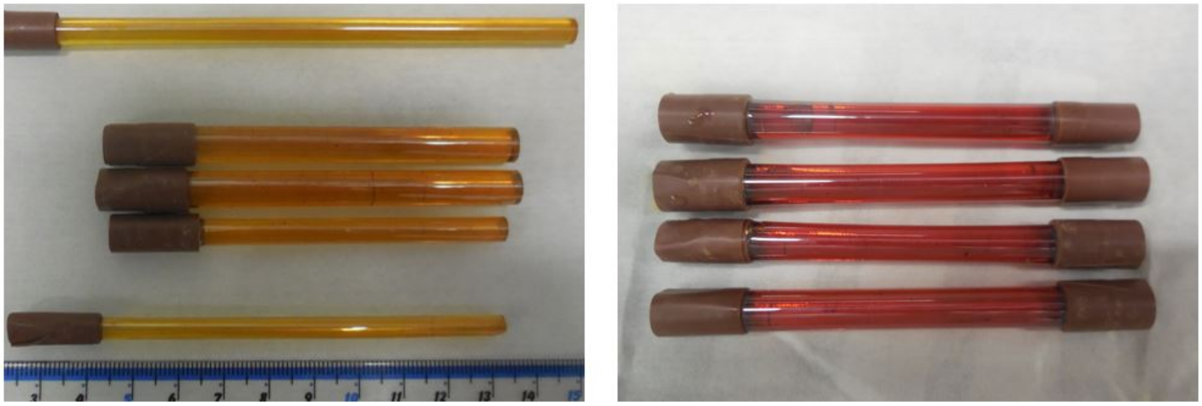

Figure 57: On the left-hand side, polished GLSO rods directly cut from a GLSO ingot. On the right, polished GLSSe20% rods made from casts.

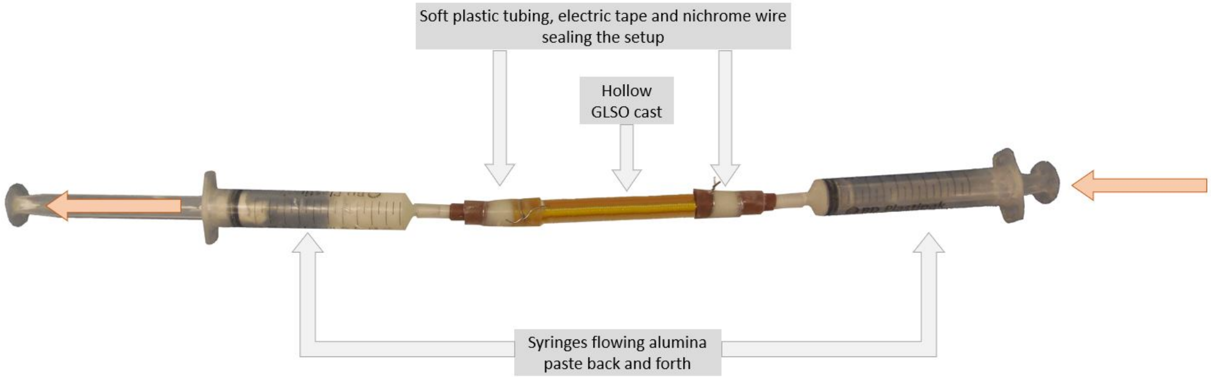

Figure 58: First method tested to polish the inside of hollow preforms, using flowing diamond paste and disposable syringes.

A greater degree of success was achieved by coating a pipe cleaner with diamond paste, securing it in the chuck of the portable lathe, while attaching the preform to the tailstock and translating the tailstock back and forth while the lathe was spinning. The paste immediately started to darken due to the removal of graphite residue from the inside of the hollow preform. Because of the coarse bristles of the pipe cleaner, however, it was observed that the polishing quality achieved this way remained poor.

As such, the pipe cleaner was advantageously replaced with a piece of nichrome wire wrapped in cleanroom wipes soaked in 1μ diamond paste. Using this method, not only could the graphite residue be removed, but the surface quality of the hollow core became visibly enhanced, as shown in Figure 59. Pressure could be adjusted by increasing or decreasing the amount of cleanroom wipes, and the preform would get noticeably hot, in a similar fashion as when exerting pressure during polishing of the outer surface. Once this hollow GLSO preform was polished to the highest degree achievable, it was drawn into optical fibre as shown in Section 10.3.4 Figure 85.

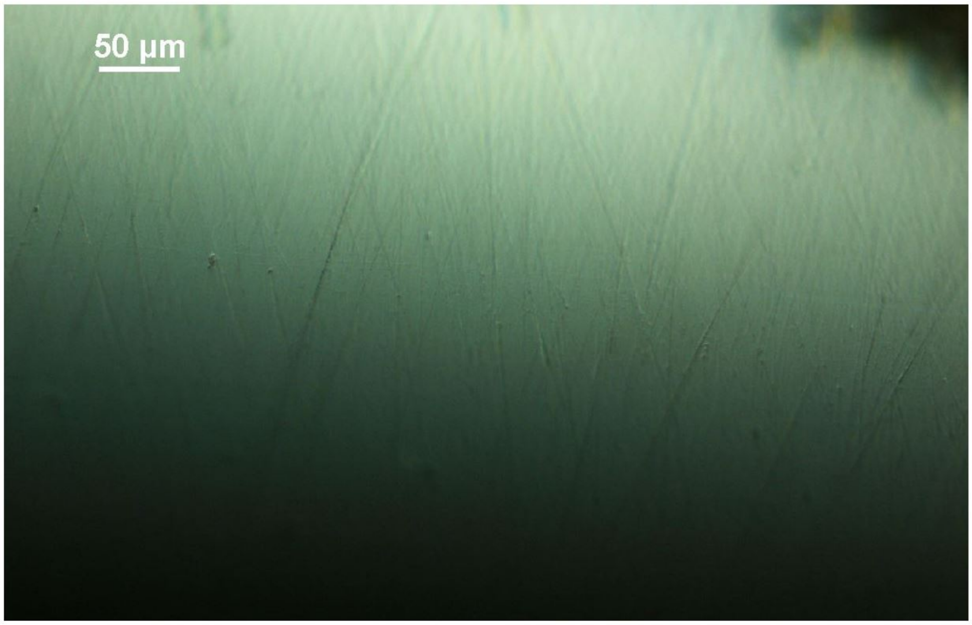

Figure 59: Quality of the inner polishing achieved on a hollow cast using the cleanroom wipe soaked with alumina paste method.

7 Relmelting

7.1 Large window fabrication

Using the same portable furnace as the one used for casting, remelts were attempted using the largest crucible that could fit inside. 150 g of pre-made GLSO glass were used in a 10 minutes melting test to produce a 95 mm wide GLSO window. During the course of that experiment, it became apparent that removing the large crucible from the portable furnace would no longer be possible, as it had become stuck due to tightness of its fit inside the furnace, as seen in Figure 60 (a). However, once the furnace was turned off and left to cool down to room temperature overnight, the crucible could be removed. As seen in Figure 60 (b), the window produced was entirely glassy. This observation was unexpected, as previously leftover glass in the portable furnace typically would become crystallized.

Following this observation, an additional experiment was made to produce a similar window out of GLSSe20%. However, as seen in Figure 60 (c), it failed to produce a glassy disk. Then, the natural ramp down rate of the portable furnace was measured, and the GLSSe20% sample was remelted. It was then quenched as fast as possible while remaining in the furnace, by opening and closing the furnace door at equally spaced intervals. This method managed to produce a glassy GLSSe20% window, shown in Figure 60 (d).

The detailed temperature ramp-downs used in the fabrication processes used to make these three windows and their interactions with the crystallization-prone region are shown in Figure 61. It may be noted that, as the crucibles are not removed from the furnace, the large diameter windows manufactured benefit from a relatively slow quenching rate and cool-down to room temperature, which may explain the absence of any cracks. This could be exploited in order to anneal even larger glass samples in situ.

7.2 Rapid quenching

The possibility of taking 1100 °C hot glass melts directly out of the portable furnace and the observation that the size of the glass forming region is quenching-rate dependent were exploited to reprocess samples that do not form a glass in the standard glass melt-quench process and thus manufacture glasses of compositions that were not previously available. Such a sample was taken out of the furnace and quenched in liquid nitrogen, to evaluate the effect of such an extreme temperature quenching. Unsurprisingly, that sample shattered

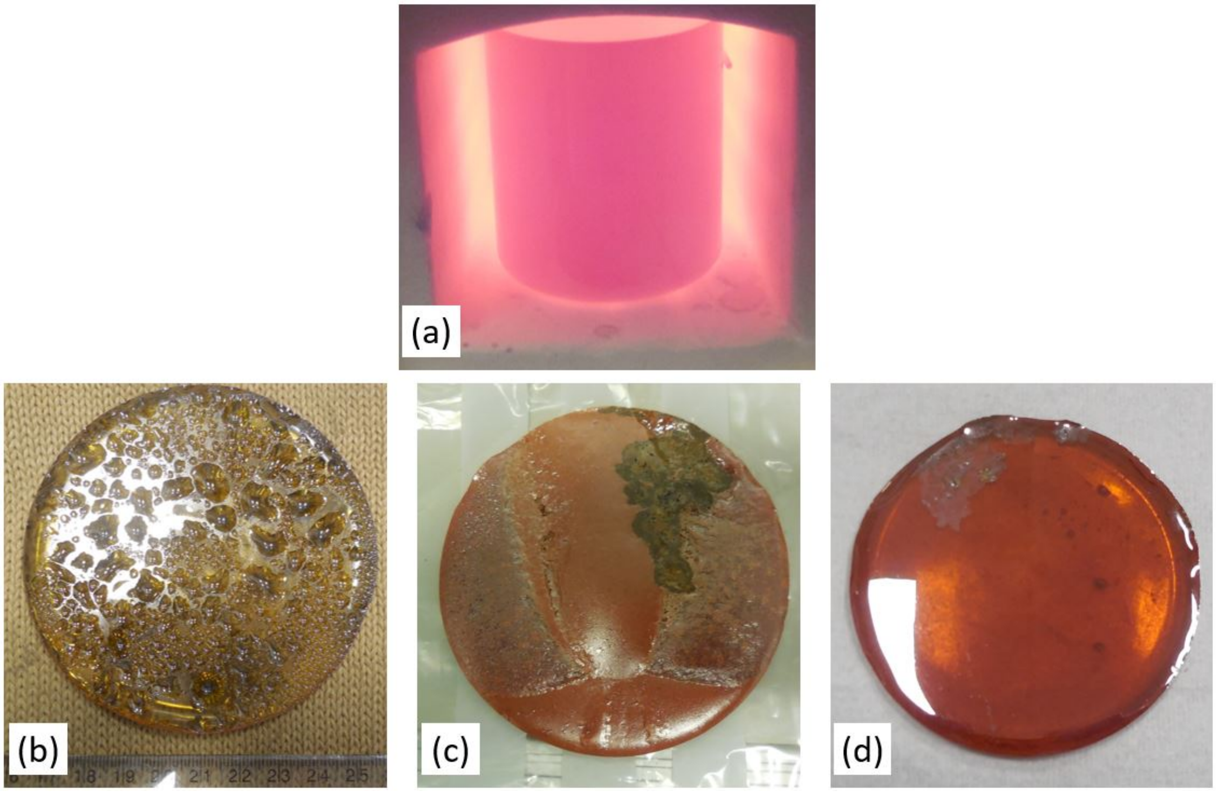

Figure 60: First attempts at manufacturing large-diameter (95 mm) GLS windows. (a), portable furnace at melting temperature (1100 °C). (b), 150 g GLSO window fabricated using a 7 °C/min quenching rate. (c), 150 g crystallized GLSSe20% window fabricated using a 7 °C/min quenching rate. (d), 150 g glassy GLSSe20% window fabricated using a 22 °C/min quenching rate.

into very small pieces upon being removed from the crucible.

In a considerably less extreme fashion, crucibles could either be quenched directly in air, or they could be placed onto a steel heat sink. For example, a sample of GLS 65:35 containing 1% molar mass of added copper was made to switch from a completely crystallized state to a glassy state by being quenched using the steel heat sink. The evolution of the process and the associated sample is shown in Figure 62, where a crystallized GLS sample with high copper content, initially made in order to investigate the feasibility of electrically conductive GLS, was successfully remelted into transparent, crystal-free glass.

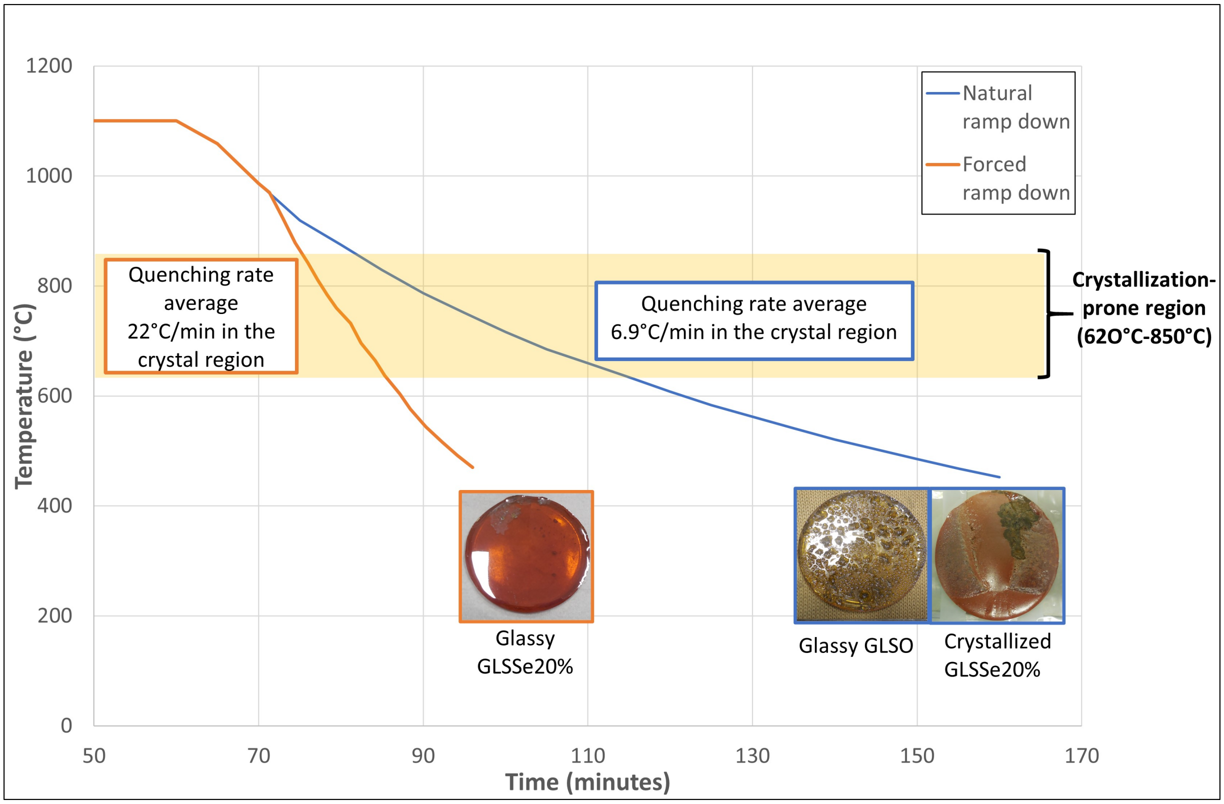

Figure 61: Graphic representation of the different quenching rate required to produce glassy windows of GLSO and GLSSe20%.

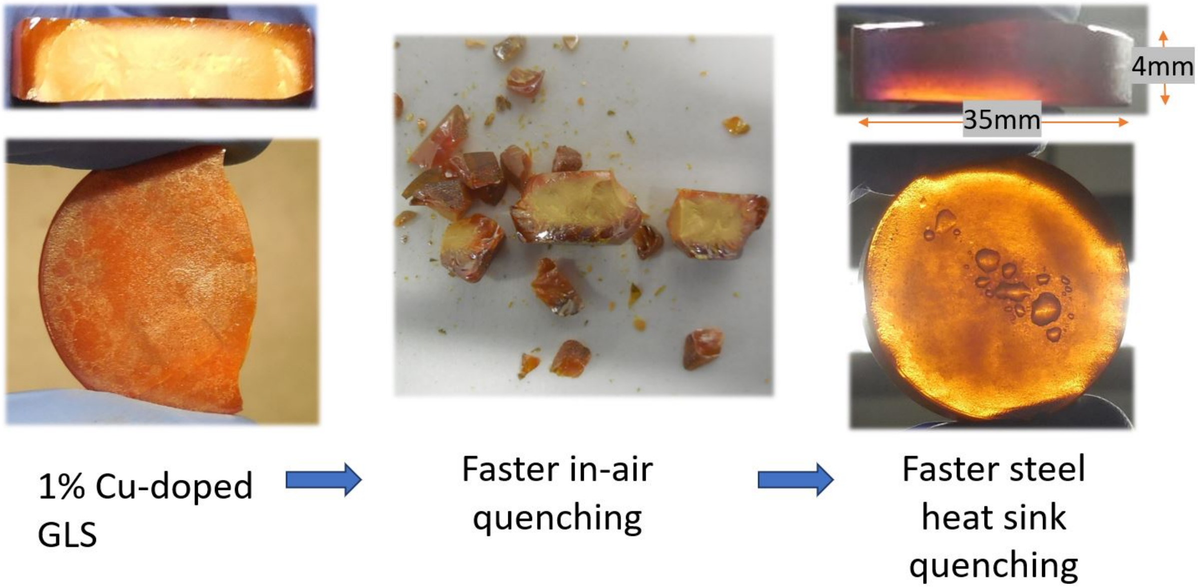

Figure 62: Effect of an increasingly rapid quenching process on 1% Copper-doped GLS, eventually resulting in a glass rather than a ceramic.

8 Fibre fabrication

8.1 Rod drawing

The standard procedure for rod drawing consists of attaching the short ($\approx$ 100 mm long) preform to a silica tube using nichrome wire. Notches are made to both extremities of the preform so that it can easily be tied to the preform holder on one end and to a 50 g weight on the other, as shown in Figure 63. Particular care has to be taken to ensure that the preform is straight and is tied as close as possible to the preform holder. It is preferable to tie the preform to at least 3 points so that it remains stable and does not oscillate during the drawing process.

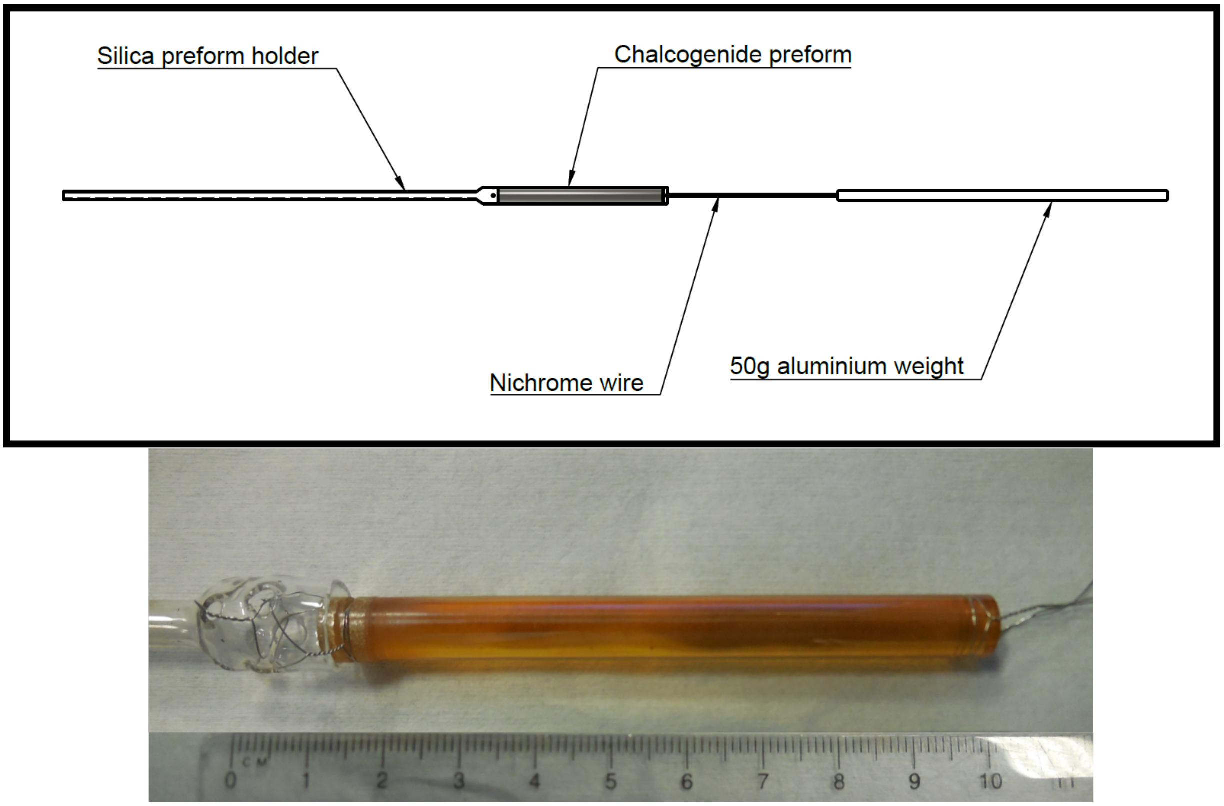

Figure 63: Schematic representation of a preform assembly for fibre drawing (top) and corresponding picture of an unstructured hand polished GLS rod used in draw NT842 (bottom).

Once the preform is tightly secured to it, the preform holder is inserted into the chuck, which is then aligned so that the preform is centred into the furnace assembly. The position of the preform is adjusted vertically, so that its lower end is around 20 mm below the highest temperature spot of the hot zone. This starting position was established empirically so as to minimize the amount of glass lost to necking while preventing the preform from necking at the notches rather than where the glass is thicker. It was observed that if the preform necks at the notches, it does so more rapidly, but the cross section of the fibre produced is not circular. As the preform is slowly fed into the furnace, the fibre cross-section eventually becomes circular, but as feeding progresses and it transitions to a thicker part of the preform, the volume of glass is suddenly increased, which risks breaking the fibre and interrupting the draw.

The furnace used for fibre drawing is custom made from silica tube. A cylindrical graphite susceptor is placed inside it, with a thermocouple inserted longitudinally half-way into its 5 mm thick wall, to monitor and adjust temperature as needed. It is heated using a water-cooled RF induction coil for high responsiveness. The graphite susceptor chamber and the preform chamber are both under independently adjustable nitrogen purge. This furnace is illustrated in Figure 64. It is made of 3 different parts: the top cap, to which gaseous purge is applied so that it flows into the preform chamber, the main body, which carries the susceptor, and a support tripod, through which the necking preform can be guided by hand when it stretches out from the hot zone.

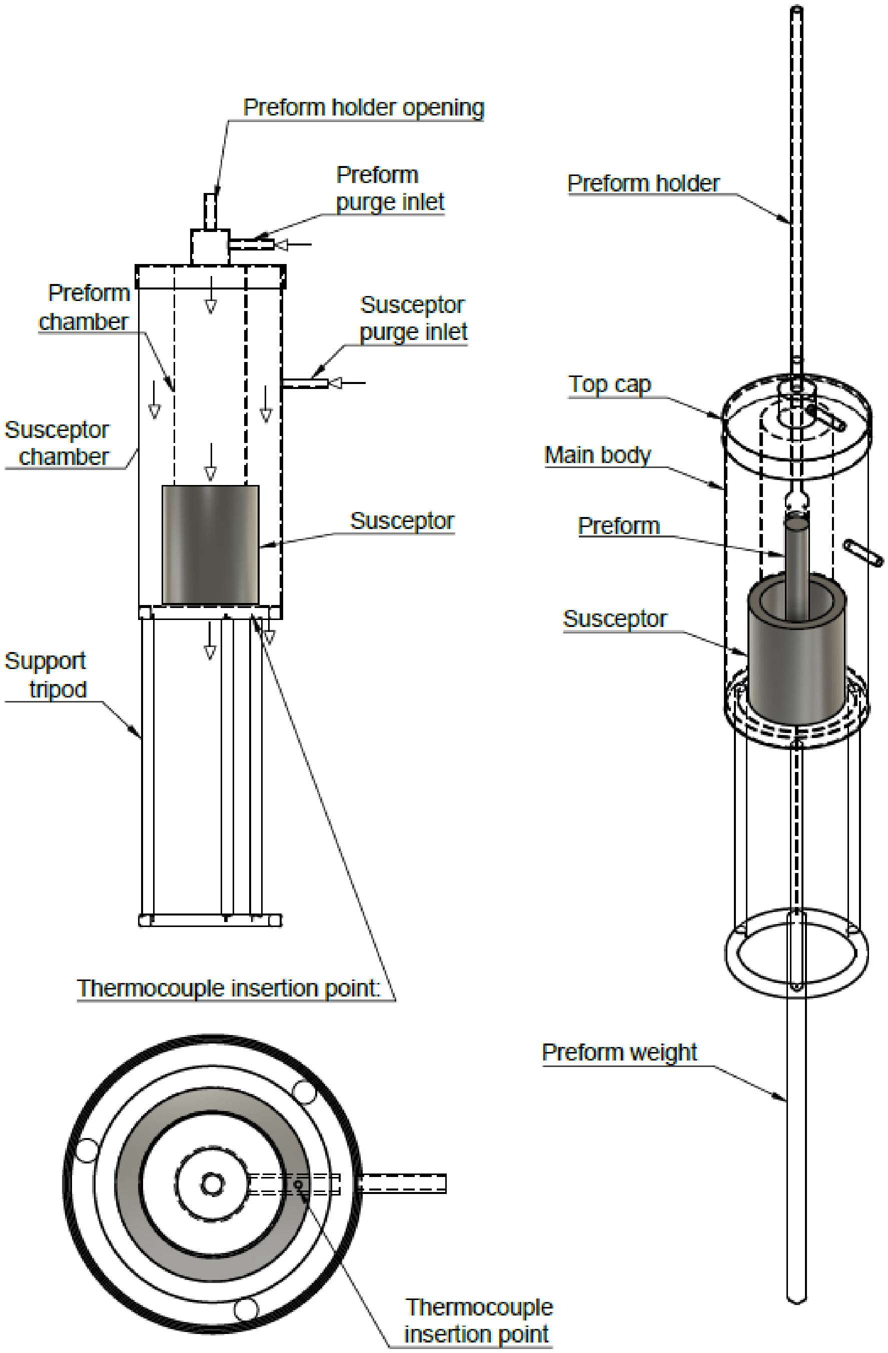

Figure 64: Schematic representation of the rod/preform fibre drawing furnace assembly showing the insertion points of the purge and the loading procedure of a preform.

Once the preform has been set up and is centred, the gaseous purge is activated, the graphite susceptor is heated up at 100 °C/min until the desired drawing temperature is reached. This temperature is selected either from the literature, previous experiments or TG/DTA measurements. It usually takes around 10 minutes for a GLS preform to soften and neck using the 50 g weight.

As soon as the neck has visibly formed and the glass is beginning to stretch, the preform feed is turned on, lowering the chuck at a constant speed of a few mm per minute, so that the material removed from the hot zone by the drawing process gets continuously replenished and the fibre diameter remains constant. Once the fibre is formed, the bottom half of the neck is snapped off, and the fibre is threaded through the open coating cup and the UV curing lamp by hand, to be finally taped onto the drum below. The speed of the drum is matched to that of the feed according to the following formula, in order to produce fibre of a desired diameter: $\mathrm{d}_{\mathrm{fibre}} \cdot \mathrm{S}_{\mathrm{drum}} = \mathrm{d}_{\mathrm{preform}} \cdot \mathrm{S}_{\mathrm{feed}}$, where d_{fibre} is the diameter of the fibre produced, $\mathrm{d}_{preform}$ is the diameter of the preform, S_{drum} is the drum speed and S_{feed} is the feeding speed of the preform in the hot zone. This process is illustrated in Figure 65.

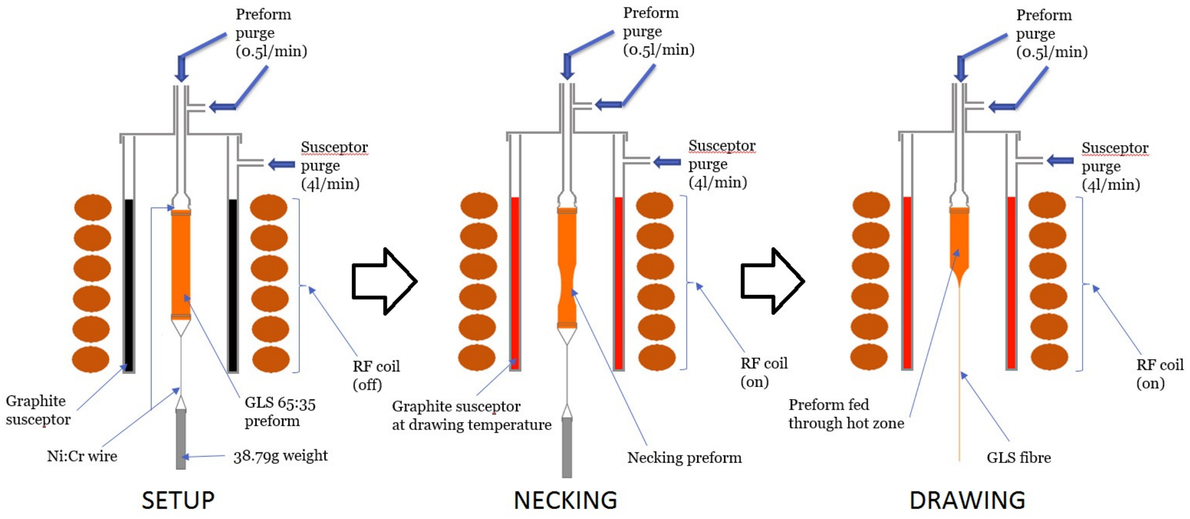

Figure 65: Schematic representation of the three key stages of the preform/rod drawing process.

The first fibre drawing experiments yielded fibre that contained crystals as shown in Figure 66. The remaining preform is also shown, providing further evidence of crystal growth that stems from the surface, and develops inwards. It may also be noted that there is a slight asymmetry in the distribution of the crystals, which may be explained by improper alignment in that particular experiment. Several hypotheses were put forward to explain the presence and distribution of crystals. The first one to be tested was surface

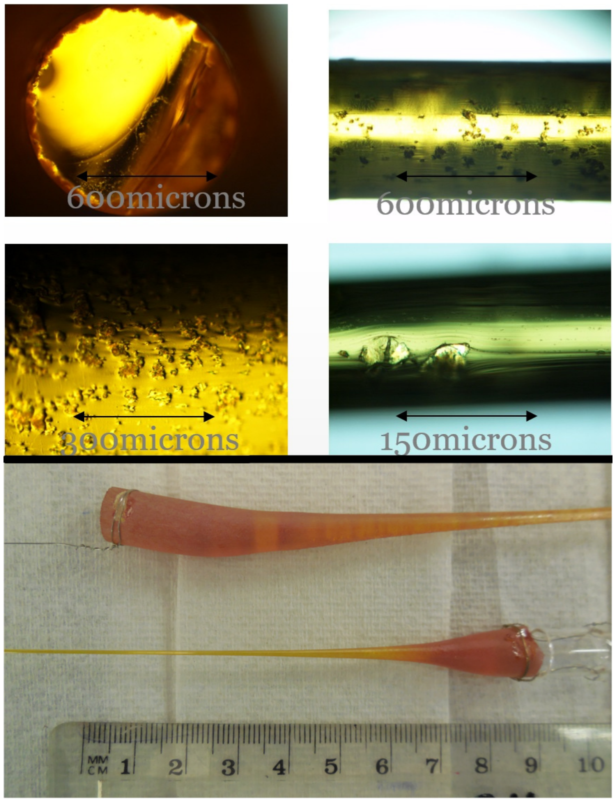

Figure 66: Cross-section and side view of surface crystallization of GLS fibre drawn from a GLS rod (top). Necked preform covered in surface crystals that give it a cloudy appearance (bottom).

imperfections on the preform, shown in Figure 67, acting as nucleation sites for crystal growth. This issue was addressed by ensuring the preform is polished to a perfect finish before drawing. Another potential factor explaining crystal formation is insufficient purge, which could be responsible for particles, such as airborne graphite dust emanating from the susceptor, forming nucleation sites by adhering to the softening preform surface. This concern was initially addressed by increasing the amount of purge used, without visible improvements. Afterwards, this concern was properly addressed by using a fully sealed silica furnace, trading the versatility of a furnace made up of different, individually customizable pieces, for the improved purge control of a fully sealed vessel. Finally, the temperature difference between the surface and the core of the preform was studied, and its relation to the ramping rate and to the amount of purge used was investigated. Subsequent changes in the experimental methodology were made to minimize it. These changes are described in Section 8.3.1, Figure 79.

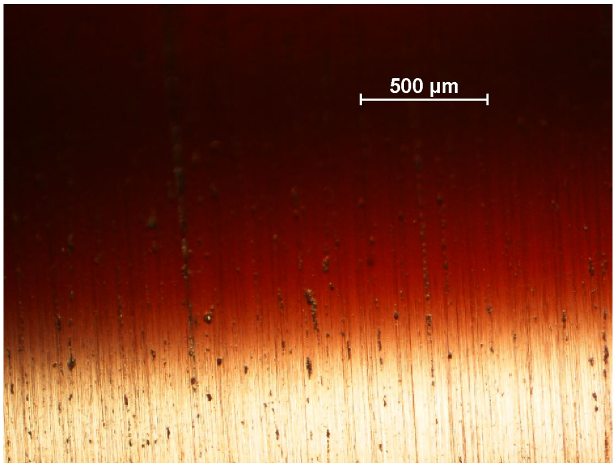

Figure 67: Optical microscope image of the surface imperfections on a preform that seems optically smooth with the naked eye.

8.2 Rod-preform drawing enhancements

To improve the understanding and control of the temperature distribution within the furnace, and thus increase the chances of obtaining crystal-free fibre, a thorough calibration study was carried out. The calibration tests performed enable to monitor the effects of changes to the structure of the silica furnace, changes to the shape and size of the graphite susceptor, and changes to the amounts of gaseous purge as well as its points of insertion.

In Figure 68 can be seen the calibration preform used in all calibration experiments, unless specified otherwise. This calibration preform is a silica cylinder 10 mm in diameter and 100 mm in length, which is the standard size of chalcogenide preforms established by previous work [10, 108].

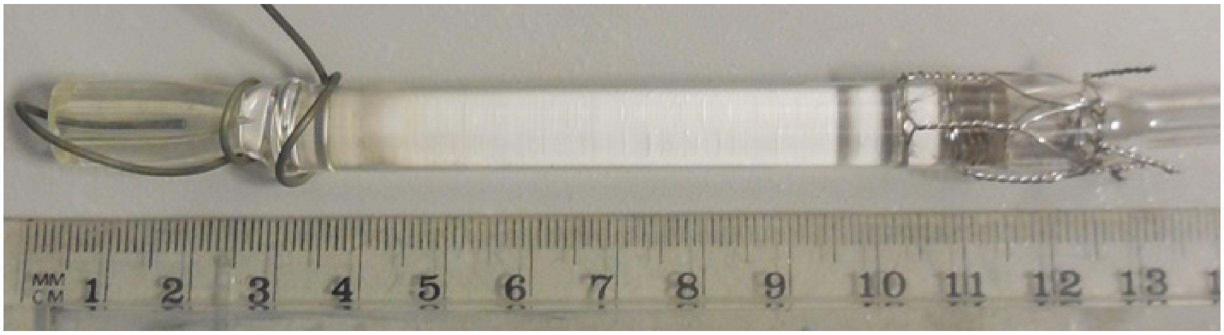

Figure 68: Silica calibration preform used in vertical scanning calibration measurements.

A hole is located at its end in which a thermocouple is inserted. The hole is 20 mm deep and ends in a waist section of the calibration preform, which mimics the shape and location of the expected necking region. This calibration preform is scanned vertically through the hot zone in order to establish the corresponding temperature gradient in a preform during a fibre drawing experiment. Two limitations of this method are expected to produce inaccuracies in these measurements, when compared with the temperature in a chalcogenide preform. First is the fact that the calibration preform is made from a different material, which possesses different thermal and optical properties than chalcogenide glass. These different properties are difficult to account for, as the heating process from a graphite susceptor is a combination of all three heat transfer processes: convection (from the flowing gas purge), radiation (from the glowing graphite susceptor) and conduction (from the surface of the preform inwards). Also, the presence of the thermocouple and thermocouple hole will conduct heat more rapidly to the core of the preform than it would naturally spread through glass. Still this calibration method is expected to provide essential information regarding the shape of the hot zone.

8.2.1 Susceptor size

Calibration experiments using 100 mm and 60 mm long susceptors are shown in Figure 69. The selected susceptor temperature for these experiments was 800 °C, as it neighbours the drawing temperature used for most GLS composition variants. It can be observed that even though the susceptors have different lengths, the maximum temperature of the hottest spot in the preform is relatively close, only 13 °C apart when both susceptors are at 800 °C. This small difference can be easily offset by increasing the chosen temperature of the shorter susceptor. The only remaining difference in the width and symmetry of the temperature distribution. For the 100 mm susceptor, the slope of the temperature curve is lower around the hottest point, which is expected to result in a larger section of the glass softening at once. That in turn was observed to result in a lower required temperature for fibre drawing experiments. It is also asymmetric, the hottest spot being 15 mm closer to the lower end of the susceptor than its center point. This is caused by the RF heating coil used being slightly undersized and off-center to the susceptor. This asymmetry can be viewed as beneficial, as the formed fibre will have to travel a lesser distance to exit the hot zone, which should result in it being quenched more rapidly that it would be if it were symmetrical. Both the lower fibre drawing temperature and this asymmetry may be of help to avert crystallization.

Previous work made a major breakthrough in GLS fibre drawing by increasing the

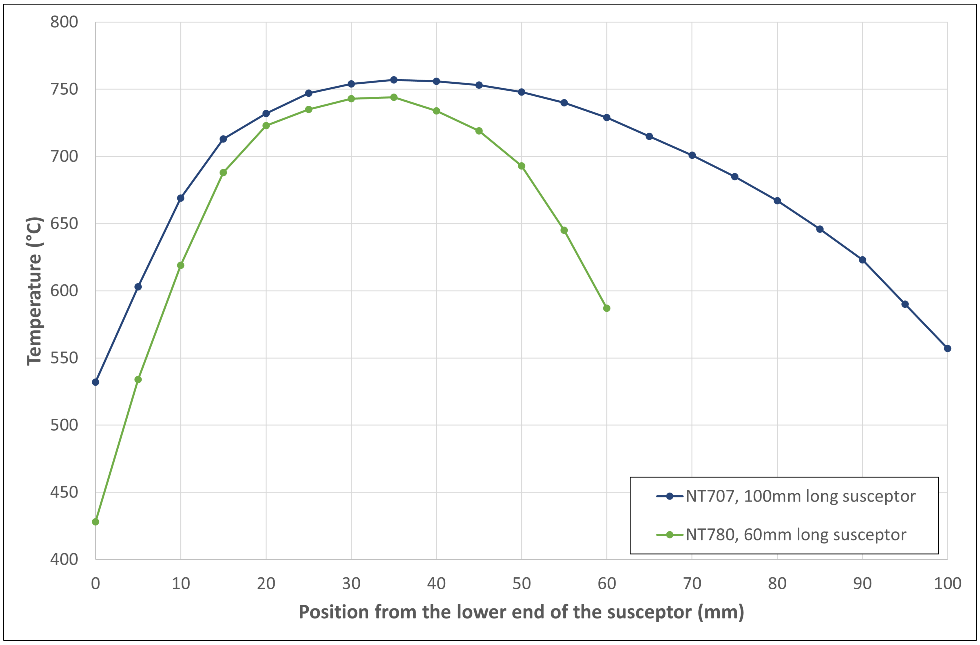

Figure 69: Vertical scanning calibration measurements comparing a 100 mm long to a 60 mm long susceptor.

susceptor size to 55 mm. The rationalization for this change was that pre-heating the preform reduced the temperature at which fibre drawing is feasible. However, it is also true that a larger hot zone means a larger section of the glass softening, which should enable to work at lower temperatures, as tension in the glass should be alleviated by a larger section of glass being able to stretch. In any case, this change enabled to successfully produce crystal-free GLSO fibre in the past [10]. In a similar way, an even longer susceptor was initially chosen for this work (100 mm long) to meet the needs of the more crystallization-prone oxygen-free GLS for fibre fabrication. However, as crystallisation results from the combination of excessive temperature and long time of exposure, it became apparent that this change promoted nucleation in the pre-heated part of the preform. Indeed, as this susceptor is exceptionally long, the section of the preform that is pre-heated is longer, resulting in excessive time of exposure to heat before the glass makes its way to the hottest spot and forms fibre. As such, the length of the susceptor was brought back down to 60 mm, which did not promote crystal growth to the same extent, and yet is of a comparable length to that of the previously established standard.

8.2.2 Single-piece furnace

In Figure 70 can be seen the difference in the calibration of an almost airtight furnace in which every element was fused together, and a standard "puzzle" furnace composed of several pieces stacked together, with all other parameters kept identical. The corresponding furnace assemblies are shown in Figure 71.

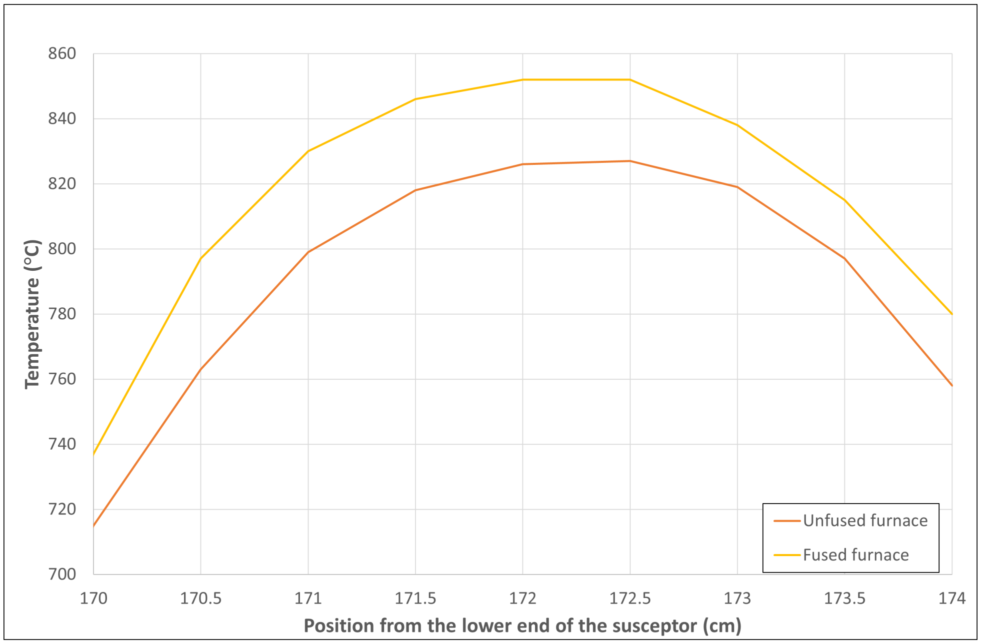

Figure 70: Vertical scanning calibration measurement of a single piece fused furnace compared to that of a "puzzle" unfused furnace at 900 °C, susceptor purge 0.5 L/min, preform purge 0.5 L/min.

As expected, the amount of heat leaking from the fused furnace is significantly lower than that of the unfused one, enabling to reach considerably higher temperatures in the hot zone for the same susceptor temperature. Due to fewer leaks, this narrower temperature gap is accompanied by a faster response in terms of temperature fluctuations of the preform when adjusting the susceptor temperature. A fused furnace also enables to lower the amount of purge, thus minimizing the possibility of turbulent flow, which may be causing instability to the heat distribution or contamination of the preform surface. In addition, a 4 mm silicon ring was slid around the preform holder, resting on the top of the preform holder opening shown in Figure 64. It slightly grips onto the preform holder, and as the feed slowly lowers the preform into the hot zone, it forms a tight seal preventing the nitrogen purge from escaping at the top and instead forcing it downwards.

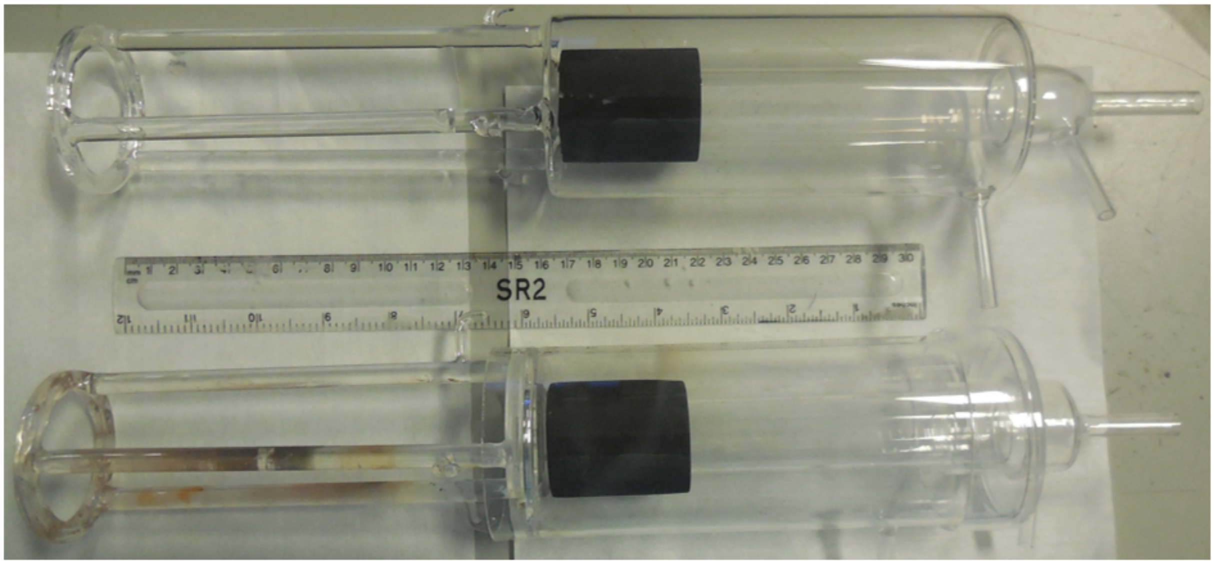

Figure 71: Single-piece fused furnace (top) and "puzzle" unfused furnace (bottom).

8.2.3 Cold finger

In Figure 72 and 73 can be observed the effects of varying amounts of purge applied to the top cap, also referred to as the preform purge. A cold finger was tested at the bottom of the chamber, shown in Figure 74. The motivation for its use was to rapidly cool forming fibre so that crystallization can be averted as early as possible.

In Figure 72, it can be observed that a large amount of purge used in the cold finger has a small effect on the shape of the distribution of calibration experiment NT706. However, this minor change is dwarfed by the impact of a similar increase to the amount of purge used at the top in calibration experiment NT777. From this measurement, it was concluded that the cold finger is fit for purpose, as it impacts neither the maximum temperature or the shape of the hot zone for the 100 mm susceptor. In Figure 73 however, the hottest point in the susceptor can be moved by several centimetres by varying the purge ratio between the top and the cold finger. So as to minimize the chances of crystallization, the fibre has to travel the lowest possible distance before exiting the furnace. This is found where the cold finger has no gas flowing to it. For the experiments carried out with this 60 mm susceptor, the cold finger was therefore removed.

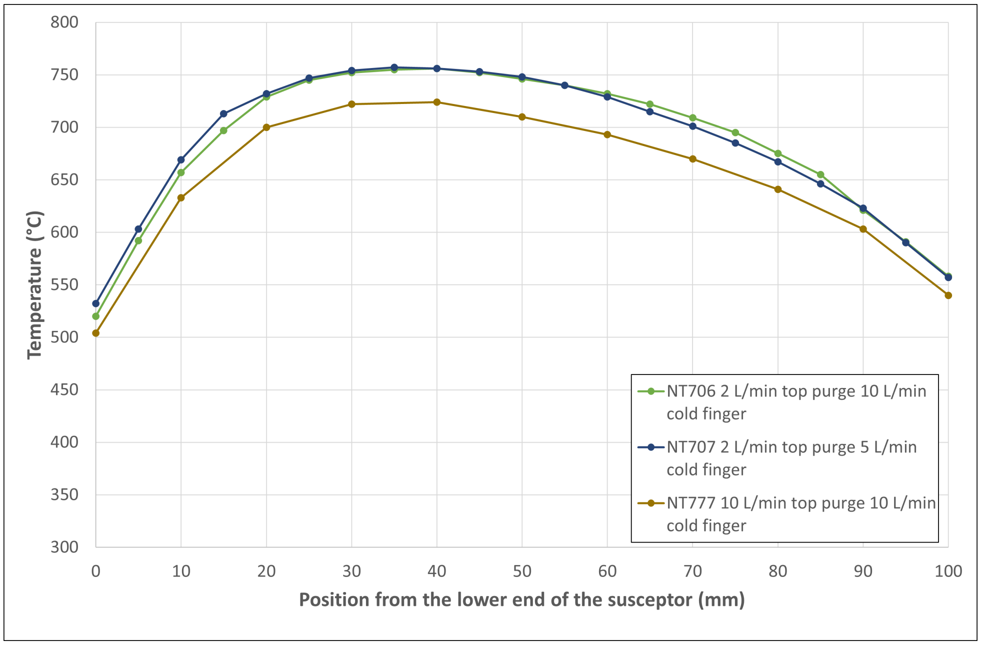

Figure 72: Vertical scanning calibration measurements of the 100 mm susceptor under varying amounts of purge to the cold finger and top cap.

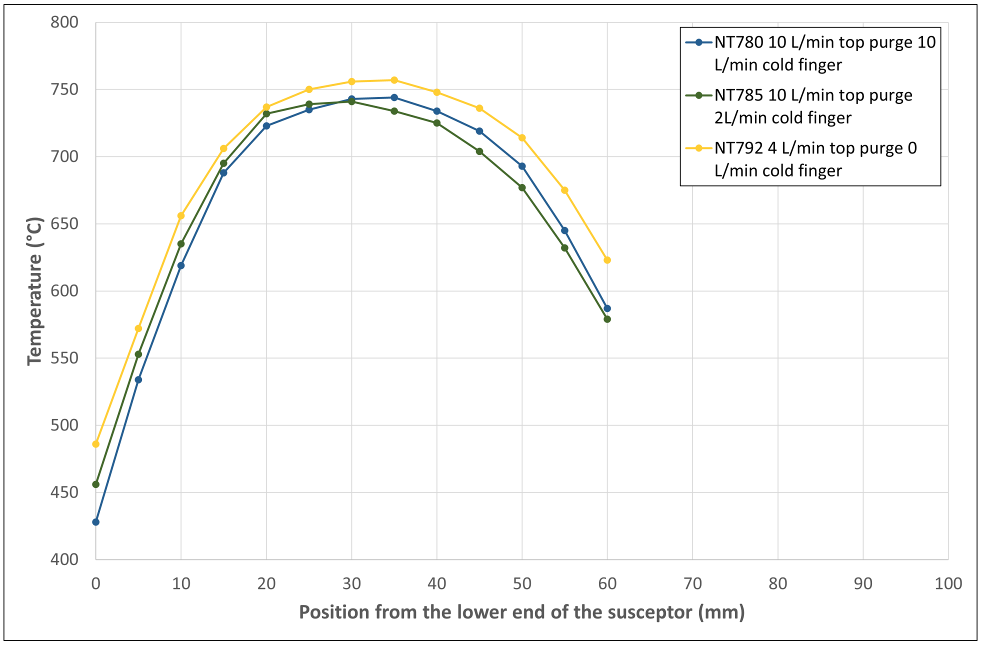

Figure 73: Vertical scanning calibration measurements of the 60mm susceptor under varying amounts of purge to the cold finger and top cap.

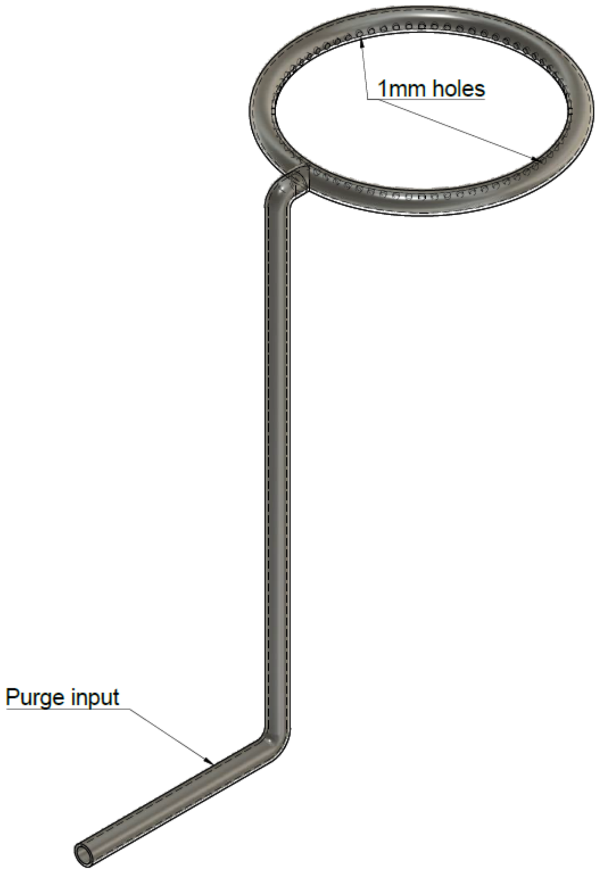

Figure 74: Hollow silica ‘cold finger’ installed under the furnace assembly in an attempt to quench fibre and prevent crystallization.

8.2.4 Exposed susceptor

In Figure 75 is shown the effect of using a furnace with an exposed-susceptor design, wherein there is no silica wall separating the preform from the susceptor. The other parts of the furnace design are identical, and only the inner wall of the susceptor is exposed, to maximize the heat transmission to the preform, while maintaining the system as closed as possible.

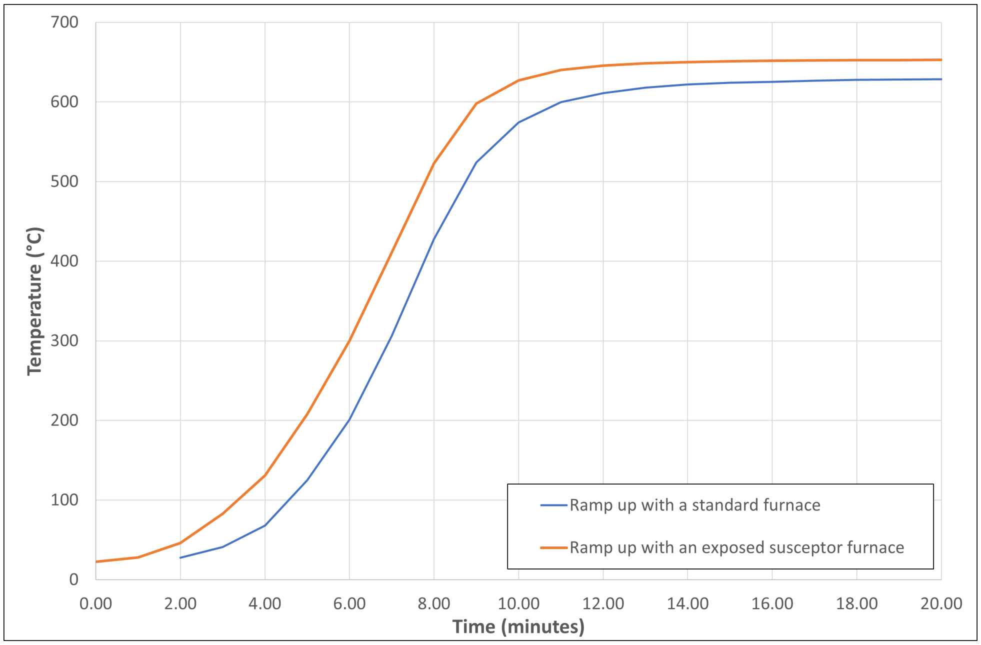

Figure 75: Calibration preform thermocouple response as a function of time in thr hottest spot for the standard and exposed susceptor furnace design, all other parameters kept constant (target susceptor temperature 800 °C, preform chamber purge 0.5 L/min, susceptor purge 0.5 L/min) during a ramp-up from room temperature.

Unsurprisingly, an exposed susceptor design results in a more rapid response of the thermocouple inserted in the calibration preform. The final temperature is also higher by 25 °C for the exposed susceptor design. Such responsiveness is more desirable, but it comes at the cost of a vulnerable susceptor. This design may also allow for cross-contamination between the susceptor and the softened glass. In addition, when using the same susceptor for many experiments, it will slowly become oxidized, as there will always be a small amount of oxygen coming into contact with it while it is still hot. When it becomes oxidized, it starts to lose material, and this process slowly increases its inner diameter. This results in variation in the heat transfer from the susceptor to the preform from one experiment to the next. Also, it may accidentally happen that the softening preform comes into contact with the susceptor, contaminating and damaging it, which then requires replacing for the next experiment. Therefore, using such an exposed susceptor design was not implemented, although it does represent another viable modification to the furnace assembly should it be necessary.

Figure 76 shows a calibration experiment made using a non-standard calibration preform with two 20 mm deep thermocouple holes rather than one. These holes were drilled in the silica rod lengthwise using an ultrasonic drill equipped with diamond tips. They were made using a diamond tip of the same dimensions as the thermocouples to ensure the tightest fit possible. And indeed, the vibrations of the drill produced a bore hole only a few tens of microns larger than what was strictly necessary. One of the holes was drilled in the centre, and the other 0.1 mm underneath the preform surface, as shown in Figure 77.

From the following calibration measurement, it can be observed that the core temperature lags behind the surface temperature by 5 to 10 °C during the ramp up. Once stable, the core temperature remains behind by 3 to 5 °C for over 10 minutes. This observation is consistent with the time required for a 10 mm thick preform to start necking during a fibre drawing experiment, which was noted to be at least 10 minutes.

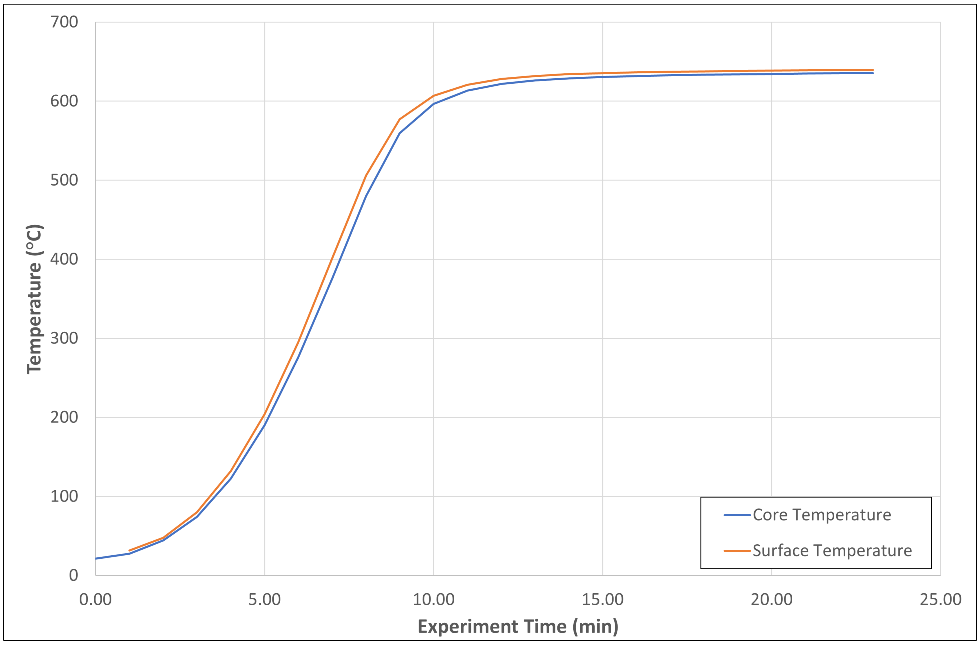

Figure 76: Temperature response of the surface and core thermocouples in the hottest spot as a function of time during a furnace ramp-up to 800 °C (0.5L /min preform and susceptor purge).

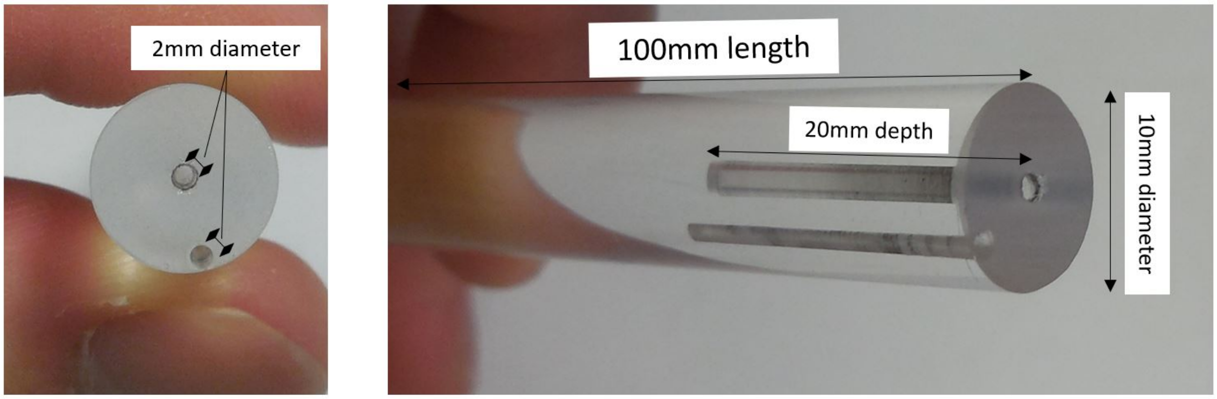

Figure 77: Dual-thermocouple calibration preform used to assess the radial temperature gradient inside a preform during fibre drawing.

In order to offset this temperature difference, the amount of purge used in the preform chamber was increased in an attempt to cool the surface of the calibration preform relative to its core. The result of this experiment is shown in Figure 78.

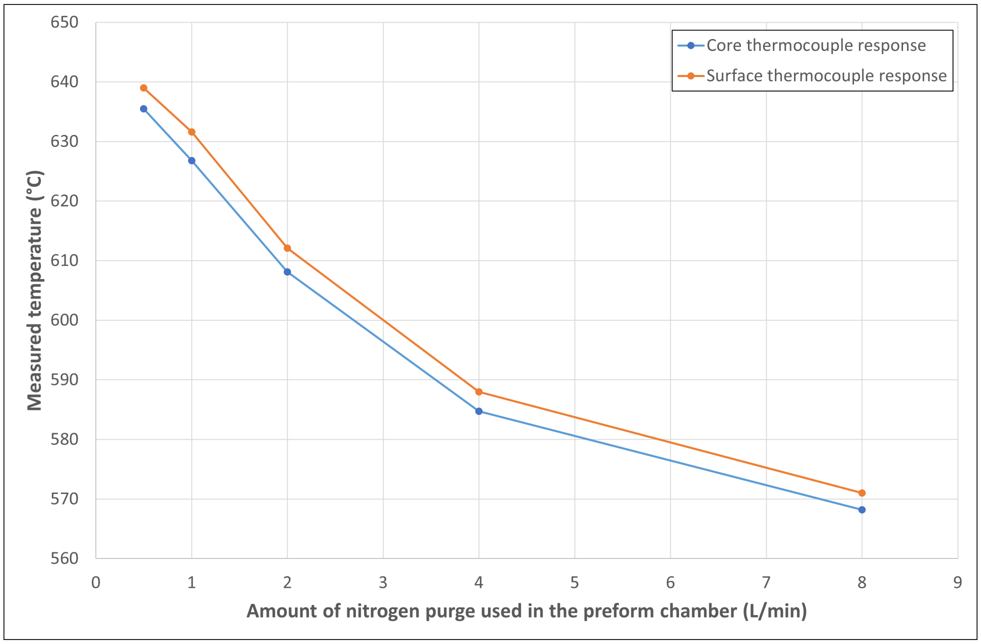

Figure 78: Temperature response of the surface and core thermocouples in dual-thermocouple calibration preform as a function of the amount of top cap purge at 800 °C (0.5L /min preform and susceptor purge).

It seems that the temperature of the core closely follows that of the surface, and that the offset isn't reduced by an increased purge. This can be explained by the temperature of the core not resulting primarily from radiative heating, but by conduction from the surface. It is likely that the material the calibration preform is made from, silica, plays an important role in this behaviour. In a GLS preform, it may be the case that the core temperature follows more closely that of the surface, as most GLS compositions transmit wavelengths up to 12 μm. To verify that prediction, it would be necessary to make a GLS preform with similar core and surface thermocouple holes. The measurement would have to be made at a significantly lower temperature of 500 °C but would still provide useful information.

From these calibration experiments, the design of the furnace and susceptor were both progressively adjusted. A fused furnace using a 50 mm OD, 60 mm long susceptor was selected. The fused furnace was shown to minimize heat leaks. The 60 mm long susceptor proved to be an acceptable compromise between the long susceptor standard set by past work [10] and the issues caused by the excessively long 100 mm susceptor. And a 50 mm OD (40 mm ID) susceptor is close enough to the preform to enable rapid heat transfer without excessively risking the preform touching the inner walls of the furnace. The amount of purge was also greatly reduced to become suitable for a fused furnace, with 0.5 L/min nitrogen for the susceptor purge and 0.5 to 2 L/min for the preform purge. These changes eventually lead to the experimental results shown in the following section.

8.3 Rod-preform drawing results

8.3.1 Crystallization work-around

Via the application of thorough polishing techniques, the re-designing of the furnace and an improved understanding of the temperature profile during fibre drawing, the production of crystal-free GLSSe fibre was achieved. In order to reach this point, however, it was necessary to modify the fibre drawing method which originally simply consisted of first heating the preform until it necks, then feeding it through and attaching the formed fibre to the drum. The lack of suitability of this approach was demonstrated by observing that the lower half of the necked preform typically had visible surface crystallization, as shown in Figure 66. These crystals would usually become fewer and fewer as the fibre drawing experiment went on, due to the combination of the glass stretching into thinner fibre and the increase of both the drum speed and the feeding rate.

The justification for a longer susceptor introduced by Brady et al [10] was reconsidered as a possible solution to address this issue. Indeed, the longer susceptor resulted in pre-heating the glass before it gets to the fibre drawing temperature, which enabled to draw at a lower temperature and at a faster pace. However, this pre-heating achieved via a longer susceptor would not have any impact on the region of the preform in which necking begins, as this glass would directly be brought up to the drawing temperature as before, and this is the region in which crystallization would start. As such, a pre-heating step was introduced to achieve a comparable effect on the initial necking region.

So as to quicken the necking process even further and prevent crystallization due to excessive time of exposure rather than excessive temperature, the temperature at which the susceptor would be initially held was chosen to be 20 °C higher than the fibre drawing temperature established during previous experiments. This change resulted in the time required for necking to start being nearly halved, from over 10 minutes down to around 5 minutes. As soon as the necked preform could be pulled down by hand, the temperature would be reduced down to the original fibre drawing temperature, and the drawing process could thus be initiated as quickly as possible. This process is documented in Figure 79.

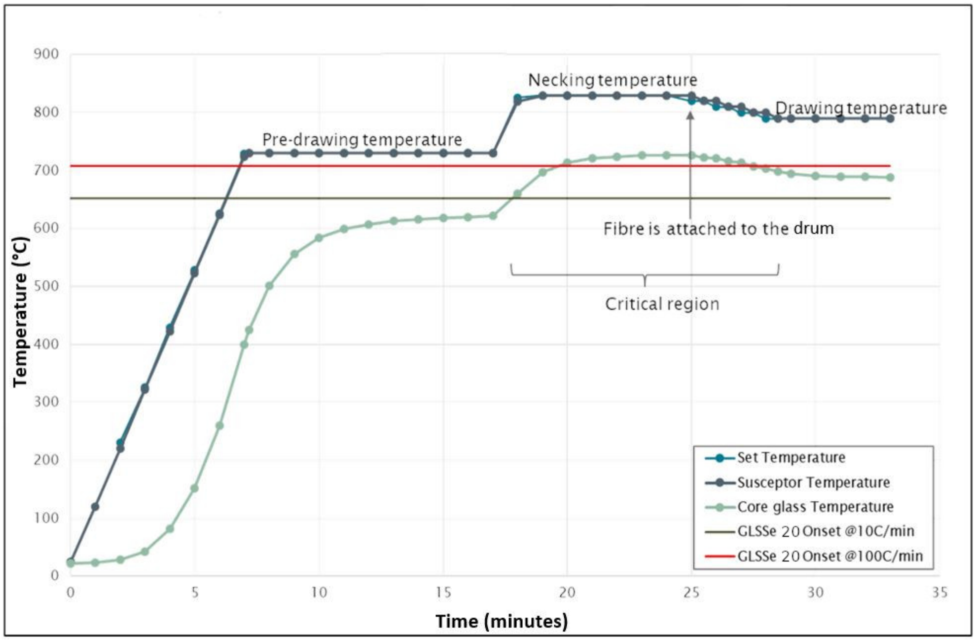

Figure 79: Three-stages fibre drawing method used to minimize crystallization in GLSSe 20% rods.

As can be observed, the calculated core glass temperature in the preform is maintained below the crystallization onset temperature measured at both 10 °C/min and 100 °C/min during the pre-heating step, lasting for 10 minutes. The susceptor temperature is then rapidly brought to the high necking temperature, where the crystallization process is expected to be well on its way. As soon as necking takes place, the temperature is brought back down to the fibre drawing temperature, the fibre is attached to the drum and fibre drawing begins at an accelerated pace.

This method was met with initial success with a cast GLSSe20% rod in the fibre drawing experiment NT834. The outcome of this novel process is shown in Figure 80, where tens of metres of crystal-free fibre could be produced. Once polishing techniques were perfected, however, and assuming the preforms didn't have previous thermal history that would result in nucleation, the precautions taken to avoid crystallization used here were found to be unnecessary in most cases. Still, this method does provide increased chances of success, and may become useful when attempting to make optical fibre out of preforms that have significant enough thermal history for nucleation or imperfections to be of concern.

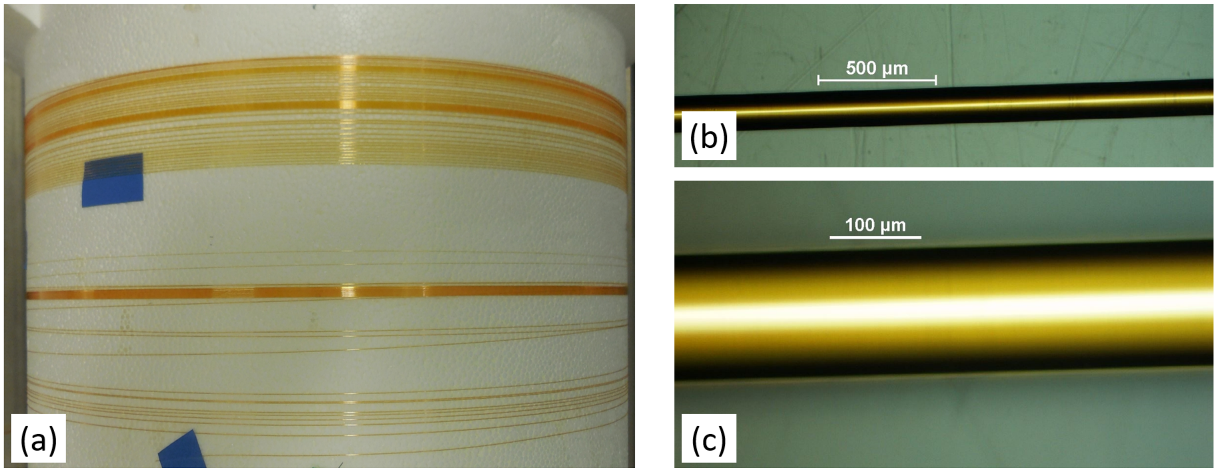

Figure 80: Unstructured GLSSe20% rod-drawn from an imperfectly polished cast and yet presenting no visible traces of crystallization (NT834).

8.3.2 GLS core fibre

The experiments carried out by P. Bastock [108] to produce Schott Duran$^{\text{TM}}$ Borosilicate glass/metal core fibre were successfully reproduced with copper and silver. It was observed that the process fully melts the strands of metal inserted in the hollow borosilicate tube. A similar experiment was carried out in which the metal wires were replaced by previously drawn GLSSe20% canes. These canes had visible defects and crystals, and it was hoped that these defects would be removed due to their melting at 1200 °C during the drawing process, recorded in experiment NT794. The outcome of this experiment is shown in Figure 81. This test demonstrates the feasibility of drawing GLS glasses in borosilicate in spite of the large difference in their respective drawing temperatures. However, it appears that pristine GLS cane should be used, as crystals do not have enough time to remelt, and the drawing speeds should be kept low in order to avoid breakage of the core.

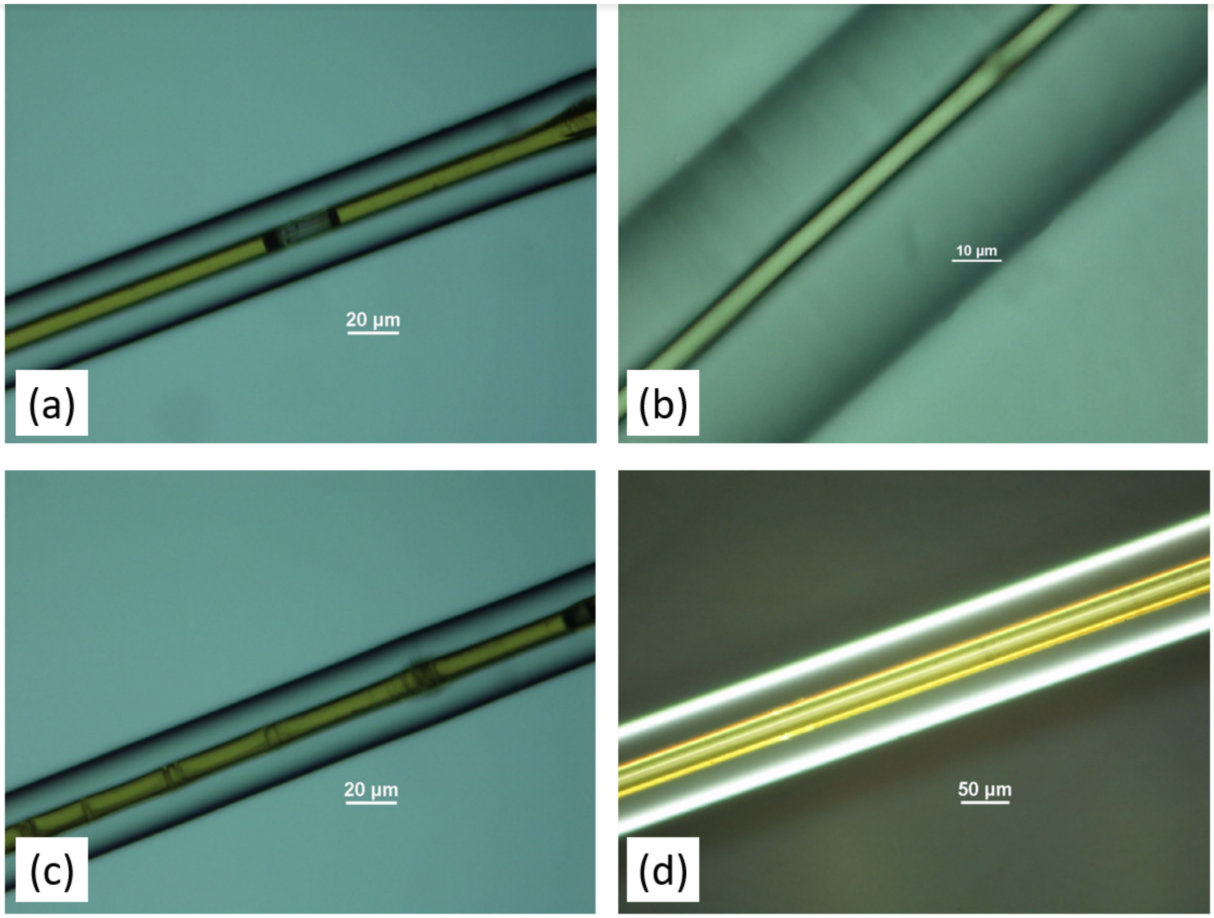

Figure 81: GLSSe20% cane redrawn in borosilicate cladding. (a) Breaks caused by excessive drawing speeds, (b) Ultrathin crystal-free core (5μm), (c) Crystals failing to remelt due to the fast drawing speed, (d) Crystal and defect-free section (NT794).

8.3.3 Turned rod drawing

Using the fibre drawing method described in Section 9.3.1, the unstructured turned rod produced in Section 6.1 was made into the fibre shown in Figure 82. As seen in this

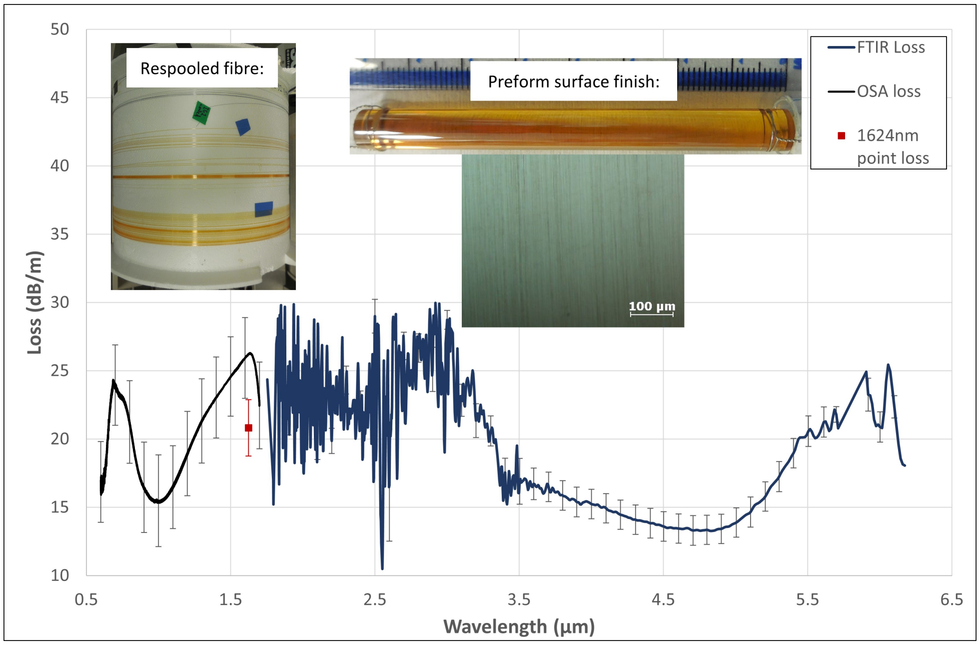

Figure 82: Preform, fibre and loss measurement produced from an unstructured GLS 65:35 rod fabricated by combining the rod turning and the hand polishing method devised in-house. Fibre diameter 200 μm, length used 1.5 m.

figure, the loss is above 10 dB/m from 0.5 to 6.2μm. However, combining rod turning, rod polishing methods with the enhancements of the rod drawing method presented in Section 10.2 have enabled to produce oxygen-free and crystal-free GLS fibre. The transmission range has been extended past 5 μm, reaching 6.2 μm, and this fibre also transmits light where the 3 μm OH peak strongly absorbs in GLSO fibre, as shown in contrast with Figure 83. A loss of less than 10 dB/m was achieved with a polished GLS rod manufactured in the same conditions in NT841. However, the measurable transmission window stops at 5.2 μm, where the signal to noise ratio becomes excessive. This earlier transmission cutoff is a consequence of this fibre being considerably thinner than the one measured in Figure 82 (100 μm as opposed to 200 μm). It results in a smaller amount of light being successfully coupled into it, which reduces the maximum measurable loss to only 10 dB/m as opposed to 30 dB/m. It does, however, show promise of what could be achieved in terms of loss once core-clad preforms become more available. The limiting factor for these fibres is currently the exposure of the core. In a theoretical core-clad fibre made of oxygen-free GLS, the loss is expected to be below 1dB/m, according to the FTIR thick/thin measurement of Figure 11.

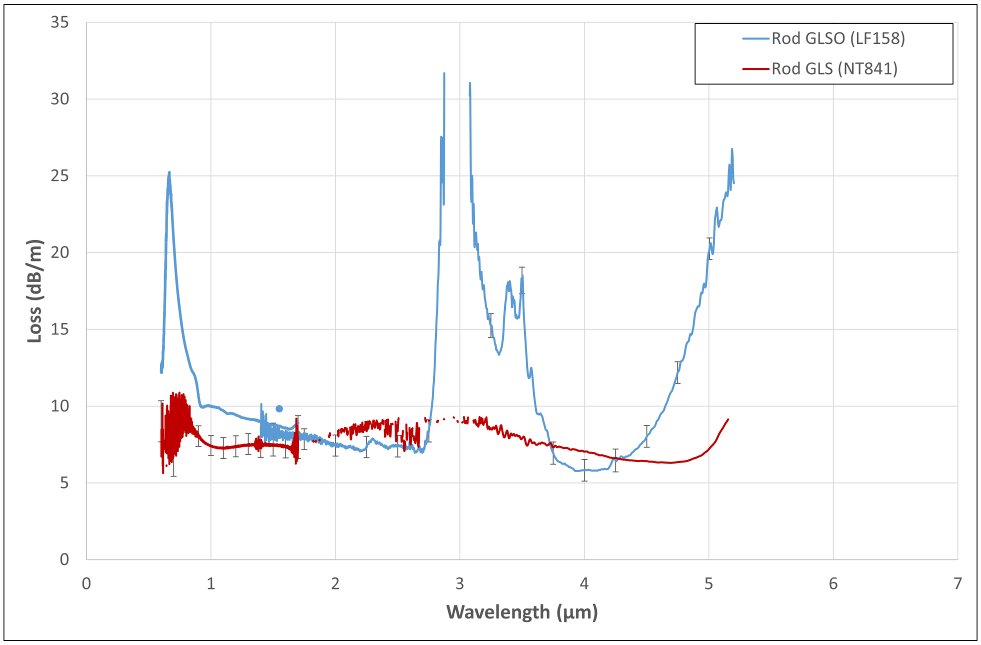

Figure 83: Transmission difference between unstructured rod-drawn GLSO and GLS fibre. LF158 and NT841 both produced 100 μm fibre, 1.5m of each was used for the loss measurement.

8.3.4 Cast drawing

The most successful core-clad casts, with GLSSe20% cladding and GLSO core were drawn into fibre at 820 °C in the fibre drawing experiment NT890. Images of the resulting fibre are shown in Figure 84. As can be observed, the fibre fabricated from these core-clad casts show no signs of crystallization. This is a significant departure from the considerable issue that it is for core-clad preforms manufactured by extrusion [119]. The reason for the absence of crystals can be attributed to the minimal thermal treatment of the cladding glass, as it is directly poured from a melt. On the other hand, the core glass being a cane of GLSO did not benefit from a direct fabrication process. However, GLSO has been demonstrated to be far less prone to crystallization than GLSSe or GLS. As such, it is unsurprising that it behaved in such a way to allow for the production of fibre without crystallizing. Unfortunately, its thermal properties are clearly too different from GLSSe20% to allow it to be drawn together to produce a good interface, as while GLSSe20% softens and stretches, the GLSO core remains too brittle and breaks into pieces, resulting in most of the produced fibre being hollow, as shown in Figure 84 (c).

Significantly better success was achieved with the hollow GLSO casts. They were suc-

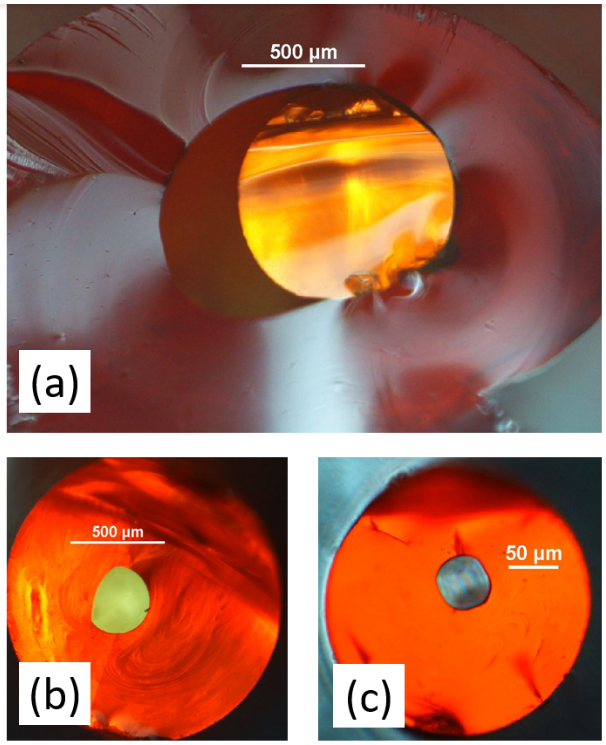

Figure 84: Fibre produced from a GLSO cane embedded in a GLSSe20% cast. (a), deformation due to the softening of the cladding but not of the core. (b), off-centre and misshapen GLSO core. (c), Hollow core fibre resulting of the cladding softening and stretching, while the core breaks into small fragments (NT890).

cessfully drawn into fibre in experiment NT896, the outcome of which is shown in Figure 85. A loss measurement was attempted using the FTIR with no success. For this measurement, the outside of the fibre was coated with Alfa Aesar alcohol based graphite adhesive product number 41213 [120], to remove cladding modes. As soon as it was applied to the coupled fibre, the amount of light detected by the FTIR dropped to zero, demonstrating that the light transported was carried entirely by the cladding. This phenomenon can easily be explained by the higher refractive index of the cladding, combined with the fibre being significantly bent while inserted in the Fibermate^{TM} adapter. Unfortunately, the fibre having to be bent is inherent to the design of the Fibermate^{TM} adapter, as its input and output ports are parallel to one another, as shown in Figure 37. For the GLSO hollow fibre, this resulted in light being guided by the cladding, and therefore being completely absorbed of the light by the graphite adhesive coating upon its application. A loss measurement was made in the visible using the OSA, while maintaining the fibre as straight as possible without allowing for any slack. It was noted that even though applying graphite

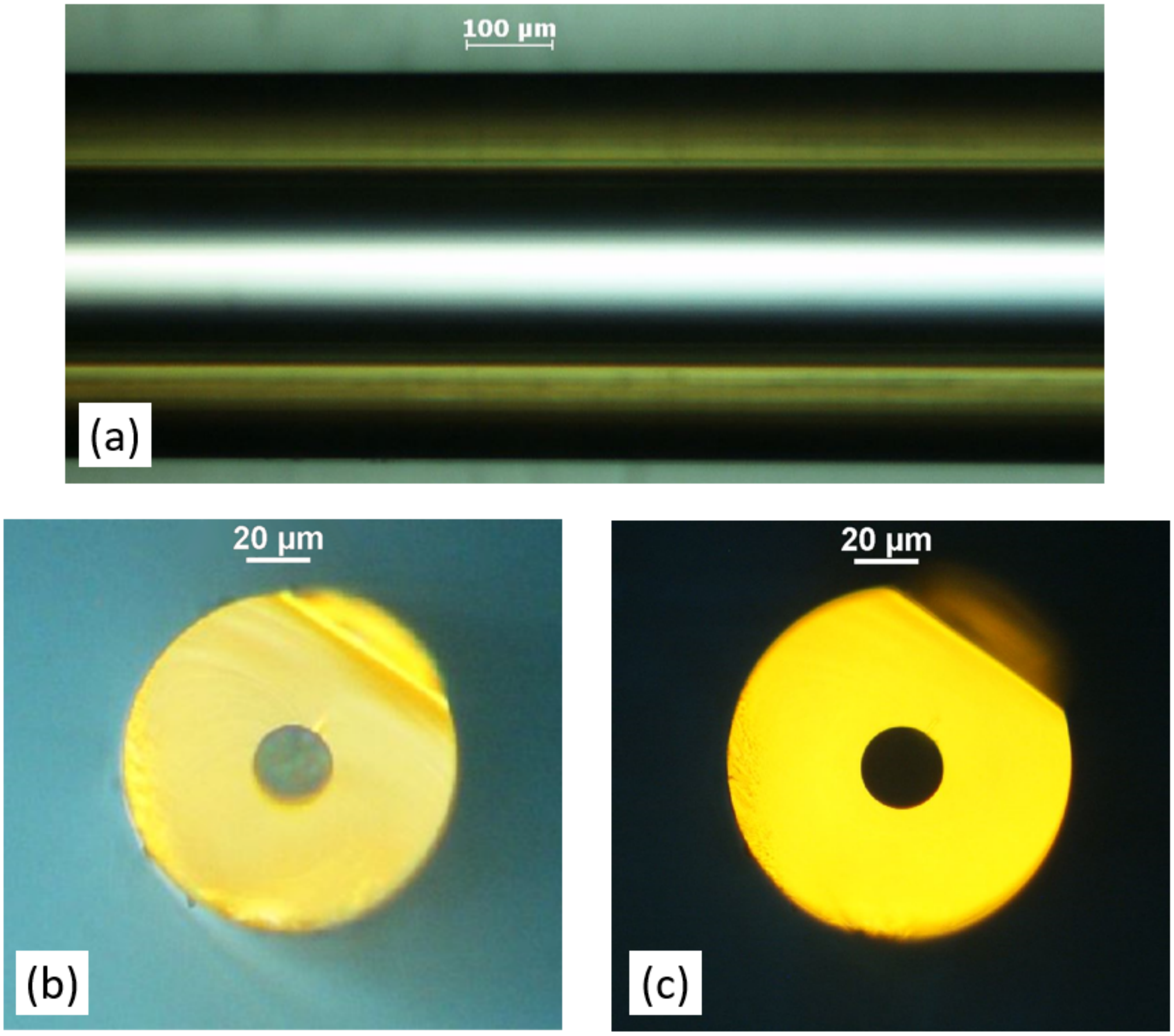

Figure 85: Fibre produced from a hollow GLSO cast polished inside and out down to 1 μm grit. (a), side view of the thick sections of fibre showing the absence of crystals or polishing imperfections. (b), face end of the fibre showing the size of the hole to be 20 μm for 100 μm diameter. (c), same end face with light coupled from the other end, to demonstrate both the absence of crystals anywhere in the glass as well as the smoothness and concentricity of the core.

adhesive reduced the intensity of the light transmitted, a sufficient amount remained to allow for a loss measurement as long as the fibre was kept straight. This measurement is shown in Figure 86. It shows an exponential drop of the loss from the visible end of the spectrum towards 5 dB/m from 1 μm onwards. However, such a measurement could not be repeated in the infra-red using any of the loss setups available due to the impossibility of maintaining the fibre perfectly straight throughout the experiment, as the infra-red detector setup does not constitute a single, easily translatable block, contrary to the OSA.

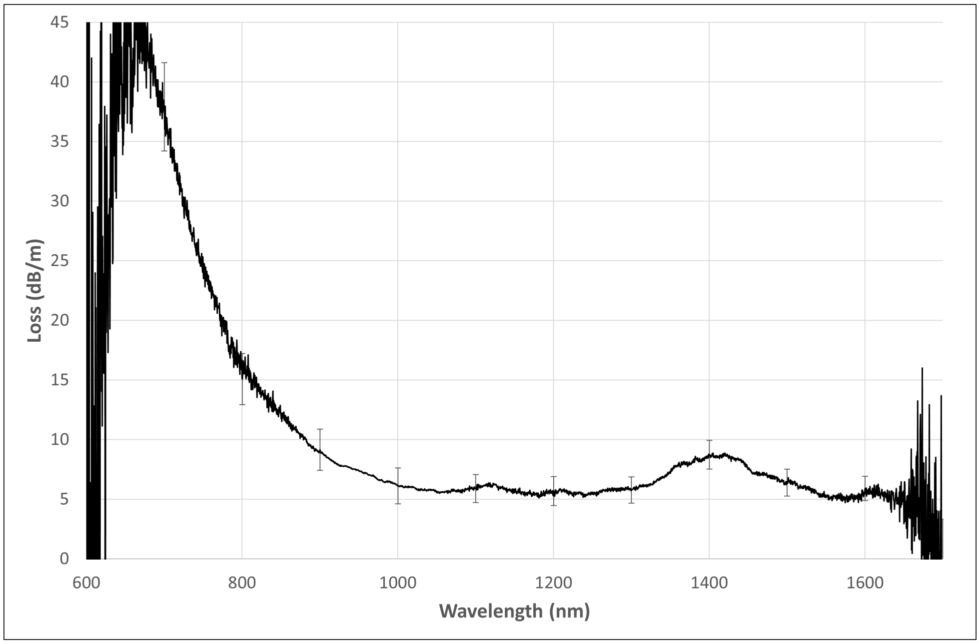

Figure 86: OSA-based visible fibre loss measurement performed on the straightened hollow-core GLSO from NT896. The fibre was 140 μm in diameter and 1.5m was used for the loss measurement.

8.4 Crucible drawing

Initial tests for the development of crucible drawing were carried out using graphite crucibles at the bottom of which a hole had been drilled. Cullet glass was placed inside them, and crucibles were held in the hot zone by a custom made silica crucible holder. The furnace structure remained identical to the one used for rod drawing, except for an increase to the top cap opening size and to the susceptor, to accommodate for the larger diameter of the graphite crucible and crucible holder. As the glass melts, it exits the crucible through its hole, forming a fibre.

This procedure was successfully tested using borosilicate glass, then IG5, and finally it was experimented with using GLS, GLSO and GLSSe. A fibre loss measurement was performed on the unstructured IG5 fibre made using this technique, and it was compared to that of rod drawn IG5. This measurement is shown in Figure 87. Several absorption bands can be identified. Se-H/SeH_2 at 4.5 μm, Ge-H at 5 μm, As_4O_6, GeO_2 and SeO_2 at 8 μm, and As_4O_6 at 9.2 μm [77, 121, 122, 41, 65]. This Figure demonstrates the improved quality of crucible drawn fibre compared to that of rod drawn fibre. The amount of noise in the crucible drawn fibre is indeed lower near the 1.5 μm cutoff, the overall loss is reduced in the 1.5 μm to 4.5 μm region and, to a lesser extent, in the 5.5 μm to 7.5 μm region. This

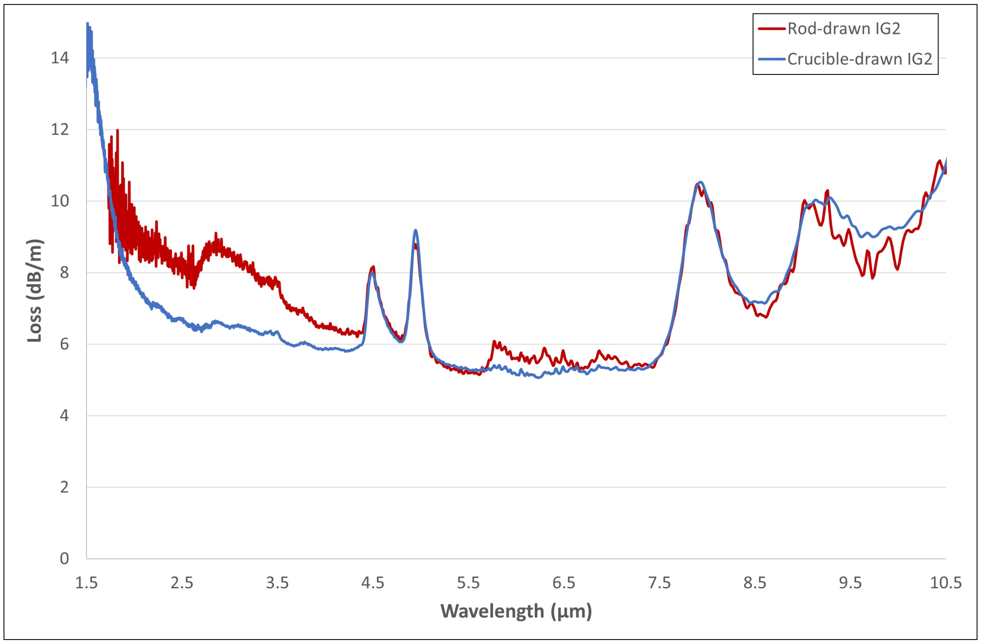

Figure 87: FTIR continuous loss measurement for crucible drawn and rod drawn unstructured IG5 fibre.

observation motivates the development of crucible drawing capabilities for GLS glasses.

For GLS and its derivatives, it soon became apparent that the standard procedure of crucible drawing by directly heating solid glass was not suitable, as it would crystallize rapidly, even before it had time to soften and make its way through the crucible hole. As such, a different approach was implemented, where the hole was initially blocked using a tapered graphite plug and the glass fully molten in the crucible for 10 minutes. After melting the glass in this fashion, temperature was rapidly reduced, a short amount of time was given for the contents of the crucible to reach a thermal equilibrium, and the plug was finally removed. Simultaneously, pressure was applied to the crucible holder to help push the soft glass out of the crucible. This GLS crucible drawing process is illustrated in Figure 88.

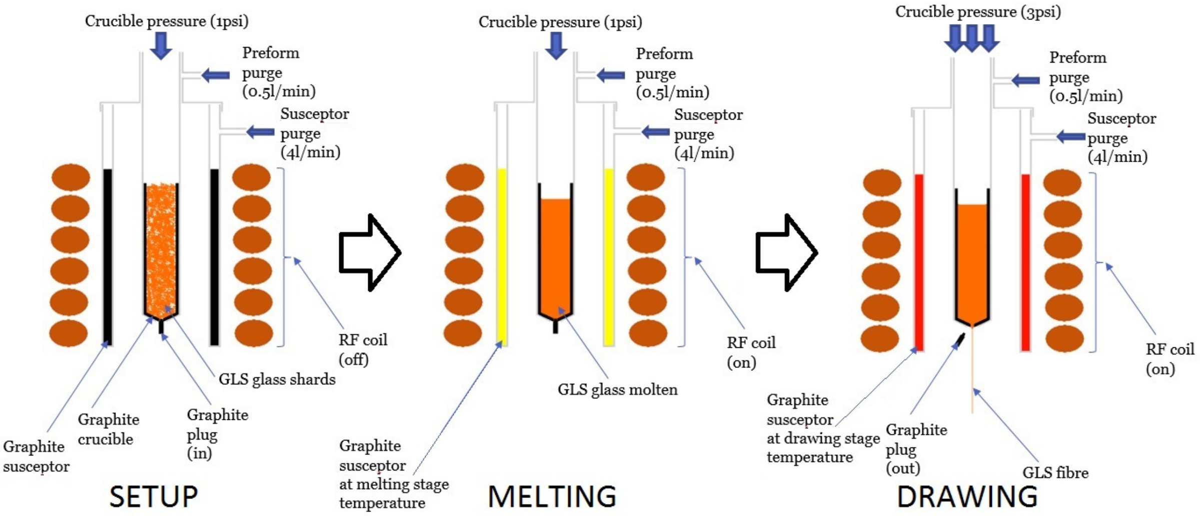

Figure 88: Cutout representation of the three step crucible drawing process developed for GLS compositions.

During the first experiments, three stages of fibre production could be observed. First, crystal-free fibre would fall from the crucible uncontrollably, without any of it being slow enough to be taped to the drum. Then, the fibre would slow down to the point where several metres of it could be spooled onto the drum with relative ease. Rapidly however, crystals would start forming and increase in number until the fibre eventually snapped. The reason for such behaviour was believed to be the graphite crucible being too long compared to the size of hot zone. This resulted in a lengthwise temperature gradient being maintained in the crucible. As such, the first lengths of fibre are above the crystallization temperature, yet not viscous enough to be caught and spooled in a controlled fashion. The short crystal-free lengths that follow correspond to the small portion of the melt that is at the desired drawing temperature, where the glass is both viscous enough to be drawn and yet is still crystal-free. And finally, the increasingly crystallized fibre corresponds to the glass being maintained too close to the crystallization temperature for too long, which prevents any further production of useful fibre. This understanding provided the motivation to perform a sequence of experiments aiming to optimize the drawing temperature and the time given for the melt to thermally equilibrate, in order to maximize the amount of crystal-free fibre that could be collected onto the drum.

Firstly, the size of the hot zone was extended to match that of the graphite crucible used, so as to reduce the thermal gradient as much as possible. This goal was achieved by stacking two identical 60 mm-OD/50 mm-long susceptors in the furnace. This enabled to obtain a more even glass temperature in the crucible, as illustrated by the observation that the crystallized fibre became increasingly scarce, as fibre drawing experiments became more consistent throughout. This change was maintained for all following experiments, producing the final furnace design shown in Figure 89.

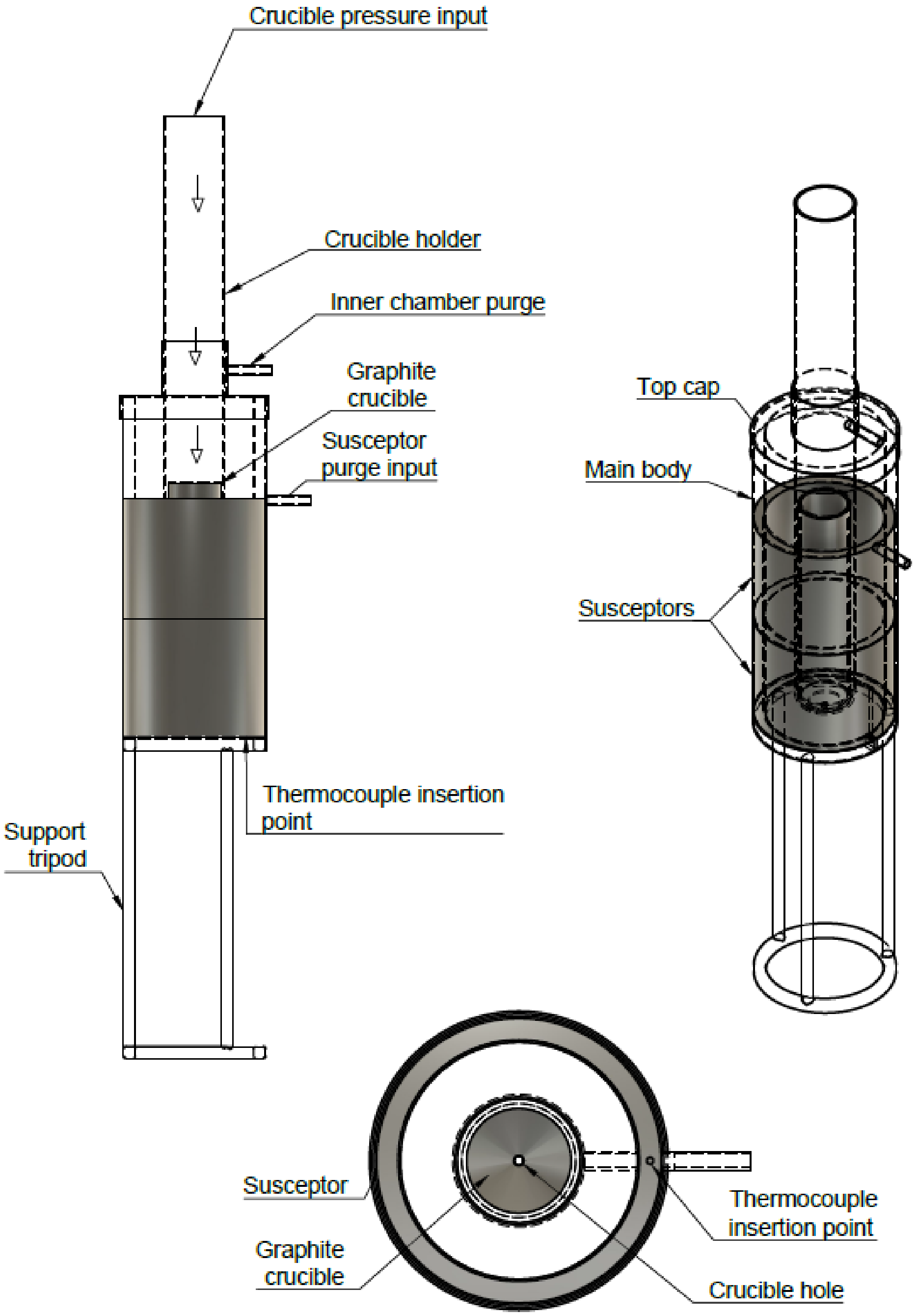

Figure 89: Schematic representation of the crucible drawing furnace design and purge insertion points loaded with a graphite crucible without nozzle.

8.5 Crucible drawing enhancements

8.5.1 Temperature-time optimization

To obtain the ideal drawing parameters for which the entirety of the fibre produced is both controllable and crystal-free, the system was optimized for temperature and time given for the melt to settle and even out in a full factorial set of experiments, to suitably monitor the extent of the crystallisation process. The results of this optimization are shown in Figure 90.

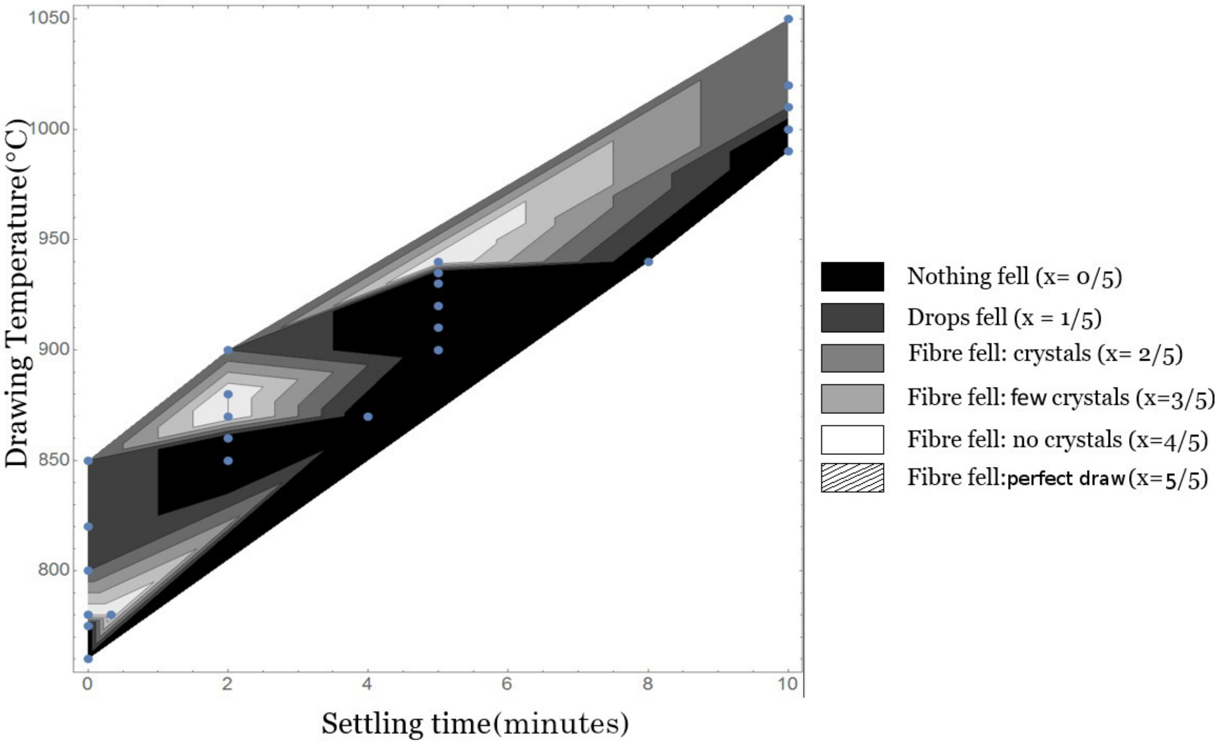

Figure 90: Crucible drawing settling time versus drawing temperature optimization process for GLS 65:35.

In Figure 90, the drawing temperature was varied in 10 °C steps and the time given for the melt to settle at that temperature was varied in 1 minute steps. A simple contour plot was produced in an attempt to locate the ideal fibre drawing parameters. These experiments resulted in the production of large amounts of unstructured crystal-free fibre, shown in Figure 91, however they failed to achieve the desired ideal where viscosity is low enough for fibre drawing to be fully controlled, and yet the fibre is still crystal-free. This experiment serves to demonstrate the necessity of designing a different process, where the glass is maintained at the fibre drawing temperature for as little time as possible, as the formation of crystals seems to be inevitable when the glass is kept viscous enough to be drawn for more than a few minutes.

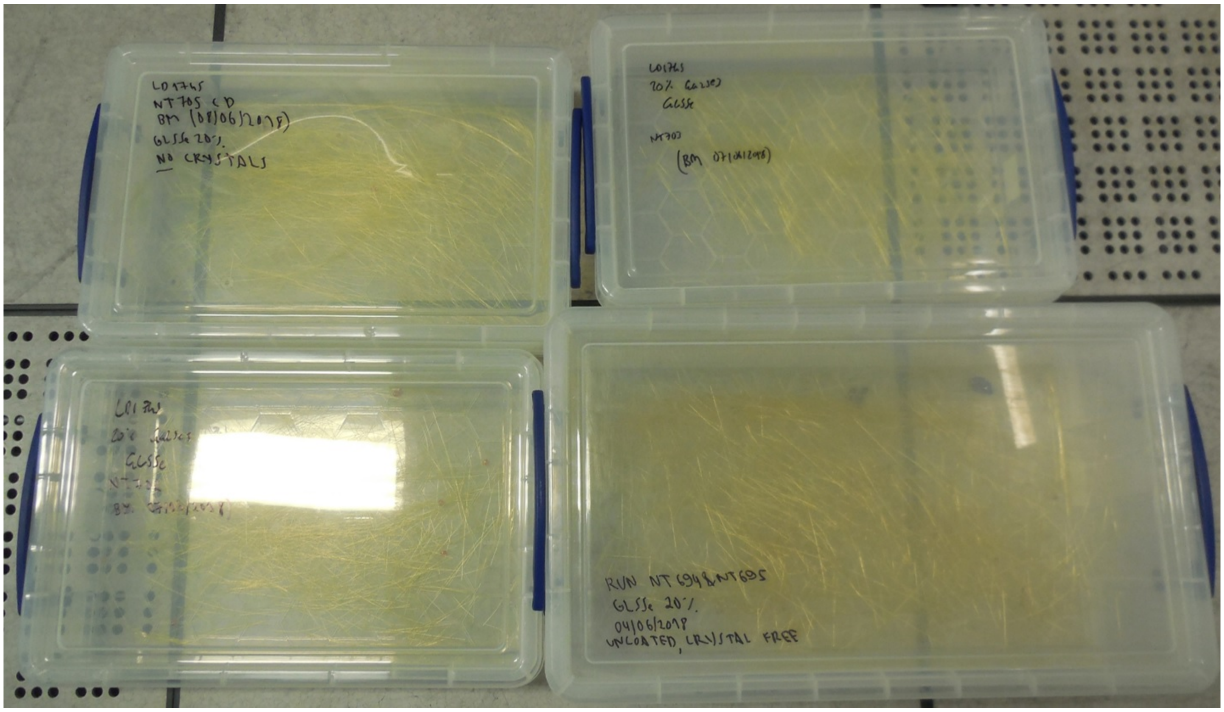

Figure 91: Early production of crystal-free, uncontrolled GLSSe20% made by crucible drawing, each set of fibres represents a difference crucible temperature.

Attempts were still made to catch this crystal-free fast-falling fibre so as to become able to respool and potentially use it. Traditionally, the fibre is simply taped onto the drum, but in this case, the drum had to be sped up above 100 m/min, which makes taping the fibre directly onto it practically impossible. Several alternative methods were tested, such as applying double sided tape onto the drum, replacing the automated drum with a hand operated bar drum, and using a slotted bobbin with thick aluminium foil wrapped around it. Some examples and their outcome are shown in Figure 92. These attempts produced unreliable results, which lead to the focus being maintained onto improving the fibre drawing process qualitatively, rather than trying to find a work-around.

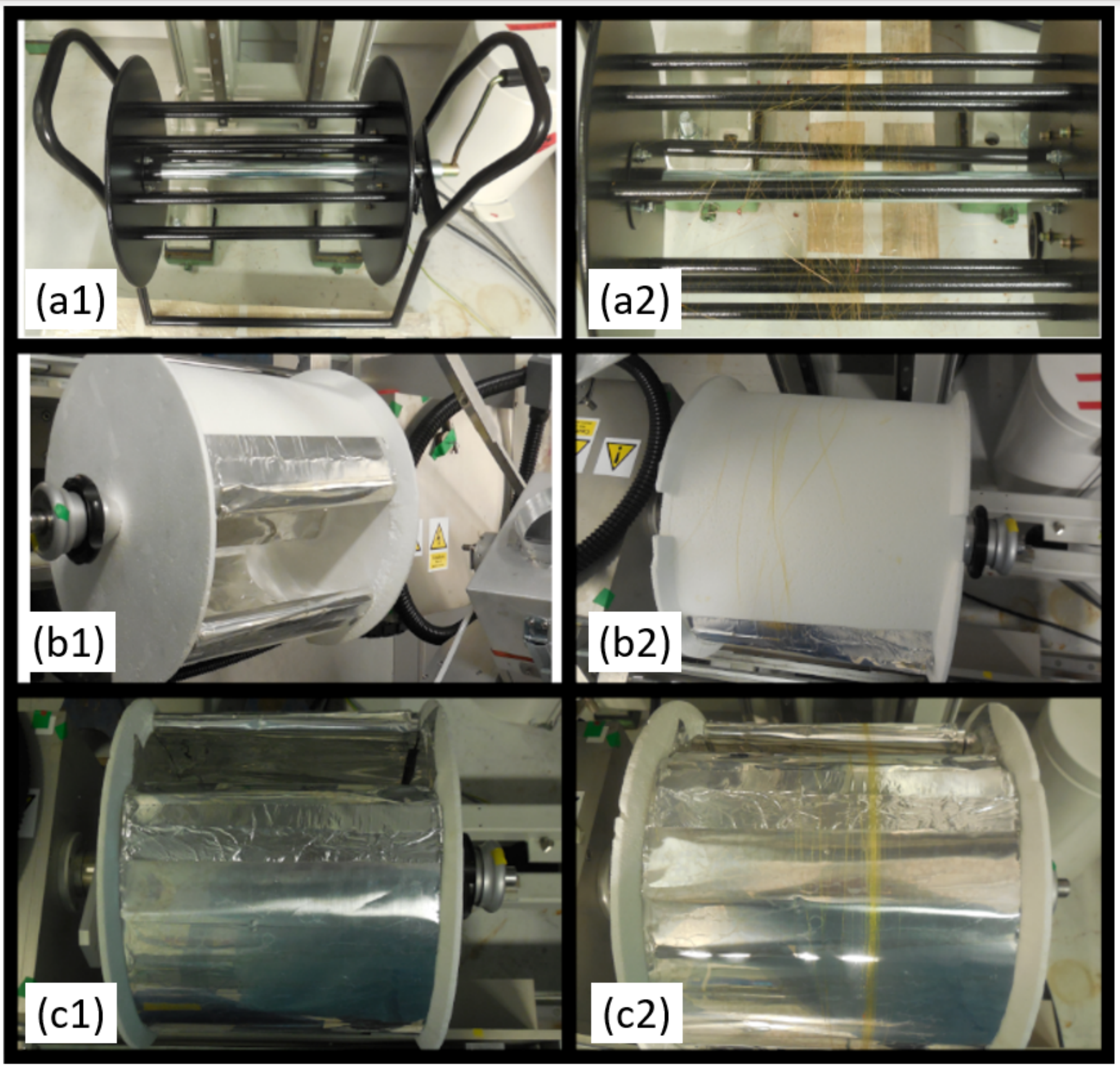

Figure 92: Alternative drum designs tested in attempts to catch and preserve fast-falling GLS fibre. (a), bar drum (lightweight, easy to wind, but has a tendency to break fibre upon winding). (b), slitted bobbin (no need to respool the fibre, but hot fibre becomes fused on its surface). (c), aluminium slitted bobbin (may be used with hot fibre, but requires respooling by hand).

8.5.2 Crucible hole size

Another key parameter for crucible drawing is the size of the hole used, 3 mm, 2 mm and 1 mm holes were used alternatively in order to assess the ideal size. Corresponding plugs were manufactured in house on a lathe and were slightly tapered to produce a unique match of each crucible hole. The amount of care placed on their quality prevents the plugs from falling out, getting stuck or leaking during the draw, and the slight elasticity of graphite ensures the plugs are firmly inserted, yet can be removed with relative ease. The seal provided by the graphite plugs was systematically tested for strength and tightness by applying and monitoring pressure to the plugged crucible before starting the experiment. It was observed that the smaller the size of the hole, the higher the temperature needed to be for the glass to be able to be pushed out of the crucible. A small hole was therefore expected to yield the most crystal-free results. However, this comes at the cost of making the draw more difficult to control, as hotter fibre falls faster. In addition, the likelihood of the graphite plug breaking inside the hole is also increased, as it is thinner and more fragile. The most reliable compromise was found with the 2 mm hole and plug.

8.5.3 Pressure application

Pressure was initially applied to the crucible holder, rather than the crucible itself. This significantly cooled down the tip of the crucible during the draw, which offers the interesting advantage of rapidly cooling the exiting fibre in addition to pressurizing the crucible. Although this secondary effect potentially makes the falling fibre slower and more easily manageable, it ties together two parameters that should be controlled independently, namely pressurizing the crucible and altering the temperature of the tip of the crucible. Attempts were made to resolve that problem by sealing the space between the graphite crucible and the crucible holder, with relative success. A short purging coil similar to the one shown in Figure 74, but only 40 mm in diameter was made to replace and independently control the cooling effect around the crucible hole. These alterations were successful in separating the two parameters, but came at the expense of making both the crucible holder and the graphite crucibles single use, as they were irreversibly bonded together by the ceramic and contaminated with GLS. Another piece of equipment was designed, in the form of a long silica tube with a tapered and sand-blasted end, shown in Figure 93. This piece of glassware enabled pressure to be directly applied to the graphite crucibles, as it could be pressed down into the top opening of the crucibles, taking advantage of the elasticity of graphite to produce a temporary seal. It was an imperfect solution, as it would often pop out of the crucible if the pressure exceeded 2 PSI.

Finally, experiments were conducted in which some of the molten glass accidentally came into contact with silica. It was observed that silica would not shatter while GLS

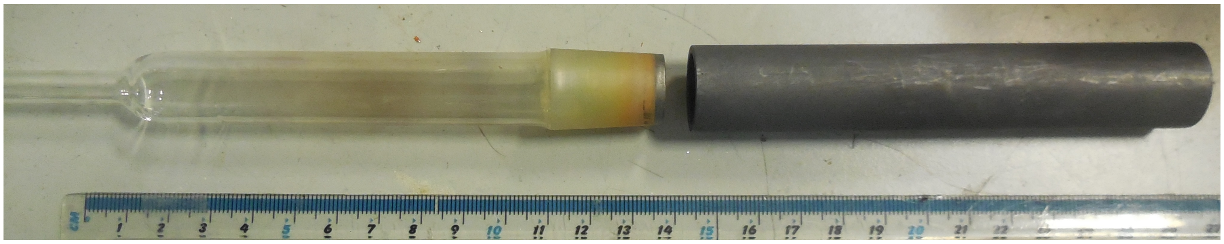

Figure 93: Custom made silica tube used to pressurize graphite crucibles for fibre drawing experiments.

remains molten. Silica would still not break until the glass reached around 200 °C. As such, some tests were carried out directly in silica crucibles made out of re purposed crucible holders. Due to the complete elimination of leaks, the flow meter initially used to apply pressure was replaced with a Horiba MFC SEC-Z500X[123] that can be controlled digitally.

8.5.4 Crucible drawing in silica

The first tests in silica were performed using a graphite crucible in which the melt would take place, and the crucible hole would allow the molten glass to drip down into a secondary silica crucible, so as to minimize the amount of molten GLS directly in contact with silica at any time, and ensure the experiment could be carried out as safely as possible. This particular design is shown in Figure 97 (b). While this experiment did not manage to produce fibre, the amount of molten GLS in the silica crucible could be safely gradually increased and exited through the bottom hole without cracks appearing in the crucible. This observation motivated the change to design 97 (c), in which the entirety of the experiment is carried out directly in silica. This change conveniently solves the issue of pressure application, as it offers no path available for leaks to the gas purge used to pressurize the crucible. It also allows for the direct observation of the melt. In spite of the new advantages, these experiments still failed to produce fibre, but confirmed that crucible drawing experiments in silica are perfectly safe, as long as a significant amount of GLS is not allowed to fully cool down and solidify while in the crucible. An example of GLS fully solidifying in silica is shown in Figure 94.

As can be observed, GLS bonds to the surface of the silica crucible, which results in both of them shattering if the amount of GLS is more than a thin layer. They may remain loosely bonded together even though there are cracks, but any small shock or vibrations

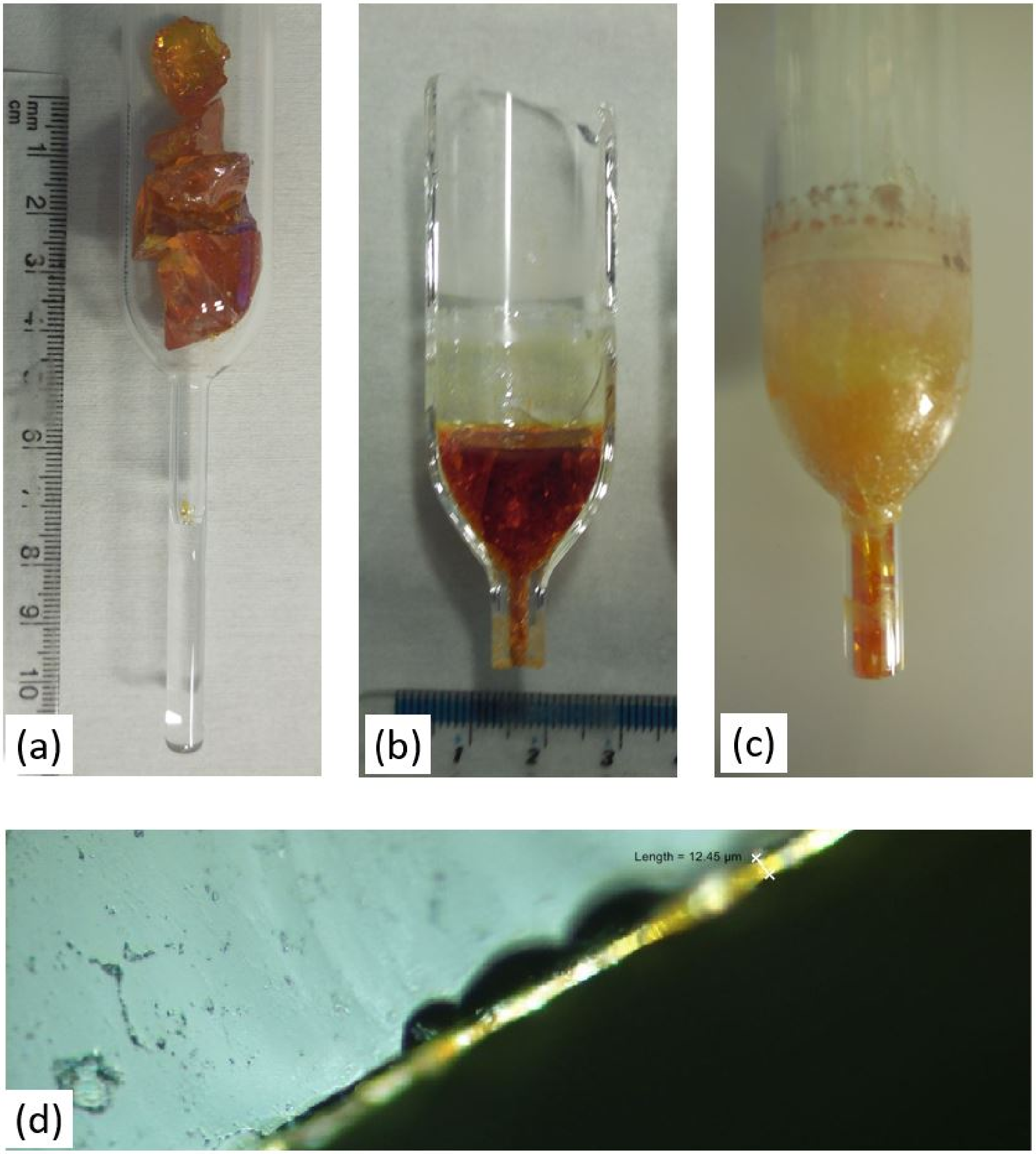

Figure 94: Effect of GLS interacting with silica during crucible drawing. (a), initial crucible filled with cullet glass. (b), GLS melted and quenched inside the silica crucible due to plug failure (shattered). (c), successfully emptied silica crucible (remains in one piece). (d), microscope image of the GLS layer leftover on the inner surface of the crucible (10 μm thick).

break them apart. If, however, the amount of GLS is sufficiently small, then it alone will crack, leaving the silica crucible intact, but contaminated. The early crucible drawings attempts in silica were performed using long silica plugs with a sandblasted and sharpened tip. These plugs were held up inside the hole using a strip of steel springing them up from their base, as can be seen in Figure 95. While this usually enabled successful fibre drawing experiments, leaks would tend to happen near the hole during the melting phase, forming a ring of crystallized glass around it. This ring would then break into small fragments during the draw, contaminating any fibre with crystals as they formed, as shown in Figure 96. As such, this plugging technique was abandoned and replaced by small silica plugs lightly fused on the rim of the nozzle, as can be seen in Figure 97 (d). These experiments

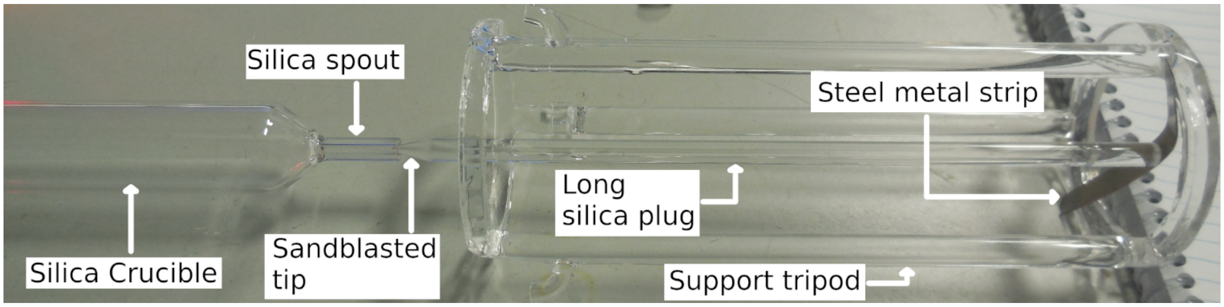

Figure 95: Simple method used to maintain the first plugs used with silica crucibles firmly inserted.

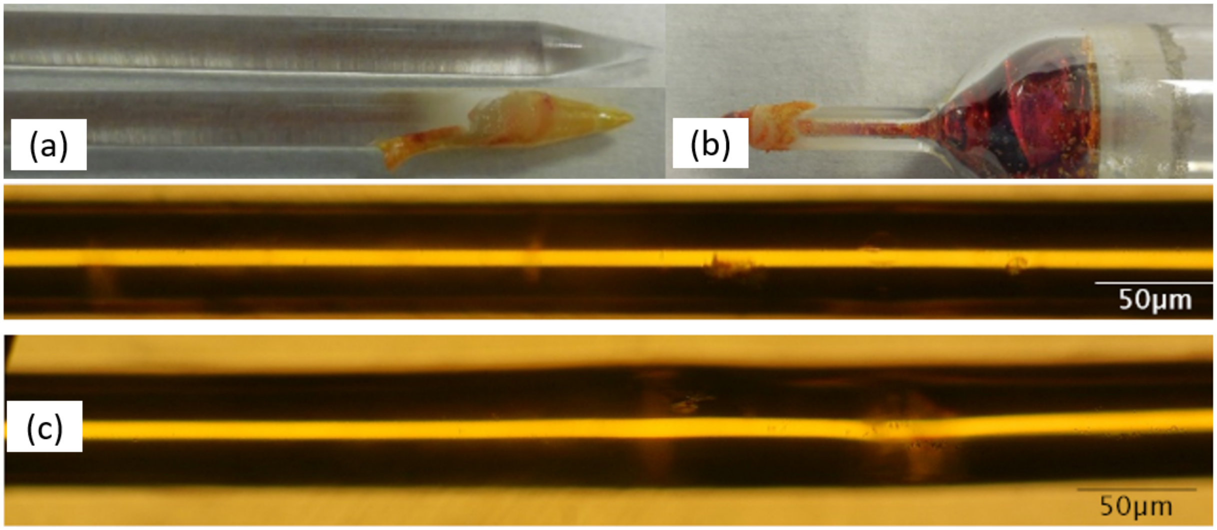

Figure 96: Example of leaks caused by improper plug fit (a), (b) and its consequences on the fibre produced (c).

could reliably produce crystal-free fibre, but the issue of free-falling fibre remained. The silica crucibles were slowly altered over time, developing a bottleneck, so as to facilitate glass flow. Longer silica tips were fused over the crucible hole, to facilitate their breaking, as seen in Figure 97 (e).

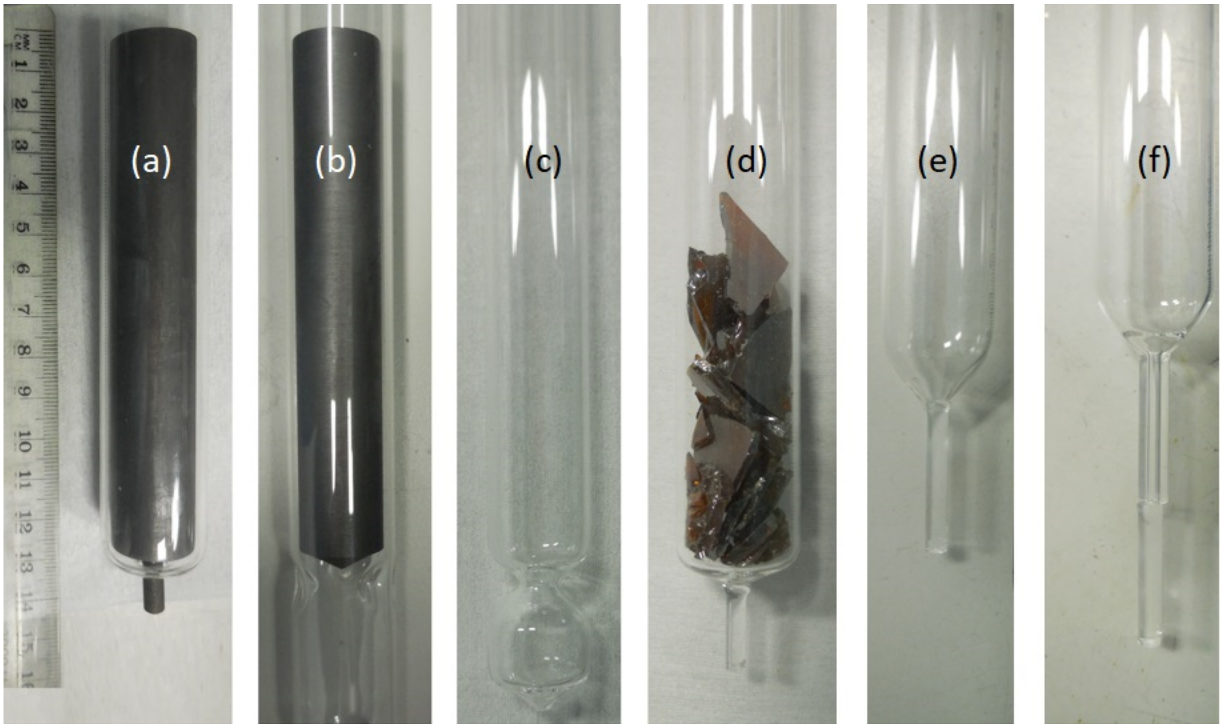

Figure 97: Crucible design changes. (a), graphite crucible fitted with a graphite plug in a silica crucible holder. (b), hybrid crucible allowing for molten GLS to drip down into a secondary crucible. (c), silica crucible with two chambers: melting (top) and fibre formation (bottom). (d), silica crucible with lightly fused breakable plugs. (e), silica crucible with a bottleneck. (f), silica crucible with a nozzle.

Although this technique proved to be more reliable, it was still imperfect, as leaks would occasionally take place and breaking the plug did not always produce a clean-cut nozzle exit, which in turn significantly altered the flow parameters and prevented reproducible results. A possible effect of an imperfect nozzle snapping is wavy fibre, shown in Figure 98.

Finally, the plugs were made by solidly fusing the end of a 40 mm nozzle and scoring it at the 15 mm mark (Figure 97 (g)). This enabled a perfectly tight seal as well as an ideal, flat, 2 mm inner diameter opening formed upon snap-cutting this plug with a pair of steel pliers. In these circumstances, it was noted that a pocket of gas would form in the

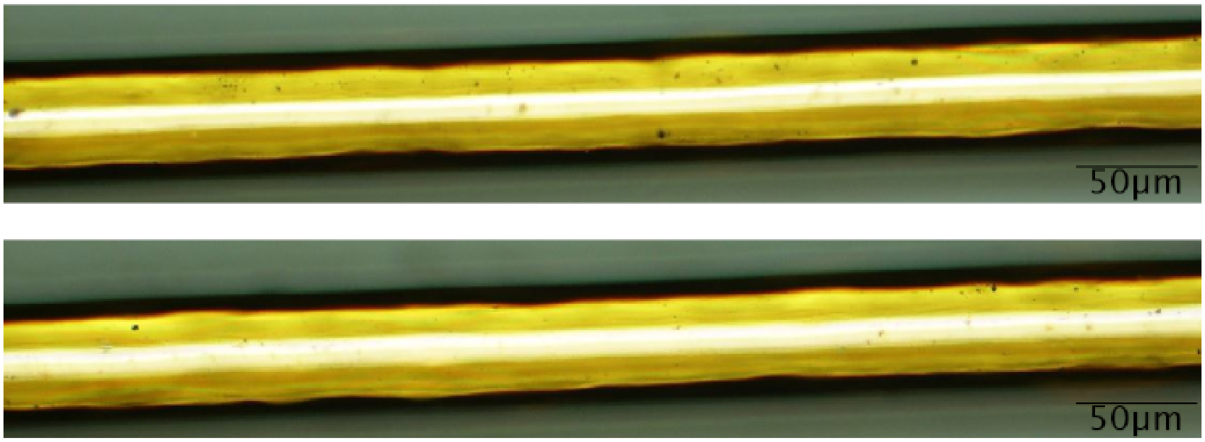

Figure 98: Wavy fibre produced from a silcia crucible featuring an imperfectly snapped fused plug.

nozzle during the melting phase of the experiment. Upon breaking off the tip, the glass could then be observed slowly making its way through, slowly filling that gap until it exits the crucible. This phenomenon enabled the monitoring of the GLS viscosity in real time and roughly predict its exit speed. Adjustments could then be made on the spot to the vertical positioning and the pressure applied to the crucible, so as to enable a stable draw as soon as glass starts exiting the crucible and the first drop formed. The final position of the crucible based on these small adjustments had the nozzle sticking out of the susceptor by about 10 mm. This method was remarked upon as an inversion of what had enabled the initial experiments to produce a few lengths of crystal-free fibre. Indeed, there is a temperature gradient in place in this case as well, but it has been reversed, with the glass higher up in the crucible being above both the crystallization and drawing temperature. The temperature gradient is restricted to the nozzle, which prevents crystallization in the bulk of the glass up above. As the glass flowing in the tip rapidly cools down, it is pushed through and forms a fibre, without being given the time to crystallize.

8.5.5 Viscosity optimization

In order to achieve controllable fibre production, an optimization experiment was carried out using a set of viscosity standards. The experimental setup used is shown in Figure 99. The viscosity standard is placed in a silica crucible with varying nozzle design, and pressure is applied to the crucible to push the viscous liquid out. Mass flow is monitored using a set of scales placed under the crucible. A HeNe laser is positioned to cross the

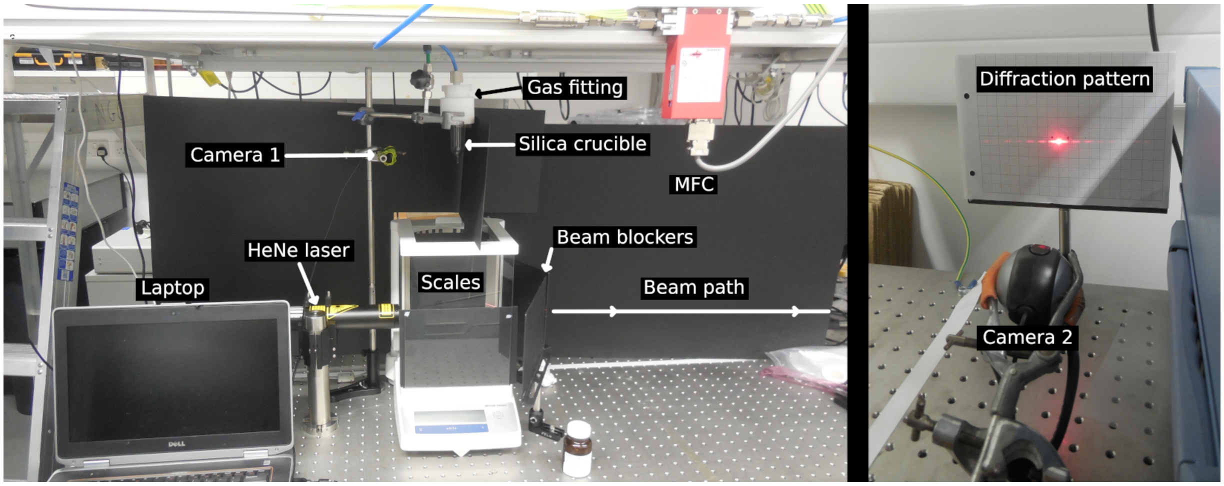

Figure 99: Viscosity experiment setup enabling to monitor mass flow and thickness as a function of pressure, crucible nozzle inner diameter and length. Camera 1 records neck shape, Camera 2 records the corresponding diffraction pattern.

stream of fluid at a normal angle to produce a diffraction pattern, enabling to monitor fibre thickness simultaneously to mass flow. Several small silica crucibles with different length and inner diameter nozzles were tested to produce the results shown in Figures 100, 101 and 102.

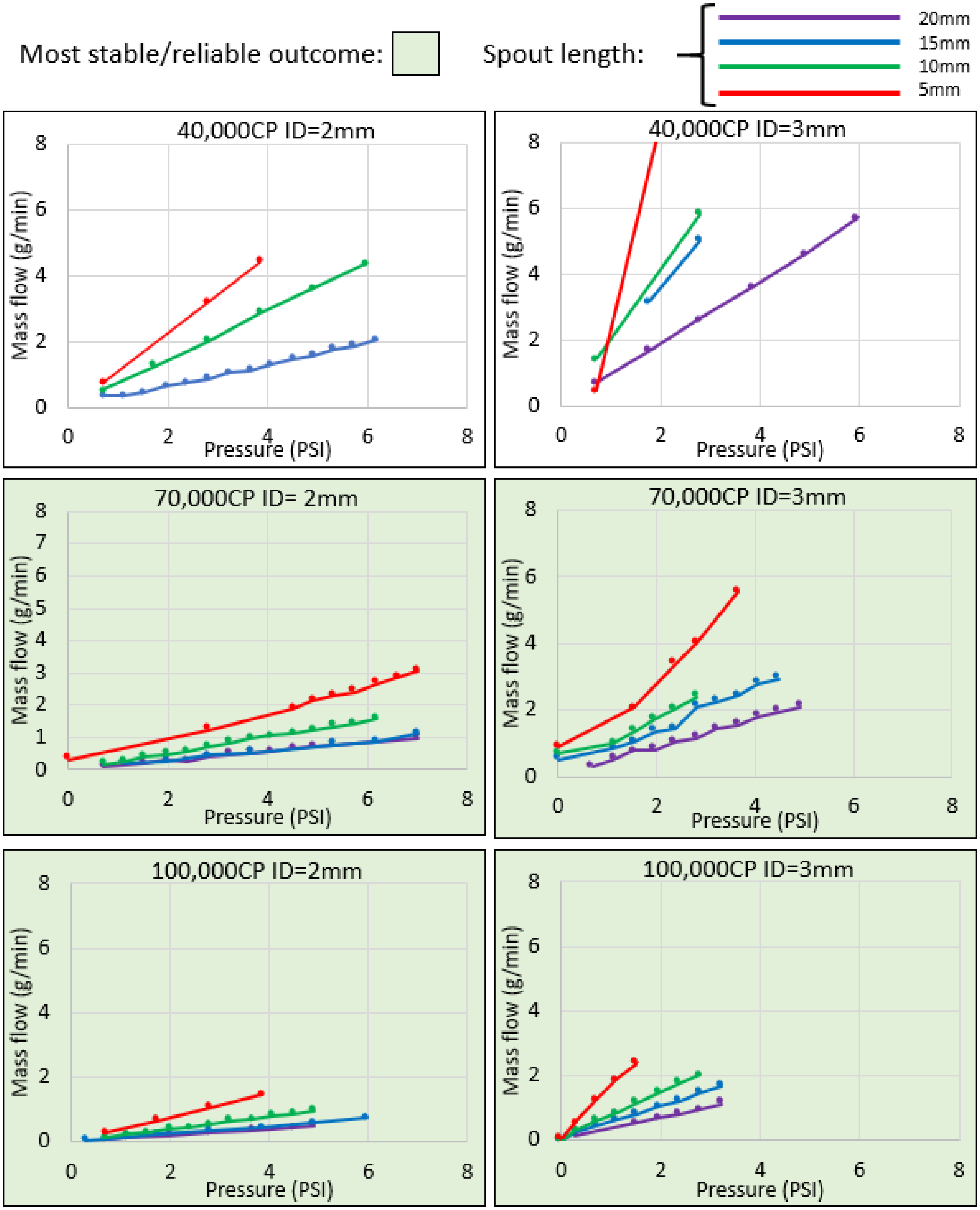

Figure 100: Array of mass flow measurements as a function of viscosity, hole size and nozzle length.

The plots shown in Figure 100 demonstrate the expected correlation between mass flow and hole size, as well as mass flow and pressure. These tests also enabled to safely demonstrate the feasibility of using pressure up to 6 PSI. The exceedingly large and narrow nozzle hole sizes of 1 mm and 4 mm were eliminated as non-viable, due to the uncontrollable and discontinuous nature of their respective outputs, which could not be successfully averted by adjusting other parameters. The most reliable and tunable results were obtained with the 70,000 centipoise (cP) and 100,000 cP viscosity standards, which confirm that, in GLS crucible drawing experiments, viscosity should be considered the most important parameter, and therefore, the one that should be optimized first.

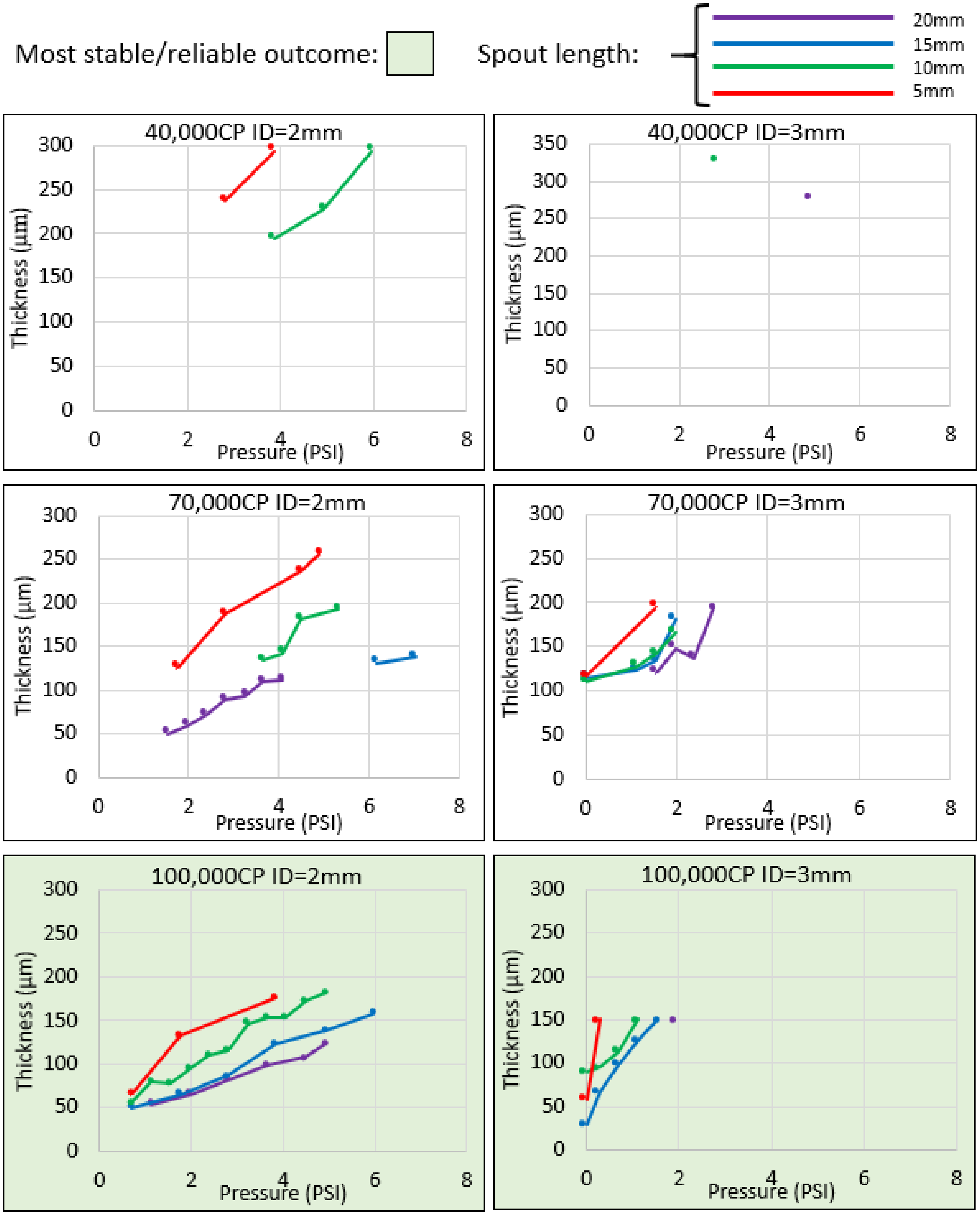

Figure 101: Array of fluid thickness measurements as a function of viscosity, hole size and nozzle length.

The data shown in Figure 101 was acquired simultaneously to the data shown in Figure 100, using the live recording of the diffraction pattern measured by camera 2. The data points are fewer, due to the omission of experiments where excessive oscillations in stream thickness could not enable an accurate measurement. In a fibre drawing experiment, such oscillations must be avoided, which narrows down the ideal fibre drawing viscosity to at least 100,000 cP. It also appears that thickness is slightly more controllable for a 2 mm nozzle inner diameter than it is for a 3 mm inner diameter nozzle.

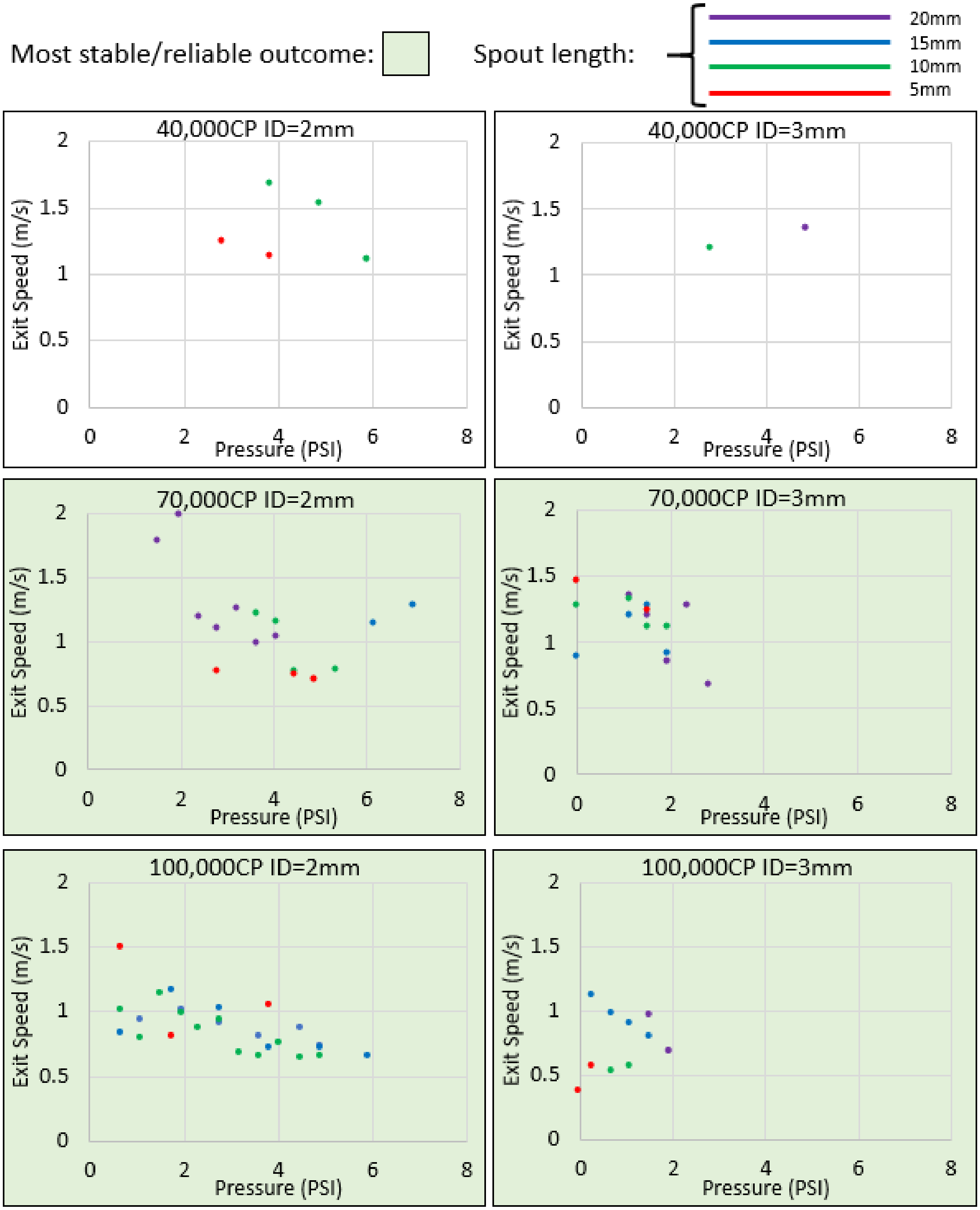

Figure 102: Array of exit speed measurements as a function of viscosity, hole size and nozzle length.

Figure 102 was produced by combining mass flow and stream thickness measurements to calculate the exit speed, which had previously proven to be the limiting factor in GLS crucible drawing experiments. As can be observed, a precise correlation of exit speed with applied pressure is difficult to establish, although for the most reliable parameters of viscosity 100,000 cP and nozzle inner diameter 2 mm, it appears that exit speed is inversely correlated with pressure. Because thickness is positively correlated with pressure, it can be argued that exit speed is lower with higher pressure due to that increase in thickness. Indeed, for constant flow, an increase in the cross-section should result in a proportional reduction in speed. This means that it should be the case that, during GLS crucible drawing experiments, pressure may reduce falling speed rather than increase it, which initially seems counter-intuitive.

In conclusion, a nozzle length of 15 mm and a hole size of 2 mm enabled to maximize the range of reliable fibre diameter and falling speed available from the application of 0 to 6 PSI of pressure to the crucible. As such, this design was adopted for all further fibre drawing experiments in silica crucibles. Also, it is clear that a sufficiently high viscosity (above 100,000 cP) is the most important condition for a successful crucible drawing experiment. In addition, to extract the most information from this sizeable data set, establishing mathematical relations and understanding how some of the factors studied interact was sought using design of experiments (DOE) data analysis.

Design of experiments is a statistical analysis method meant to be used in conjunction with the acquisition of experimental data in order to optimize a tunable system in terms of outcome, stability and reproducibility. To that end, DOE enables to determine factor interaction and can analyze several factors simultaneously, which is particularly fitting to empirical scientific study. As such, this method was used here to provide a better understanding of the dynamics at play. In particular, it was used to produce normal plots, to study the effect of varying a factor or combination of factors. Normal plots enable to assess the validity of the null hypothesis for individual and combined factors, the null hypothesis being that the factor or combination of factors has no significant effect on the outcome. The further each point stray from the normal distribution line, the higher the likelihood of significant correlation between the factor(s) it represents and the monitored variable (and the lower the chance that the null hypothesis is correct) [124]. The information obtained this way is shown in Figure 103. It was extracted using the Minitab software for data analysis [125].

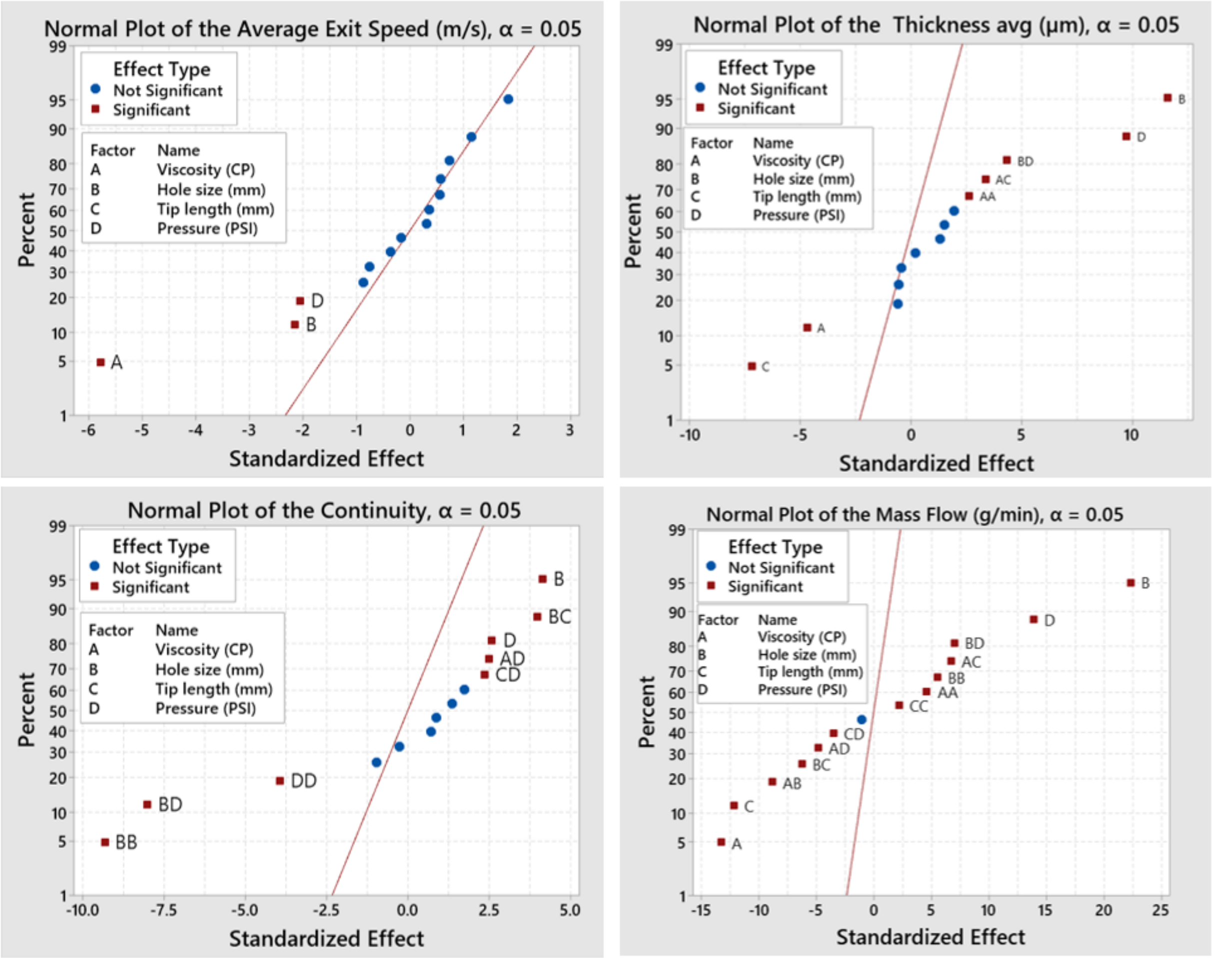

Figure 103: Normal plots of the key parameters of the crucible drawing viscosity study.

It appears that the average exit speed is mostly affected by viscosity and pressure, while the continuity of the flow mostly depends on tip length and pressure. However, the parameters that affect thickness of the stream as well as the mass flow show strong interactions with one another that complicate attempts at optimizing the outcome. The minitab software is also able to produce a predictive model for the response variables based on this analysis, by producing a polynomial contour plot and extracting the corresponding set of equations. The behaviour of each key parameter is modelled by equations 16,17 and 18 in which up to two-level factor interactions are taken into account [125].

$$\begin{gathered} Mf = 1.14 - 6.4 * 10^{-5}V + 1.22Hs - 1.7 * 10^{-1}Tl + 5.5 * 10^{-1}P + 4.7 * 10^{-1}Hs^2 \\ + 5.0 * 10^{-3}Tl^2 - 2.1 * 10^{-2}P^2 - 2.8 * 10^{-5}V * Hs + 3 * 10^{-6}V * Tl \\ - 8 * 10^{-6}V * P - 8.2 * 10^{-2}Hs * Tl + 4.2 * 10^{-1}Hs * P - 2.2 * 10^{-2}Tl * P \end{gathered} \tag{16}$$

$$\begin{gathered} Th = 542 - 7.2 * 10^{-3}V - 7.7 * 10^{1}Hs - 10^{1}Tl - 3.5 * 10^{1}P + 1.3 * 10^{1}Hs^2 \\ - 6.5 * 10^{-2}Tl^2 - 6.1 * 10^{-1}P^2 + 4.0 * 10^{-4}V * Hs + 9.3 * 10^{-5}V * Tl \\ + 2.2 * 10^{-4}V * P + 1.9 * 10^{-1}Hs * Tl + 2.4 * 10^{1}Hs * P - 2; 4 * 10^{-1}Tl * P \end{gathered} \tag{17}$$

$$\begin{gathered} AvS = 3.43 - 1.4 * 10^{-5}V - 8.0 * 10^{-1}Hs + 2.4 * 10^{-2}Tl - 2.3 * 10^{-1}P \\ + 1.4 * 10^{-1}Hs^2 + 3.7 * 10^{-4}Tl^2 + 1.2 * 10^{-2}P^2 - 2 * 10^{-6}V * Hs \\ + 10^{-6}V * P - 3.1 * 10^{-3}Hs * Tl + 3.5 * 10^{-2}Hs * P - 3.7 * 10^{-3}Tl * P \end{gathered} \tag{18}$$

For the parameters in the equations above, Th is the thickness of the viscous stream (in μm), AvS is the average exit speed (in m/s), Mf is the mass flow (in g/min). For the factors, V is the viscosity (in centipoise), Hs is the hole size (in mm), Tl is the tip length (in mm) and P is the pressure (in PSI). These equations may be used to calculate the theoretical behaviour of a stream of fibre exiting the crucible in a fibre drawing experiment.

8.6 Crucible drawing results

The first fully-controllable and crystal-free crucible-drawn production of GLS fibre was achieved by combining the silica crucibles and the information extracted from the viscosity optimization study. The crucible used had a 2 mm inner diameter 15 mm long nozzle. The glass was melted for 10 minutes at 1350 °C susceptor temperature (corresponding glass temperature 1050 °C), with the tip of the nozzle of the crucible 15 mm above the bottom of the susceptor. Temperature was then ramped down to 920 °C (corresponding glass temperature 740 °C) and held for 5 minutes. The crucible was then lowered for the nozzle to protrude 10mm out of the susceptor. The nozzle was immediately snapped cut using pliers and 0.3 PSI of nitrogen pressure was applied (340 arbitrary units on the pressure controller), to facilitate glass flow. The exact details of this experiment are recorded in the NT824 log. The resulting fibre drum and microscope images of bare fibre are shown in Figure 104.

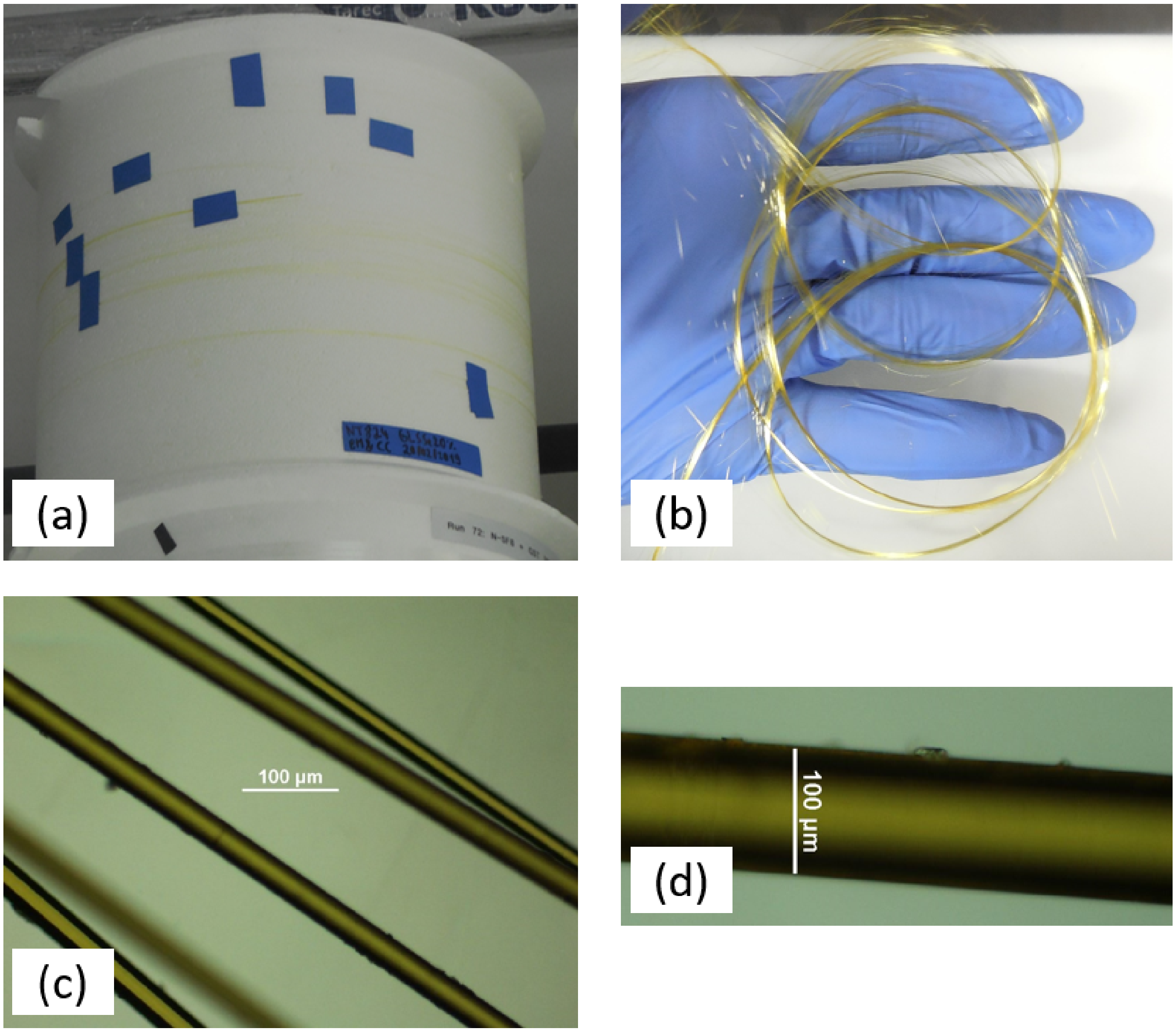

Figure 104: First controllable production of GLSSE20% fibre using crucible drawing in silica. (a), respooled fibre. (b), 50 μm diameter crystal-free, highly flexible bundle. (c) and (d), microscope images of fibre demonstrating the ability to vary in fibre diameter (NT824).

It may be noted that the fibre is apparently crystal-free, unclad, and gets as thin as 10 μm in diameter. This demonstrates an ideal method for fabricating a bundle for imaging applications. Further experiments aiming at maintaining a constant fibre diameter throughout the draw were carried out in NT829 and NT834. Fibre loss measurements were made on the fibre produced and compared to the loss of free-falling GLSSe20% fibre fabricated in NT705. This is shown in Figure 105.

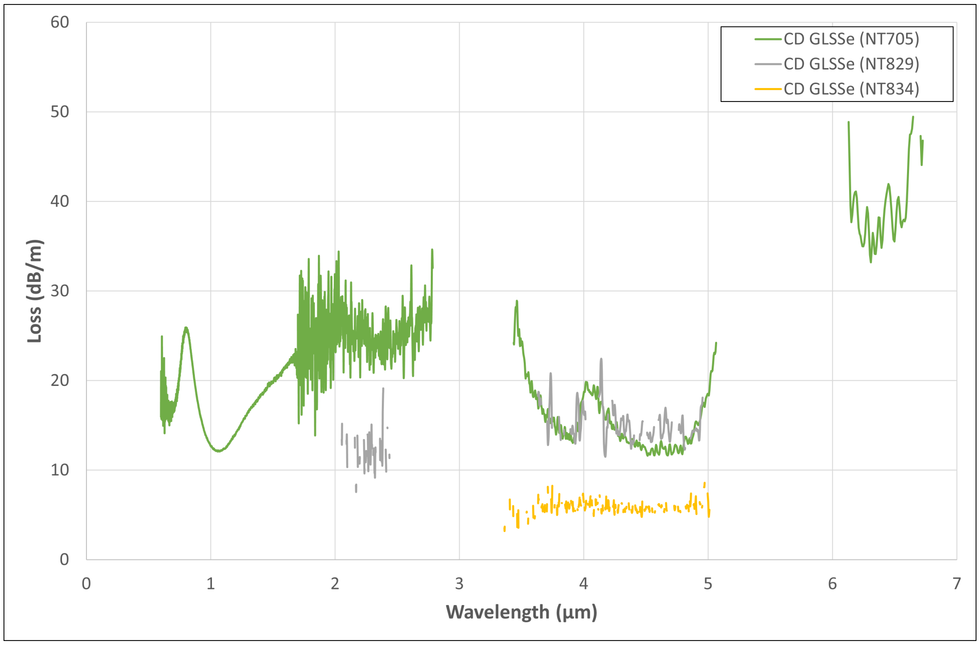

Figure 105: Successive improvements to fibre loss achieved by improving the consistency of fibre diameter (NT705, NT829 and NT834). Fibre diameter was 120, 90 and 50 μm respectively, and 1.5m of fibre was used for each cutback measurement.

The loss in the fibre produced by crucible drawing is considerably high, contrary to what should be expected from its visual quality and physical resilience. There are two broad absorption peaks located at 2.9 μm and 6 μm, demonstrating the presence of OH and H_2O respectively. It is similar to what can be observed in Figure 12, albeit to a greater extent. As such, it is most likely caused by the long exposure of molten GLS with silica. Therefore, in an attempt at reducing the optical losses in the crucible drawn fibre, silica crucibles with an inner carbon coating were fabricated with assistance from SandFire Scientific. Hydroxyl-free silica tubes could also be made into silica crucibles as an alternative. It can be noted in Figure 105 that the amount of light transmitted (and therefore the size of the measured transmission window) through the fibre gets reduced with each successive fibre drawing experiment. However, this does not pertain to fibre quality, but rather reflects the fact fibre diameter was becoming progressively thinner during the optimization process for constant fibre diameter. This in turn, explains why an increasingly smaller portion of the light could be coupled in the fibre during fibre loss measurements, while the loss minimum would be improved due to the improved consistency of fibre diameter. Indeed, fibre diameter for NT705 had ± 5 μm variation across the full length of the cutback, NT829 had ± 2 μm and NT834 ± 1 μm.

8.7 Coating method enhancements

The established method used to coat fibre relies on a coating cup in which Desolite^{TM} [84] is poured. At the bottom of the cup, a cut-out dye is closed around the fibre, leaving only a thin layer of resin on the exiting fibre. Then, the coated fibre passes through a UV curing lamp, and it is collected onto the drum once cured. This process is shown in Figure 106.

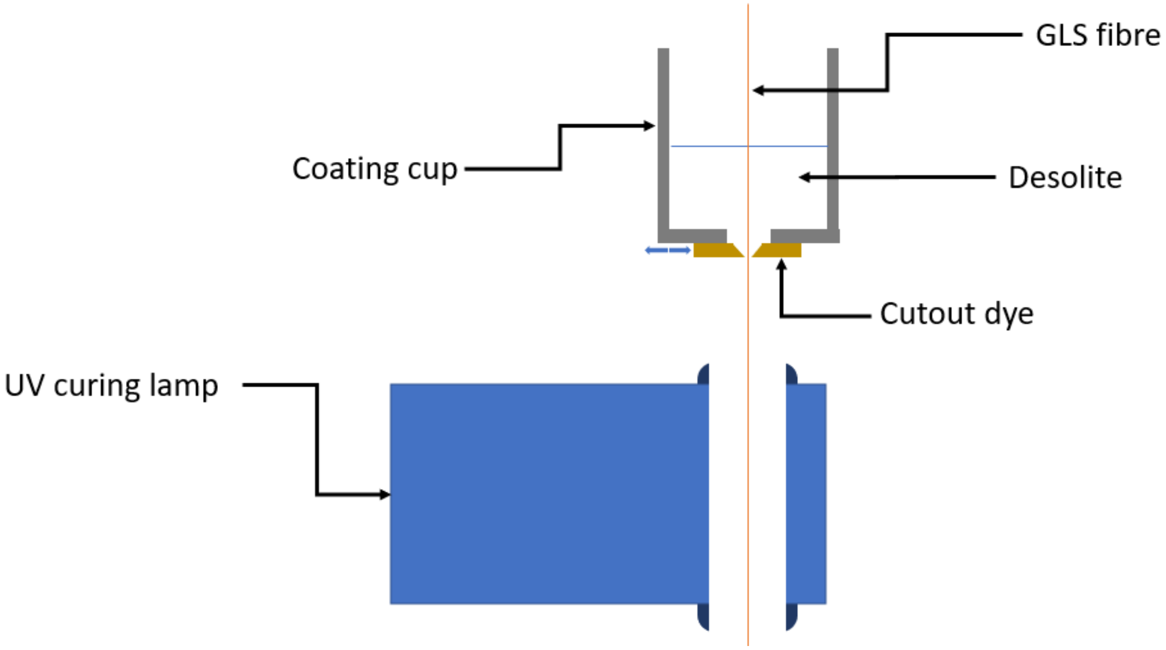

Figure 106: Standard fibre coating procedure using a coating cup and a cut-out dye.

This method requires careful alignment of the setup, a constant and stable fibre diameter, and is complicated by the presence of sticky, viscous uncured resin, which requires copious amounts of acetone to be removed. Also, if the fibre drawing process is interrupted by fibre breakage, the coating process takes several minutes to restart, as the fibre must be passed through the dye while it is fully open, which requires the coating cup to be empty and clean in the first place.

Due to these added complications, an alternate fibre coating system was designed, in which the coating was applied using high-viscosity liquid atomizing spray nozzle (MMAE/MMA)[126]. Such a system would greatly simplify the experimental setup, requiring little to no alignment and being easily slid in and out of the fibre path, as opposed to the fibre needing to be carefully threaded through several pieces of equipment. Figure

107 demonstrates the experiment carried out to demonstrate proof of principle for the feasibility of spray coating Desolite^{TM} onto fibre and cure it. Using a single nozzle, a borosilicate preform was drawn into fibre, coating was applied to it and it was cured in the UV lamp. Figure 108 shows microscope images of the resulting layer of coating.

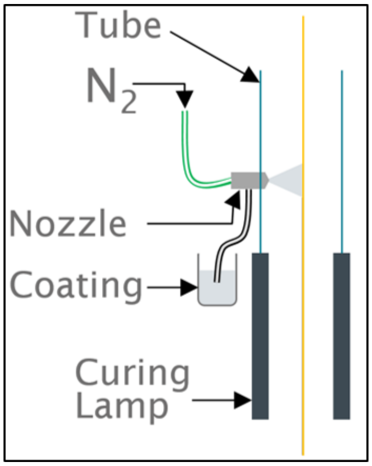

Figure 107: Schematic representation of the spray coating experiment producing the results shown in Figure 108.

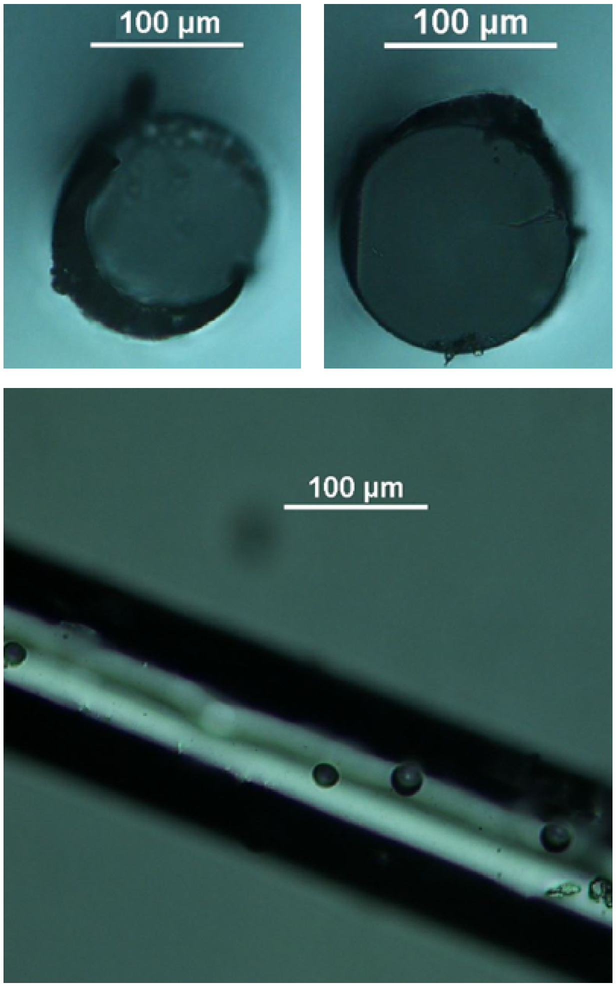

Figure 108: Outcome of a spray coating experiment performed on borosilicate fibre (NT825) demonstrating asymmetric cured coating.

As can be seen, due to the presence of only one nozzle, the coating is asymmetric. However, from these images can be inferred that three nozzles placed 120° apart should suffice to coat the fibres evenly.

8.8 Ultrathin fibre

It was noted that, both in GLS crucible drawing and rod drawing experiments, the production of fibre of 50 μm in diameter is a common occurrence. However, some sections of the fibre before the diameter became stable would occasionally reach a diameter as low as 10 μm. Attempts were made to adjust the experimental parameters to achieve the manufacture of fibre of such small diameter in a stable, continuous process, by adapting both crucible drawing and rod drawing techniques.

For crucible drawing, a stable diameter of 10 μm was achieved by lowering the silica crucible nozzle as far as possible without the fibre breaking, while maintaining the other parameters constant in NT881. The process had to be monitored carefully to ensure the glass accumulating at the nozzle of the crucible was kept to an absolute minimum. Indeed, since the diameter of the fibre drawn is so small, if a drop were to form at the end of the crucible, it would have a sufficient amount of time to form crystals, as its contents are drained at an exceedingly slow pace. It was noted that it is feasible to reach stable drawing parameters where there is no noticeable glass build-up at the nozzle, and the glass seems to stream directly from the inside of the nozzle. Achieving such a stable regime is challenging, as the formation of a meniscus at the nozzle of the crucible is normally desirable, since it acts as a temporary buffer when the drum speed is changed. In this case however, if the uptake of fibre by the drum is too rapidly increased, the available glass immediately runs out and the fibre breaks. The 10 μm GLSSe20% fibre obtained in experiment NT881 is shown in Figure 109.

For rod drawing, a stable diameter of 10 μm was achieved by incrementally increasing both the susceptor drawing temperature from the ordinary 900 °C to 1350 °C, and the drum speed from 10 m/min to 40 m/min, while maintaining the feed rate to very small values (0.01 mm/min) with hollow Schott Duran$^{\text{TM}}$ Borosilicate (6 mm OD, 2.5 mm ID). Using a 10 mm in diameter/100 mm long non-hollow NF2 titanium oxide-doped silica glass [127] preform, a diameter of 5 to 3 μm was achieved in a similar fashion, with the susceptor heated to 1000 °C, the feed at 0.01 mm/min, and a drum speed of 490 m/min. The fibre drawing process remained stable, allowing the production of several kilometres of fibre. Microscope images of this fibre are shown in Figure 110.

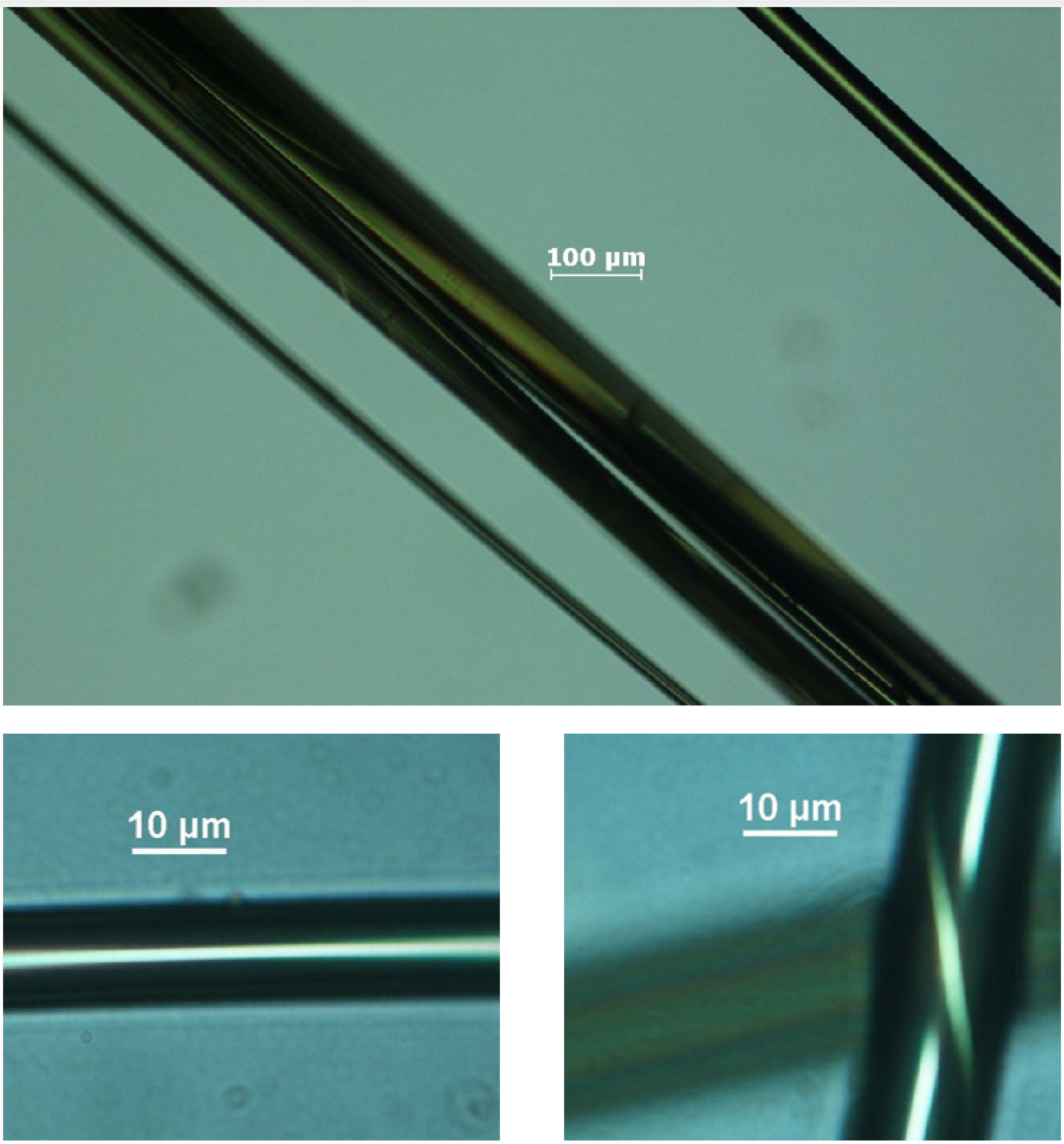

Figure 109: 10 μm GLSSe20% fibre manufactured in a crucible drawing experiment performed in silica (NT881).

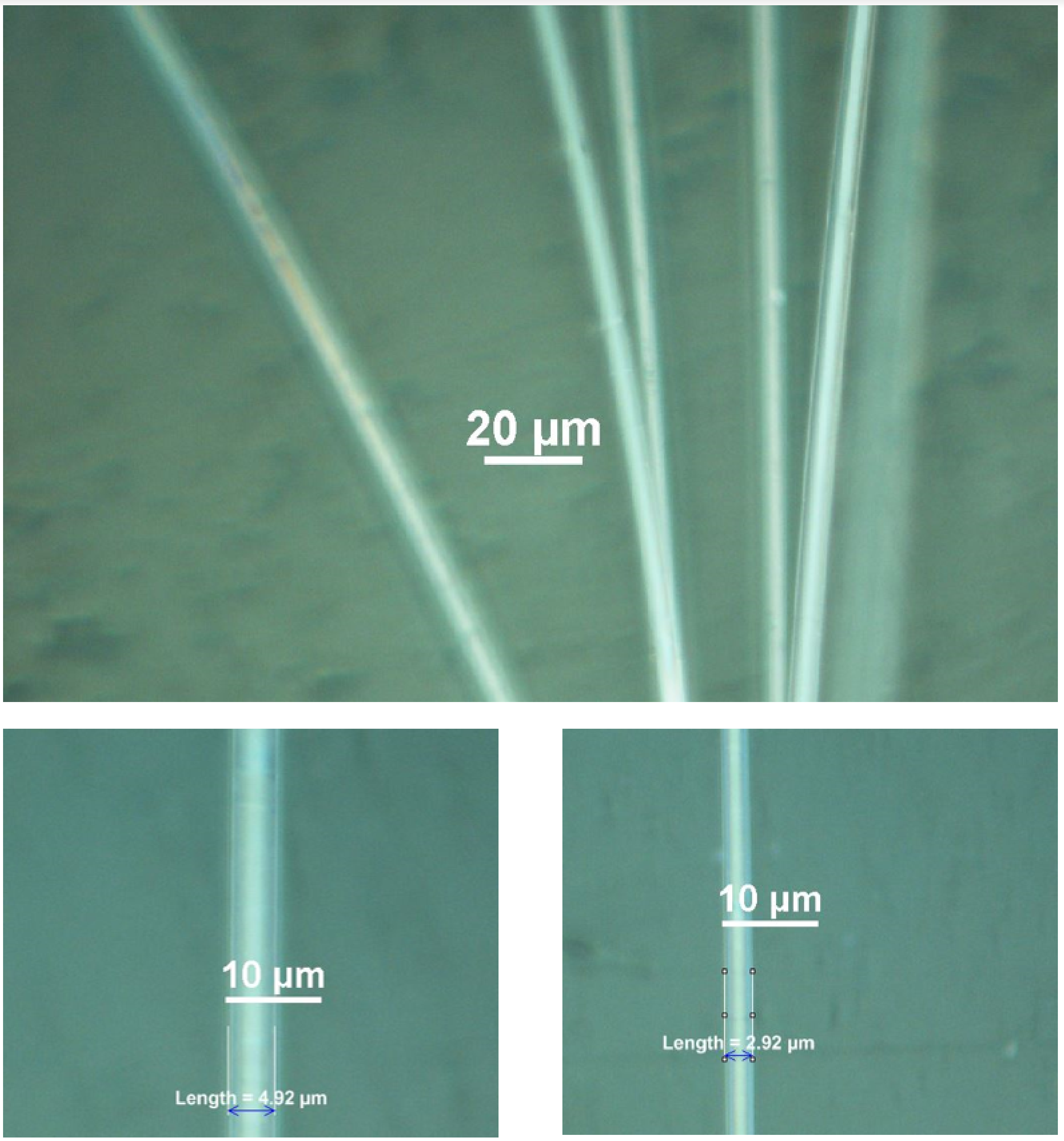

Figure 110: 10 to 3 μm unclad NF2 fibre manufactured in a rod drawing experiment (NT898).

9 Conclusion

The family of chalcogenide glasses based on gallium lanthanum sulphide benefits from the exceptional properties that come with its core composition. In particular, its transmission range encompassing both the visible and infra-red, its high chemical tuneability and its high transition temperatures represent a unique combination of advantages among chalcogenides. However, the shaping of GLS glasses is particularly challenging, as any thermal or mechanical treatment presents risks of crystallizing and/or contaminating the glass, thus compromising its light transmission window.

Characterization techniques have been newly implemented for GLS, both for bulk glass samples and optical fibre, in order to provide a better understanding of its properties and more accurately tailor its utilization. For shaping the glass, remelting techniques have been investigated and a novel expertise has been developed to produce large diameter chalcogenide windows (>90 mm in diameter) along with methods to expand the glass forming region.The previously established fibre drawing methods have been revisited and improved upon. In turn, they have enabled to achieve novel results, such as the fabrication of oxygen-free and crystal-free GLS and GLSSe fibre with an expanded transmission range. Methods of GLS preform fabrication and processing have been successfully introduced, such as rod turning, cylindrical polishing, and preform casting, enabling rapid prototyping of optical fibre drawing with GLS glass compositions. In addition, the in-house production of hollow GLS preforms and canes provides the opportunity to fabricate core-clad fibre using the rod-in-tube method. Crucible drawing has been implemented for the first time with GLS, working from a melt to circumvent crystallization, and establishing reliable methods of unclad fibre production for fibre bundle applications. Finally, ultra-thin fibre with a smaller diameter than previously thought possible was successfully fabricated by exploring the practical limits of fibre drawing, and an improved method of fibre coating has been demonstrated using spray nozzles so as to streamline the fibre drawing procedure.

Because of these advances, new possibilities and challenges has been uncovered and further research into the GLS family of glasses has been incentivized. New perspective on the issue of interface bubbles has been acquired from casting experiments, and their elimination was advanced to maximize the dimensions of GLS samples. A comprehensive array of testing was developed to assess the effects of exposure of GLS to corrosive environments, in particular when they have previously been plasma ashed. Future work enabled by this includes large window fabrication, with the purchase of larger casting furnaces and vitreous carbon crucibles, which should enable the fabrication of up to 150 mm diameter GLS windows. Carbon-coated silica crucibles of the same design as the ones used for crucible drawing have been purchased and will be tested in order to achieve the highest possible transmission in crucible-drawn unstructured GLS fibre, while double-crucible designs should be developed to achieve crucible drawn core-clad optical fibre.

Bibliography

[1] L. Calvez. Chalcogenide glasses and glass-ceramics: Transparent materials in the infrared for dual applications. *Comptes Rendus Physique*, (18:5-6):314–322, 2017. doi: 10.1016/j.crhy.2017.05.003.

[2] J. S. Sanghera, L. B. Shawn, and I. D. Aggarwal. Applications of chalcogenide glass optical fibers. *Comptes Rendus Chimie*, (5), 2002.

[3] P. W. France. *Fluoride Glass Optical Fibres*. Springer, 1990. ISBN 978-9401168670.

[4] J. A. Harrington. *Infrared Fibers and Their Applications*. SPIE Press, 2004. ISBN 9780819452184.

[5] VITRON IG-2 – discover the Original. `https://www.vitron.de/files/VITRON_IG-2_Datenblatt_Jan_2015.pdf`. Accessed: 2021-04-02.

[6] A. Ravagli, C. Craig, G. A. Alzaidy, P. Bastock, and D. Hewak. Optical, Thermal, and Mechanical Characterization of Ga_2Se_3-Added GLS Glass. *Advanced Materials*, (29), 2017.

[7] L. S. Garca-Coln, L. F. del Castillo, and P. Goldstein. Theoretical basis for the Vogel-Fulcher-Tammann equation. *Phys. Rev. B*, (40:10):7040–7044, 1989. doi: 10.1103/PhysRevB.40.7040.

[8] Fibermate2™ fiber optic coupler. `http://harricksci.com/ftir/accessories/group/FiberMate2%E2%84%A2-Fiber-Optic-Coupler`. Accessed: 2017-12-27.

[9] G. S. Murugan. *Photonic Glasses and Glass-Ceramics*. Research Signpost, 2010. ISBN 978-8130803753.

[10] D. J. Brady. *Gallium Lanthanum Sulphide Based Glasses for Mid-Infrared Optical Fibres*. PhD thesis, University of Southampton, 1999.

[11] F. Sydney Eden. *Ancient Stained and Painted Glass*. BiblioLife, 2008. ISBN 978-0554836218.

[12] J. Hecht. *City of Light: The Story of Fiber Optics*. Oxford University Press, 2004. ISBN 978-0195162554.

[13] *Glass Technology Course Textbook*. CelSian, NCNG, 2016.

[14] G. Morey. *The Properties of Glass*. Reinhold Publishing Corporation, 1938. doi: 10.1021/j150391a019.

[15] C. R. Kurkjian and W. R. Prindle. Perspectives on the History of Glass Composition. *Philos. Trans.*, (191):399–440, 1898. doi: 10.1098/rsta.1898.0010.

[16] M. Cable A. Neri, C. Merrett. *The Art of Glass*. Society of Glass Technology, 2001. ISBN 978-0900682377.

[17] H. G. Pfaender. *Schott Guide to Glass*. Springer, 1998. ISBN 978-0412719608.

[18] G. Agricola, H. Hoover, and L.H. Hoover. *De Re Metallica*. Dover Publications Inc., 1998. ISBN 978-0486600062.

[19] M. A. Pasek, K. Block, and V. Pasek. Fulgurite morphology: a classification scheme and clues to formation. *Contributions to Mineralogy and Petrology*, (164):477–492, 2012. doi: 10.1007/s00410-012-0753-5.

[20] H. J. Franklin. Method of making a transparent article of silica, 27 1934. URL `https://patents.google.com/patent/US2272342A/en`. US Patent US2272342A.

[21] R. W. Douglas and S. Frank. *History of Glass Making*. G T Foulis Co Ltd, 1972. ISBN 978-0854291175.

[22] P. W. Anderson. Through the Glass Lightly. *Science*, (267):1615–1616, 1995. doi: 10.1126/science.267.5204.1615-e.

[23] E. D. Zanotto and P. K. Gupta. Do cathedral glasses flow? Additional remarks. *American Journal of Physics*, (67):260–262, 1999. doi: 10.1119/1.19236.

[24] J. Zhao, S. L. Simon, and G. B. Mckenna. Using 20-million-year-old amber to test the super-Arrhenius behaviour of glass-forming systems. *Nature Communications*, (4):1783, 2013. doi: 10.1038/ncomms2809.

[25] E. D. Zanotto and J. C. Mauro. The glassy state of matter: Its definition and ultimate fate. *Journal of Non-Crystalline Solids*, (471):490–495, 2017. doi: 10.1016/j.jnoncrysol.2017.05.019.

[26] M.M.A. Imran, D. Bhandari, and N.S. Saxena. Enthalpy recovery during structural relaxation of $Se_{96}In_4$ chalcogenide glass. *Physica B: Condensed Matter*, (239:3-4): 394–401, 2001. doi: 10.1016/S0921-4526(00)00543-3.

[27] J. Sehgal and S. Ito. Brittleness of glass. *Journal of Non-Crystalline Solids*, (253:1-3):126–132, 1999. doi: 10.1016/S0022-3093(99)00348-8.

[28] J. Tyndall. On Some Phenomena Connected With the Motion of Liquids. *Proceedings of the Royal Institution of Great Britain*, 1854.

[29] J. Ballato and P. Dragic. Glass: The Carrier of Light - A Brief History of Optical Fiber. *International Journal of Applied Glass Science*, 2016.

[30] H. Lamm. Biegsame Optische Gerate. *Z. Instrumentik*, (50):579–582, 1930.

[31] W. A. Gambling. The Rise and Rise of Optical Fibers. *IEEE JOURNAL ON SELECTED TOPICS IN QUANTUM ELECTRONICS*, (6:6):1084–1093, 2000. doi: 10.1109/2944.902157.

[32] K. C. Kao and G. A. Hockham. Dielectric-fibre surface waveguides for optical frequencies. *IEE Proceedings*, (113), 1966.

[33] F. P. Kapron, D. B. Keck, and R. D. Maurer. RADIATION LOSSES IN GLASS OPTICAL WAVEGUIDES. *Applied Physics Letters*, (17:10):423–425, 1970. doi: 10.1063/1.1653255.

[34] F. Mitschke. *Fiber Optics.* Springer, 2018. ISBN 978-3662570791.

[35] T. K. Gangopadhyay, P. Kumbhakar, and M. K. Mandal. *Photonics and Fiber Optics Foundations and Applications.* CRC Press, 2019. ISBN 9780429026584.

[36] L. B. Shaw, B. Cole, P. A. Thielen, J. S. Sanghera, and I. D. Aggarwal. Mid-wave ir and long-wave ir laser potential of rare-earth doped chalcogenide glass fiber. *IEEE Journal of Quantum Electronics*, 37(9):1127–1137, 2001. doi: 10.1109/3.945317.

[37] N. S. Kapany and R. J. Simms. Recent developments in infrared fiber optics. *Infrared Physics*, (5:2):69–76, 1965. doi: 10.1016/0020-0891(65)90009-6.

[38] A. M. Loireau-Lozac'h, M. Guittard, and J. Flahaut. VERRES FORMES PAR LES SULFURES L_2S_3 DES TERRES RARES AVEC LE SULFURE DE GALLIUM Ga_2S_3. *Materials Research Bulletin*, (11:12):1489–1496, 1976. doi: 10.1016/0025-5408(76)90099-4.

[39] R. Li, D. Furniss, H. Bagshaw, and A. B. Seddon. The decisive role of oxide content in the formation and crystallization of gallium-lanthanum-sulfide glasses. *Journal of Materials Research*, (14:6):2621–2627, 1999. doi: 10.1557/JMR.1999.0351.

[40] J. Sanghera and I. D. Aggarwal. *Infrared Fiber Optics*. CRC Press, 1998. ISBN 978-0849324895.

[41] J. Nishii, T. Yamashita, and T. Yamagishi. Chalcogenide glass fiber with a core-cladding structure. *Applied Optics*, (28:23):5122–5127, 1989. doi: 10.1364/AO.28.005122.

[42] A. Mairaj. *Optical Waveguides And Lasers In Improved Gallium Lanthanum Sulphide Glass*. PhD thesis, University of Southampton, 2002.

[43] R. Asal, P. Rivers, and H. Rutt. A structural study of gallium lanthanum sulphide glass bulk and thin films by x-ray absorption fine structure spectroscopy. *Journal of Physics: Condensed Matter*, (9):6217–6230, 1997. doi: 10.1088/0953-8984/9/29/007.

[44] S. Benazeth, M.H. Tuilier, A.M. Loireau-Lozac'h, H. Dexpert, P. Lagarde, and J. Flahaut. An EXAFS structural approach of the lanthanum-gallium-sulfur glasses. *Journal of Non-Crystalline Solids*, (110), 1989.

[45] S. Benazeth, M.H. Tuilier, H. Dexpert, M. Guittard, and D. Carre. Chalcogenide And Oxychalcogenide Glasses: Evolution Of The Gallium Surrounding With The Oxygen Content. *Le Journal de Physique Colloques*, (47), 1986. doi: 10.1051/jphyscol:1986884.

[46] A. Ravagli. *Development of Visible-to-FIR multispectral chalcogenide glasses*. PhD thesis, University of Southampton, 2018.

[47] M. Hesford. *The development of a chemical etch procedure for GLS glass preforms to improve fibre strength and quality*. PhD thesis, University of Southampton, 1999.

[48] C. Le Sergent. Chalcogenide Glass Optical Fibers - An Overview. *Proceedings of SPIE-the International Society for Optical Engineering*, (799):18–24, 1987. doi: 10.1117/12.941143.

[49] P. Klocek, M. Roth, and R. D. Rock. Chalcogenide Glass Optical Fibers And Image Bundles: Properties And Applications. *Optical Engineering*, (26(2)):260288, 1987. doi: 10.1117/12.7974032.

[50] E. M. Dianov, V. J. Masychev, V. G. Plotnichenko, V. K. Sysoev, P. J. Bailalov, G. G. Devjatykh, A. S. Konov, J. V. Schipachev, and M. F. Churbanov. Fibre-Optic cable for CO laser power transmission. *Electronics Letters*, (20:3):129–130, 1984. doi: 10.1049/el:19840087.

[51] D. Furniss and A. B. Seddon. Towards monomode proportioned fibreoptic preforms by extrusion. *Journal of Non-Crystalline Solids*, (256257):232–236, 1999. doi: 10.1016/S0022-3093(99)00463-9.

[52] T. J. Loretz, A. R. Hilton, and J. McCord. Fabrication of chalcogenide glass rods and tubes by processor-controlled extrusion techniques. *Proceedings of SPIE-the International Society for Optical Engineering*, (2977):14–19, 1997. doi: 10.1117/12.271021.

[53] S. D. Savage, C. A. Miller, D. Furniss, and A. B. Seddon. Extrusion of chalcogenide glass preforms and drawing to multimode optical fibers. *Journal of Non-Crystalline Solids*, (354:29):3418–3427, 2008. doi: 10.1016/j.jnoncrysol.2008.01.032.

[54] M. Saito, M. Takizawa, and M. Miyagi. Infrared optical fibers with vapor-deposited cladding layer. *Journal of Lightwave Technology*, (7:1):158 – 162, 1989. doi: 10.1109/50.17748.

[55] D. Blanc and J. I. B. Wilson. Plasma deposition of chalcogenide glass. *Journal of Non-Crystalline Solids*, (77-78:2):1129–1132, 1985. doi: 10.1016/0022-3093(85)90857-9.

[56] A. B. Seddon. Chalcogenide glasses: a review of their preparation, properties and applications. *Journal of Non-Crystalline Solids*, (184):44–50, 1995. doi: 10.1016/0022-3093(94)00686-5.

[57] J. E. Midwinter. *Optical Fibres for Transmission.* Krieger Pub Co, 1991. ISBN 978-0894645952.

[58] H. Aulich, J. Grabmaier, and K.-H. Eisenrith. Apparatus and method for producing light conducting fibers having a core disposed in a loose fitting cladding tube, 9 1979. URL `http://www.patents.com/us-4133664.html`. US Patent 4,133,664.

[59] J. Kobelke, M. Scheffler, and A. Schwuchow. Chalcogenide glass sinlge mode fibres - preparation and properties. *Journal of Non-Crystalline Solids*, (256-257):226–231, 1999. doi: 10.1016/S0022-3093(99)00461-5.

[60] H. H. Brongersma. Double crucible method of fabricating optical fibers, 21 1984. URL `https://www.google.com/patents/US4466818`. US Patent 4,466,818.

[61] Great western inorganics. https://www.gwi46.com/.

[62] Lorad chemical corporation. https://loradchemical.com/.

[63] Glassy carbon sigradur®. `http://www.htw-germany.com/products`. Accessed: 2020-02-04.

[64] L. J. Mattos and A. G. Clare. The crystallisation and optical properties of gallium cerium lanthanum sulphide glass. *Physics and Chemistry of Glasses*, (34:6):244–250, 1993.

[65] W. A. King, A. G. Clare, and W. C. LaCourse. Laboratory preparation of highly pure As_2Se_3 glass. *IEEE JOURNAL ON SELECTED TOPICS IN QUANTUM ELECTRONICS*, (6:6):1084–1093, 2000. doi: 10.1109/2944.902157.

[66] J. Kim, J. S. Park, E. S. Park, W. T. Kim, and D. H. Kim. Estimation of critical cooling rates for glass formation in bulk metallic glasses through non-isothermal thermal analysis. *Metals and Materials International*, (11):1–9, 2005. doi: 10.1007/BF03027478.

[67] Glassy carbon product information, spi supplies® brand glassy (vitreous) carbon products. `https://www.2spi.com/catalog/documents/Glassy-Vitreous-Carbon-Info.pdf`. Accessed: 2018-09-26.

[68] R. Clausius. Ueber die bewegende Kraft der Wärme und die Gesetze, welche sich daraus für die Wärmelehre selbst ableiten lassen. *Annalen der Physik*, (55):500–524, 1850. doi: 10.1002/andp.18501550403.

[69] M. C. Clapeyron. Mémoire sur la puissance motrice de la chaleur. *Journal de l'École polytechnique*, (23):153–190, 1834. doi: ark:/12148/bpt6k4336791/f157.

[70] T. Egami. Structural Relaxation in Metallic Glasses. *Annals of the New York Academy of Sciences*, (371:1):238–251, 1981. doi: 10.1111/j.1749-6632.1981.tb55664.x.

[71] PM5 Precision Lapping Polishing System. `https://logitech.uk.com/product/pm6-precision-lapping-polishing-system/` note = Accessed: 2020-02-10.

[72] Precision Lapping Jig PP6. `https://logitech.uk.com/?attachment_id=322` note = Accessed: 2020-02-10.

[73] F. Di Quarto, M. C. Romano, M. Santamaria, and C. Sunseri. A semiempirical correlation between the optical band gap of hydroxides and the electronegativity of their constituents. *Russian Journal of Electrochemistry*, (36:11):1203–1208, 2012. doi: 10.1007/BF02757695.

[74] D.J. Brady, T. Schweizer, J. Wang, and D.W. Hewak. Minimum loss predictions and measurements in gallium lanthanum sulphide based glasses and fibre. *Journal of Non-Crystalline Solids*, (242):92–98, 1998. doi: 10.1016/S0022-3093(98)00801-1.

[75] Y. D. West, T. Schweizer, D. J. Brady, and D. W. Hewak. Gallium Lanthanum Sulphide Fibers for Infrared Transmission. *Fiber and Integrated Optics*, (19:3):229–250, 2000. doi: 10.1080/01468030050058802.

[76] J. Sanghera and D. Gibson. Optical properties of chalcogenide glasses and fibers. In Jean-Luc Adam and Xianghua Zhang, editors, *Chalcogenide Glasses*, pages 113–138. Woodhead Publishing, 2014. ISBN 978-0-85709-345-5. doi: 10.1533/9780857093561.1.113.

[77] C. T. Moynihan, P. B. Macedo, M. S. Maklad, R. K. Mohr, and R. E. Howard. Intrinsic and impurity infrared absorption in As_2Se_3 glass. *Journal of Non-Crystalline Solids*, (19:3):229–250, 1975. doi: 10.1080/01468030050058802.

[78] V.S. Shiryaev and M.F. Churbanov. Preparation of high-purity chalcogenide glasses. In Jean-Luc Adam and Xianghua Zhang, editors, *Chalcogenide Glasses*, pages 3 – 35. Woodhead Publishing, 2014. ISBN 978-0-85709-345-5. doi: 10.1533/9780857093561.1.3.

[79] H. H. Adler and P. F. Kerr. Variations in infrared spectra, molecular symmetry and site symmetry of sulfate minerals. *American Mineralogist*, (50:1-2):132–147, 1965.

[80] M. F. Churbanov, I. Skripachev, G. E. Snopatin, and V.G. Plotnichenko. High-Purity Glasses Based on Arsenic Chalcogenides. *Optoelectronics And Advanced Materials Rapid Communications*, (3(2):9):341–349, 2001.

[81] J. Yang, Y. Zhao, and R. L. Frost. Infrared and infrared emission spectroscopy of gallium oxide -GaO(OH) nanostructures. *Spectrochimica Acta Part A: Molecular and Biomolecular Spectroscopy*, (74:2):398–403, 2009. doi: 10.1016/j.saa.2009.06.032.

[82] M. Salavati-Niasari, G. Hosseinzadeh, and F. Davar. Synthesis of lanthanum hydroxide and lanthanum oxide nanoparticles by sonochemical method. *Journal of Alloys and Compounds*, (509:10):4098–4103, 2011. doi: 10.1016/j.jallcom.2010.07.083.

[83] M. F. Churbanov. High-purity chalcogenide glasses as materials for fiber optics. *Journal of Non-Crystalline Solids*, (184):25–29, 1995. doi: 10.1016/0022-3093(94)00688-1.

[84] Desolite® 3471-2-136. `http://focenter.com/wp-content/uploads/documents/AngstromBond---Fiber-Optic-Center-AngstromBond-DSM-3471-2-136-UV-Cure-Secondary-Coating-Fiber-Optic-Center.pdf` note = Accessed: 2020-02-10.

[85] K. Hinrichs and K.-J. Eichhorn. *Ellipsometry of Functional Organic Surfaces and Films*. Springer, 2018. ISBN 978-3319758947.

[86] A. Röseler and E. Korte. Infrared spectroscopic ellipsometry. In Peter R. Griffiths John M. Chalmers, editor, *Handbook of Vibrational Spectroscopy*, pages 1112–1137. Wiley, 2002. ISBN 9780471988472,0471988472. doi: 10.1002/0470027320.s2208.

[87] J A Woollam M2000 Spectroscopic Ellipsometer. `https://qd-uki.co.uk/ellipsometers/j-a-woollam-m2000-spectrosopic-ellipsometer/`. Accessed: 2021–02-02.

[88] CompleteEASE Software, J.A. Woollam Ellipsometry Solutions. `https://www.jawoollam.com/ellipsometry-software/completeease`. Accessed: 2020-02-10.

[89] W. Sellmeier. Zur Erklärung der abnormen Farbenfolge im Spectrum einiger Substanzen. *Annalen der Physik*, (219:6):272–282, 1871. doi: 10.1002/andp.18712190612.

[90] TIE-29: Refractive Index and Dispersion. `http://ecee.colorado.edu/~ecen5616/WebMaterial/Schott%20tie-29_refractive_index_v3_us.pdf`
note = Accessed: 2020-02-16.

[91] S. I. Blokhina and N. A. Pankova. Mechanism of striation formation in sheet glass. *Glass and Ceramics*, (35):194–197, 1978. doi: 10.1007/BF00697268.

[92] K1050X RF Plasma Etcher/Asher/Cleaner. `https://www.quorumtech.com/wp-content/uploads/2020/08/K1050X_Brochure.pdf`. Accessed: 2021-01-27.

[93] M. Lee. *Optics for Materials Scientists*. Apple Academic Press, 2019. ISBN 978-1771887571.

[94] X. Cheng and Y. Jaluria. Optimization of a thermal manufacturing process:Drawing of optical fibers. *International Journal of Heat and Mass Transfer*, (48):3560–3573, 2005. doi: 10.1016/j.ijheatmasstransfer.2005.03.012.

[95] C. H. Lees. On the thermal conductivities of single and mixed solids and liquids and their variation with temperature. *Philos. Trans.*, (191):399–440, 1898. doi: 10.1098/rsta.1898.0010.

[96] F. Birch. Flow of Heat in the Front Range, Colorado. *Bull. Geol. Soc. Am.*, (61): 567–630, 1950. doi: 10.1130/0016-7606(1950)61[567:FOHITF]2.0.CO;2.

[97] Goodfellow. `http://www.goodfellow.com/`. Accessed: 2020-02-10.

[98] Gallium Lanthanum Sulphide (GLS). `https://www.crystran.co.uk/optical-materials/gallium-lanthanum-sulphide-gls`. Accessed: 2018-09-24.

[99] M.N. Petrovich, A.Favre, D.W.Hewak, H.N.Rutt, A.C.Grippo, J.F.Gubeli III, K.C.Jordan, G.R.Neil, and M.D.Shinn. Near-IR absorption of Ga:La:S and

Ga:La:S:O glasses by free-electron laser-based laser calorimetry. *Journal of Non-Crystalline Solids*, (326-327):93–97, 2003. doi: 10.1016/S0022-3093(03)00384-3.

[100] Vitron – your specialist for infrared materials infrared transmissive chalcogenide glasses. `http://www.vitron.de/english/IR-Glaeser/Daten-Infrarotglaeser.php#IG5`. Accessed: 2017-12-27.

[101] O. N. Dyatlova and V. V. Bykov. Chemical polishing of glass. *Glass and Ceramics*, (19):77–81, 1962. doi: 10.1007/BF00672421.

[102] C. Wang, P. Wang, X. Liu, L. Hu, and L. Zhanga. Influence of chemical polishing on fluorophosphate fiber preform. *Ceramics International*, (42):5629–5634, 2016. doi: 10.1016/j.ceramint.2015.12.080.

[103] P. B. Adams and D. L. Evans. Chemical durability of borate glasses. In L. D. Pye, V. D. Fréchette, and N. J. Kreidl, editors, *Borate Glasses Structure, properties, applications*, pages 525–537. Plenum Press, 1978. ISBN 978-1-4684-3359-3. doi: 10.1007/978-1-4684-3357-9_28.

[104] B. C. Bunker, G. W. Arnold, D. E. Day, and P. J. Bray. The effect of molecular structure on borosilicate glass leaching. *Journal of Non-Crystalline Solids*, (87:1-2): 226–253, 1986. doi: 10.1016/S0022-3093(86)80080-1.

[105] H. Bach and N. Neuroth. *The Properties of Optical Glass*. Springer, 1998. ISBN 978-3-642-57769-7.

[106] P. Gabbott. *Principles and Applications of Thermal Analysis*. Blackwell Publishing, 2008. ISBN 978-1-4051-3171-1.

[107] A. Marotta, A. Buri, and F. Branda. Nucleation in glass and differential thermal analysis. *Journal of Materials Science*, (16):341–344, 1981. doi: 10.1007/BF00738622.

[108] P. Bastock. *Manufacturing novel fibre*. PhD thesis, University of Southampton, 2015.

[109] A. Hruby. Evaluation of glass-forming tendency by means of DTA. *Czechoslovak Journal of Physics B*, (22):1187–1193, 1972. doi: 10.1007/BF01690134.

[110] C. Zweben, W. S. Smith, and M. W. Wardle. Test Methods for Fiber Tensile Strength, Composite Flexural Modulus, and Properties of Fabric-Reinforced Laminates. *Composite Materials/ Testing and Design (Fifth Conference)*, pages 244–250, 1978.

[111] A; Napolitano, J. H. Simmons, D. H. Blackburn, and R. E. Chidester. Analysis of Low Temperature Viscosity Data for Three NBS Standard Glasses. *Journal of Research of the National Bureau of Standards - A. Physics and Cheminstry*, (78A): 323–329, 1974. doi: 10.6028/jres.078A.017.

[112] R. Hui and M. O'Sullivan. *Fiber Optics Measurement Techniques.* Elsevier, 2009. ISBN 978-0-12-373865-3.

[113] E. Hartouni and J. J. Mecholsky. Mechanical Properties Of Chalcogenide Glasses. In Robert W. Schwartz, editor, *Infrared and Optical Transmitting Materials*, volume 0683, pages 92 – 97. International Society for Optics and Photonics, SPIE, 1986. doi: 10.1117/12.936421. URL `https://doi.org/10.1117/12.936421`.

[114] W. Weibull. A Statistical Distribution Function of Wide Applicability. *Journal of Applied Mechanics*, (18):293–2971, 1951.

[115] J.Su, S. Dai, L. Jiang, C. Lin, C. Yang, N. Zhang, and Y. Yuan. Fabrication and bending strength analysis of low-loss $Ge_{15}As_{25}Se_{40}Te_{20}$ chalcogenide glass fiber: a potential mid-infrared laser transmission medium. *Optical Materials Express*, (9), 2019.

[116] SNOL 1100 °C Laboratory Furnaces. `https://www.wolflabs.co.uk/document/TMS-europe_furnaces_SNOL-1100.pdf`. Accessed: 2020-03-08.

[117] Z. Zhang, J. Cao, J. Zheng, M. Peng, S. Xu, and Z. Yang. Bismuth-doped germanate glass fiber fabricated by the rod-in-tube technique. *Chinese Optics Letters*, (15:12): 121601–, 2017.

[118] Q. Chen, H. Wang, Q. Wang, Q. Chen, and Y. Hao. Modified rod-in-tube for high-NA tellurite glass fiber fabrication: materials and technologies. *Applied Optics*, (54:4):946–952, 2015. doi: 10.1364/AO.54.000946.

[119] F. Guzman. *Fabrication of structured GLS-Se glass preforms for fibre drawing.* PhD thesis, University of Southampton, 2020.

[120] 41213 Graphite adhesive, alcohol based. `https://www.alfa.com/en/catalog/041213/`. Accessed: 2020-04-08.

[121] J.A. Savage and S.Nielsen. Chalcogenide glasses transmitting in the infrared between 1 and 20 — a state of the art review. *Infrared Physics*, (5:4):195–204, 1965. doi: 10.1016/0020-0891(65)90023-0.

[122] S.Shibata, Y.Terunuma, and T.Manabe. Sulfide glass fibers for infrared transmission. *Materials Research Bulletin*, (16:6):703–714, 1981. doi: 10.1016/0025-5408(81) 90271-3.

[123] SEC-Z500X Multi Range/Multi Gas Digital Mass Flow Controller SEC-Z500X. `https://www.horiba.com/en_en/products/detail/action/show/Product/sec-z500x-729/`. Accessed: 2021-04-29.

[124] D. R. Cox and N. Reid. *The Theory of the Design of Experiments*. Chapman and Hall/CRC, 2000. ISBN 978-1584881957.

[125] Minitab® Powerful statistical software everyone can use. `https://www.minitab.com/en-us/products/minitab/`. Accessed: 2020-04-08.

[126] Fine atomizing high-viscosity liquid spray MMA Mini Atomizing Nozzle. `https://www.everloy-spray-nozzles.com/en/support/pdf/MMA.pdf`. Accessed: 2021-04-29.

[127] N-F2 620364.265, SCHOTT Advanced Optics. `https://shop.schott.com/advanced_optics/en/N-F2/c/glass-N-F2`. Accessed: 2021-08-20.

A Appendix: Fibre drawing report structure

NT836 fibre drawing report page 1, summary:

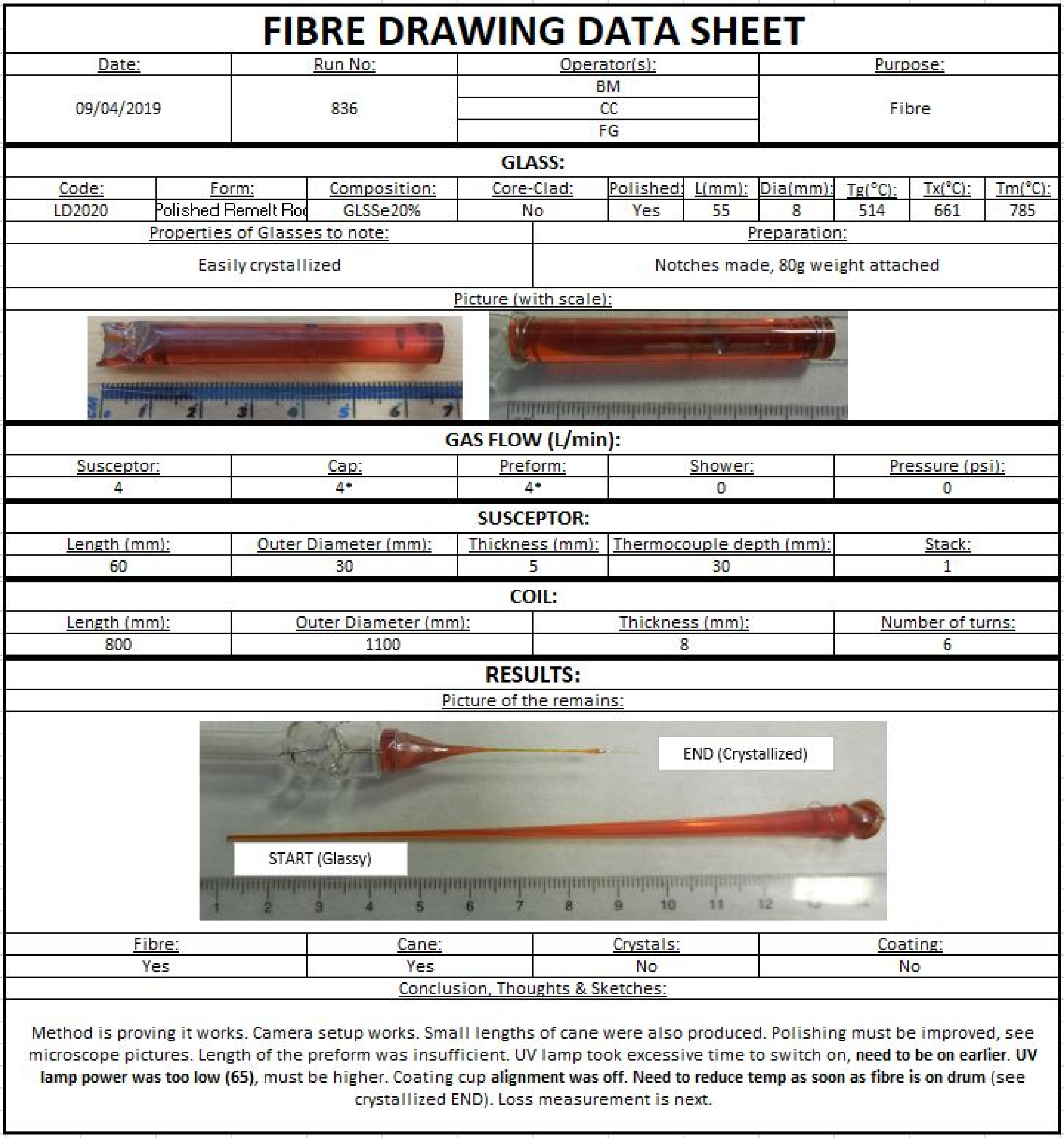

FIBRE DRAWING DATA SHEET

Date:	Run No:	Operator(s):	Purpose:
09/04/2019	836	BM CC FG	Fibre

GLASS:

Code:	Form:	Composition:	Core-Clad:	Polished:	L(mm):	Dia(mm):	Tg(°C):	Tx(°C):	Tm(°C):
LD2020	Polished Remelt Ro	GLSSe20%	No	Yes	55	8	514	661	785

Properties of Glasses to note:	Preparation:
Easily crystallized	Notches made, 80g weight attached

Picture (with scale):

GAS FLOW (L/min):

Susceptor:	Cap:	Preform:	Shower:	Pressure (psi):
4	4*	4*	0	0

SUSCEPTOR:

Length (mm):	Outer Diameter (mm):	Thickness (mm):	Thermocouple depth (mm):	Stack:
60	30	5	30	1

COIL:

Length (mm):	Outer Diameter (mm):	Thickness (mm):	Number of turns:
800	1100	8	6

RESULTS:

Picture of the remains:

Fibre:	Cane:	Crystals:	Coating:
Yes	Yes	No	No

Conclusion, Thoughts & Sketches:

Method is proving it works. Camera setup works. Small lengths of cane were also produced. Polishing must be improved, see microscope pictures. Length of the preform was insufficient. UV lamp took excessive time to switch on, **need to be on earlier**. **UV lamp power was too low (65)**, must be higher. Coating cup **alignment was off. Need to reduce temp as soon as fibre is on drum** (see crystallized END). Loss measurement is next.

NT836 fibre drawing report page 2, fibre drawing timeline (table and automated graph):

FIBRE DRAWING RUN SHEET

Time	Temperature (°C) Set	Control	Monitor/ Prediction	Gas Flow (litre/min) N_2	Ar	O2	Feed Rate (mm/min)	Drum Speed (m/min)	Predicted Fibre OD (um)	Fibre OD (µm)	Fibre Length (m)	Notes	
0.00	820	25	25	4				5.00	0			ramp up to pre temp, everything ready, lamp, drum, feed speed.	1
8.07	820	820	720	4				5.00	0			Get to set temp, wait 5 min before raising up the temp again	2
13.07	830	820	720	4				5.00	0				3
13.20	830	830	720	4				5.00	0			raised 10 C	
14.37	840	830	730	4				5.00	0				4
14.48	840	840	740	4				5.00	0			raised 10 C, no necking	5
15.48	850	840	740	4				5.00	0				6
16.48	860	850	750	4				5	0			raised 10 C, no necking	7
18.26	860	860	760	4			3	5	195.959			necking, quite stiff, feed on	8
19.39	860	860	760	4			0	5	0			feed off	9
19.56	870	860	760	4			0	5	0			raised 10 C	10
20.39	870	870	770	4			5	5	252.982			Feed on, well necking, pulled by hand	11
22.10	870	870	770	4			7	5	299.333			through the coating cup	12
22.56	870	870	770	4			7	5	299.333			on the drum	13
23.28	870	870	770	4			7	10	211.66			drum speed faster for thinner fibre	14
24.52	870	870	770	4			7	10	211.66			UV lamp on (bit of a struggle)	15
25.03	870	870	770	4			7	10	211.66			desolite poured	16
25.29	870	870	770	4			7	10	211.66			Mistake of drum speed, fibre broke. Preform end anyway.	17

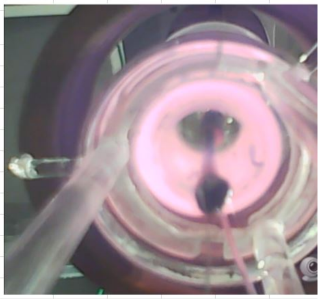

Neck

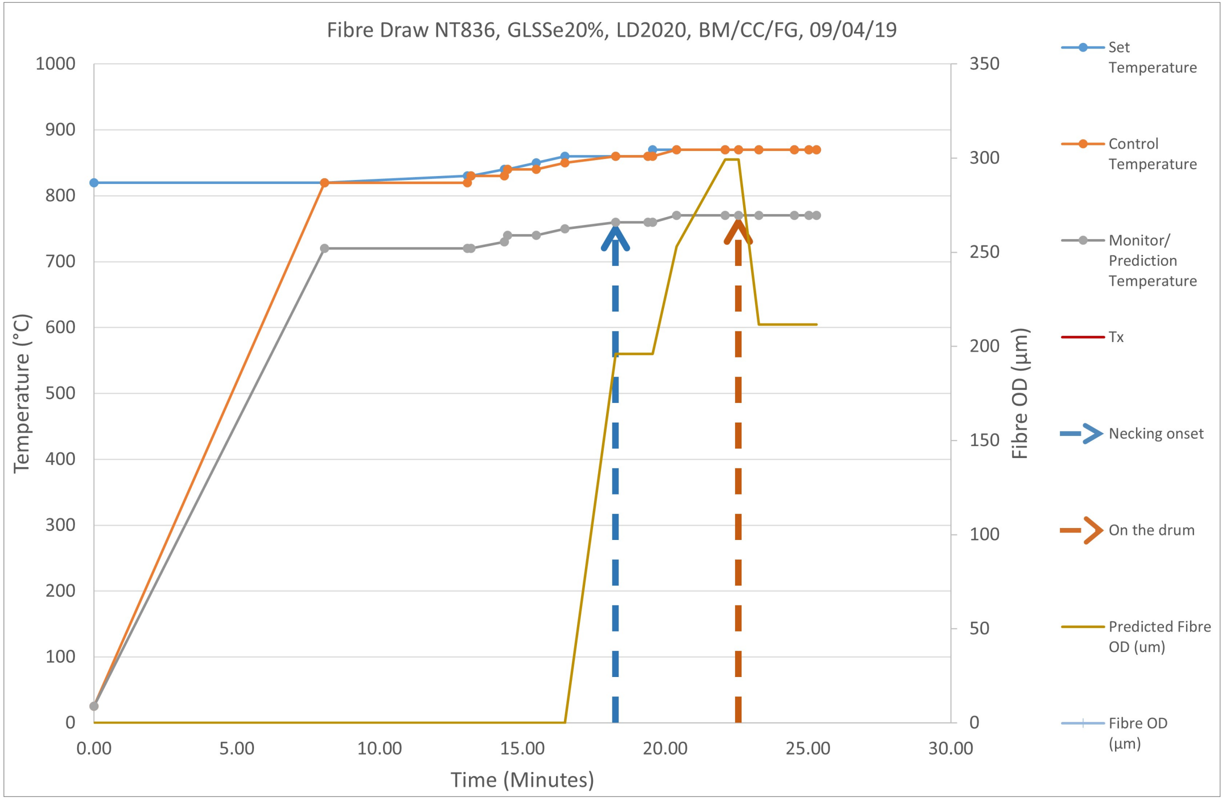

NT836 fibre drawing report page 3, drum and bobbin details:

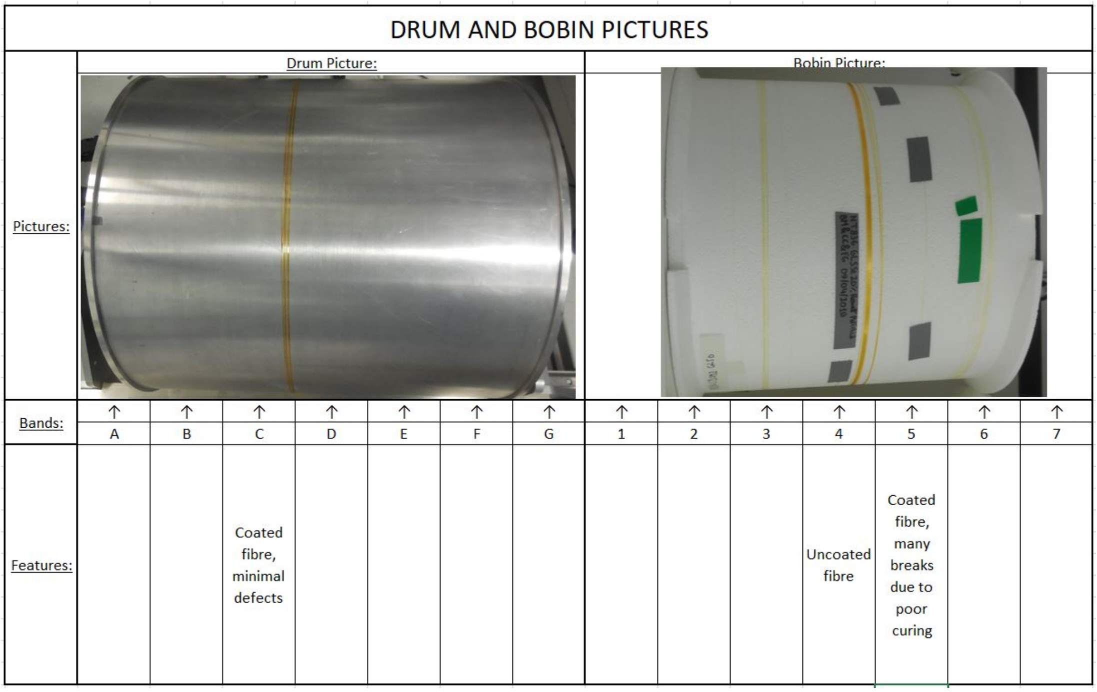

DRUM AND BOBIN PICTURES

	Drum Picture:							Bobin Picture:						
Pictures:														
Bands:	↑	↑	↑	↑	↑	↑	↑	↑	↑	↑	↑	↑	↑	↑
	A	B	C	D	E	F	G	1	2	3	4	5	6	7
Features:			Coated fibre, minimal defects								Uncoated fibre	Coated fibre, many breaks due to poor curing		

NT836 fibre drawing report sheet page 4, fibre microscope pictures:

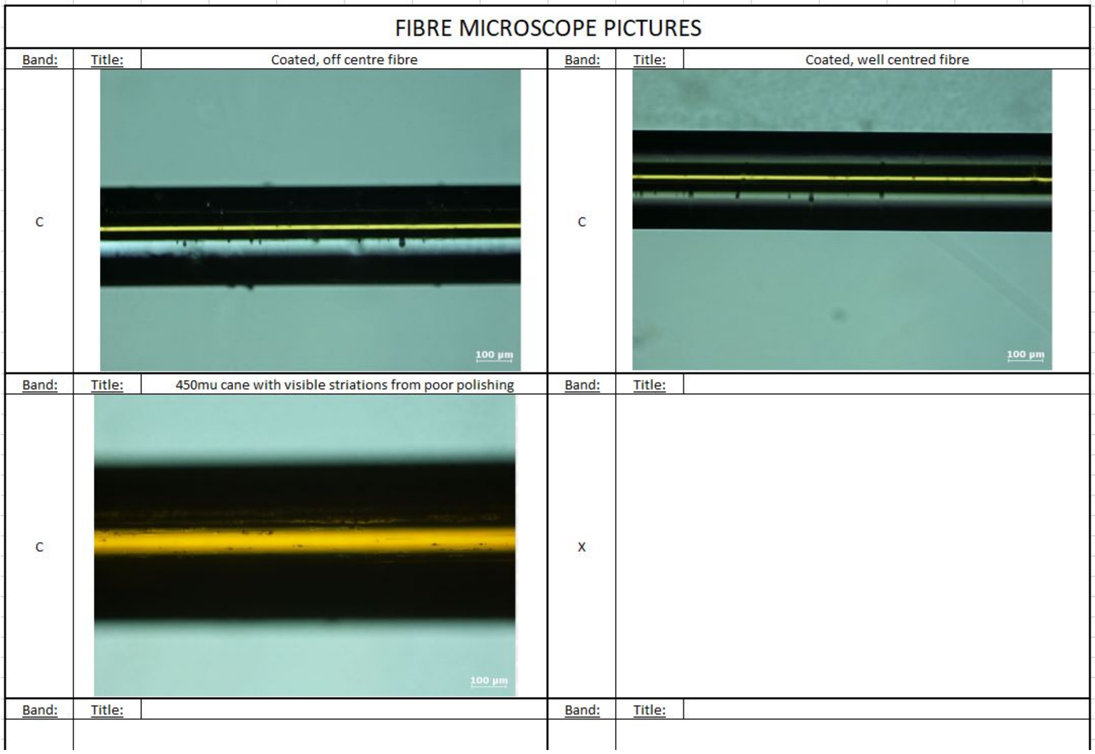

FIBRE MICROSCOPE PICTURES

Band:	Title:	Band:	Title:
C	Coated, off centre fibre	C	Coated, well centred fibre
C	450mu cane with visible striations from poor polishing	X	

B Appendix: Silica crucible drawing summary

Excerpt of the silica crucible drawing summary:

Details					Parameters				Outcome			Loss (dB/m)							Notes
Run	Melt	Date	Composition	Source	Hole size	Canal length	End Height (mm)	End Temp (°C)	Fibre	Fibre diam (µm)	Stability	Laser Diode	OSA	Spectrometer		FTIR			
												1.625µm	**1.625µm**	**4.5µm**	**5µm**	**1.625µm**	**4.5µm**	**5µm**	
807	XXXX	22/01/19	PBG 78	Crushed	1mm	10mm	162.5	800	No	NA	No								Too cold
809	LD2013	23/01/19	GLSSe20%	Crushed	2mm	10mm	162.5	940	NoD	250-150	No								Too hot
810	LD2013	25/01/19	GLSSe20%	Crushed	2mm	10mm	162.5	920	NoD	NA	No								Pressure misapplied
811	LD2013	25/01/19	GLSSe20%	Crushed	2mm	10mm	162.5	910	NoD	250-150	No								Too hot
812	LD2013	28/01/19	GLSSe20%	Crushed	2mm	10mm	162.5	910	No	NA	No								Too cold
813	LD2013	29/01/19	GLSSe20%	Crushed	2mm	10mm	162.5	900	No	NA	No								Emergency Stop
814	LD2013	**29/01/19**	**GLSSe20%**	**Crushed**	**2mm**	10mm	**163.5**	**900**	**Cryst**	**50-25**	**Yes**								**On drum, Few crystals**
815	**LD2013**	**29/01/19**	**GLSSe20%**	**Crushed**	**2mm**	10mm	**163.5**	**920**	**Cryst**	**50-25**	**Yes**								**On drum, More crystals**
816	LD2013	30/01/19	GLSSe20%	Crushed	2mm	10mm	163.5	910	No	NA	No								Emergency Stop, to be fixed before next
817	LD2013	31/01/19	GLSSe20%	Crushed	2mm	10mm	163.5	930	No	NA	No								dripping misunderstood as too cold: means too hot
818	**LD2013**	**02/04/19**	**GLSSe20%**	**Crushed**	**2mm**	10mm	**163.5**	**910**	**Cryst**	**50-25**	**Yes**								**lots on drum but full of crystals**
819	**LD2014**	**02/05/19**	**GLSSe20%**	**Crushed**	**1mm**	**20mm**	**163.5**	**930**	**Cryst**	**50-25**	**Yes**								**lots on drum but full of crystals**
820	LD2014	14/02/19	GLSSe20%	Crushed	1mm	20mm	164	930	NoD	150-25	No								1mm hole is too small
821	**LD2014**	**18/02/19**	**GLSSe20%**	**Crushed**	**1mm**	**20mm**	**164**	**950**	**Cryst**	**200-50**	**Yes**								**on drum, wavy, crystals, temp too low**
822	LD2014	18/02/19	GLSSe20%	Crushed	1mm	20mm	164	NA	No	NA	No								plug fell
823	**LD2014**	**19/02/19**	**GLSSe20%**	**Crushed**	**1mm**	**20mm**	**164**	**1050**	**Yes**	**100-15**	**Yes**								**very thin fibre, seems crystal-free but no light through**
824	LD2014	20/02/19	GLSSe20%	Crushed	1mm	20mm	162.5	1150	No	NA	No								1mm hole is too small
826	LD2014	03/05/19	GLSSe20%	Crushed	2mm	20mm	163	1100	No	NA	No								1mm hole is too small
827	**LD2014**	**03/06/19**	**GLSSe20%**	**Crushed**	**2mm**	**20mm**	**163**	**930**	**Cryst**	**250-200**	No								**Temp too low**
828	**LD2014**	**03/06/19**	**GLSSe20%**	**Crushed**	**2mm**	**20mm**	**163**	**1000**	**Cryst**	**250-25**	No								**Temp too low**
829	**LD2014**	**03/06/19**	**GLSSe20%**	**Crushed**	**2mm**	**20mm**	**163**	**1000**	**Yes**	**50-25**	**Yes**					**10**	**14**	**19**	**Seemingly crystal-free, exceedingly thin**
830	LD2014	03/11/19	GLSSe20%	Crushed	2mm	20mm	163	960	NoD	NA	No								Pressure misapplied
831	**LD2014**	**03/12/19**	**GLSSe20%**	**Crushed**	**2mm**	**20mm**	**163**	**960**	**Yes**	**250-150**	**Yes**								**lots on drum but very wavy**
856	LD2020	08/05/19	GLSSe20%	Crushed	4mm	20mm	163	960	No	NA	No								unexpectedly too cold
857	LD2020	08/06/19	GLSSe20%	Crushed	4mm	20mm	163	960	NoD	150-25	No					24	25	34	unexpectedly too cold
858	LD2020	08/06/19	GLSSe20%	Crushed	4mm	20mm	163	960	Cryst	?	No								full of crystals
860	LD2047	13/08/19	GLSSe20%	Crushed	4mm	20mm	161	960	No	NA	No								Too low
864	LD2047	21/08/19	GLSSe20%	Crushed	5mm	20mm	162	960	No	NA									Too high
865	LD2047	22/08/19	GLSSe20%	Crushed	5mm	20mm	161	960	No	NA									Too low
866	LD2047	22/08/19	GLSSe20%	Crushed	5mm	20mm	161	960	No	NA									Pressure too high, hole must be too big
878	LD2193	28/01/20	GLSSe20%	Cleaved	2mm	15mm	161	960	Cryst	~50	Yes								Correct position is around 161cm, could be SEEN due to the capillary filling up
879	LD2193	29/01/20	GLSSe20%	Cleaved	2mm	15mm	161	960	NoD	>200	No								Pressure was full on when remelting the tip, all fell
880	LD2193	29/01/20	GLSSe20%	Cleaved	2mm	15mm	Vary	960	NoD	250-200	No								First bit almost extruded out, rest fell out: temp too high
881	LD2193	29/01/20	GLSSe20%	Cleaved	2mm	15mm	162	930	Yes	100-40-10	Yes								Temperature is more correct, gradient is reasonable, try to get thicker
882	LD2193	30/01/20	GLSSe20%	Cleaved	2mm	15mm	162	920	Yes		Yes								Thicker fibre achieved, easy and stable experiment

C Appendix: Rod drawing summary

Excerpt of the rod/preform drawing summary:

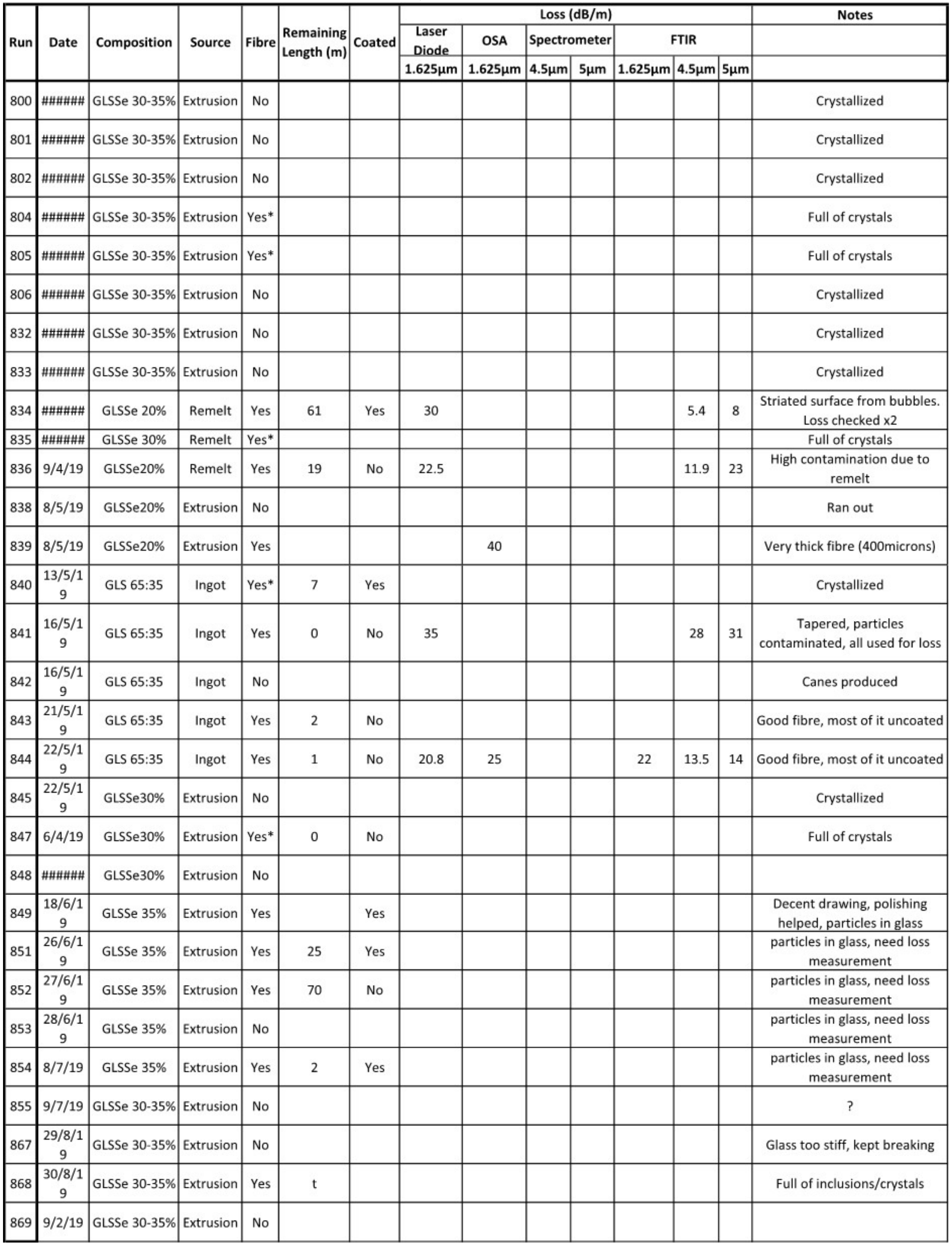

Run	Date	Composition	Source	Fibre	Remaining Length (m)	Coated	Loss (dB/m)							Notes
							Laser Diode	OSA	Spectrometer		FTIR			
							1.625µm	1.625µm	4.5µm	5µm	1.625µm	4.5µm	5µm	
800	######	GLSSe 30-35%	Extrusion	No										Crystallized
801	######	GLSSe 30-35%	Extrusion	No										Crystallized
802	######	GLSSe 30-35%	Extrusion	No										Crystallized
804	######	GLSSe 30-35%	Extrusion	Yes*										Full of crystals
805	######	GLSSe 30-35%	Extrusion	Yes*										Full of crystals
806	######	GLSSe 30-35%	Extrusion	No										Crystallized
832	######	GLSSe 30-35%	Extrusion	No										Crystallized
833	######	GLSSe 30-35%	Extrusion	No										Crystallized
834	######	GLSSe 20%	Remelt	Yes	61	Yes	30					5.4	8	Striated surface from bubbles. Loss checked x2
835	######	GLSSe 30%	Remelt	Yes*										Full of crystals
836	9/4/19	GLSSe20%	Remelt	Yes	19	No	22.5					11.9	23	High contamination due to remelt
838	8/5/19	GLSSe20%	Extrusion	No										Ran out
839	8/5/19	GLSSe20%	Extrusion	Yes				40						Very thick fibre (400microns)
840	13/5/19	GLS 65:35	Ingot	Yes*	7	Yes								Crystallized
841	16/5/19	GLS 65:35	Ingot	Yes	0	No	35					28	31	Tapered, particles contaminated, all used for loss
842	16/5/19	GLS 65:35	Ingot	No										Canes produced
843	21/5/19	GLS 65:35	Ingot	Yes	2	No								Good fibre, most of it uncoated
844	22/5/19	GLS 65:35	Ingot	Yes	1	No	20.8	25			22	13.5	14	Good fibre, most of it uncoated
845	22/5/19	GLSSe30%	Extrusion	No										Crystallized
847	6/4/19	GLSSe30%	Extrusion	Yes*	0	No								Full of crystals
848	######	GLSSe30%	Extrusion	No										
849	18/6/19	GLSSe 35%	Extrusion	Yes		Yes								Decent drawing, polishing helped, particles in glass
851	26/6/19	GLSSe 35%	Extrusion	Yes	25	Yes								particles in glass, need loss measurement
852	27/6/19	GLSSe 35%	Extrusion	Yes	70	No								particles in glass, need loss measurement
853	28/6/19	GLSSe 35%	Extrusion	No										particles in glass, need loss measurement
854	8/7/19	GLSSe 35%	Extrusion	Yes	2	Yes								particles in glass, need loss measurement
855	9/7/19	GLSSe 30-35%	Extrusion	No										?
867	29/8/19	GLSSe 30-35%	Extrusion	No										Glass too stiff, kept breaking
868	30/8/19	GLSSe 30-35%	Extrusion	Yes	t									Full of inclusions/crystals
869	9/2/19	GLSSe 30-35%	Extrusion	No										

D Appendix: Casting summary

Excerpt of the casting experiments summary:

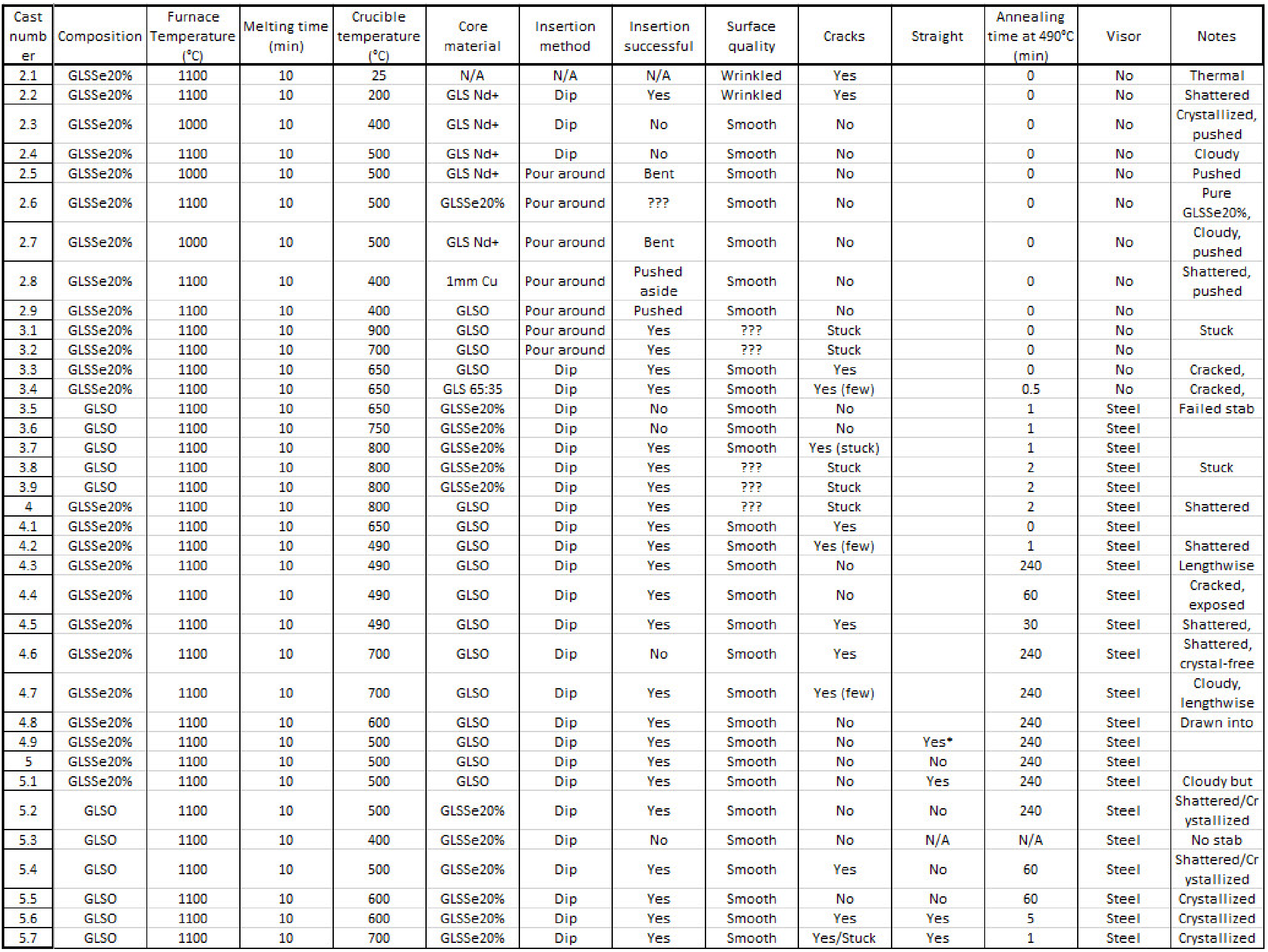

Cast number	Composition	Furnace Temperature (°C)	Melting time (min)	Crucible temperature (°C)	Core material	Insertion method	Insertion successful	Surface quality	Cracks	Straight	Annealing time at 490°C (min)	Visor	Notes
2.1	GLSSe20%	1100	10	25	N/A	N/A	N/A	Wrinkled	Yes		0	No	Thermal
2.2	GLSSe20%	1100	10	200	GLS Nd+	Dip	Yes	Wrinkled	Yes		0	No	Shattered
2.3	GLSSe20%	1000	10	400	GLS Nd+	Dip	No	Smooth	No		0	No	Crystallized, pushed
2.4	GLSSe20%	1100	10	500	GLS Nd+	Dip	No	Smooth	No		0	No	Cloudy
2.5	GLSSe20%	1000	10	500	GLS Nd+	Pour around	Bent	Smooth	No		0	No	Pushed
2.6	GLSSe20%	1100	10	500	GLSSe20%	Pour around	???	Smooth	No		0	No	Pure GLSSe20%,
2.7	GLSSe20%	1000	10	500	GLS Nd+	Pour around	Bent	Smooth	No		0	No	Cloudy, pushed
2.8	GLSSe20%	1100	10	400	1mm Cu	Pour around	Pushed aside	Smooth	No		0	No	Shattered, pushed
2.9	GLSSe20%	1100	10	400	GLSO	Pour around	Pushed	Smooth	No		0	No	
3.1	GLSSe20%	1100	10	900	GLSO	Pour around	Yes	???	Stuck		0	No	Stuck
3.2	GLSSe20%	1100	10	700	GLSO	Pour around	Yes	???	Stuck		0	No	
3.3	GLSSe20%	1100	10	650	GLSO	Dip	Yes	Smooth	Yes		0	No	Cracked,
3.4	GLSSe20%	1100	10	650	GLS 65:35	Dip	Yes	Smooth	Yes (few)		0.5	No	Cracked,
3.5	GLSO	1100	10	650	GLSSe20%	Dip	No	Smooth	No		1	Steel	Failed stab
3.6	GLSO	1100	10	750	GLSSe20%	Dip	No	Smooth	No		1	Steel	
3.7	GLSO	1100	10	800	GLSSe20%	Dip	Yes	Smooth	Yes (stuck)		1	Steel	
3.8	GLSO	1100	10	800	GLSSe20%	Dip	Yes	???	Stuck		2	Steel	Stuck
3.9	GLSO	1100	10	800	GLSSe20%	Dip	Yes	???	Stuck		2	Steel	
4	GLSSe20%	1100	10	800	GLSO	Dip	Yes	???	Stuck		2	Steel	Shattered
4.1	GLSSe20%	1100	10	650	GLSO	Dip	Yes	Smooth	Yes		0	Steel	
4.2	GLSSe20%	1100	10	490	GLSO	Dip	Yes	Smooth	Yes (few)		1	Steel	Shattered
4.3	GLSSe20%	1100	10	490	GLSO	Dip	Yes	Smooth	No		240	Steel	Lengthwise
4.4	GLSSe20%	1100	10	490	GLSO	Dip	Yes	Smooth	No		60	Steel	Cracked, exposed
4.5	GLSSe20%	1100	10	490	GLSO	Dip	Yes	Smooth	Yes		30	Steel	Shattered,
4.6	GLSSe20%	1100	10	700	GLSO	Dip	No	Smooth	Yes		240	Steel	Shattered, crystal-free
4.7	GLSSe20%	1100	10	700	GLSO	Dip	Yes	Smooth	Yes (few)		240	Steel	Cloudy, lengthwise
4.8	GLSSe20%	1100	10	600	GLSO	Dip	Yes	Smooth	No		240	Steel	Drawn into
4.9	GLSSe20%	1100	10	500	GLSO	Dip	Yes	Smooth	No	Yes*	240	Steel	
5	GLSSe20%	1100	10	500	GLSO	Dip	Yes	Smooth	No	No	240	Steel	
5.1	GLSSe20%	1100	10	500	GLSO	Dip	Yes	Smooth	No	Yes	240	Steel	Cloudy but
5.2	GLSO	1100	10	500	GLSSe20%	Dip	Yes	Smooth	No	No	240	Steel	Shattered/Crystallized
5.3	GLSO	1100	10	400	GLSSe20%	Dip	No	Smooth	No	N/A	N/A	Steel	No stab
5.4	GLSO	1100	10	500	GLSSe20%	Dip	Yes	Smooth	Yes	No	60	Steel	Shattered/Crystallized
5.5	GLSO	1100	10	600	GLSSe20%	Dip	Yes	Smooth	No	No	60	Steel	Crystallized
5.6	GLSO	1100	10	600	GLSSe20%	Dip	Yes	Smooth	Yes	Yes	5	Steel	Crystallized
5.7	GLSO	1100	10	700	GLSSe20%	Dip	Yes	Smooth	Yes/Stuck	Yes	1	Steel	Crystallized

E Appendix: Viscosity DOE data

Viscosity optimization data recording scheme:

Viscosity (CP)	Hole size (mm)	Tip length (mm)	Pressure (readout)	Pressure (PSI)	Continuity	Mass flow (g/min)	Neck shape	Thickness (µm)	Thickness (µm)	Thickness average (µm)	Max Exit speed (m/s)	Min Exit speed (m/s)	Avg Exit speed (m/s)
100,000	2	20	340	0.281	No		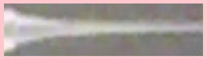	#N/A	#N/A	#N/A	#N/A	#N/A	#N/A
100,000	2	20	350	0.702	No	0.067	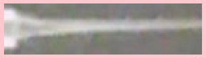	#N/A	#N/A	#N/A	#N/A	#N/A	#N/A
100,000	2	20	360	1.123	Yes	0.121		50	57	53.5	1.0555806	0.812235	0.9339078
100,000	2	20	380	1.965	Yes	0.19	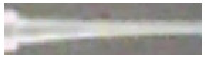	60	70	65	1.1510578	0.8456751	0.9983665
100,000	2	20	400	2.807	Yes	0.275		75	90	82.5	1.066243	0.7404465	0.9033448
100,000	2	20	420	3.649	Yes	0.35		90	107	98.5	0.9423865	0.6667247	0.8045556
100,000	2	20	440	4.491	Yes	0.45		100	115	107.5	0.9814282	0.7421007	0.8617645
100,000	2	20	450	4.912	Yes	0.5		120	125	122.5	0.7572749	0.6979045	0.7275897
100,000	2	15	340	0.281	No	0.0492	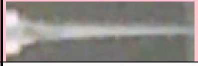	#N/A	#N/A	#N/A	#N/A	#N/A	#N/A
100,000	2	15	350	0.702	Yes	0.095	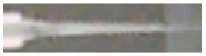	47	54	50.5	0.9379375	0.7105295	0.8242335
100,000	2	15	375	1.7545	Yes	0.225	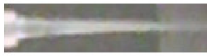	60	71	65.5	1.3630948	0.973446	1.1682704
100,000	2	15	400	2.807	Yes	0.34	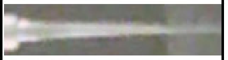	79	94	86.5	1.1881486	0.8392073	1.0136779
100,000	2	15	425	3.8595	Yes	0.465	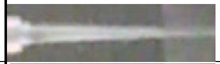	106	140	123	0.9025832	0.5174196	0.7100014
100,000	2	15	450	4.912	Yes	0.618		133	142	137.5	0.7619583	0.6684329	0.7151956
100,000	2	15	475	5.9645	Yes	0.74		150	166	158	0.7172907	0.5856816	0.6514862
100,000	2	10	330	-0.14	No		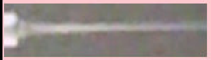	#N/A	#N/A	#N/A	#N/A	#N/A	#N/A

F Appendix: Published work

- **Conference paper:**

  Morgan, K. Zeimpeikis, I., Huang, CC., Feng, Z. Craig, C., Weatherby, E., Aspiotis, N., Alzaidy, G.A., Ravagli, A., **Moog, B.J.**, Guzman Cruz, F.A.,Lewis, A., Delaney, M. and Hewak, D. (2019) *"Chaclogenide materials and applications: from bulk to 2D (Invited Talk)"*. Electronic Materials and Applications 2019 (EMA 2019), Orlando, United States. 23-25 Jan 2019. 1pp.

  Abstract: In this talk, we give an overview of our chalcogenide material and device capabilities and the applications they are driving, scaling from bulk glasses to two-dimensional films. Using a melt-quench technique, we routinely manufacture a family of Ga:La:S semiconducting glasses which offer considerable advantages over commercially available chalcogenides, expanding uses in defense, medical and sensing. We use these glasses to produce optical fibers using extrusion, rod and crucible drawing. We are also developing these materials further, for example by incorporating selenium resulting in improved infrared transmission, enabling both thermal and visible imaging for object recognition. Transition metal dichalcogenides (TMDCs) are promising alternatives to graphene, with bandgaps tunable through composition and number of layers. Today's challenge remains in the fabrication of large area atomically thin TMDCs on desired substrates. We have developed chemical vapor and atomic layer deposition techniques to deposit highly crystalline TMDCs, from nanometers down to a monolayer on up to 6 inch wafers. We recently developed novel patterning techniques that result in defect free devices. Our applications range from 3D photonic crystals to photovoltaics and transistors. Finally we deposit chalcogenide thin films via sputtering and demonstrate applications which exploit their phase change and thermoelectric properties.

- **Conference paper:**

  Guzman Cruz, F.A., Ravagli, A., Craig, C., **Moog, B.J.** and Hewak, D. (2019) *"Fabrication of structured GLS-Se glass preforms by extrusion for fibre drawing"*. OSA Fron- tiers in Optics Laser Science APS/DLS, Washington, United States. 15-19 Sep 2019. 2pp. (doi.org/10.1364/fio.2019.jw4a.11).

  Abstract: Chalcogenide glasses due to their low phonon energy and high ion solubility, make them an ideal candidate for active and passive fibres for infrared applications. Co-extrusion process for structured preform fabrication is explored.

- **Conference paper:**

  Ravagli, A., **Moog, B.J.**, Guzman Cruz, F.A., Craig, C., Kar, A., Mackenzie, M., Morris, J. and Hewak, D. (2018) *"Chalcogenide materials: Novel compositions and new applications"*. Advanced Architectures in Photonics 2018, Cambridge, United Kingdom. 02-05 Sep 2018.

  Abstract: In this talk, we describe our recent work on selenium modified Ga:La:S glasses. The addition of Se improves the infrared transmission sufficiently to capture enough of the 8-12 micron window to allow thermal imaging, while at the same time, allowing sufficient visible transmission for object recognition using conventional image capturing. The addition of Se has other implications, increasing the optical nonlinearity, providing longer fluorescent lifetimes when doped with rare earth ions and expanding the transmission window in the important 3-5 micron region. Ga:La:S glasses are superior to commercially available chalcogenides based on alloys of Ga and/or As with S, Se and/or Te. They offer significantly higher alkaline resistance, greater mechanical strength and over 300oC higher working temperature (Tg ¿ 500oC). All of these new features suggest Ga:La:S-Se may be a material suitable for the next generation of mid-IR sources through supercontinuum or rare earth doping.

- **Conference paper:**

  Guzman Cruz, F.A., Ravagli, A., Craig, C., **Moog, B.J.** and Hewak, D. (2018) *"Chalcogenide optical fibres based on gallium lanthanum sulphide-Se for passive and active applications"*. São Paulo School of Advanced Science on Frontiers in Lasers and their Applications, São Paulo, Brazil. 16-27 Jul 2018.

  Abstract: Chalcogenide optical fibres contain mixtures of chalcogen elements (i.e. S, Se and Te) bonded covalently to other metallic elements that facilitate a stable glass formation. Our work in particular focuses on chalcogenide glasses containing a high proportion of lanthanum, that is gallium lanthanum sulphide glasses (GLS). These glasses due to their nature are characterized by a range of desirable properties such as chemical durability, host for rare-earth (RE) ions, low thermal expansion, high laser damage threshold, density and refractive index and a good transparency in the infrared (IR) region. Characteristics that are beneficial for active and passive applications such as sensors or high-energy IR laser power delivery, as examples. To increase the IR transmission window of GLS glasses a new family of chalcogenides have been developed, incremental additions of Se to the GLS glasses have proved their value to improve the transmission spectrum from visible to Long Wavelength Infrared (LWIR) range up to 15m, depending on the composition. The strong thermal and mechanical characteristics of GLS-Se glasses compared to GLS have also shown that they can suit the production of optical elements, such as optical fibres that require certain thermal and mechanical stability for fibre drawing to avoid crystallization and breakages. Theoretical minimum loss predictions in GLS based optical fibres have shown up to 0.5 dB km-1 at 3.5 m, used in thermal imaging, unfortunately we are still far from that value but big efforts are being made to improve the production of optical fibres as shown in Fig. 1 by obtaining novel processes and more pure raw materials. Chalcogenide RE doped glasses have demonstrated laser action, showing that they are suitable for active applications such as optical amplifiers and lasers. The aim of this research is to join the well-known properties of chalcogenides glasses for the IR region with the development of a novel process to obtain functional passive and active optical fibres and prove the reliability as a host for RE ions, future work will include laser demonstration.

- **Journal paper:**

  Guzman Cruz, F.A., Craig, C., **Moog, B.J.**, Ravagli, A. and Hewak, D. (2020) *"GLS-Se optical fibre from extruded glass structured preforms and rods for the IR region"* Optical Materials Express 11(1):157-170 (doi.org/10.1364/OME.411571)

  Abstract: Depending on composition, chalcogenide glasses have been proven as a reliable medium to transmit light in the range from the visible to the long-wave infrared (LWIR), specialty glasses based on gallium lanthanum sulfide (GLS) with a selenium (Se) addition. This family of glasses offers a broad transparency window depending on the composition. Their optical, mechanical, and thermal properties have been exploited in their bulk form. In this paper, we demonstrate the fabrication of optical fibres from extruded structured (core-clad) preforms and rods, with an emphasis on maintaining the intrinsic characteristics of the glass and exploiting the optical fibre geometry for light delivery.

- **Conference poster:**

Moog, B.J., Craig, C., Guzman Cruz, F.A. and Hewak, D. (2021) *"Processing of Infrared Chalcogenide Glass Fabrication of Infrared Fibre, Ultra-thin Fibre, Multi-Spectral Windows, and extending the composition range of Gallium Lanthanum Sulphide (GLS)"* Royce Student Summit 2021 (Poster). 2-3 Mar 2021.

- **Conference paper:**

  Moog, B.J., Craig, C., Guzman Cruz, F.A. and Hewak, D. (2021) *"The fabrication of infrared chalcogenide glass fibre, ultra-thin fibre and large diameter gallium lanthanum sulfide windows."* Royce Student Summit 2021. 2-3 Mar 2021 (Presentation).

  Abstract: The development of specialty infrared glasses have produced a number of alternative compositions which have become well established for many applications, both for industrial use and academic research. Among them, gallium lanthanum sulfide glass is a particularly suitable competitor. Indeed, its transmission window ranging from 500 nm to 16µm in bulk glass, along with its mechanical strength and high transition temperatures compared to currently available chalcogenides make it a viable candidate for a variety of applications, such as thermal imaging and chemical sensing. The thermal properties of gallium lanthanum sulfide make shaping it to a specific end delicate and challenging work. In particular, its crystallization temperature lies near its softening temperature, making any process involving the manipulation of softened or molten glass highly time and temperature constrained. In this work, several methods have been employed to enable gallium lanthanum sulfide to fulfill new applications. It has been crucible-drawn, made into ultrathin (10µm) fibre, cast and cut into fibre drawing preforms, made into large diameter (¿90mm) windows and significant progress is being made towards achieving graded-index, by taking advantage of its wide composition variability.

- **Journal paper:**

  Guzman Cruz, F.A., Craig, C., **Moog, B.J.**, Ravagli, A., Morgan, K. and Hewak, D. (20201) *"Manufacturing of GLS-Se glass rods and structured preforms by extrusion for optical fiber drawing for the IR region"* Optical Engineering 60(4): 045101 (doi.org/10.1117/1.OE.60.4.045101)

  Abstract: Chalcogenide glasses are amorphous solid materials formed from chalcogen elements bonding with metals to form typically in binary or tertiary compounds.

One family of chalcogenide glasses, based on gallium and lanthanum sulphides, possesses properties important for the infrared (IR) window transmissions and IR applications; these include thermal stability, high solubility of rare earth ions, low phonon energy and high laser damage threshold. Efforts have been made to produce new chalcogenide glasses that can extend the IR transmission window further into the IR. Work has led to the successful melting of a selenium-modified gallium lanthanum sulphide (GLS-Se) glass that can transmit up to 15m, however these glasses have, to date, only been demonstrated in bulk glass form. We aim to develop processes for the fabrication of chalcogenide optical fiber to exploit the properties of chalcogenide glasses. Several potential applications include sensing for the civil, medical, and military areas, as these materials offer transmission over much of the molecular fingerprint region (2 to 25m). The aim of our work is to understand and control the thermal properties and stability of GLS-Se glasses without compromising their optical properties, in order to produce transparent glass rods and demonstrate the feasibility in fabrication for structured optical preforms by extrusion, as the first step to achieve optical fiber from GLS-Se glass.